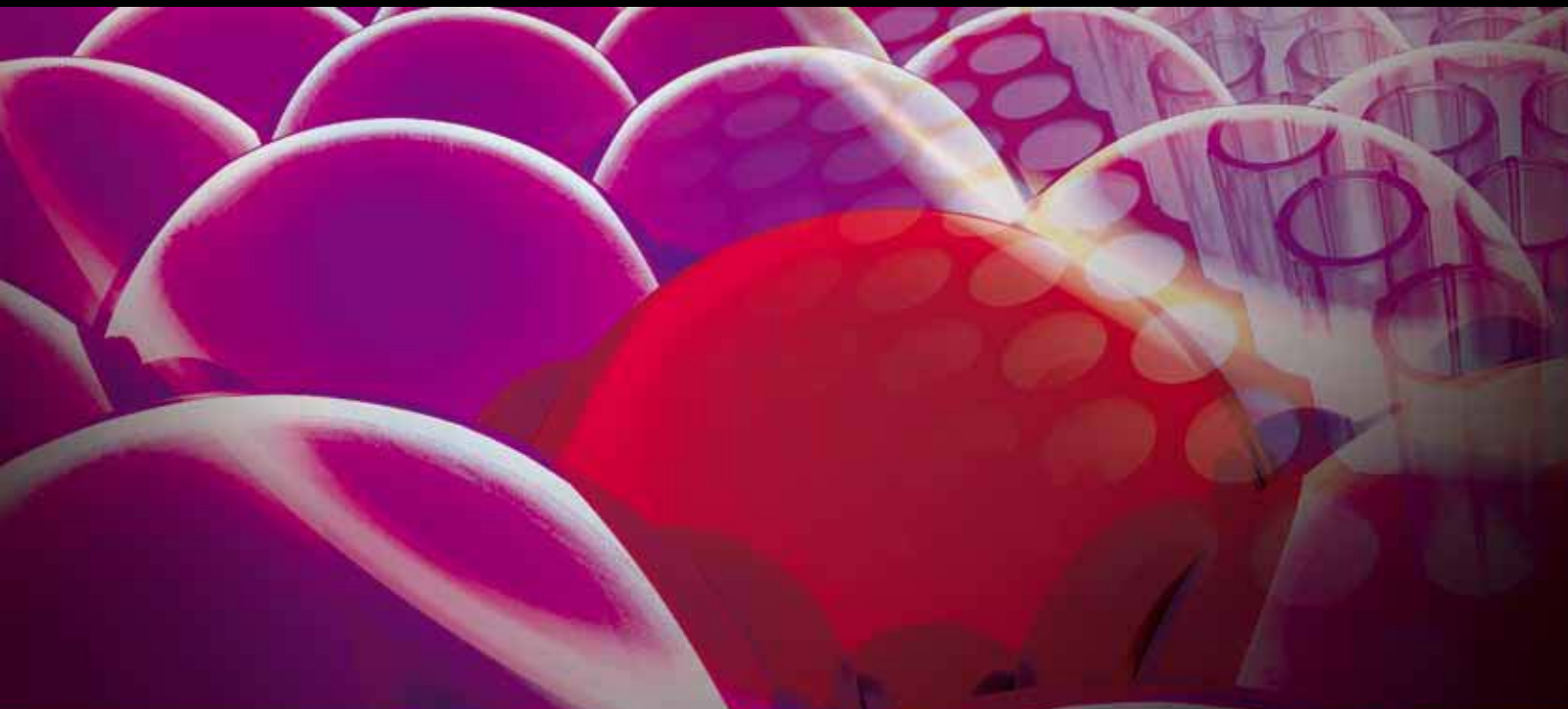# Advances in Mixing Technology: Recent Advances in Mixing Research and Development

Guest Editors: Shunsuke Hashimoto, Naoto Ohmura, See-Jo Kim, and Shaliza B. Ibrahim

Advances in Mixing Technology: Recent Advances in Mixing Research and Development

Advances in Mixing Technology: Recent Advances in Mixing Research and Development

Guest Editors: Shunsuke Hashimoto, Naoto Ohmura, See-Jo Kim, and Shaliza B. Ibrahim

Editorial Board

Contents

Editorial

Advances in Mixing Technology: Recent Advances in Mixing Research and Development

Shunsuke Hashimoto,[1] Naoto Ohmura,[2] See-Jo Kim,[3] and Shaliza B. Ibrahim[4]

[1] *Division of Chemical Engineering, Graduate School of Engineering Science, Osaka University, 1-3 Machikaneyama, Toyonaka, Osaka 560-8531, Japan*

[2] *Department of Chemical Science and Engineering, Graduate School of Engineering, Kobe University, Rokkodai, Nada, Kobe 657-8501, Japan*

[3] *Department of Mechanical Design Engineering, Andong National University, Songchon-Dong, Kyungbuk, Andong 760-749, Republic of Korea*

[4] *Department of Civil Engineering, University of Malaya, 50603 Kuala Lumpur, Malaysia*

Correspondence should be addressed to Shunsuke Hashimoto, shunsuke@cheng.es.osaka-u.ac.jp

Mixing has been one of essential unit operations for chemical engineering processes. Among a number of mixers, stirred tanks that are available in a wide variety of tank sizes and impeller shapes are the most frequently adopted to homogenize different substances and to conduct chemical reactions in industrial chemical processes. In addition, there are various technologies for fluid mixing: static mixer, micromixer, unsteady agitation, eccentric agitation, and so on. Recently in various industrial processes, a wide range of operation for stirred tank is required depending on purposes and conditions, and high efficiency on mixing has been strongly required. In addition, the techniques of computer simulation analyses by the use of CFD software have been dramatically developed, which is essential to analyze the mixing mechanism. The main goal of this special issue was to gather contributions dealing with the latest breakthrough of mixing techniques. There is a collection of twelve papers in this special issue focused on mixing fundamental (2 papers), multiphase mixing (3 papers), chemical reactive mixing for metallurgical industry, and biotechnology (4 papers), and new technology of mixing (3 papers) ranging in topic from laminar-to-turbulent mixing by means of both experimental analyses and numerical simulations. The highlights of each paper are introduced as follows.

In the paper entitled by "*Design mixers to minimize effects of erosion and corrosion erosion*", E. E. Janz and J. Fasano from Chemineer, Inc. provide techniques for minimizing the wear on impellers cover the choice of impeller, size and speed of the impeller, alloy selection, and surface coating or coverings. An example is provided as well as an assessment of the approximate life improvement.

In the work entitled by "*Effect of impeller agitation on preparation of tetra-n-butyl ammonium bromide semiclathrate hydrate slurries*", S. Hashimoto et al. from Osaka University, which shows the effect of impeller agitation on particle size distribution and aggregation of tetra-n-butyl ammonium bromide (TBAB) semiclathrate hydrate slurries. The slurries containing TBAB solution and its semiclathrate hydrate have attracted a lot of interest as latent heat transport media. First of all, the effects of impeller rotational speed and impeller type on the particle size and frequency of aggregation are investigated. The results suggest that the particle size distribution and the frequency of particle aggregation are strongly affected by the intensity of shear rate and its uniformity, which is controllable with impeller type and its rotation speed.

In the research entitled by "*Correlation of power consumption for several kinds of mixing impellers*", Y. Kato et al. review the correlations of power consumption in nonbaffled and baffled agitated vessels with several kinds of impellers, which are developed in a wide range of Reynolds numbers from laminar-to-turbulent flow regions. The power correlations are based on Kamei and Hiraoka's expressions for paddle and pitched paddle impellers. The calculated correlation values

agree well with experimental ones, and the correlations will develop the other types of impellers.

In the paper entitled by "*Effect of temperature change on geometric structure of isolated mixing regions in stirred vessel*", N. Ohmura et al. show the effect of temperature change on the geometric structure of isolated mixing regions (IMRs) in a stirred vessel by the decolorization of fluorescent green dye by acid-base neutralization. The step temperature-change can dramatically reduce the elimination time of IMRs, as compared with a steady temperature operation. During the transient process from an initial state to disappearance of IMR, the IMR showed interesting three-dimensional geometrical changes, that is, simple torus with single filament, simple torus without filaments, a combination of crescent shape and circular tori, and doubly-entangled torus.

In the work entitled by "*Phosphorus removal from wastewater using oven-dried alum sludge*", S. A. Rashid and W. T. Mohammed deal with the removal of phosphorus from wastewater by using oven-dried alum sludge (ODS) as an adsorbent that was collected from Al-Qadisiya treatment plant (Iraq). The results show that the percent removal of phosphorus increases with the increase of oven dried alum sludge dose, but thr pH of solution has insignificant effect. In addition, the oven-dried alum sludge was effective in adsorbing phosphorus, and percent removal of phosphorus reaches 85% with increasing of contact time.

In the paper entitled by "*Laminar mixing in stirred tank agitated by an impeller inclined*", K. Takahashi et al. show the mixing performance in a vessel agitated by an impeller inclined itself, which is considered one of the typical ways to promote mixing performance by the spatial chaotic mixing. The effect of eccentric position of inclined impeller on mixing time was also studied and a significant reduction of mixing time is observed. To confirm the experimental results, the velocity profiles are calculated numerically and two novel numerical simulation methods are proposed.

In the research entitled by "*Characterization of minimum impeller speed for suspension of solids in liquid at high solid concentration, using gamma ray densitometry*", P. A. Tanguy et al. exhibit the limitations of applying conventional measurement techniques for the accurate characterization of critical impeller speed for just off-bottom suspension (Njs) at high solid concentrations. Subsequently, the Gamma-Ray Densitometry technique for characterizing Njs is introduced, which can overcome the limitations of previous experimental techniques. The theoretical concept of this method is explained and experimental validation is presented to confirm the accuracy of the Gamma-Ray Densitometry technique. By utilizing the similarity to the incipient movement of solid particles in other systems, a theoretical model for Njs prediction is presented.

In the work entitled by "*The effects of mixing, reaction rates and stoichiometry on yield for mixing sensitive reactions—Part I: model development*", S. M. Kresta et al. provide the model and design of the effect of mixing, reaction rates, and stoichiometry on yield for mixing sensitive reactions: competitive-consecutive and competitive-parallel reactions. A detailed investigation of the effects of initial mixing condition (striation thickness), dimensionless

reaction rate ratio and reaction stoichiometry on the yield of desired product shows that the stoichiometry has a considerable effect on yield. All three variables are found to interact strongly. Model results for 12 stoichiometries are used to determine the mixing scale and relative rate ratio, needed to achieve a specified yield for each reaction scheme. The results show that all three variables need to be considered when specifying reactors for mixing sensitive reactions. Incidentally, Professor S. K. also organizes another paper.

In the paper entitled by "*Effect of mixing on microorganism growth in loop bioreactors*", A. M. Al Taweel et al. show the impact of mixing on the promotion of microorganism growth rate using a multiphase forced circulation pipe-loop reactor model capable of identifying conditions under which it is possible to convert natural gas into single cell protein (SCP). The impact of mixing in the interphase mass transfer is found to exert a critical role in determining the overall productivity of the bioreactor, particularly at the high cell loadings needed to reduce the capital costs associated with the large-scale production needed for the production of relatively low-value SCP in a sustainable manner.

In the paper entitled by "*Investigation of the pulsed annular gas jet for chemical reactor cleaning*", C. V. Fedorovich et al. provide the study of aerodynamic efficiency of the impulse system carried by numerical modeling and experimentally with the help of a specially created experimental facility. The characteristics of the pulsed jets mixing are investigated and designed pulsed peelings system has shown high efficiency and reliability in functioning that allows us to recommend it for wide spreading in chemical industry.

The research of S. Ibrahim entitled by "*Zwietering's equation for the suspension of porous particles and the use of curved blade impellers*" reveals Njs of porous palm shell activated carbon (PSAC) particles for a few impeller blades. Specific power per unit mass for all three impellers showed reduction towards minima as the concentration of particles increased. The result means that the Zwietering equation can be used to predict suspension for porous particles with adjustment to the solid particle density. *S* values for curved-blade impellers are presented for the first time.

In the work entitled by "*The effects of mixing, reaction rates and stoichiometry on yield for mixing sensitive reactions—part II: design protocols*", S. M. Kresta et al. provide the design strategy of the effect of mixing, reaction rates, and stoichiometry on yield for mixing sensitive reactions.

Acknowledgments

Research Article

The Effects of Mixing, Reaction Rates, and Stoichiometry on Yield for Mixing Sensitive Reactions—Part II: Design Protocols

Syed Imran A. Shah,[1] Larry W. Kostiuk,[2] and Suzanne M. Kresta[1]

[1] *Department of Chemical and Materials Engineering, University of Alberta, 9107-116 Street, 7th Floor ECERF,*
  Edmonton, AB, Canada T6G 2V4
[2] *Department of Mechanical Engineering, University of Alberta, 4-9 Mechanical Engineering Building,*
  Edmonton, AB, Canada T6G 2G8

Correspondence should be addressed to Suzanne M. Kresta, suzanne.kresta@ualberta.ca

Competitive-consecutive and competitive-parallel reactions are both mixing sensitive reactions where the yield of desired product depends on how fast the reactants are brought together. Recent experimental results have suggested that the magnitude of the mixing effect may depend strongly on the stoichiometry of the reactions. To investigate this, a 1D, dimensionless, reaction-diffusion model was developed at the micromixing scale, yielding a single general Damköhler number. Dimensionless reaction rate ratios were derived for both reaction schemes. A detailed investigation of the effects of initial mixing condition (striation thickness), dimensionless reaction rate ratio, and reaction stoichiometry on the yield of desired product showed that the stoichiometry has a considerable effect on yield. All three variables were found to interact strongly. Model results for 12 stoichiometries are used to determine the mixing scale and relative rate ratio needed to achieve a specified yield for each reaction scheme. The results show that all three variables need to be considered when specifying reactors for mixing sensitive reactions.

1. Introduction

Mixing-sensitive reactions are reactions which are particularly sensitive to the rate at which the reactants are brought together, that is, how fast they are mixed. These reactions are of two main types: the competitive-consecutive (C-C) reaction scheme, which involves two competing reactions where the second unwanted reaction consumes the desired product from the first reaction, and the competitive-parallel (C-P) reaction scheme, where two reactions compete for a limiting reagent, forming a desired and undesired product. The effects of mixing and relative reaction rates of the competing reactions have been investigated previously and it is known that mixing can affect the product distribution significantly. Past work has concentrated on the investigation of a single classical stoichiometry for each of the reaction schemes [1–25]. This work investigates whether the

stoichiometry of the reaction plays a role in determining the maximum final yield of desired product and how the three reactor design variables—mixing, reaction, rate and stoichiometry interact.

In a previous paper by Shah et al. [26], a model was developed to capture the effects of reaction stoichiometry, mixing, (characterized by the Damköhler number (Da)), and relative reaction rates, (characterized by a dimensionless reaction rate ratio (k_2/k_1)). General forms of the reactions as given in Table 1 were used to derive mass balance equations. From the equations a single Damköhler number that is common to both reaction types and all stoichiometries (Da) and a dimensionless reaction rate ratio (k_2/k_1) that is specific to each reaction type were obtained. Both Da and k_2/k_1 depend on the stoichiometric coefficients of the reaction scheme, making the potential impact of stoichiometry immediately

evident. The expression for the general Damköhler number is:

$$\begin{aligned} \text{Da} &= k_1' \left(\frac{\rho_T}{M}\right)^\epsilon \frac{L_B^2}{D_B} = \frac{k_1' \left(\rho_T/M\right)^\epsilon}{\left(D_B/L_B^2\right)} \\ &= \frac{\text{rate of desired reaction}}{\text{rate of diffusion}} \\ &= (\text{rate of desired reaction}) * (\text{diffusion time}). \end{aligned} \quad (1)$$

The effect of stoichiometry on the Damköhler number is given by ϵ, the stoichiometric coefficient of the limiting reagent (B) in the desired reaction. The diffusion time in the smallest eddies is determined by the mixing scale, L_B, the thickness of the smallest striation of concentration homogeneity, and the molecular diffusivity, D_B, which completes the variables needed to determine the diffusion time at the smallest scales of segregation.

The effect of the relative reaction rates of the competing reactions is also of interest. The model provides dimensionless reaction rate ratios for the C-C and C-P reactions as follows:

$$\text{C-C:} \quad \frac{k_2}{k_1} = \left[\frac{\beta}{\alpha}\left(\frac{\alpha}{1+\epsilon}\right)^\beta \left(\frac{\rho_T}{M}\right)^{\beta+\gamma-\epsilon-1} \right] \frac{k_2'}{k_1'}, \quad (2)$$

$$\text{C-P:} \quad \frac{k_2}{k_1} = \left[\frac{\gamma}{\epsilon}\left(\frac{\rho_T}{M}\right)^{\gamma-\epsilon} \right] \frac{k_2'}{k_1'}. \quad (3)$$

These dimensionless reaction rate ratios are specific to the type of mixing sensitive reaction, C-C or C-P, and incorporate the effect of the relative reaction rates of the competing reactions (k_2'/k_1') as well as the effect of stoichiometry. The model was validated for the classical reaction stoichiometry where all coefficients are equal to 1. This work extends the simulations to ten new stoichiometries where one or more of the coefficients are greater than one.

For both the C-C and C-P simulations, the Damköhler number was varied from 0.01 to 10 000 in 100x increments, where 0.01 is the best and 10 000 is the worst mixing. The dimensionless reaction rate ratio (k_2/k_1) was varied from 1 to 0.00001 in 10x increments, where 1 is the worst ratio and 0.00001 is the best ratio. For the C-C reactions, ϵ was always 1 and α, β, γ were given a value of either 1 or 2. For the C-P reactions, ϵ and γ were either 1 or 2. Table 2 shows the different C-C reaction scheme stoichiometries investigated, with the corresponding dimensionless reaction rate ratios. Table 3 shows the same terms for the C-P reaction schemes.

We caution the reader that this model is highly simplified. Elementary reactions involving 4 molecules do not exist, so the kinetic expressions for Cases 7 and 8 for the C-C reaction schemes and for Case 4 for the C-P reactions will assuredly have a different and more complex form for real reactions with similar stoichiometries. The mixing model is equally flawed when considering real systems. The simple striation model does not allow for variation of striation thickness with time as mixing progresses or between eddies; it includes no consideration of the effects of stretching and no mixing between layers. The dynamics of a more realistic model of turbulence would be much more complex. Keeping these limitations in mind, the goal of this work is to investigate whether a hypothesis that the reaction stoichiometry can have a significant impact on the course of mixing sensitive reactions is reasonable.

TABLE 1: General mixing sensitive reaction schemes.

Competitive consecutive (C-C)	Competitive parallel (C-P)
$A + \epsilon B \xrightarrow{k_1'} \alpha P$	$A + \epsilon B \xrightarrow{k_1'} P$
$\beta P + \gamma B \xrightarrow{k_2'} S$	$C + \gamma B \xrightarrow{k_2'} S$

2. Numerical Details

Simulation of the systems of five or six PDEs for the C-C and C-P reaction schemes, respectivelyr (shown in Tables 4 and 5), was carried out using COMSOL 3.4, a finite element PDE Solver. It is worth noting that for the C-C reaction scheme only four of the equations are independent while for the C-P reaction scheme there are five independent equations. The 1D, transient, convection, and diffusion mass transport model was used, with the mass fractions for each species specified as the independent variables. The default Lagrangian-quadratic element was chosen. The specified 1D geometry line of unit length was split equally into two subdomains and a mesh of 2048 equally spaced elements with 2049 nodes was generated. The mesh was tested for grid independence, and it was found that 1024 elements was sufficient resolution to ensure repeatable results to within the required tolerance of the solver, which was set to 10^{-6}. Since the geometry was only 1D and the computational cost was minimal, a finer mesh than the minimum required resolution was used. The total time taken per simulation was approximately 30 seconds. The boundary conditions were specified for no net mass transfer across the boundaries.

Figure 1 shows the initial conditions for the C-C and C-P schemes. For the C-C cases, the initial conditions were chosen such that all of the mass initially present could be converted to desired product P. This was done by specifying a ratio of $A:B$ as $1:1$ in all the simulations, with A and B being present in pure striations, $w_{A_0} = w_{B_0} = 1$. For the C-P scheme, owing to the parallel nature of the reactions, the initial conditions were a bit more complicated. They were chosen such that either A or C could consume the entire limiting reagent B by themselves, that is, the initial ratios depended on the stoichiometric coefficients in the reaction scheme. In order to satisfy the constant mass concentration assumption of the model, it was necessary to include the inert in the C-P simulations. w_{B_0} and w_{IZ_0} were always set to 0.5, and $w_{A_0} w_{C_0}$, w_{IY_0} were calculated accordingly.

For most cases the limiting reagent, B, was completely consumed by $\text{Da} \cdot t^* = 500$ so the transient simulation results are shown from $\text{Da} \cdot t^* = 0$ to $\text{Da} \cdot t^* = 500$. $\text{Da} \cdot t^*$ is equivalent to a dimensionless reaction time where $\text{Da} \cdot t^* = t/\tau_R$, so running all simulations to $\text{Da} \cdot t^* = 500$ is the same as running all simulations for 500 reaction times.

TABLE 2: Stoichiometries of reaction schemes and the corresponding dimensionless reaction rate ratio for the eight different C-C reactions. Da was always Da $= k_1'(\rho_T/M)(L_B^2/D_B)$.

Case	Reaction scheme	$\epsilon, \alpha, \beta, \gamma$	k_2/k_1
1	$A + B \xrightarrow{k_1'} 2P$ $P + B \xrightarrow{k_2'} S$	1, 2, 1, 1	$(1/2)(k_2'/k_1')$
2	$A + B \xrightarrow{k_1'} P$ $P + B \xrightarrow{k_2'} S$	1, 1, 1, 1	$(1/2)(k_2'/k_1')$
3	$A + B \xrightarrow{k_1'} P$ $2P + B \xrightarrow{k_2'} S$	1, 1, 2, 1	$(1/2)(\rho_T/M)(k_2'/k_1')$
4	$A + B \xrightarrow{k_1'} 2P$ $2P + B \xrightarrow{k_2'} S$	1, 2, 2, 1	$(\rho_T/M)(k_2'/k_1')$
5	$A + B \xrightarrow{k_1'} 2P$ $P + 2B \xrightarrow{k_2'} S$	1, 2, 1, 2	$(1/2)(\rho_T/M)(k_2'/k_1')$
6	$A + B \xrightarrow{k_1'} P$ $P + 2B \xrightarrow{k_2'} S$	1, 1, 1, 2	$(1/2)(\rho_T/M)(k_2'/k_1')$
7	$A + B \xrightarrow{k_1'} P$ $2P + 2B \xrightarrow{k_2'} S$	1, 1, 2, 2	$(1/2)(\rho_T/M)^2(k_2'/k_1')$
8	$A + B \xrightarrow{k_1'} 2P$ $2P + 2B \xrightarrow{k_2'} S$	1, 2, 2, 2	$(\rho_T/M)^2(k_2'/k_1')$

TABLE 3: Stoichiometries of reaction schemes and the corresponding dimensionless reaction rate ratio and Damköhler number for the four different C-P reactions.

Case	Reaction scheme	ϵ, γ	k_2/k_1	Da
1	$A + B \xrightarrow{k_1'} P$ $C + B \xrightarrow{k_2'} S$	1, 1	k_2'/k_1'	$k_1'(\rho_T/M)(L_B^2/D_B)$
2	$A + B \xrightarrow{k_1'} P$ $C + 2B \xrightarrow{k_2'} S$	1, 2	$2(\rho_T/M)(k_2'/k_1')$	$k_1'(\rho_T/M)(L_B^2/D_B)$
3	$A + 2B \xrightarrow{k_1'} P$ $C + B \xrightarrow{k_2'} S$	2, 1	$(1/2)(\rho_T/M)^{-1}(k_2'/k_1')$	$k_1'(\rho_T/M)^2(L_B^2/D_B)$
4	$A + 2B \xrightarrow{k_1'} P$ $C + 2B \xrightarrow{k_2'} S$	2, 2	k_2'/k_1'	$k_1'(\rho_T/M)^2(L_B^2/D_B)$

The modelled equations allow for specification of the Damköhler number, the dimensionless reaction rate ratio and the stoichiometry. All possible combinations of the values of reaction rate ratio, Damköhler number, and stoichiometry for the C-C reaction scheme (stoichiometries given in Table 2) and the C-P reaction scheme (stoichiometries given in Table 3) were investigated. This resulted in 192 converged cases for the C-C and 96 converged cases for the C-P reaction scheme.

3. Results and Discussion

The results obtained for the simulations are profiles of mass fraction for each of the species over the space x^* for all dimensionless times t^*. Samples of these results were given in Shah et al. [26] (Figures 2 and 3, resp.).

Since the main process objective is to maximize the production of desired product P, the profiles of mass fraction of P are of most interest. These profiles were integrated over the domain to obtain the total mass of desired product and the instantaneous yield using the formula:

$$Y_P = \frac{\text{mass of species } P \text{ at } t^*}{\text{max mass of } P \text{ obtainable}} = \frac{\int_{-0.5}^{0.5} w_P dx^*(t^*)}{0.5 w_{B_o}(1 + 1/\epsilon)}. \quad (4)$$

Following Y_P over time gives the progression of yield over time. The total production of P as time progresses can be observed in a plot of Y_P versus dimensionless time $Da \cdot t^*$. Figures 4 and 5 in Shah et al. [26] show examples of such plots.

The final yield of P at $Da \cdot t^* = 500$ was plotted against Da and k_2/k_1 to assess the effects of each of the variables on the final yield of desired product. Representative figures are presented here. The results (Y_P versus Da and k_2/k_1)

TABLE 4: System of equations for competitive-consecutive reaction scheme, to be used with (1) and (2).

Species	Mass balance partial differential equation
A	$\partial(w_A)/\partial t^* = \left(\partial^2(w_A)/\partial x^{*2}\right) - [\mathrm{Da}\, w_A w_B^\epsilon]$
B	$\partial(w_B)/\partial t^* = \left(\partial^2(w_B)/\partial x^{*2}\right) - \epsilon[\mathrm{Da}\, w_A w_B^\epsilon] - (\alpha\gamma/\beta)\left[\mathrm{Da}(k_2/k_1)w_P^\beta w_B^\gamma\right]$
P	$\partial(w_P)/\partial t^* = \left(\partial^2(w_P)/\partial x^{*2}\right) + (1+\epsilon)\left[\mathrm{Da}\, w_A w_B^\epsilon - \mathrm{Da}(k_2/k_1)w_P^\beta w_B^\gamma\right]$
S	$\partial(w_S)/\partial t^* = \left(\partial^2(w_S)/\partial x^{*2}\right) + (1+\epsilon+(\alpha\gamma/\beta))\left[\mathrm{Da}(k_2/k_1)w_P^\beta w_B^\gamma\right]$
I	$\partial(w_I)/\partial t^* = \partial^2(w_I)/\partial x^{*2}$

TABLE 5: System of equations for competitive-parallel reaction scheme, to be used with (1) and (3).

Species	Mass balance partial differential equation
A	$\partial(w_A)/\partial t^* = \left(\partial^2(w_A)/\partial x^{*2}\right) - [\mathrm{Da}\, w_A w_B^\epsilon]$
B	$\partial(w_B)/\partial t^* = \left(\partial^2(w_B)/\partial x^{*2}\right) - \epsilon[\mathrm{Da}\, w_A w_B^\epsilon] - \epsilon\left[\mathrm{Da}(k_2/k_1)w_c w_B^\gamma\right]$
C	$\partial(w_C)/\partial t^* = \left(\partial^2(w_C)/\partial x^{*2}\right) - (\epsilon/\gamma)\left[\mathrm{Da}(k_2/k_1)w_c w_B^\gamma\right]$
P	$\partial(w_P)/\partial t^* = \left(\partial^2(w_P)/\partial x^{*2}\right) + (1+\epsilon)[\mathrm{Da}\, w_A w_B^\epsilon]$
S	$\partial(w_S)/\partial t^* = \left(\partial^2(w_S)/\partial x^{*2}\right) + (\epsilon+(\epsilon/\gamma))\left[\mathrm{Da}(k_2/k_1)w_c w_B^\gamma\right]$
I	$\partial(w_I)/\partial t^* = \partial^2(w_I)/\partial x^{*2}$

make up a 3D surface for each stoichiometry. Slices of the results are presented as follows: a base case set of six slices of Y_P versus Da is presented to show the effects of mixing (Da) and dimensionless reaction rate ratio (k_2/k_1) on yield of desired product. Where a point needs to be clarified, the results are replotted by taking a slice along the k_2/k_1 axis or by expanding the time variable. The results are then revisited to focus on the effect of stoichiometry and how it interacts with mixing and reaction rate. The same set of plots is repeated for the C-P reaction schemes. The results are then summarized to show a possible design specification space of Da and k_2/k_1 for a specified yield.

3.1. Competitive-Consecutive (C-C) Reaction.
Figures 2(a) to 2(f) are semilog plots of the final Y_P versus Damköhler number for decreasing dimensionless reaction rate ratio, k_2/k_1. The curves on each of the plots represent the eight C-C stoichiometry cases. The effects that are of interest are the effects of the Damköhler number (mixing), reaction rate ratio k_2/k_1 (chemical kinetics), and the reaction stoichiometry (Cases 1 to 8). The Damköhler number is plotted on the x-axis and the results are first presented from this perspective. Next, the effect of ratio k_2/k_1 is observed by comparing graphs (a) to (f). Finally the effect of stoichiometry (Cases 1 to 8) within each graph is reviewed and summarized. At each step, selected results are replotted either to illustrate a point more clearly or to provide a perspective on the data.

3.1.1. The Effect of Damköhler Number (Da): The Well-Mixed Limit.
The plots in Figure 2 show a decrease in yield of desired product with increasing Damköhler number. This trend is true for all stoichiometries and at all values of k_2/k_1. A larger Damköhler number represents worse mixing (larger striations) and a smaller Damköhler number represents improved mixing (smaller striations). The yield for Da = 1 and Da = 0.01 is the same for all stoichiometries at all

k_2/k_1. The yield at Da = 100 decreases for the cases with unfavourable dimensionless reaction rate ratios ($k_2/k_1 \geq 0.01$) but remains for same for the favourable k_2/k_1 ratios ($k_2/k_1 \leq 0.001$). By Da = 10000 the yield always decreases, regardless of the value of k_2/k_1.

The data is replotted in Figures 3(a) and 3(b) for the best (Case 7) and worst (Case 2) stoichiometry cases to confirm the Y_P versus k_2/k_1 trends. This shows that the results for Da = 0.01 and Da = 1 lie exactly on top of one another. When Da is increased from 1 to 100 the curves diverge over part of the domain: for Case 2 when $k_2/k_1 \geq 0.001$ and for Case 7 when $k_2/k_1 \geq 0.01$. It is concluded that Da = 1 is the well-mixed limit for large k_2/k_1, while Da = 100 is the well-mixed limit for small k_2/k_1 and that the meaning of "large k_2/k_1" depends on the stoichiometry.

3.1.2. The Effect of Dimensionless Reaction Rate Ratio (k_2/k_1): Can Chemistry Solve the Problem?
Looking at the changes in Figure 2 from (a) to (f), as k_2/k_1 decreases the yield increases. This result is as expected, since a smaller k_2/k_1 gives a slower undesired side reaction. As k_2/k_1 is decreased it is also clear that the curves for the different stoichiometric cases approach, collapsing onto one curve by $k_2/k_1 = 0.0001$. The results are replotted to directly compare the effect of k_2/k_1 on the 8 cases in Figure 4(a): $Da = 1$ (well mixed), (b) $Da = 100$ and (c) $Da = 10000$ (badly mixed).

Y_P increases to 1 as k_2/k_1 decreases for all stoichiometries, with the 8 cases collapsing at about $k_2/k_1 = 0.001$ for the well-mixed cases and at $k_2/k_1 = 0.0001$ for Da = 10000, the badly mixed case. The yield of the badly mixed case is about half of what was obtained in the well-mixed results. This brings up an interesting question: "Is it possible to get perfect yield of desired product, that is, $Y_P \sim 1$, for Da = 10000, a badly mixed case?". The simulations for the Da =10000 cases were rerun for a hundred times longer to Da $\cdot t^* = 50000$ instead of Da $\cdot t^* = 500$. Figure 5 shows the results of these simulations. To obtain a perfect yield with
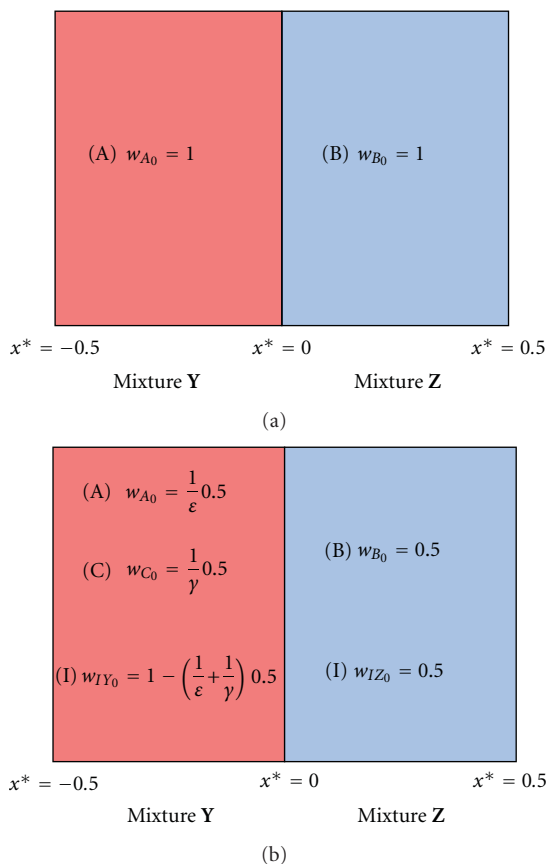
FIGURE 1: Initial conditions for (a) C-C and (b) C-P reaction scheme simulations.

insufficient mixing, both a 100x longer reaction time and 100x better chemistry are required. This clearly illustrates the need for an improved understanding of mixing.

3.1.3. Effect of Stoichiometry. Returning for a final time to Figure 2 there is a clear effect of stoichiometry on the final yield of desired product, and the effect of stoichiometry shows interactions with both the mixing scale and the dimensionless reaction rate ratio.

In Figure 2(a) ($k_2/k_1 = 1$) the curves are widely separated, coming closer together as Da increases and the effect of bad mixing becomes dominant. There is a clear distinction between stoichiometries, with Cases 7 and 8 having the highest yields and therefore the most favourable stoichiometry, and Cases 1 and 2 having the lowest yields, meaning they have the least favourable stoichiometries. Cases 1 and 2 require only two molecules for the side reaction, while Cases 7 and 8 require four molecules. This places a mass transfer and collision probability limitation on the side reaction for Cases 7 and 8, hence making them more favourable for the desired reaction. Cases 3–6 all consume 3 molecules in the undesired reaction, making the mass transfer limit similar; however, at the large values of k_2/k_1, Cases 3 and 4 have a much lower yield of P than Cases 5 and 6, forming two bands.

Comparing the stoichiometries of Cases 1–4 with Cases 5–8, for the first 4 cases, 1 molecule of B is consumed in the second reaction, and in the last 4, 2 molecules of B are consumed. Comparing Case 3 to Case 6 and Case 4 to Case 5, the desired reactions are identical, whereas the stoichiometric coefficients on the undesired reaction are different. Of particular interest is the larger stoichiometric coefficient on reagent B in Cases 5 and 6. An examination of the local concentration profiles showed that B is the limiting reagent locally in the second reaction. Since Cases 5 and 6 require two molecules of the limiting reagent in the undesired reaction, making it harder for the reaction to proceed, it makes sense that the yield of P will be higher for Cases 5 and 6 as compared to Cases 3 and 4.

Now comparing the stoichiometries within pairs, in three of the four pairs producing more P in the first reactions leads to an increase in P consumption in the second reaction and a drop in yield. In other words, at large k ratios, the two reactions compete effectively for reagents. Under these conditions, when less P is produced in the desired reaction, the side reaction is slowed down. The trend is reversed for Cases 3 and 4. These are the only cases where more P is consumed than B in the undesired reaction, so in this case it appears that the mass transfer limit on P relative to B overwhelms the effect of producing more P.

These trends continue in Figure 2(b) ($k_2/k_1 = 0.1$) and Figure 2(c) ($k_2/k_1 = 0.01$). For $k_2/k_1 \leq 0.001$ the curves collapse onto each other and the effect of stoichiometry vanishes. For the very bad mixing condition ($Da = 10000$) that was allowed to proceed for a very long time, Figure 5, the effect of stoichiometry creeps back into the picture, affecting yield at all the way to $k_2/k_1 = 0.00001$.

3.1.4. Summary of Results for the C-C Reaction Scheme. For competitive-consecutive reactions, we have the following.

(a) Da $\leq$ 1 is the well-mixed limit when $k_2/k_1 \geq 0.01$ and Da $\leq$ 100 is the limit when $k_2/k_1 < 0.01$.

(b) $k_2/k_1 \leq 0.001$ with Da $\leq$ 100 provides yields >95% at Da $\cdot t^* = 500$.

(c) The effect of stoichiometry can be large if the k_2/k_1 is unfavourable. This effect vanishes at $k_2/k_1 \leq$ 0.001 for short reaction times and good mixing. At longer reaction times with bad mixing conditions, the effect of stoichiometry reappears and requires a much smaller value of k_2/k_1 to eradicate.

(d) The most favorable stoichiometry is one where the desired reaction consumes fewer molecules than the undesired reaction, thus placing a mass transfer limitation on the undesired reaction.

3.2. Competitive-Parallel (C-P) Reaction. The analysis proceeds through the same questions posed for the C-C reaction.

(i) What is the well mixed limit (Da)?

(ii) How much can chemistry contribute (k_2/k_1)?

(iii) Is the stoichiometry important?
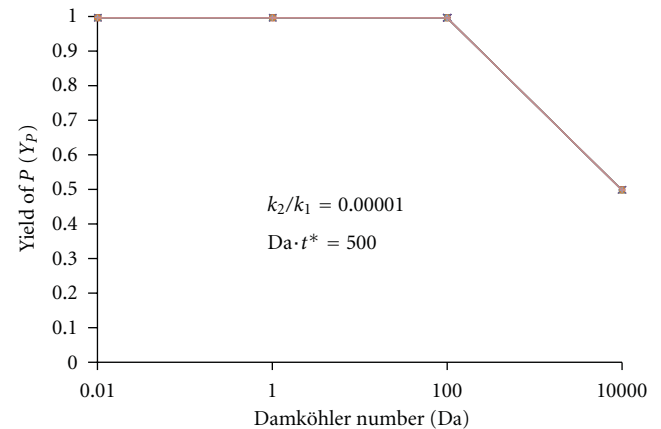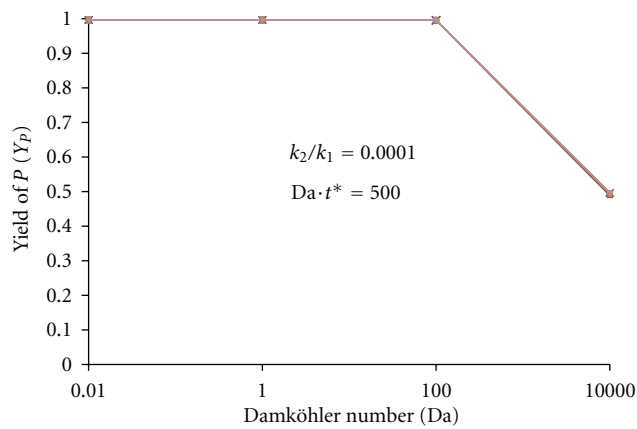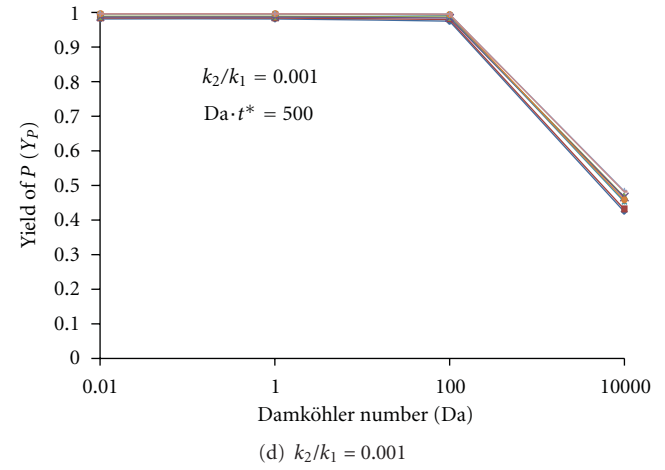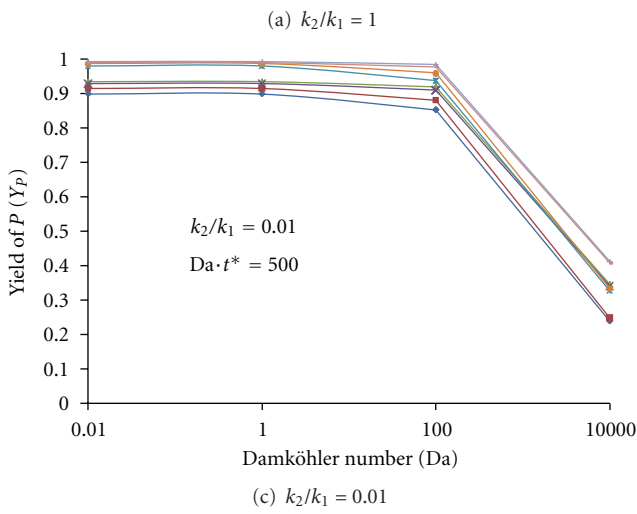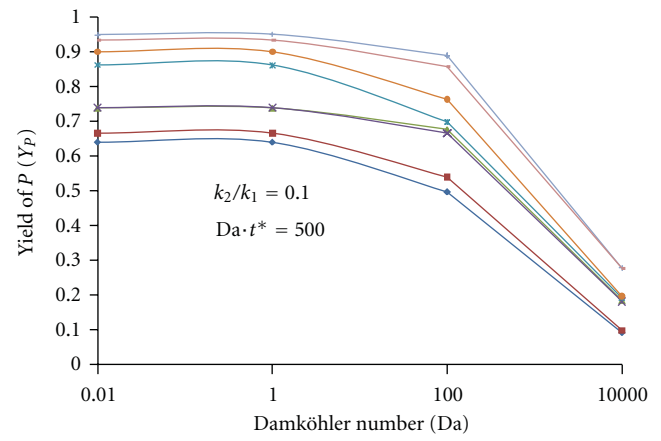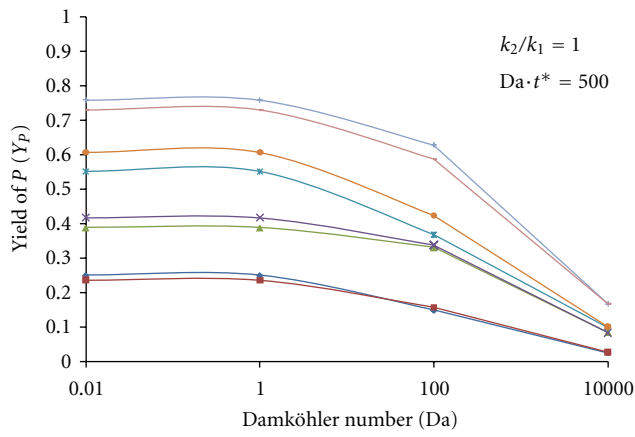
Figure 2: Plots of yield of P versus Da for decreasing k_2/k_1 ratios for the C-C cases.

(a) C-C stoichiometry Case 2: $A + B \xrightarrow{k'_1} P; P + B \xrightarrow{k'_2} S$

(b) C-C stoichiometry Case 7: $A + B \xrightarrow{k'_1} P; 2P + 2B \xrightarrow{k'_2} S$

Figure 3: Plots of Yield of P versus k_2/k_1 for two sample C-C stoichiometries. The curves represent the different Da. Curves for Da = 0.01 lie exactly under the curves for Da = 1.

(a) Da = 1
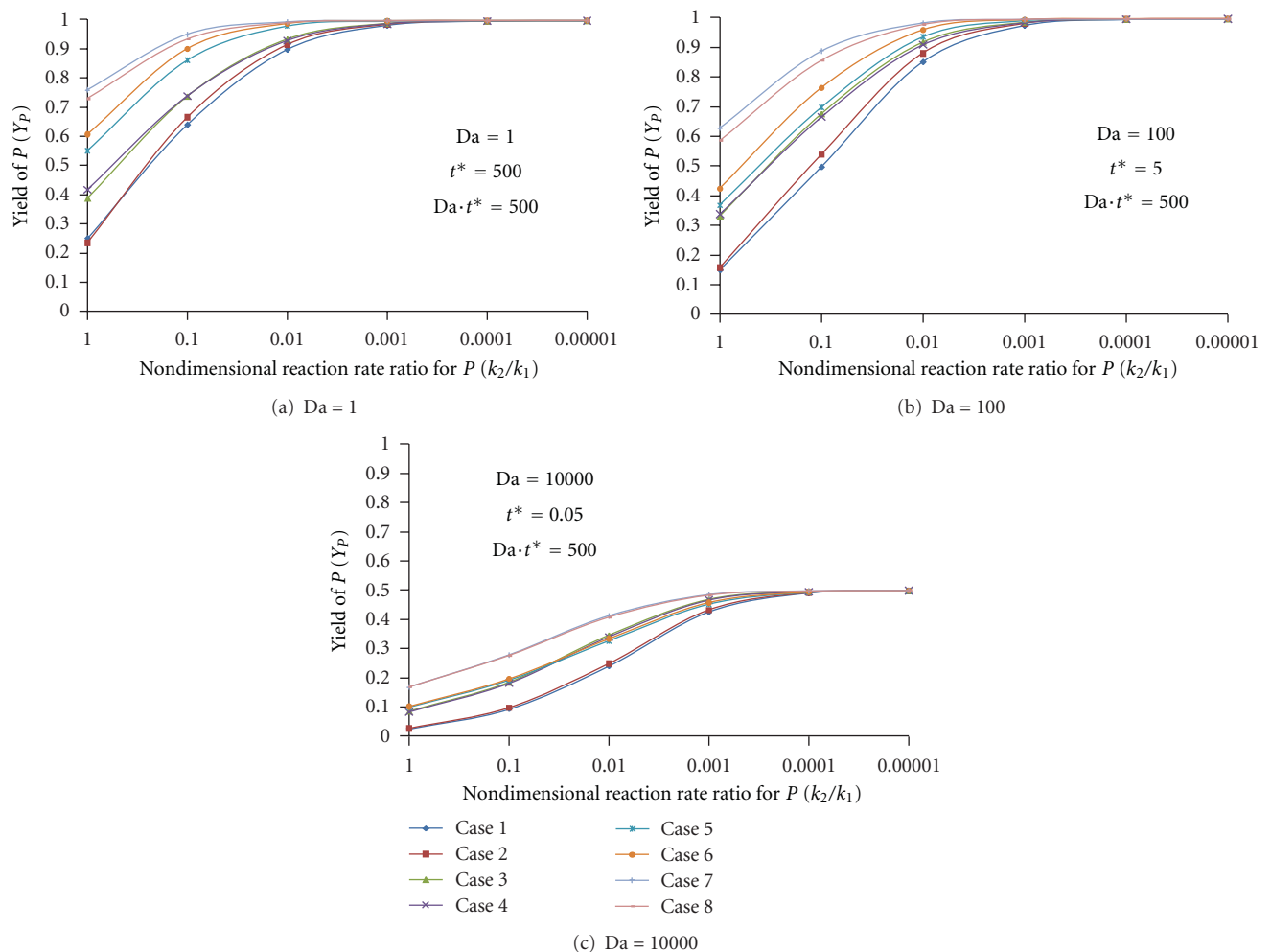
(b) Da = 100

(c) Da = 10000

Figure 4: Plots of yield of P versus k_2/k_1 for various Da at $Da \cdot t^* = 500$ for C-C cases.
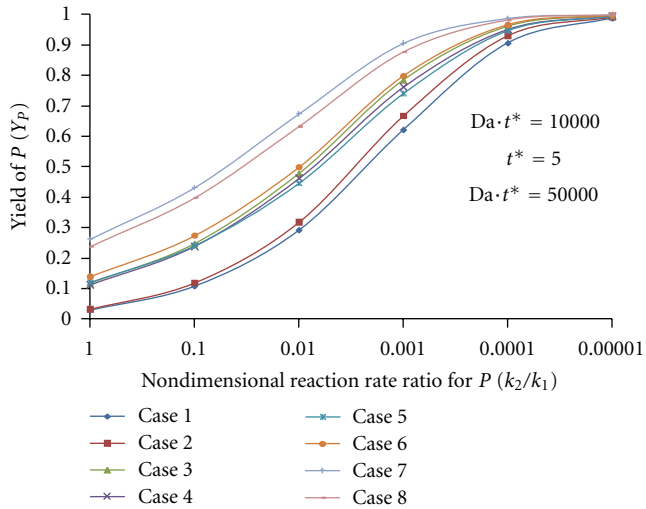
Figure 5: Plot of yield of P versus k_2/k_1 for Da =10000 at Da $\cdot$ t^* = 50000 for C-C cases.

The base data is presented in Figure 6, with selected data replotted in Figures 7–9.

3.2.1. Effect of Damköhler Number (Da). The plots in Figure 6 show a large drop in Y_P when Damköhler number increases from 100 to 10000 with the exception of Case 3 at k_2/k_1 = 1 where the yield increases steadily with increasing Da. Case 3 is the only stoichiometry where the desired reaction consumes more molecules than the undesired reaction, so when the reaction rates are equal and mixing is good, the mass transfer limitation on the desired reaction will push the yield toward the secondary reaction. Since the reactions are parallel, there is no barrier to the production of S over P.

For the C-P reaction pair, yield is constant for Da $\leq$ 100, giving a well-mixed limit of Da = 100. Figures 7(a) and 7(b) confirm this result for Cases 1 and 3, respectively. The curves show the four values of Da investigated. The curves for Da = 0.01 and Da = 1 lie exactly on top of each other and the curve for Da = 100 is very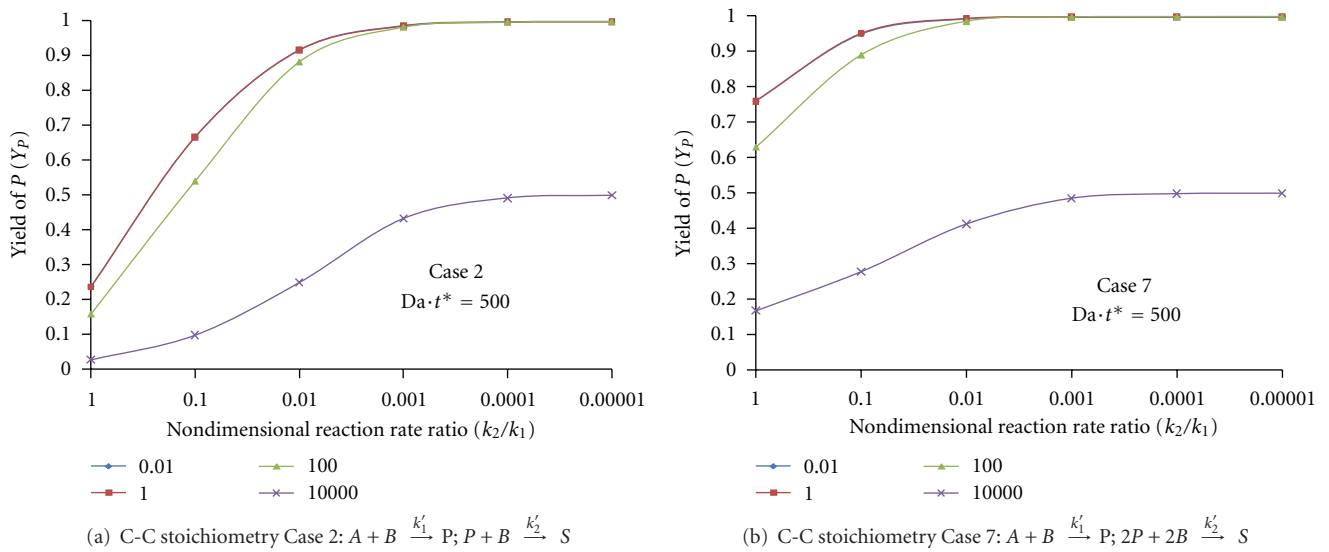 close, but increasing Da to 10 000 drops the yield significantly. These results are very similar to the C-C results. It is concluded that Da = 100 is the well-mixed limit for C-P reactions.

3.2.2. Effect of Dimensionless Reaction Rate Ratio (k_2/k_1). Looking at Figure 6 from the perspective of reaction rate ratio, as k_2/k_1 is decreased, the curves for all the stoichiometries move upwards, increasing the yield for all cases at all values of Da. As expected, a smaller k_2/k_1 increases the yield of desired product. For Cases 1 and 2 the maximum yield is approximately 1 and for Cases 3 and 4 it is 0.88. The curves for Cases 1 and 2 collapse at k_2/k_1 = 0.001 (Figure 6(d)) and the curves for Cases 3 and 4 collapse at k_2/k_1 = 0.0001 (Figure 6(e)). The largest change with improving k_2/k_1 is seen for Case 3, while Case 2 improves the least. These trends are confirmed in Figure 8, showing a persistent effect of stoichiometry on the maximum attainable yield. The poorly mixed condition (Da = 10 000) may not have reached

completion at Da $\cdot$ t^* = 500 since the yield is only about 50%.

In Figure 9 the poorly mixed condition is allowed to progress 100x longer. At this point, the yield can increase to above 90% but only for a 100x smaller k_2/k_1 ratio. The curves seem to collapse at k_2/k_1 = 0.00001, but at lower k_2/k_1's the effect of stoichiometry persists, even at long times. Once again, 100x more residence time and 100x better chemistry are required to eliminate all the effects of 100x worse mixing.

3.2.3. Effect of Stoichiometry. Figures 6(a) to 6(f) illustrate a significant effect of stoichiometry for the C-P case. At k_2/k_1 = 1 (Figure 6(a)) the difference in yield for the different stoichiometries is enormous, and there is a clear distinction between the most favourable and least favourable reaction stoichiometries (Case 2 and Case 3, respectively). This difference decreases as k_2/k_1 decreases (Figures 6(b) to 6(f)). For the C-P scheme, the effect of stoichiometry persists even at k_2/k_1 = 0.00001, where the difference in yield between Cases 1 and 2 and Cases 3 and 4 is more than 10%. This is different from the C-C stoichiometries where the effect of stoichiometry disappeared by $k_2/k_1 \leq 0.001$.

Referring to Table 3, Cases 1 and 4 require the same number of molecules for both reactions, while Case 2 favors the desired reaction (fewer molecules) and Case 3 favors the side reaction. Case 3 is the only case of all 12 stoichiometries considered where the desired reaction consumes more molecules than the side reaction, imposing a mass transfer and collision probability limitation on the desired reaction. This explains the dramatically different results observed for Case 3 and suggests that this class of reaction stoichiometry must be handled more carefully than the others.

3.2.4. Summary of Results for the C-P Reaction Scheme. For competitive-parallel reactions, we have the following.

(a) Da $\leq$ 100 is the well-mixed limit for all k_2/k_1.

(b) For all cases with favourable stoichiometries, at Da $\cdot$ t^* = 500, $k_2/k_1 \leq 0.001$ provides the maximum yield, as for the C-C reaction scheme, but for the C-P reaction scheme the maximum yield depends on the stoichiometry. Case 3, the only case with an unfavourable stoichiometry, requires $k_2/k_1 \leq 0.0001$ to achieve maximum yield.

(c) Stoichiometry affects the maximum obtainable yield to some degree for all mixing conditions and all k_2/k_1.

(d) As for the C-C scheme, increasing the number of molecules in the side reaction imposes a mass transfer limitation on that reaction, making conditions more favorable for the desired reaction. Case 3 in the C-P scheme clearly illustrates that when the desired reaction consumes more molecules than the undesired reaction, it is more difficult to achieve a high yield of desired product.

3.3. Phase Plots of Variables for C-C And C-P Reaction Schemes for the Purpose of Design. The purpose of design

(a) $k_2/k_1 = 1$

(b) $k_2/k_1 = 0.1$

(c) $k_2/k_1 = 0.01$

(d) $k_2/k_1 = 0.001$

(e) $k_2/k_1 = 0.0001$

(f) $k_2/k_1 = 0.00001$
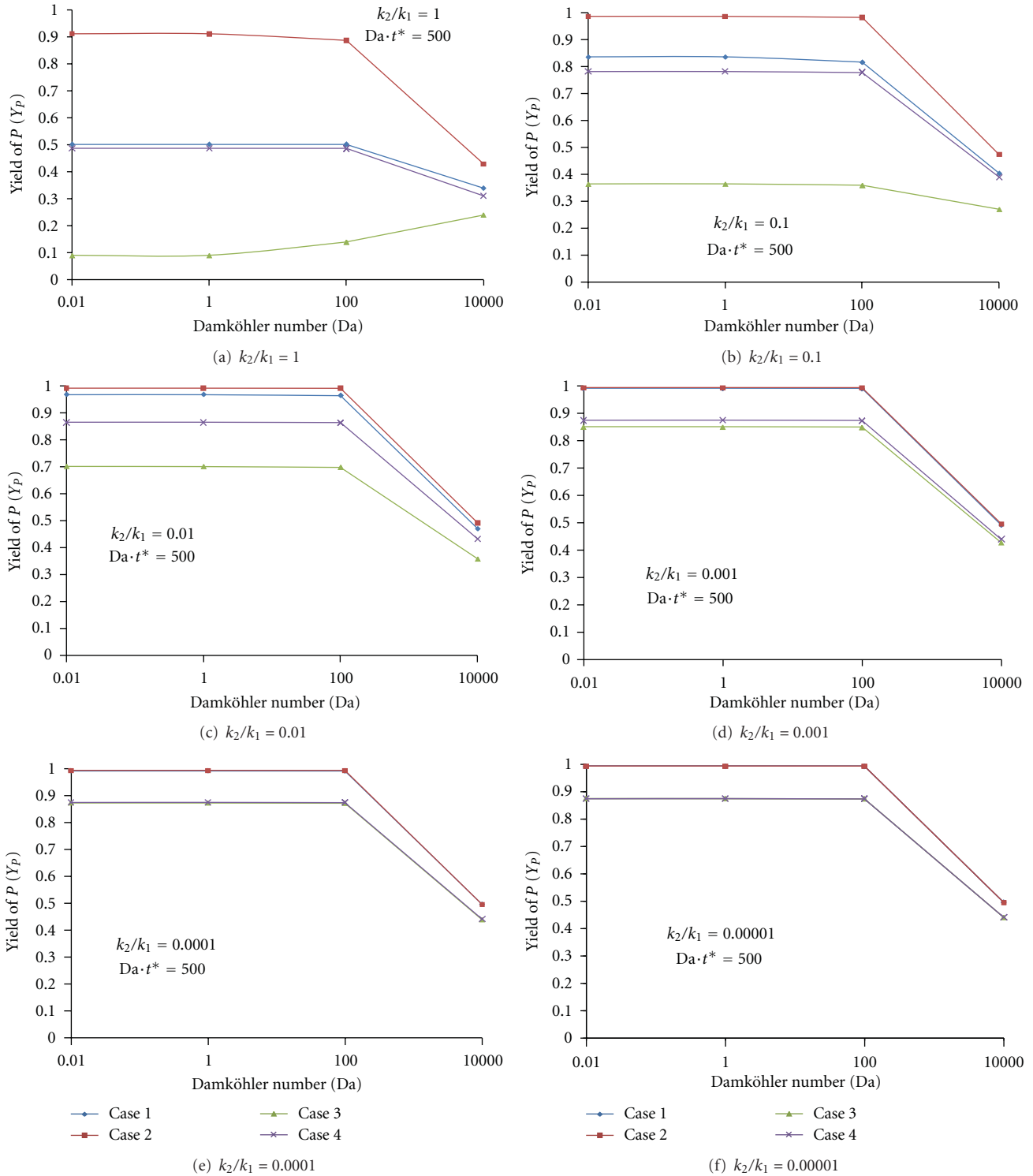
FIGURE 6: Plots of yield of P versus Da for decreasing k_2/k_1 ratios for the C-P cases.

graphs, in the context of mixing sensitive reactions, is to provide a direct method of predicting the yield of desired product without extensive calculations and investigation of the different variables. For our purposes, design graphs would incorporate the effects of stoichiometry, mixing, and k_2/k_1 and the combinations of the three that could possibly

give a certain specified yield of desired product. The purpose of the graphs would be to assist in the design of the following problem.

"If one has a certain mixing sensitive reaction and a target yield of desired product in mind, what

(a) C-P stoichiometry Case 1: $A + B \xrightarrow{k'_1} P; C + B \xrightarrow{k'_2} S$

(b) C-P stoichiometry Case 3: $A + 2B \xrightarrow{k'_1} P; C + B \xrightarrow{k'_2} S$

FIGURE 7: Plots of yield of P versus k_2/k_1 for two sample C-P stoichiometries. The curves represent the different Da. Curves for Da = 0.01 lie exactly under the curves for Da = 1.

(a) Da = 1
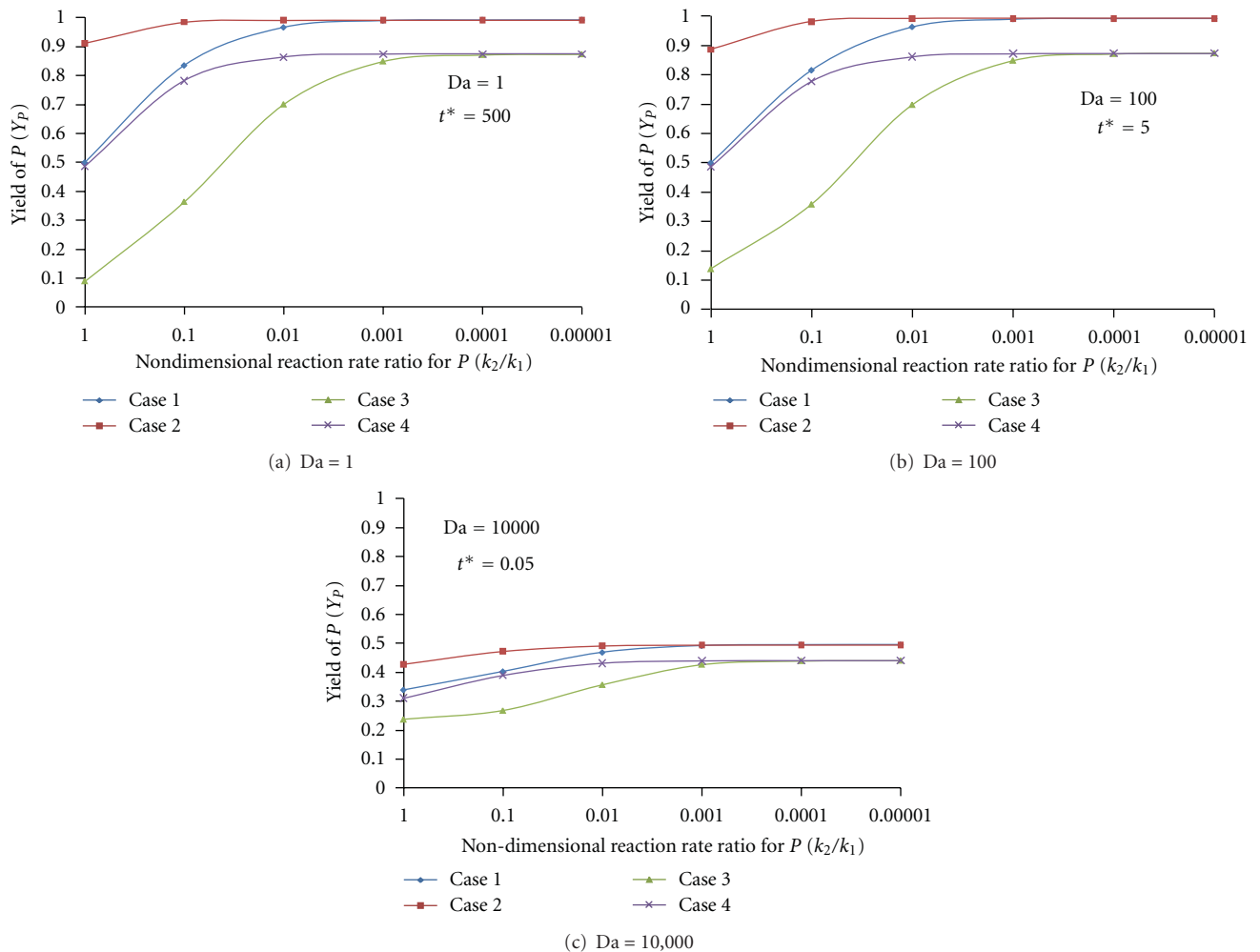
(b) Da = 100

(c) Da = 10,000

FIGURE 8: Plots of yield of P versus k_2/k_1 for various Da at Da $\cdot$ t^* = 500 for C-P cases.
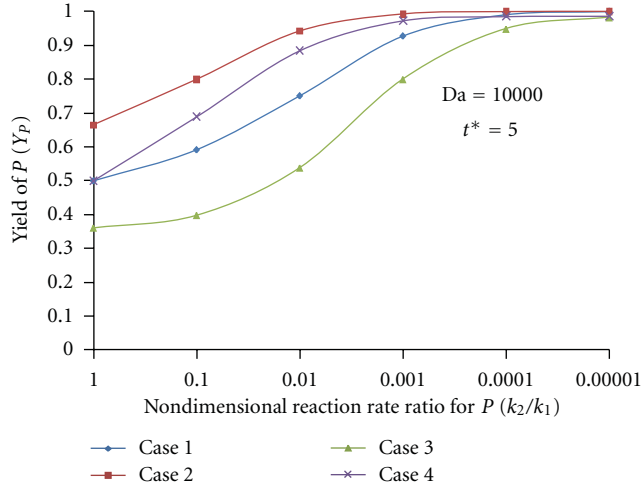
FIGURE 9: Plot of yield of P versus k_2/k_1 for Da $= 10000$ at Da $\cdot t^* = 50000$ for C-P cases.

range of values of dimensionless reaction rate ratio and Damköhler would be required to ensure that the target yield of desired product will be obtained? If one of the variables is inadequate, is it still possible to obtain the target yield? If it is possible, how much do the other variables need to change to accommodate for that inadequacy, if at all?"

The figures should allow for a design space to be established within which decisions can be made based on different criteria and restrictions.

Figure 10 and Figure 11 show the required Damköhler number (x-axis) versus the dimensionless reaction rate ratio (y-axis) for yields of desired product of (a) 85% or more, (b) 95% or more, and (c) 99% or more at a time of Da $\cdot t^* = 500$. They are set up such that the axis intersection (origin) represents the most favourable conditions for both k_2/k_1 and Damköhler number. The figures have marked regions of required k_2/k_1 and Da where a specified yield can be obtained for different stoichiometries. These figures are essentially a filtered summary of the results presented in the previous sections. The effect of stoichiometry quickly becomes evident as the specified yield is increased. For the C-C cases, the requirements on the k_2/k_1 and Da become more stringent as Y_P increases. For C-P Cases 3 and 4, yields greater than 90% were unachievable for $Da \cdot t^* = 500$.

In order to link these results to physical process variables, the diffusion time is replaced with an analogous mixing time scale for turbulent flow. The Batchelor time scale gives the diffusion time for a Kolmogorov sized eddy and is numerically equal to the Kolmogorov time scale, which is the lifetime of the same smallest eddy before the momentum is diffused by viscosity. Replacing the molecular diffusion time in a slab in our definition of Da with the expression for the Kolmogorov time scale in a turbulent eddy gives the following:
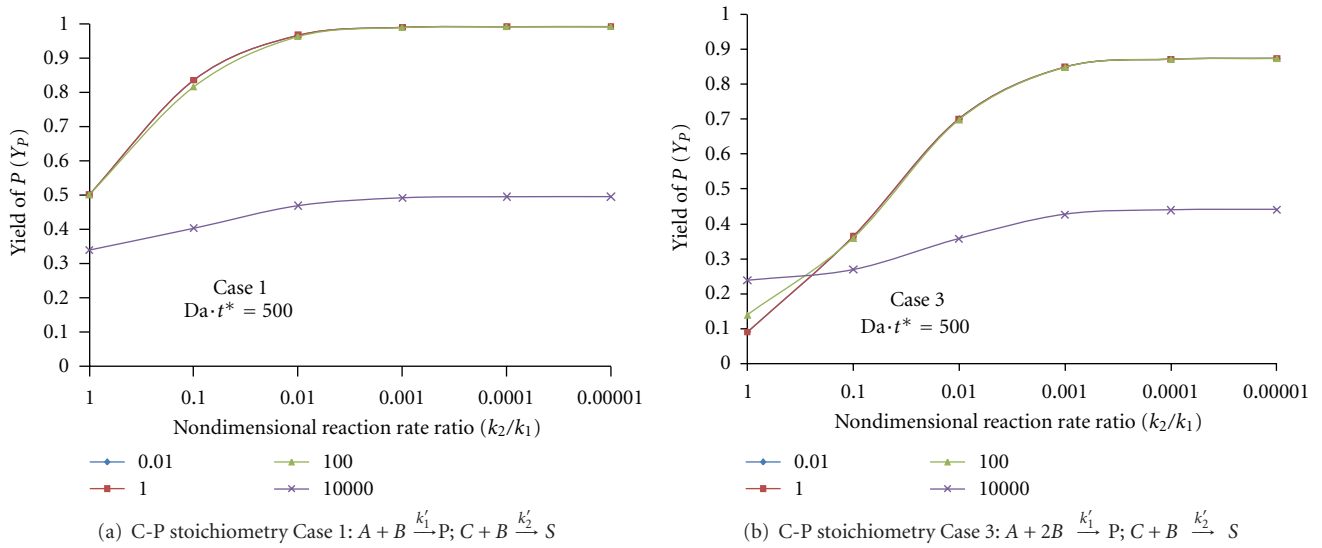
$$\mathrm{Da} = k_1' \left(\frac{\rho_T}{M}\right)^\epsilon \left(\frac{\nu}{\varepsilon_D}\right)^{1/2} \qquad (5)$$
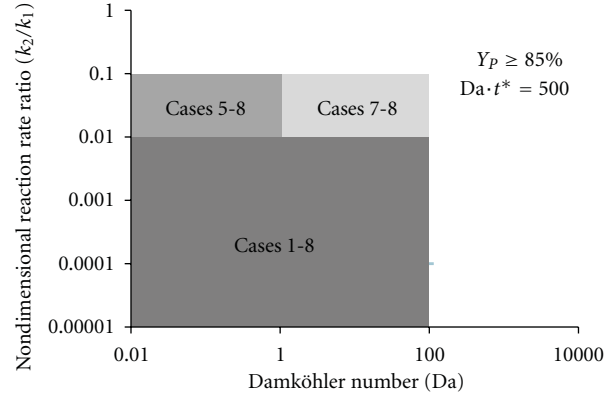
(a) Y_P is at least 0.85 (85%)
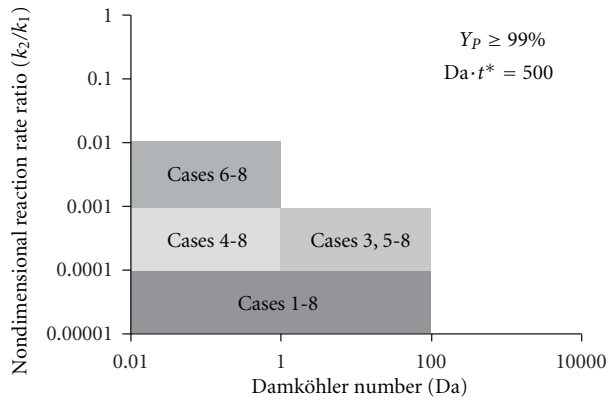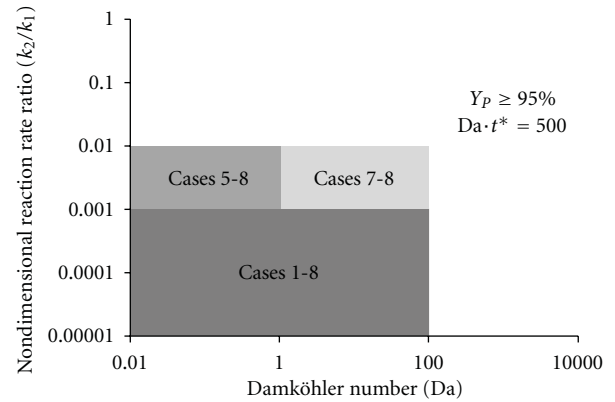
FIGURE 10: Design spaces for yield of P for Da and k_2/k_1 at Da $\cdot t^* = 500$ for C-C cases.

where ν is the kinematic viscosity and ε_D is local rate of dissipation of turbulent kinetic energy (TKE) per mass. Rearranging to solve for ε_D gives the following:

$$\varepsilon_D = \nu \left(\frac{k_1' (\rho_T/M)^\epsilon}{\mathrm{Da}}\right)^2. \qquad (6)$$

This expression proposes a relationship between the rate of dissipation of turbulent kinetic energy (ε_D), the reaction kinetics of the desired reaction (k_1'), and the reaction stoichiometry (ϵ) which might be used to compare bench scale performance with the Da and reaction rate ratio from the phase plot. For example, for a C-C reaction of the type

(a) Y_P is at least 0.85 (85%)
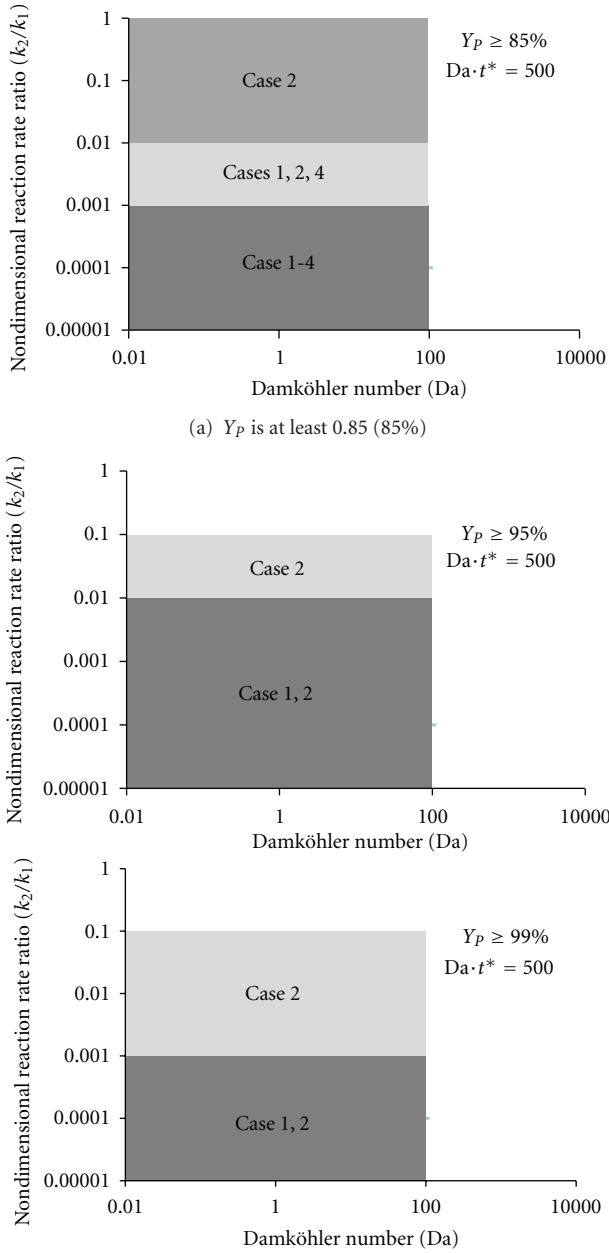
FIGURE 11: Design spaces for yield of P for Da and k_2/k_1 at Da $\cdot t^* = 500$ for C-P cases.

Case 1 ($\epsilon = 1$), using typical values for water ($\nu = 1 \times 10^{-6}$ m²/s, $\rho_T = 1000$ kg/m³, $M = 18$ kg/kmole), ε_D for Da = 1 becomes

$$\varepsilon_D = 3.09 \times 10^{-3} k_1'^2. \tag{7}$$

This gives a first-order estimate for the required level of dissipation at the bench scale. Since the model is based on a static striation thickness rather than the dynamic stretching and cutting field present in both chaotic and turbulent flows, this should be considered a starting point for further investigations in the context of more accurate models of mixing and diffusion.

4. Conclusions

The three effects of initial mixing condition, dimensionless reaction rate ratio, and reaction stoichiometry were investigated in detail using a 1D, transient, reaction-diffusion model for competitive-consecutive (C-C) and competitive-parallel (C-P) reactions. It was found that smaller values of Damköhler number and dimensionless reaction rate ratio are desirable to maximize the yield of desired product for both the C-C and C-P reaction schemes. It was also found that the stoichiometry of the reaction can affect the final yield of desired product considerably and needs to be taken into consideration in the design of reactors for such reactions. The following limits were found for each of the variables.

(i) Da ≤ 1 is the well-mixed limit for the C-C reaction when $k_2/k_1 \geq 0.01$. With $k_2/k_1 \leq 0.01$, the well-mixed limit can be relaxed to Da ≤ 100.

(ii) Da ≤ 100 is the well-mixed limit for all k_2/k_1 for the C-P reaction.

(iii) $k_2/k_1 \leq 0.001$ with Da ≤ 100 provides the maximum yield at Da $\cdot t^* = 500$ for both the C-C and the C-P reactions with favourable stoichiometries. For the C-P case with the most unfavourable stoichiometry $k_2/k_1 \leq 0.0001$ is required.

(iv) The effect of stoichiometry is significant. Where the secondary reaction consumes more molecules than the primary reaction, it is subject to a mass transfer constraint which favors the primary reaction. For the C-P scheme the effect of stoichiometry is persistent, affecting the final yield by more than 10% even for a well-mixed case with favorable k_2/k_1.

The model used here is intended to illustrate the importance of the previously uninvestigated effect of stoichiometry on the yield of desired product and to provide general forms of the Damköhler number and reaction rate ratio for C-C and C-P reactions. The results are not intended to give accurate predictions of yield but to illustrate the trends in a quantitative way. It is hoped that the results will guide development of experimental reaction schemes which serve as mixing probes and development of more realistic reactor models which incorporate mixing, reaction kinetics, and stoichiometry.

Nomenclature

Da: Damköhler number [−]
D: Diffusivity [m²/s]
k_1': Rate constant 1 [m³/kmols]
k_2': Rate constant 2 [varies]
$\dfrac{k_2}{k_1}$: Dimensionless reaction rate ratio [−]
L: Striation thickness [m]
M: Molecular weight [kg/kmol]
R: Reaction term [kg/m³ s]
t: Time [s]

t^*: Dimensionless time $[-]$
w: Mass fraction $[-]$
x: Distance [m]
x^*: Dimensionless distance $[-]$
Y_P: Yield of desired product $P[-]$.

Greek Letters

$\alpha, \beta, \gamma, \epsilon$: Stoichiometric coefficients $[-]$
ε_D: Local dissipation of turbulent kinetic energy per mass $[\text{m}^2/\text{s}^3]$
ρ: Mass concentration $[\text{kg/m}^3]$
ν: Kinematic viscosity $[\text{m}^2/\text{s}]$
τ_M: Mixing time [s]
τ_R: Reaction time [s].

Subscripts

A: Species A (reactant)
B: Species B (reactant)
C: Species C (reactant)
i: Species A, B, C, I, P, or S
I: Species I (inert)
0: Initial value
P: Species P (product)
S: Species S (byproduct)
T: Total
Y, Z: Species mixtures.

Acknowledgments

References

[1] J. Baldyga and J. R. Bourne, "Interactions between mixing on various scales in stirred tank reactors," *Chemical Engineering Science*, vol. 47, no. 8, pp. 1839–1848, 1992.

[2] J. Baldyga and J. R. Bourne, *Turbulent Mixing and Chemical Reactions*, Wiley, Chichester, UK, 1999.

[3] J. Bałdyga and R. Pohorecki, "Turbulent micromixing in chemical reactors—a review," *The Chemical Engineering Journal and the Biochemical Engineering Journal*, vol. 58, no. 2, pp. 183–195, 1995.

[4] J. Bałdyga, J. R. Bourne, and S. J. Hearn, "Interaction between chemical reactions and mixing on various scales," *Chemical Engineering Science*, vol. 52, no. 4, pp. 457–466, 1997.

[5] S. Bhattacharya, *Performance improvement of stirred tank reactors with surface feed [Ph.D. thesis]*, University of Alberta, Alberta, Canada, 2005.

[6] M. J. Clifford, "A Gaussian model for reaction and diffusion in a lamellar structure," *Chemical Engineering Science*, vol. 54, no. 3, pp. 303–310, 1999.

[7] M. J. Clifford and S. M. Cox, "Simple model for a two-stage chemical reaction with diffusion," *IMA Journal of Applied Mathematics*, vol. 63, no. 3, pp. 307–318, 1999.

[8] M. J. Clifford, E. P. L. Roberts, and S. M. Cox, "The influence of segregation on the yield for a series-parallel reaction," *Chemical Engineering Science*, vol. 53, no. 10, pp. 1791–1801, 1998.

[9] M. J. Clifford, S. M. Cox, and E. P. L. Roberts, "Lamellar modelling of reaction, diffusion and mixing in a two-dimensional flow," *Chemical Engineering Journal*, vol. 71, no. 1, pp. 49–56, 1998.

[10] M. J. Clifford, S. M. Cox, and E. P. L. Roberts, "Reaction and diffusion in a lamellar structure: the effect of the lamellar arrangement upon yield," *Physica A*, vol. 262, no. 3-4, pp. 294–306, 1999.

[11] M. J. Clifford, S. M. Cox, and E. P. L. Roberts, "The influence of a lamellar structure upon the yield of a chemical reaction," *Chemical Engineering Research and Design*, vol. 78, no. 3, pp. 371–377, 2000.

[12] S. Cornell and M. Droz, "Exotic reaction fronts in the steady state," *Physica D*, vol. 103, no. 1–4, pp. 348–356, 1997.

[13] S. M. Cox, "Chaotic mixing of a competitive-consecutive reaction," *Physica D*, vol. 199, no. 3-4, pp. 369–386, 2004.

[14] S. M. Cox and M. D. Finn, "Behavior of the reaction front between initially segregated species in a two-stage reaction," *Physical Review E*, vol. 63, no. 5, Article ID 051102, 7 pages, 2001.

[15] S. M. Cox, M. J. Clifford, and E. P. L. Roberts, "A two-stage reaction with initially separated reactants," *Physica A*, vol. 256, no. 1-2, pp. 65–86, 1998.

[16] R. O. Fox, "On the relationship between Lagrangian micromixing models and computational fluid dynamics," *Chemical Engineering and Processing*, vol. 37, no. 6, pp. 521–535, 1998.

[17] R. O. Fox, *Computational Models for Turbulent Reacting Flows*, Cambridge University Press, Cambridge, UK, 2003.

[18] I. Hecht and H. Taitelbaum, "Perturbation analysis for competing reactions with initially separated components," *Physical Review E*, vol. 74, no. 1, Article ID 012101, 2006.

[19] O. Levenspiel, *Chemical Reaction Engineering*, Wiley, New York, NY, USA, 2 edition, 1972.

[20] F. J. Muzzio and M. Liu, "Chemical reactions in chaotic flows," *The Chemical Engineering Journal and the Biochemical Engineering Journal*, vol. 64, no. 1, pp. 117–127, 1996.

[21] G. K. Patterson, E. L. Paul, S. M. Kresta, and A. W. Etchells, "Mixing and Chemical Reactions," in *Handbook of Industrial Mixing—Science and Practice*, E. L. Paul, V. A. Atiemo-Obeng, and S. M. Kresta, Eds., Wiley, Hoboken, NJ, USA, 2004.

[22] M. Sinder, "Theory for competing reactions with initially separated components," *Physical Review E*, vol. 65, no. 3, Article ID 037104, 4 pages, 2002.

[23] M. Sinder, J. Pelleg, V. Sokolovsky, and V. Meerovich, "Competing reactions with initially separated components in the asymptotic time region," *Physical Review E*, vol. 68, no. 2, Article ID 022101, 4 pages, 2003.

[24] H. Taitelbaum, B. Vilensky, A. Lin, A. Yen, Y. E. L. Koo, and R. Kopelman, "Competing reactions with initially separated components," *Physical Review Letters*, vol. 77, no. 8, pp. 1640–1643, 1996.

[25] J. Villermaux and L. Falk, "A generalized mixing model for initial contacting of reactive fluids," *Chemical Engineering Science*, vol. 49, no. 24, pp. 5127–5140, 1994.

[26] S. I. A. Shah, L. W. Kostiuk, and S. M. Kresta, "The effects of mixing, reaction rate and stoichiometry on yield for mixing sensitive reactions part I: model development," *International Journal of Chemical Engineering*, vol. 2012, Article ID 750162, 16 pages, 2012.

Research Article

Zwietering's Equation for the Suspension of Porous Particles and the Use of Curved Blade Impellers

S. Ibrahim, S. N. Jasnin, S. D. Wong, and I. F. Baker

Department of Civil Engineering, Faculty of Engineering, University of Malaya, 50603 Kuala Lumpur, Malaysia

Correspondence should be addressed to S. Ibrahim, shaliza@um.edu.my

The minimum speed for just-suspension, N_{js}, of porous palm shell-activated carbon (PSAC) particles has been determined in a 15 cm diameter cylindrical tank using a 6-curved blade (6CB) impeller, compared to a 6-blade downpumping mixed-flow (6MFD) impeller and a Rushton turbine (6DT). The particles size ranged from 0.75–1.00 mm, 1.00–1.40 mm, and 1.40–2.36 mm with concentrations between 0 and 5% by weight. The 6CB being a radial impeller performed similarly to 6DT in terms of speed and power requirement at just-suspension, and particles distribution on the base. The 6MFD, with power requirement 100% to 200% less than the radial impellers, was the most efficient for suspending the particles, as usually reported for the range of solid concentrations used here. Specific power per unit mass for all three impellers showed reduction towards minima as the concentration of particles increased. The geometric factor, S, values agreed reasonably with published data, when the particle density was adjusted taking into account water filling the pores of the submerged activated carbon. This result means that Zwietering's equation can be used to predict suspension for porous particles with adjustment to the particle density. S values for curved-blade impellers are presented for the first time.

1. Introduction

The suspension of solid particles in liquid in a stirred tank occurs in a wide variety of processes from crystallization to ore processing [1, 2]. Downpumping mixed or axial impellers have been reported to be the most efficient geometries for suspending solids, while radial impellers require substantially higher power to achieve suspension [3, 4]. Radial impellers are, however, still relevant in solid-liquid mixing since this impeller geometry is efficient for gas-liquid dispersion, and many such systems also contain solids [5–9] such as in aerobic fermentation and activated sludge treatment. The curved blade impeller has gained popularity as an alternative to the Rushton due to its efficiency in gas-liquid dispersion as the shape of the curve eliminates or minimizes the formation of cavities that lead to substantial drop in power. There is few reported work, if any, on the use of curved blade impellers for particle suspension.

In solid suspension studies, the particles used are usually fully solid, where the density is simply the particle density [10–21]. The use of porous particles is not commonly reported, although porous particles are relevant in processes such as adsorption. Adsorption processes are usually carried out in columns; nevertheless, it is also of interest to study the suspension of these particles in the stirred tank as this would be a potential configuration for application in water or wastewater treatment and similar processes. When porous particles are submerged in a fluid, the fluid will gradually fill the pores of the particle, and the particle density would have to incorporate the fluid density by a factor of the pore percentage. If Zwietering's [22] correlation is to be used to predict N_{js} for the porous particles, using the adjusted density value for the particles would be more appropriate.

The objective of this paper is to assess the solid-suspension ability of the curved blade impeller and the use of Zwietering's equation to predict just-suspension of porous particles.

2. Materials and Methods

The experiments were conducted in a 0.15 m diameter (T) cylindrical-baffled (standard) vessel filled with distilled water
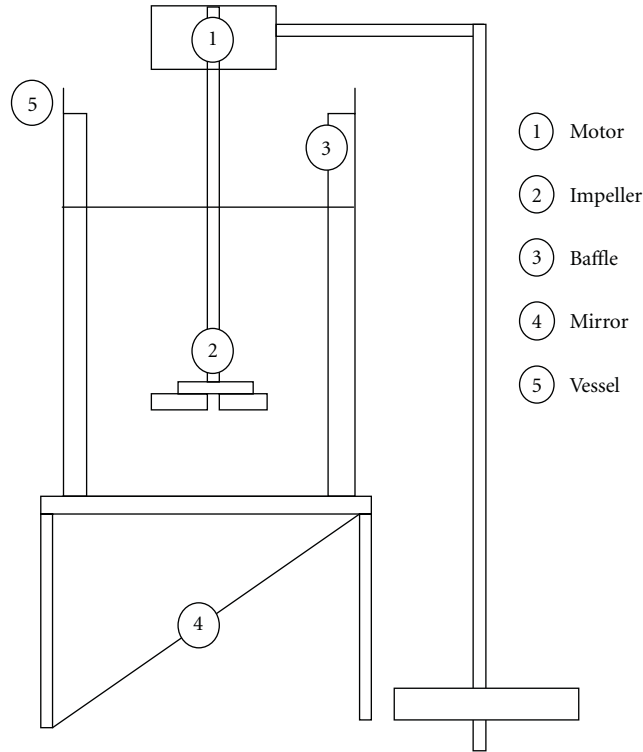
FIGURE 1: Schematic of experimental setup of motor, agitator, tank, and mirror.

(a) 6CB (top)

(b) 6CB (side)
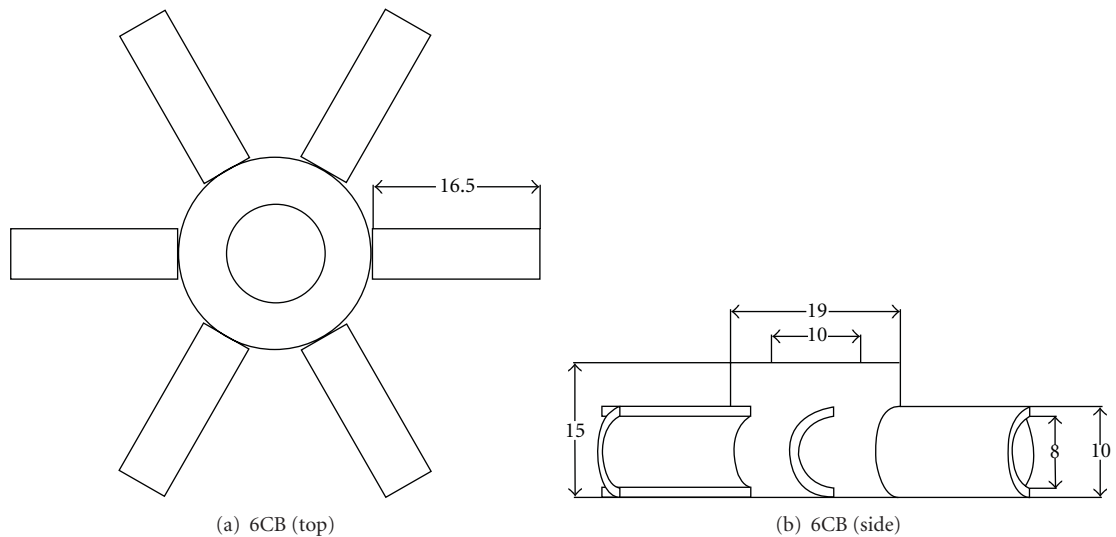
FIGURE 2: 6CB.

to a height equal to the diameter, giving a volume of 2.65 L. Figure 1 shows a schematic of the setup. Three types of impellers used were 6-blade mixed flow pumping downward (6MFD), the 6-blade Rushton turbine (6DT), and a 6-curved blade turbine (6CB). Schematic diagrams of the impellers are provided by Figures 2, 3, and 4. The curved blade used in this work does not have a central disc as does the Rushton turbine.

The experiments were performed at a constant liquid depth ($H = T$) and with a constant impeller clearance ($C = T/4$). An impeller diameter of 5 ± 0.1 cm gives a D/T ratio of about 1/3. The impeller is mounted on a shaft connected to a motor that displays speed and torque readings. The speed can be set from 0 rpm to 2000 rpm. The power of agitation is calculated based on the difference between torque reading during impeller rotation in air and rotation in the actual

(a) 6DT (top)

(b) 6DT (side)

FIGURE 3: 6DT.

(a) 6MFD (top)

(b) 6MFD (side)
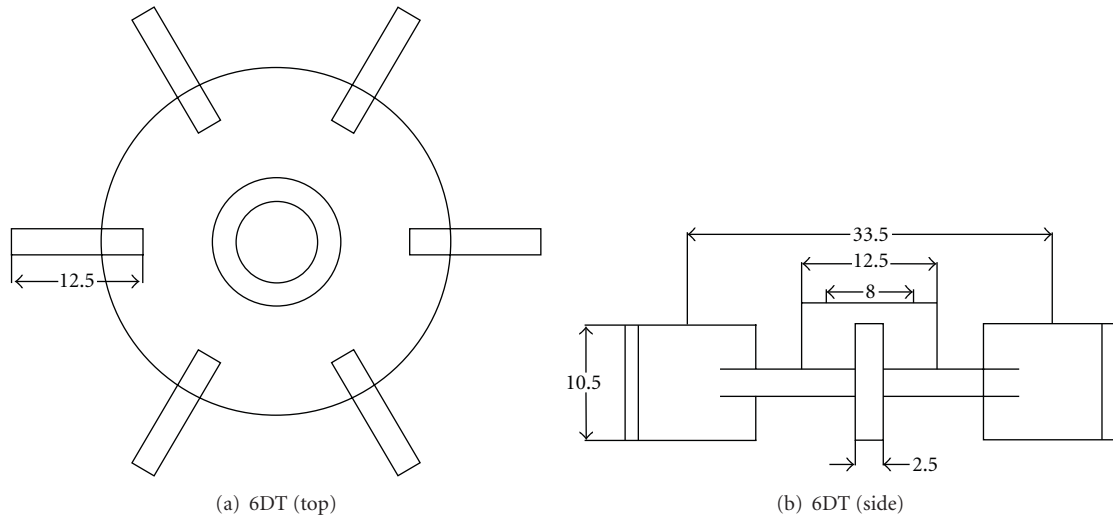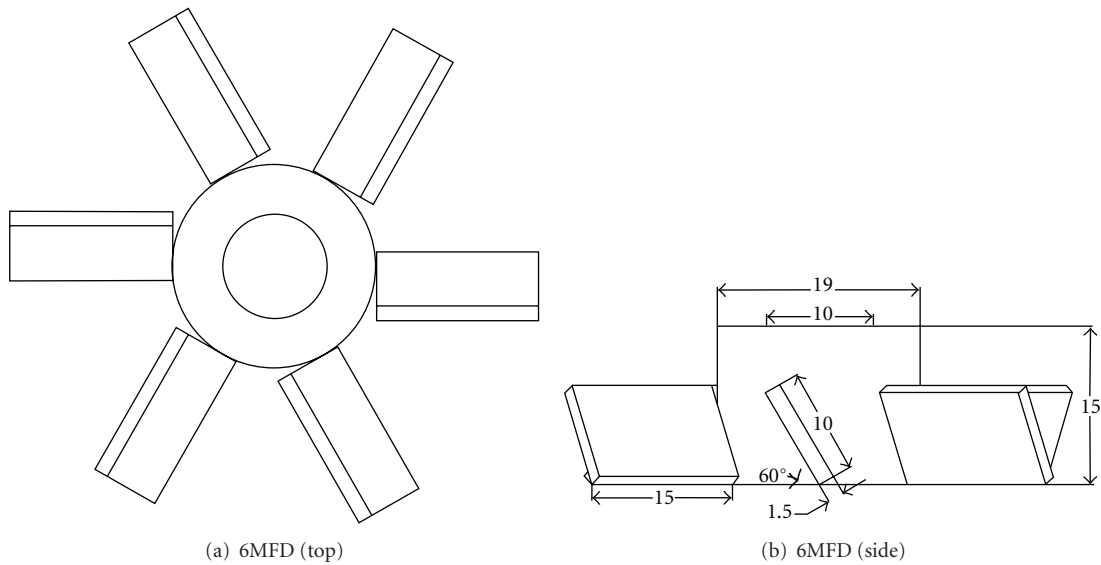
FIGURE 4: 6MFD.

fluid. Before experimental runs, the motor was warmed up for at least 20 minutes.

Palm shell-activated carbon (PSAC) was used as the porous solids to be suspended. The properties of the particles are given in Table 1 based on a sample of the particles. The assumption made in this work is that the same characteristics apply for all the size ranges. The particles were segregated by sieving according to the size range: 0.75–1.00 mm, 1.00–1.40 mm, and 1.40–2.36 mm. Any superficial impurities were cleaned to ensure that no other substances were included in the experiments.

The PSAC solid density has been determined to be 1700 kg/m^3. This is higher than water density, and the particles were observed to readily sink in the tank as soon as they were poured into the water. However, particle density value in Zwietering's equation should incorporate the fact

TABLE 1: Results of BET test for PSAC particles.

Parameter (unit)	Value
BET surface area (m^2/g)	941
Micropore area (m^2/g)	764
Average pore diameter (nm)	2.213
Pore volume (cm^3/g)	0.524
Micropore volume (cm^3/g)	0.496

that the activated carbon pores are filled with water once they are submerged. It is necessary to consider this fluid-filled pores, when it concerns the lifting or suspension of these

FIGURE 5: N_{js} (rpm) versus concentration (%), at varying impeller geometries. (a) size of activated carbon: 1.40–2.36 mm, (b) size of activated carbon: 1.00–1.40 mm, (c) size of activated carbon: 0.75–1.00 mm.

particles in water. This effective density of the submerged particle can be calculated as follows:

$$\rho_{s,\text{eff}} = (1 - \varepsilon)\rho_s + \varepsilon\rho_L$$
$$= (1 - 0.524) \times 1700 + (0.524 \times 1000) \quad (1)$$
$$= 1333.2 \, \text{kg m}^{-3}.$$

The effective density is used in Zwietering's equation.

The concentrations of activated carbon (solids) ranged from 0.0 to 4.8% by weight, with 0.1% increments for 6CB and 6MFD, and 0.5% increments for 6DT. Since the solids volume is relatively low, the total water volume is assumed constant at 2.65L throughout the experiments Solids mass, x, was calculated based on solids-to-liquid ratio. As an example:

0.5 g PSAC/100 g water = 5 g PSAC/kg water = 5 g PSAC/liter water,

5 g PSAC/liter water × 2.65 liter = 13.25 g PSAC = x.

An increment of "0.1%" means an additional 0.1 g PSAC/100 g water = 1 g PSAC/kg water = 1 g PSAC/liter water, hence 2.65 g of PSAC for each increment. There are 50 experimental points each for 6MFD and 6CB at every particle size range, while the Rushton had 10 experimental points for every particle size range. N_{js} was determined visually for each concentration of particles and experimental condition.

In using Zwietering's equation to calculate S values, the solids concentration (X) is given as:

$$X(\%) = \frac{x}{x + \text{water mass}} \times 100\% = \frac{x}{x + 2.65 \, \text{kg}} \times 100\%, \quad (2)$$

where x is mass of solids in kg.

(a)

(b)

(c)

— 6CB
— 6DT
— 6MFD
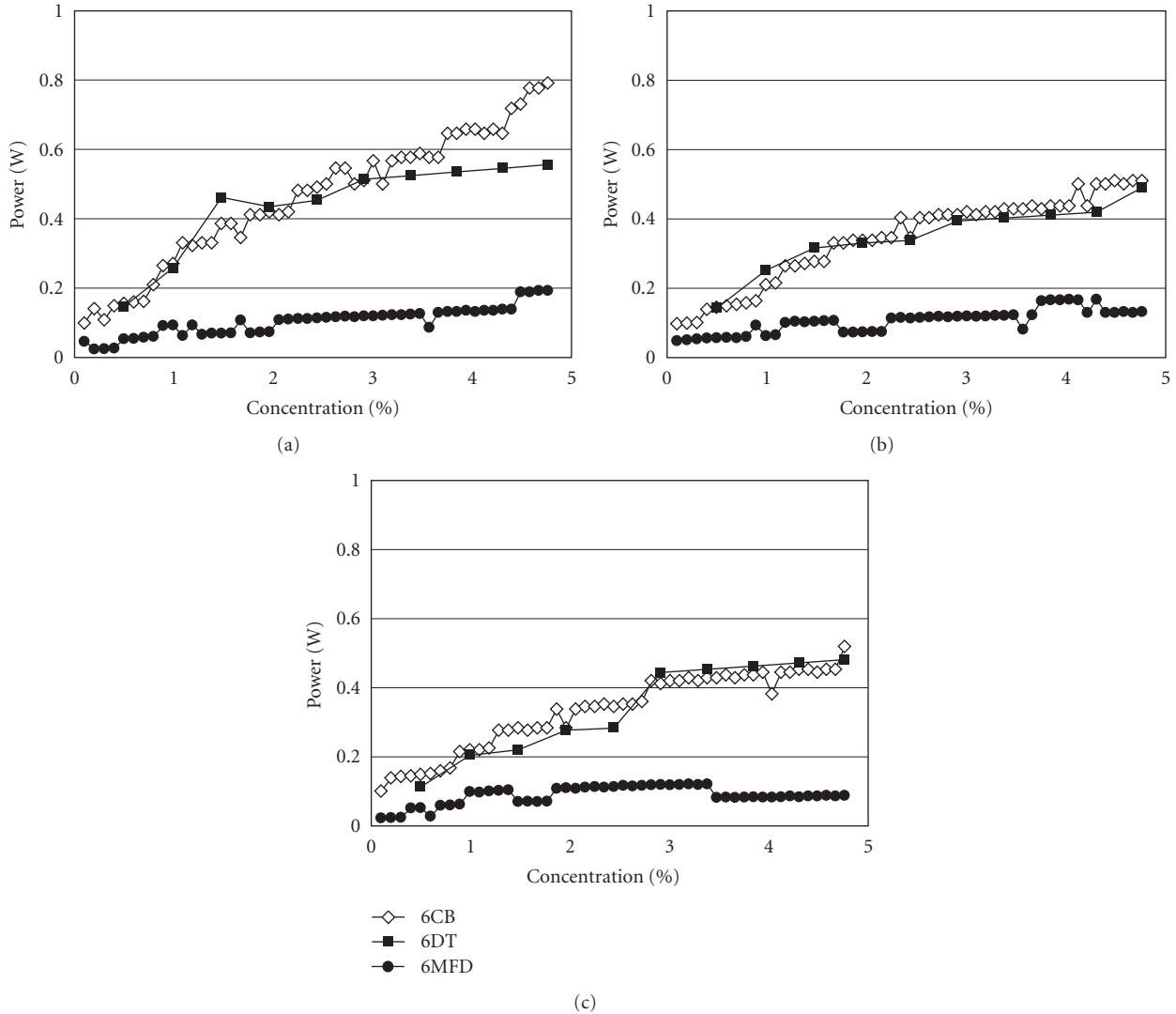
Figure 6: Power (watt) versus concentration (%), at varying impeller geometries. (a) size of activated carbon 1.40–2.36 mm. (b) size of activated carbon 1.00–1.40 mm. (c) size of activated carbon 0.75–1.00 mm.

2.1. Determining the N_{js}. The minimum speed for just suspension, N_{js} was ascertained by increasing the motor speed ranging from 0 rpm until complete suspension is deemed achieved based on the 1-2 s Zwietering criteria. The suspension of particles was observed with the naked eye, aided by a mirror located at an angle below the vessel and a halogen lamp shone from the side. Particle distribution with each impeller was observed and recorded. It was not easy to view the particles due to the black color of the solids rendering the whole tank completely dark. Nevertheless, it was still possible to distinguish the individual particles on the base for all the concentrations studied here. The use of a lamp was helpful to a certain extent.

2.2. Power Consumption. The torque value displayed on the motor screen was recorded once the minimum speed for complete suspension was determined. At that speed of N_{js}, torque readings were later taken again with the impeller

rotating in air. This gives a baseline reading which is subtracted from the earlier value obtained in the solid-liquid mixture, to give the actual net torque for agitation at N_{js} during just-suspension. In other words, the actual torque value for the impeller at N_{js} is obtained by deducting the torque value in the liquid-solid mixture with the torque value in air. Then, the data is put into the equation below for power calculation:

$$\text{Power (Watt)} = \text{torque (N} \cdot \text{m)} \times 2\pi \times N_{js} \text{ (rps)}. \quad (3)$$

2.3. Determining S Values. S, the dimensionless geometric factor in Zwietering's equation, is calculated from Zwietering's equation below, upon the visual determination of N_{js}. S values agreeing with published data imply that the use of Zwietering's equation to predict N_{js} for the given system

(a)

(b)

(c)

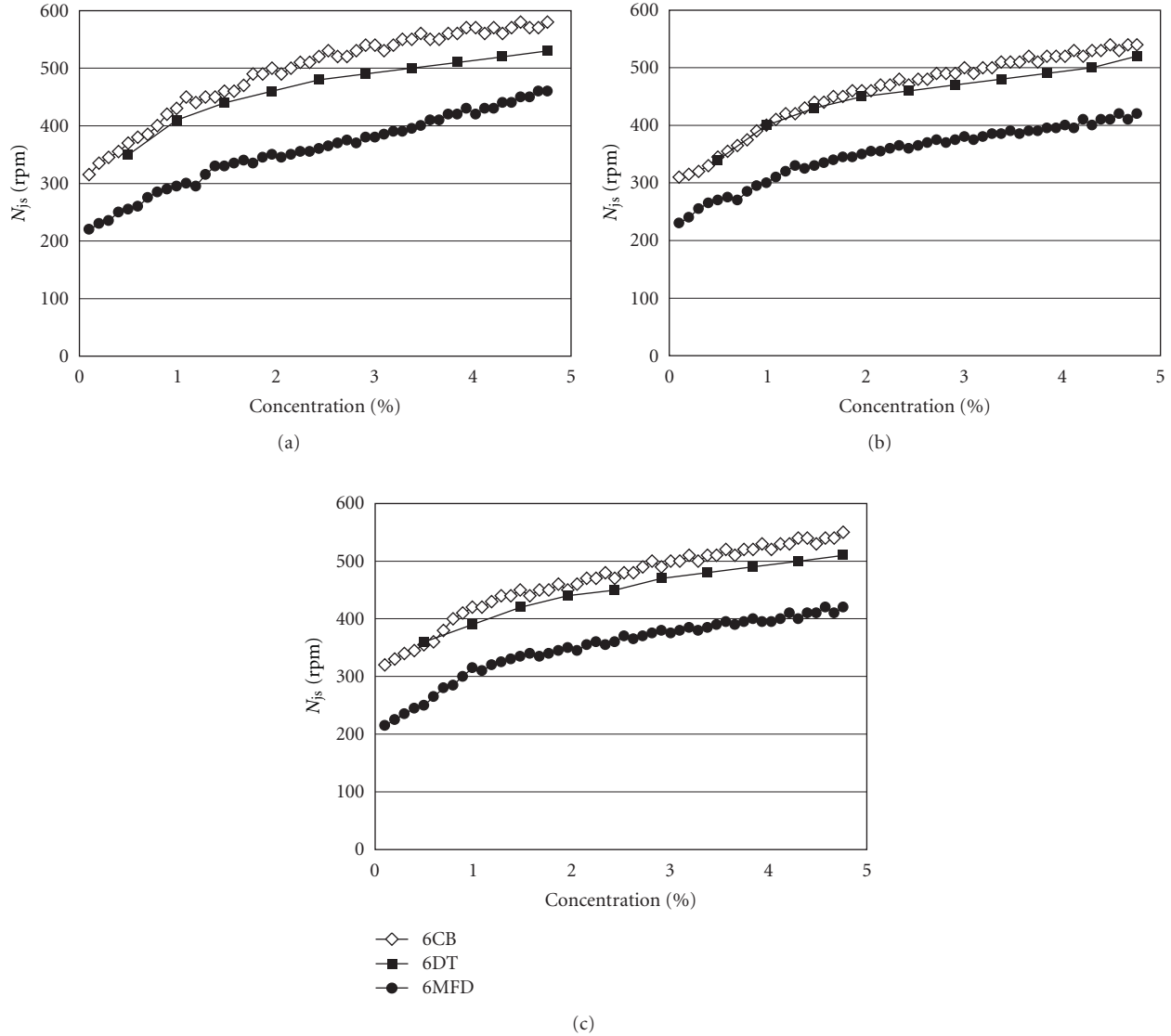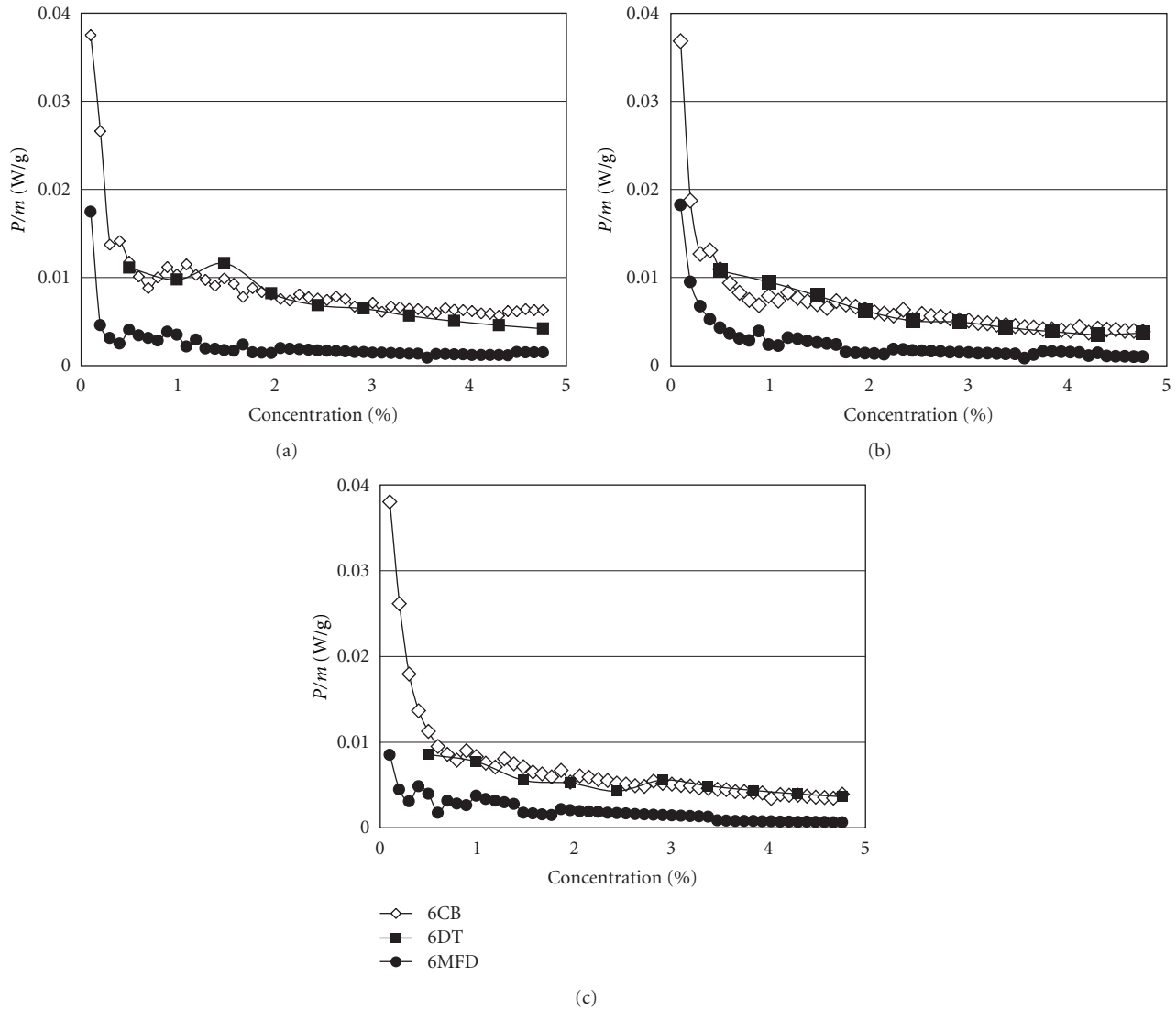FIGURE 7: Power per unit solid mass (W/g) versus concentration (%), at varying impeller geometries. (a) size of activated carbon 1.40–2.36 mm, (b) size of activated carbon 1.00–1.40 mm, and (c) size of activated carbon 0.75–1.00 mm.

will produce values within the range obtained by visual observation:

$$N_{js} = \frac{S(g\Delta\rho/\rho_L)^{0.45}(d_p)^{0.2}X^{0.13}\nu^{0.1}}{D^{0.85}}. \quad (4)$$

3. Results and Discussion

3.1. Comparing Impeller Performance. Figures 5(a) to 5(c) show the minimum speeds for each impeller to achieve just-suspension over the range of PSAC concentrations. The plots in all cases show N_{js} increasing nearly proportionally to the particle concentration, with the slope of the curves reducing at a point between 1% to 2% concentration. The graphs also clearly show that higher speeds are required for the two radial impellers, the Rushton and curved blade compared to

the downpumping mixed flow. To illustrate, at 1.0% concentration of activated carbon, N_{js} for 6MFD was 295 rpm, while for 6CB and 6DT were 430 rpm and 410 rpm, respectively.

In relation to the speed requirement, Figures 6(a) to 6(c) show the 6MFD requiring less power than the radial 6CB and 6DT at the suspension points of each solid concentration, while the power for both the 6CB and 6DT are close to each other. The increase in power demand in going from 6MFD to the radial impellers can be from 100% to higher than 200%. Hence, as reported in previous work, the mixed flow impeller achieves suspension at speeds and power inputs lower than the radial impellers [17]. The same trend is observed with the three size ranges of activated carbon particles.

Plots of specific power or power per unit mass versus concentration (Figures 7(a) to 7(c)) also show much lower values for the 6MFD compared to the radial impellers. This observation may be so because of the range of solids concentrations used here. In studies with slurries concentrations

FIGURE 8: Power per unit solid mass (W/g) versus concentration (%), at varying sizes of activated carbon. (a) 6CB impeller, (b) 6DT impeller, and (c) 6MFD impeller.

going as high as 50% by volume [23], the specific power for radial impellers was less than pitched-blade pumping axially downwards (similar to the 6MFD). Nevertheless, the plots in Figures 7(a) to 7(c) do show the drop towards minima for all cases, and the differences between the radial and down-pumping impellers getting less as the minima is approached. It is also interesting to note that since power per unit mass decreases with increase in particle concentration, it is in fact more efficient to perform the solid suspension operation in the stirred tank at higher particles concenration, until the

specific power increases again after the minimum. Hence, there is an optimum concentration for slurry mixing [23]. Figures 8(a) to 8(c) show the effect of particle size to be less important especially for the 6MFD.

The impeller geometry causes particles to be distributed at certain regions on the base before suspension occurs. As reported earlier [17], for downward pumping 6MFD parti-cles are divided in the centre and side as shown in Figure 9 with more being pushed to the side, since the impeller diameter is less than half the tank diameter [17]. As the speed

Figure 9: Particle distribution by 6MFD.

Figure 10: Particle distribution by 6CB.

Figure 11: Particle distribution by 6DT.

Activated carbon with particle size 1.40–2.36 mm required higher speeds and power because being larger, they are also heavier than particles of the 1.00–1.40 mm and 0.75–1.00 mm size range even though all the particles have the same density. This is so since the mass is related to the particle density and volume as follows:

$$\text{Mass} = \text{Density} \times \text{Volume}, \tag{5}$$

where assuming spherical shape for the particles, volume is directly dependent on particle size by the formula: $V = \pi D^2/4$. A larger volume means bigger mass and bigger weight as well, since weight = mass $\times$ gravitational acceleration.

Hence, more energy is required to move larger particles from the bottom of vessel, and thus N_{js} value increased.

Overall in this work, it is seen that in the lower size range, particle size does not have significant impact on the minimum suspension speed and power requirement, but with the larger size range from 1.40 to 2.36 mm the need for more energy is more significant and noticeable.

3.3. S Values. S, the geometric factor in Zwietering's equation is to account for variation in the geometry of the impeller and tank. Available S values are useful for the prediction of N_{js} using Zwietering's equation. In the plots against concentration (Figures 14(a)–14(c)), the S values stabilize to nearly constant after 1% particles concentration. The average values are given in Table 2(a). The 6CB has S values close to the 6DT since both have similar N_{js} readings. Compared to S from previous work [17] given in Table 2(b), the 6MFD S values are close to the earlier reported values, while that for 6DT tend to be lower in this work. This could be due to the differences in experimental condition such as particle size and concentration, and the subjective nature of the visual technique. Nevertheless, the results indicate that Zwietering's equation can be used to reasonably predict the minimum just-suspension speed for porous particles as used here, with the density adjusted to incorporate the submerged void space. If the solid density alone is used as it is in Zwietering's equation, the S values would be 28.5% lower than the values obtained here, making even greater difference from published data. In Figures 15(a) to 15(c), S seems to be affected by the particle size as shown by the 6MFD as well as

of impeller increases, particles at the centre get suspended first followed by those around the side of the base. There was tendency for some of the particles to get stuck behind the baffles. The 6DT is known to have particles pulled to the centre for suspension, and the 6CB which is also a radial impeller has shown a similar distribution although the "star" shape of the 6DT is less distinct (Figures 10 and 11).

3.2. Effect of Particle Size. In Figure 12(a) for 6CB the N_{js} for the largest size range is greater than sizes below 1.4 mm beyond a concentration of about 1.8%. With the lower two size ranges, not much difference in N_{js} values is observed between them. Data for the Rushton (Figure 12(b)) show a similar trend, but for the 6MFD (Figure 12(c)) the N_{js} values for different particle sizes, are quite similar, and the N_{js} for particles larger than 1.40 mm increase only as particle concentration increased to about 3.2%.

Figures 13(a) to 13(c) show the power consumption according to different particle sizes at different concentrations. In general the power increases with size and concentration. For the 6CB power for the largest size range is clearly higher than the lower two size range. The 6DT shows increase from one size range to another, while the 6MFD has less difference among the different sizes, with fluctuations in power as particle concentration increased.
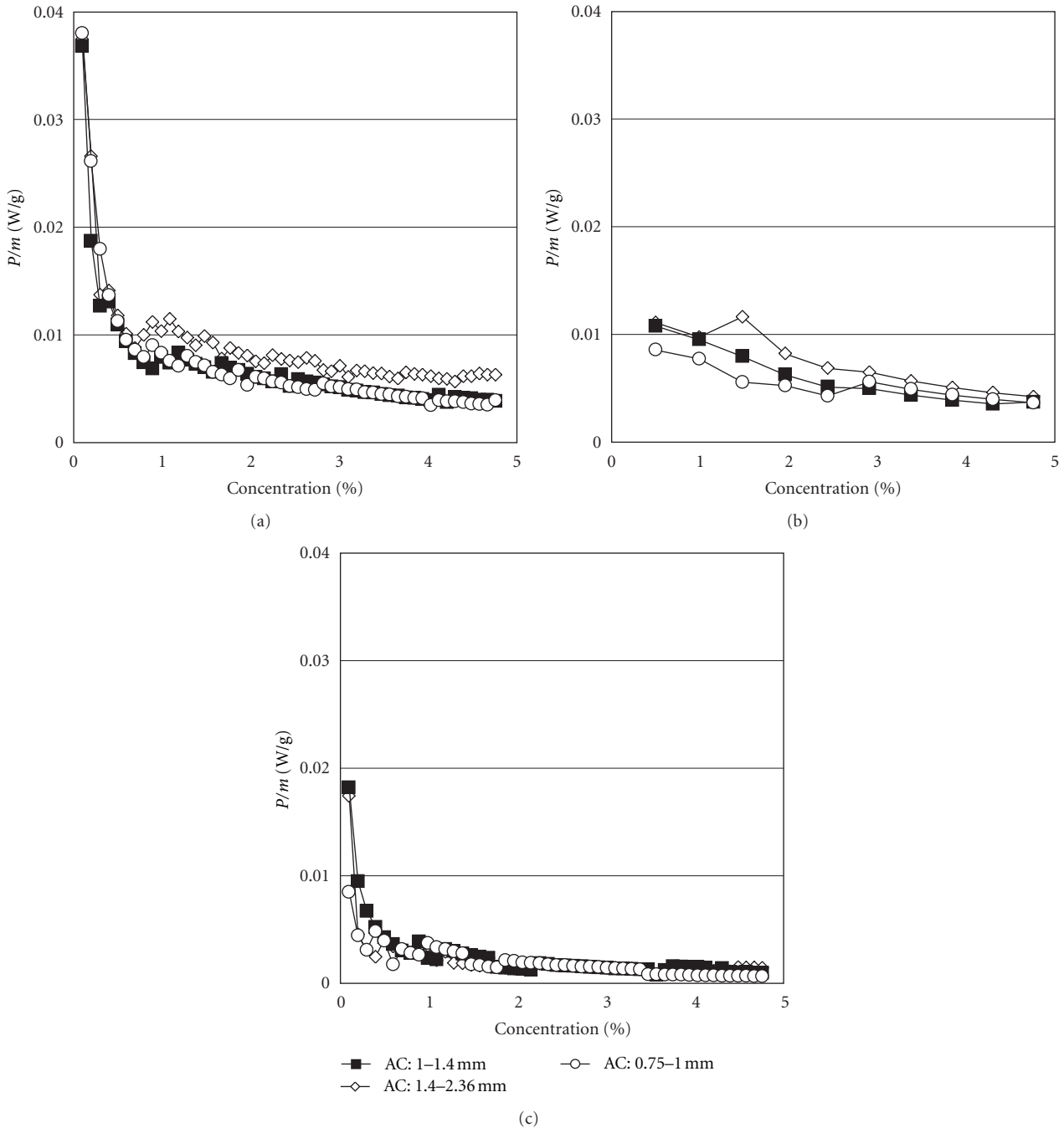
FIGURE 12: Graph N_{js} (rpm) versus concentration (%), at varying sizes of activated carbon. (a) 6CB impeller, (b) 6DT impeller, and (c) 6MFD impeller.

6DT impellers. For the 6CB the S values for the smallest size range are distinctly higher than the other two size ranges.

4. Conclusion and Recommendations

In this study, the suspension of porous activated carbon particles has been observed using 6-blade impellers of three geometries—downward pumping mixed-flow, Rushton disc turbine and curved blade. The first objective is to evaluate the performance of the curved blade turbine as compared to the 6DT and 6MFD, which has often been reported. The second objective is to evaluate the use of Zwietering's equation for

N_{js} prediction with particles of high porosity, since such particles have a high percentage of void volume that is filled with liquid when they are submerged thus altering the actual density of the particles to be suspended.

As established in the literature for solids concentration lower than 20%, the mixed-flow 6MFD showed significantly greater efficiency for particle suspension compared to the two radial impellers 6CB and 6DT, both with respect to minimum speed for suspension and power requirement. But in terms of specific power the differences reduce as the plots tend towards minima with increase in concentration, indicating that the trend may shift to the radial being better at higher concentrations as already reported by other workers

(a)

(b)

◇ AC: 1.4–2.36 mm
■ AC: 1–1.4 mm
○ AC: 0.75–1 mm

(c)
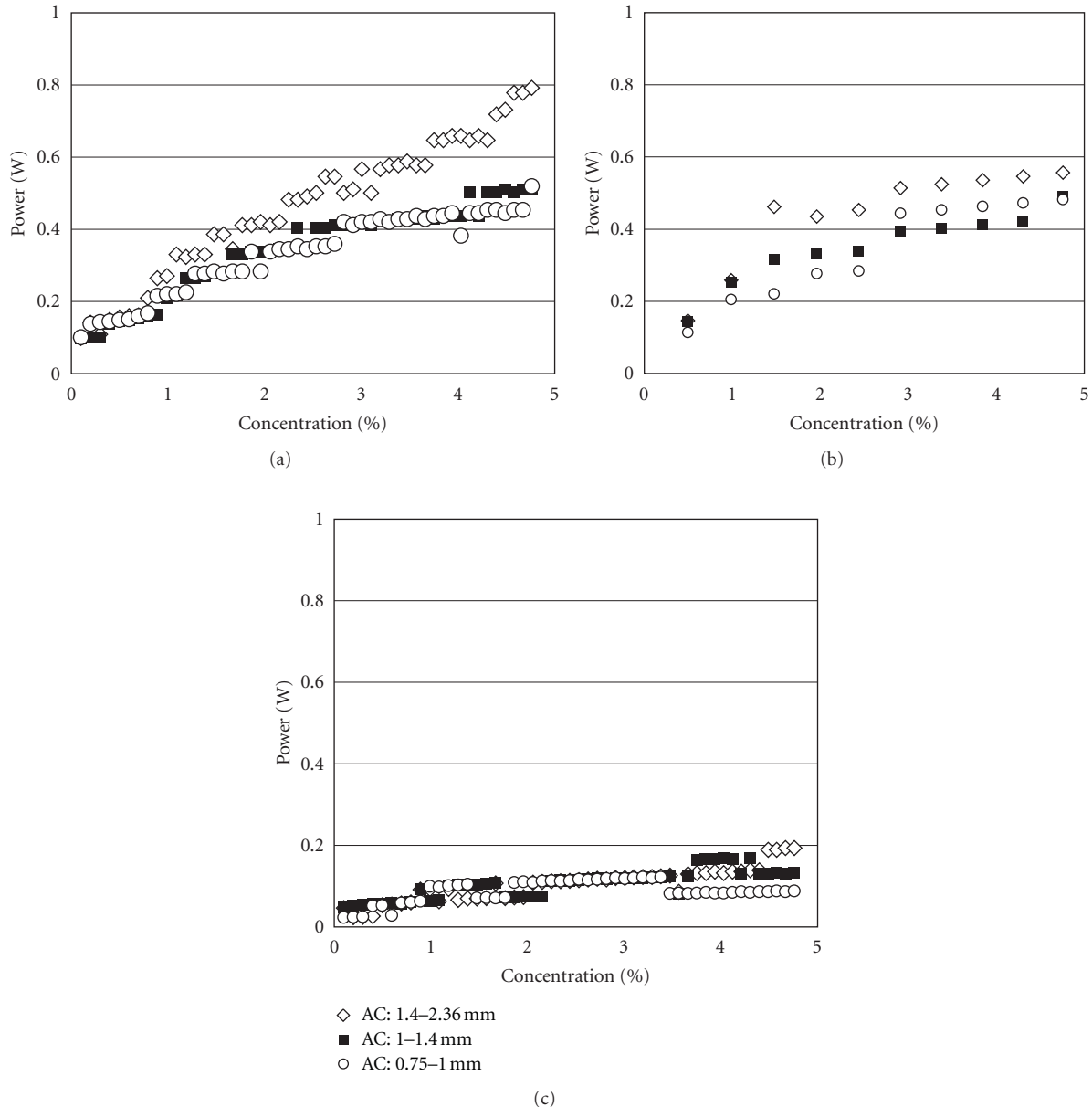
FIGURE 13: Graph power (watt) versus concentration (%), at varying sizes of activated carbon. (a) 6CB impeller, (b) 6DT impeller, and (c) 6MFD impeller.

[23]. Interestingly, both the radial impellers, the 6DT and 6CB, show similar N_{js} and power values under the same conditions. The points of last suspension are as reported [17], where with the 6MFD particles move out from the centre to the side, while for the radial impellers, particle are moved to the centre to be suspended.

Activated carbon with sizes 1.40–2.36 mm required higher speeds and power to reach just-suspension compared to particles of 1.00–1.40 mm and 0.75–1.00 mm size range. The latter two size ranges show close suspension speeds requirement.

S values have been obtained for the curved blade impeller. As expected since the N_{js} for 6CB is close to 6DT, the S values

are also similar. The S values obtained for 6MFD are lower compared to 6CB and 6DT but agree with previous reports.

Nomenclature

N_{js}: Minimum speed to achieve just-suspension (rps)
d_p: Particle size (m)
X: wt. solids/wt. liquid $\times$ 100 (%)
D: Impeller diameter (m)
C: Off-bottom clearance (m)
T: Tank diameter (m)
H: Mixing height (m)
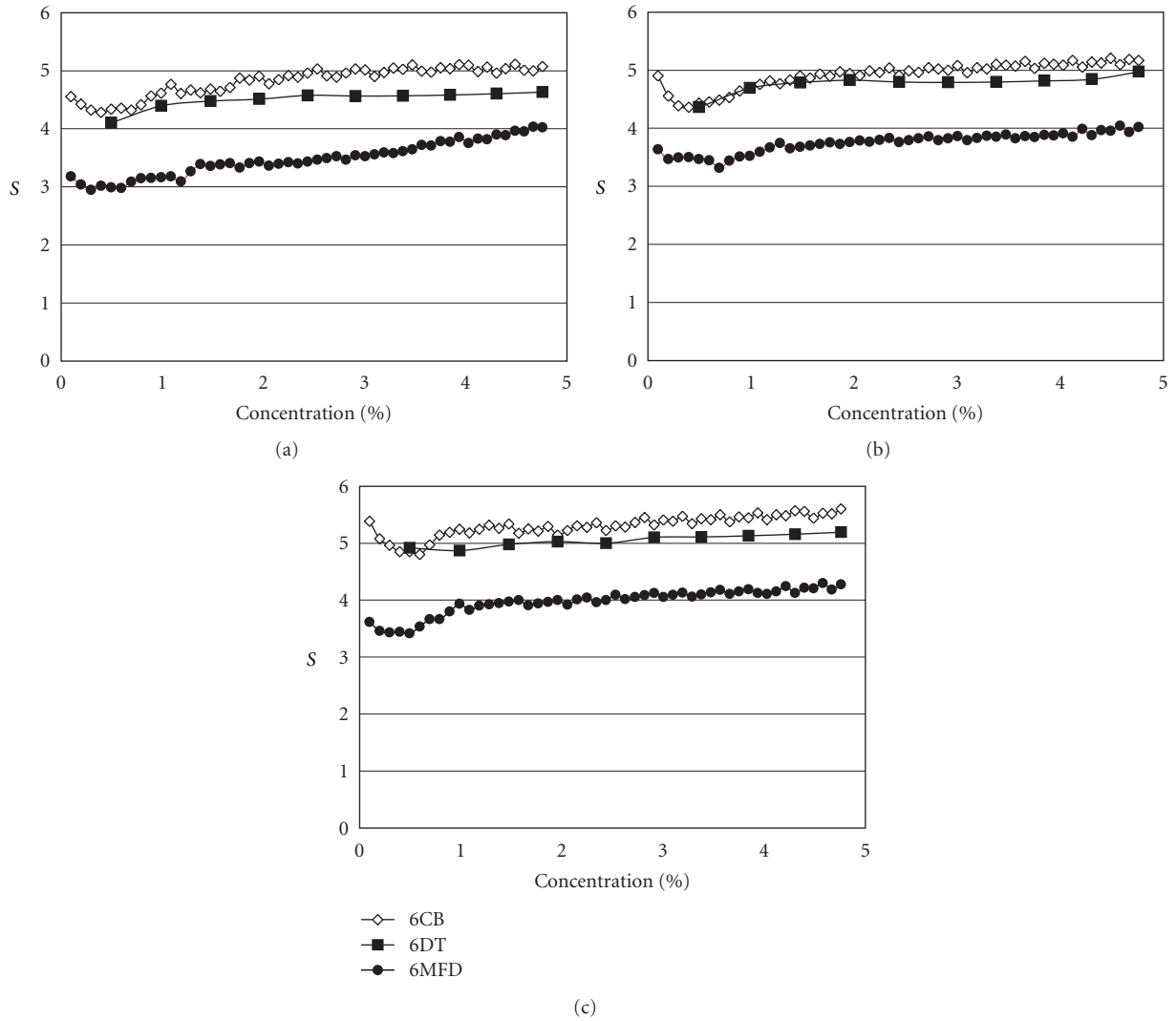
Figure 14: S values versus concentration (%), at varying impeller geometries. (a) size of activated carbon 1.40–2.36 mm, (b) size of activated carbon 1.00–1.40 mm, and (c) size of activated carbon 0.75–1.00 mm.

Table 2

(a) Average S values (present work)

Impeller	1.40–2.36 mm	1.00–1.40 mm	0.75–1.00 mm
		S	
6CB	4.82	4.91	5.31
6DT	4.50	4.77	5.05
6MFD	3.48	3.75	3.98

(b) The literature S values [17]

Impeller	D/T	C/T	BLGB (d_p = 0.6–0.71 mm)	Bronze shot (d_p = 0.5–0.6 mm)
			S	
		0.17	5.12	5.72
6DT	0.33	0.25	7.33	6.58
		0.33	8.37	
6MFD	0.33	0.25	3.94	4.03

(a)

(b)

→◇— AC: 1.4–2.36 mm
—■— AC: 1–1.4 mm
—○— AC: 0.75–1 mm

(c)
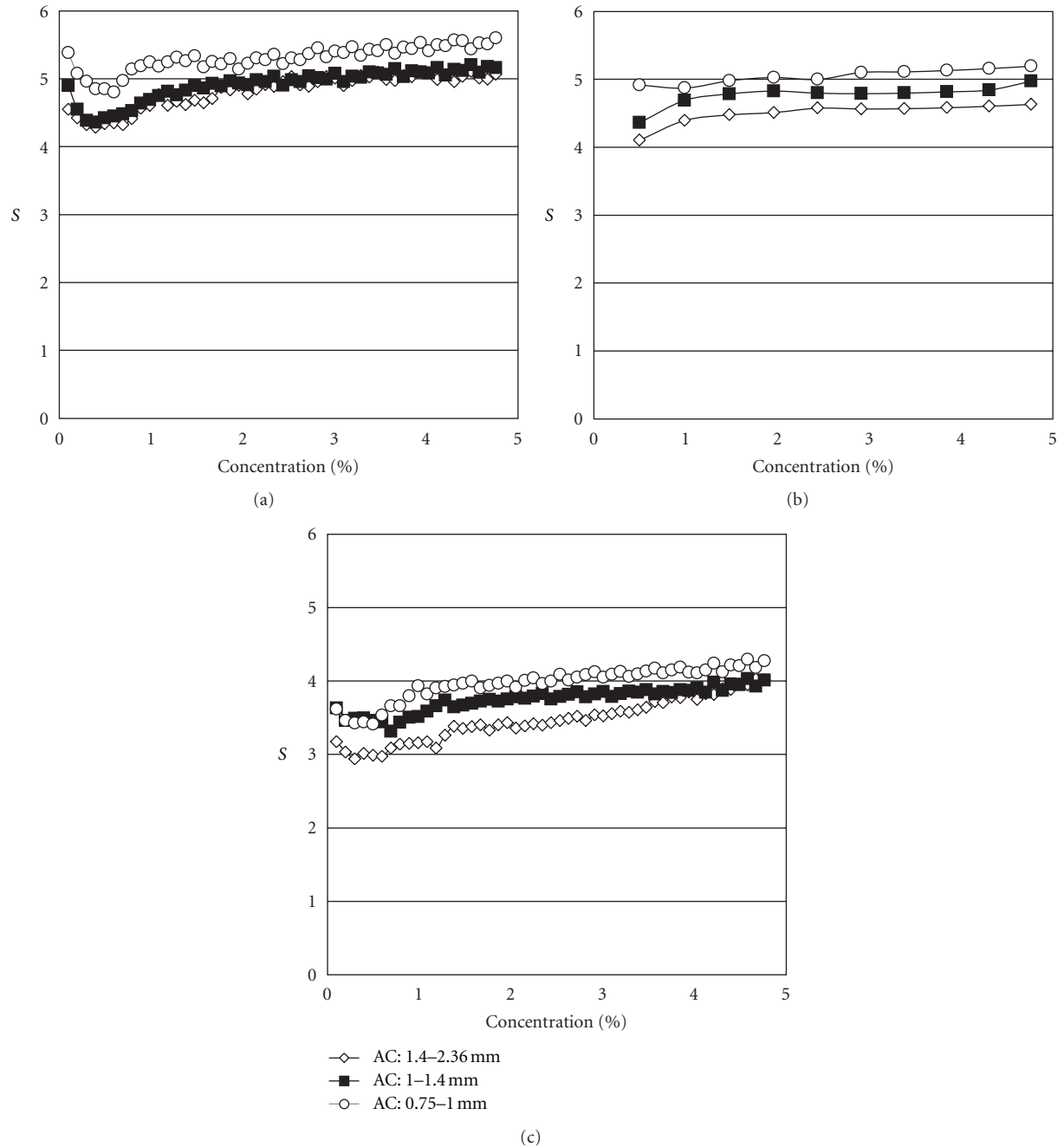
Figure 15: S values versus concentration (%), at varying sizes of activated carbon. (a) 6CB impeller, (b) 6DT impeller, and (c) 6MFD impeller.

V: Volume (m^3)
g: Gravitational constant (ms^{-2})
S: Dimensionless geometricfactor (—).

Greek Letters

$\Delta\rho$: $\rho_{s,eff} - \rho_L$, density difference ($kg\,m^{-3}$)
ρ_L: Fluid density ($kg\,m^{-3}$)
$\rho_{s,eff}$: Effective solid density ($kg\,m^{-3}$)

ρ_s: Solid density ($kg\,m^{-3}$)
ν: Kinematic viscosity ($m^2\,s^{-1}$).

Acknowledgment

References

[1] V. Kolar, "Studies on mixing X: suspending solids particles in liquids by means of mechanical agitation," *Collection of Czechoslovak Chemical Communications*, vol. 26, pp. 613–627, 1961.

[2] K. T. K. Shimizua, K. Takahashi, E. Suzukia, and T. Nomura, "Effect of baffle geometries on crystal size distribution of aluminum potassium sulfate in a seeded batch crystallizer," *Journal of Crystal Growth*, vol. 197, no. 4, pp. 921–926, 1999.

[3] J. Wu, L. Graham, S. Wang, and R. Parthasarathy, "Energy efficient slurry holding and transport," *Minerals Engineering*, vol. 23, no. 9, pp. 705–712, 2010.

[4] D. Chapple, S. M. Kresta, A. Wall, and A. Afacan, "The effect of impeller and tank geometry on power number for a pitched blade turbine," *Chemical Engineering Research and Design*, vol. 80, no. 4, pp. 364–372, 2002.

[5] M. Greaves and Y. Y. Loh, "Power consumption effect in three phase mixing," *ICHEME Symposium Series*, vol. 89, pp. 69–96, 1984.

[6] A. W. Nienow, M. Konno, and W. Bujalski, "Studies on three-phase mixing: a review and recent results," *Chemical Engineering Research and Design*, vol. 64, no. 1, pp. 35–42, 1986.

[7] C. M. Chapman, A. W. Nienow, M. Cooke, and J. C. Middleton, "Particle-gas-liquid mixing in stirred vessels part III: three phase mixing," *Chemical Engineering Research and Design*, vol. 61, no. 3, pp. 167–181, 1983.

[8] N. Dohi, T. Takahashi, K. Minekawa, and Y. Kawase, "Power consumption and solid suspension performance of large-scale impellers in gas-liquid-solid three-phase stirred tank reactors," *Chemical Engineering Journal*, vol. 97, no. 2-3, pp. 103–114, 2004.

[9] S. Ibrahim and A. W. Nienow, "The effect of viscosity on particle suspension in an aerated stirred vessel with different impellers and bases," *Chemical Engineering Communications*, vol. 197, no. 4, pp. 434–454, 2010.

[10] A. Brucato, A. Cipollina, G. Micale, F. Scargiali, and A. Tamburini, "Particle suspension in top-covered unbaffled tanks," *Chemical Engineering Science*, vol. 65, no. 10, pp. 3001–3008, 2010.

[11] G. Baldi, R. Conti, and E. Alaria, "Complete suspension of particles in mechanically agitated vessels," *Chemical Engineering Science*, vol. 33, no. 1, pp. 21–25, 1978.

[12] M. W. Chudacek, "Relationships between solids suspension criteria, mechanism of suspension, tank geometry, and scale-up parameters in stirred tanks," *Industrial and Engineering Chemistry Fundamentals*, vol. 25, no. 3, pp. 391–401, 1986.

[13] M. W. Chudacek, "Solids suspension behaviour in profiled bottom and flat bottom mixing tanks," *Chemical Engineering Science*, vol. 40, no. 3, pp. 385–392, 1985.

[14] R. Conti, S. Sicardi, and V. Specchia, "Effect of the stirrer clearance on particle suspension in agitated vessels," *Chemical Engineering Journal*, vol. 22, no. 3, pp. 247–249, 1981.

[15] F. Rieger, "Effect of particle content on agitator speed for off-bottom suspension," *Chemical Engineering Journal*, vol. 79, no. 2, pp. 171–175, 2000.

[16] D. J. Gray, "Impeller clearance effect on off-bottom particle suspension in agitated vessels," *Chemical Engineering Communications*, vol. 61, pp. 152–158, 1987.

[17] S. Ibrahim and A. W. Nienow, "Particle suspension in the turbulent regime: the effect of impeller type and impeller/vessel configuration," *Trans IChemE*, vol. 74, no. 6, pp. 679–688, 1996.

[18] S. Ibrahim and A. W. Nienow, "Suspension of microcarriers for cell culture with axial flow impellers," *Transactions of the Institutions of Chemical Engineers A*, vol. 82, no. 9, pp. 1082–1088, 2004.

[19] S. Ibrahim and A. W. Nienow, "Comparing impeller performance for solid-suspension in the transitional flow regime with Newtonian fluids," *Chemical Engineering Research and Design*, vol. 77, no. 8, pp. 721–727, 1999.

[20] J. Wu, Y. Zhu, and L. Pullum, "Impeller geometry effect on velocity and solids suspension," *Chemical Engineering Research and Design*, vol. 79, no. 8, pp. 989–997, 2001.

[21] P. M. Armenante and E. U. Nagamine, "Effect of low off-bottom impeller clearance on the minimum agitation speed for complete suspension of solids in stirred tanks," *Chemical Engineering Science*, vol. 53, no. 9, pp. 1757–1775, 1998.

[22] T. N. Zwietering, "Suspending of solid particles in liquid by agitators," *Chemical Engineering Science*, vol. 8, no. 3-4, pp. 244–253, 1958.

[23] J. Wu, Y. G. Zhu, and L. Pullum, "Suspension of high concentration slurry," *AIChE Journal*, vol. 48, no. 6, pp. 1349–1352, 2002.

Research Article

Effect of Mixing on Microorganism Growth in Loop Bioreactors

A. M. Al Taweel,[1] Q. Shah,[2] and B. Aufderheide[2]

[1] *Department of Process Engineering and Applied Sciences, Dalhousie University, Halifax NS, Canada B3J 2X4*
[2] *Process Engineering Programme of The University of Trinidad and Tobago, Point Lisas Campus, Brechin Castle, Couva, Trinidad and Tobago*

Correspondence should be addressed to A. M. Al Taweel, al.taweel@dal.ca

The impact of mixing on the promotion of microorganism growth rate has been analyzed using a multiphase forced-circulation pipe-loop reactor model capable of identifying conditions under which it is possible to convert natural gas into Single-Cell Protein. The impact of mixing in the interphase mass transfer was found to exert a critical role in determining the overall productivity of the bioreactor, particularly at the high cell loadings needed to reduce the capital costs associated with the large-scale production needed for the production of relatively low-value SCP in a sustainable manner.

1. Introduction

Industrial biotechnology uses living cells or cellcomponents (yeast, moulds, bacteria, plants, and enzymes) to synthesize products that are easily degradable, require less energy to produce, and create less waste during their production, all of which helps to decrease the environmental impact of this promising manufacturing approach. It is already used to generate large quantities of biobased products in sectors such as: chemicals, food and feed, detergents, pulp and paper, health care, textiles, bioenergy (e.g., biofuels, biogas), photocatalytic algae production, wastewater treatment, bioleaching, and biological site remediation. It also holds the promise of being a credible method for the sustainable development of many other products because it uses renewable raw materials and is capable of achieving very high efficiencies while converting nonrenewable resources to final products with minimum generation of undesirable byproducts/waste. Nevertheless, the shift to the bioprocessing route will happen only if the economic process and market demands justify the transition. However, the growing environmental pressures combined with the rapid developments in the science supporting biotechnology (sequencing of industrial bacterial and yeast genomes, metabolic engineering, bioinformatics and computer-based modeling, and process optimization) are opening up opportunities for new products and cost reductions.

One of the main factors affecting the economic viability of many of the aforementioned operations is the rate at which interphase mass transfer can take place since it is often the parameter limiting the growth rates of microorganisms encountered in many of these biotechnological processes [1–5]. The use of forced-circulation loop reactors holds the promise of overcoming such limitations in a cost-effective fashion particularly for large-scale operations [6–11]. Whereas the achievement of high productivity is usually not a high priority issue in the production of high-value biotechnological products such as medical therapeutics and pharmaceuticals, the relatively low value of the products encountered in industrial biotechnology necessitate that high utilization efficiencies for capital and raw materials be achieved to ensure sustainability [4, 5].

The objective of this study is to develop a mathematical model that is capable of quantifying the role that mixing and interphase mass transfer play in the overall performance of pipe-loop bioreactors. Particular emphasis is placed on identifying the value of $k_L a$ needed to achieve high overall reactor productivity under different design and operating

conditions (e.g., biomass loading, bioconversion rates, feed gas composition, superficial liquid velocity, and gas to liquid ratios). Judicious selection of mixing devices can then be made in order to achieve optimal conditions. A case study in which natural gas is converted into Single-Cell Protein is used to illustrate the capabilities of this approach and to identify a range of optimal conditions necessary for sustainable operations. Interest in this technology is driven by the promise of meeting the rapidly increasing worldwide demand for protein-rich nutrition in an energy-efficient and cost-effective fashion [2].

2. The Role of Mixing in Bioreactors

Bioreactors are characterized by a complex three-phase flow (liquid, gas, and biomass) and the interaction between mixing and biological reactions is complicated by the fact that such interactions take place simultaneously at the macro-, meso-, and micromixing scales.

Macromixing thus dictates the flow pattern prevalent in the bioreactor and ensures that the nutrients are reasonably well distributed throughout its volume. Large-scale bioreactors have been shown to exhibit heterogeneous hydrodynamic and concentration fields with the cells circulating through such reactors being submitted to an extracellular fluctuating environment [12]. Insufficient macromixing can consequently induce modifications of the cell metabolism, leading to the formation of byproducts and decreasing the overall reactor performance with large-scale cultivations exhibiting lower carbon conversion yields than expected from lab-scale experiments [13]. In the case of the photobioreactors used for algae production, macromixing is used to ensure proper exposure to high-intensity light and to provide alternate durations in light and dark regions, an environmental requirement for some microorganisms to achieve high growth rates and to produce the desirable product quality [14–16].

On the other hand, the Kolmogorov microscales for typical bioreactor configurations vary from 50 to $300\,\mu$m, which is far larger than the size of bacterial or yeast cells (2 and $10\,\mu$m, resp.). Microbial cells, which usually have densities very close to the aqueous environment into which they are suspended, are therefore usually engulfed by the liquid stream in which molecular diffusivity becomes the main mechanism responsible for providing substrate to the cells [13]. It is however well accepted that the size of bubbles present in turbulently flowing liquid (a factor which strongly affects the rate of gas exchange) is inversely related to the local energy dissipation rate or the local microscale [17–20]. The same requirements apply to facilitating interphase mass transfer in the liquid-liquid dispersions encountered during the biodegradation of hydrophobic substrates, or when an immiscible liquid phase is introduced to facilitate oxygen transfer [21].

High levels of microscale turbulence are therefore necessary to improve mass transfer between the phases but attention must be given to ensure that shear-sensitive cells are not damaged [19, 22]. On the other hand, recent findings
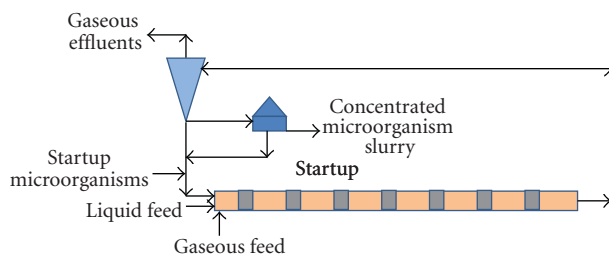
Figure 1: Schematic representation of a pipe-loop bioreactor system.

suggest that, contrary to the commonly accepted idea, a beneficial effect on the growth rate of animal cells can be achieved at moderately elevated agitation rates [23].

2.1. Forced-Flow Pipe-Loop Bioreactors. The overwhelming majority of the information dealing with the impact that mixing has on the performance of bioreactors focused on mechanically agitated tanks, bubble columns, and airlift reactors [24], with very limited attention being given to the case of pipe-loop bioreactors although they hold the promise of being used for large-scale industrial bioprocessing because of their uniform plug flow characteristics, ease of control, and low capital and operating costs. To redress this deficiency, attention in the following sections will be focused on analysing the performance of tubular loop bioreactors in which the biochemical reaction rate is usually controlled mainly by mixing and its ability to promote interphase mass transfer. A case study in which natural gas is converted into Single-Cell Protein is used to illustrate the capabilities of this approach.

The operation of a typical pipe-loop bioreactor is schematically represented in Figure 1 in which different reactor configurations can be used:

  (i) horizontal, inclined, and vertical closed-loop reactor systems in which the flow is mechanically induced using pumps and static-mixing elements are used to develop the desired flow patterns, gas dispersion, and local energy dissipation rates needed to maintain good contact [3, 25–27],

 (ii) vertical U-loop reactors [8, 11], in which axial flow mixers/pumps are used to induce the desired flow while static mixers are used at several locations along the loop to redisperse the gas and improve contact between the phases,

(iii) combinations of the above [7].

Regardless of the method used to induce fluid flow (pumps, inline axial flow mixers, or airlift), the process performance of the bioreactor can be described by the same model.

2.2. Interphase Mass Transfer in Forced-Flow Pipe-Loop Bioreactors. Static mixers have become an integral and basic component of the multitude of equipment used in the chemical process industries. Because of their simplicity and

the absence of any moving parts, these mixers are being increasingly used in a wide range of applications [28]. They are thus used for laminar and turbulent mixing of miscible liquids, in enhancing the performance of heat exchangers and tubular reactors, for laminar and turbulent homogenization, to promote coagulation and flocculation under well-controlled hydrodynamic and chemical environment as well as for the dispersion of immiscible phases.

The only source for energy dissipation that is associated with the use of static mixers is that related to the loss of pressure energy as the fluid passes through the static-mixing elements. This is usually supplied by the pump used to circulate the fermentation broth through the reactor loop. The major disadvantage of using static-mixing elements in bioreactors therefore stems from the direct coupling between the local energy dissipation rate within the mixing elements (which controls the rate of interphase mass transfer) and the velocity at which the two phases pass through such elements. This limits, to some extent, the operational flexibility of the systems but the use of multiple mixers operating in parallel can be used to overcome this difficulty.

A typical static mixer is composed of a series of identical, motionless inserts that are installed in tubular structures (pipes, columns, or reactors) with the purpose of redistributing the fluid in a direction transverse to the main flow (i.e., in the radial and tangential directions). The effectiveness of this redistribution is a function of the specific design and number of elements. On the other hand, the recently introduced screen/grid mixing elements can be considered as means for modifying the turbulent characteristics (turbulence scales and intensity) of the pipe flow, thereby providing a high degree of control on the performance of the gas/liquid contact [20, 29, 30].

Although the patent literature pertinent to static mixers and their use goes back to the 1930s, systematic investigations concerning the various factors affecting gas/liquid contacting and interphase mass transfer in such units are somewhat limited [20, 31–34]. However, the work conducted by Heyouni et al. [17] presents a very systematic investigation of the various factors affecting gas/liquid contacting in static mixers and compared their findings with the performance of other commonly used contactor types such as mechanically agitated tanks, bubble columns, and airlift reactors. They reported that the use of Lightning static mixers can enhance the interfacial area of contact between the phases by a factor of 10–25 with the value of the interphase mass transfer coefficient increasing with increasing liquid and gas velocities. Volumetric mass transfer coefficients as high as $2.5\,s^{-1}$ were obtained at local energy dissipation rates of about $100\,kW/tonne$. Similar results were also reported by several other investigators [20, 33, 34] at somewhat similar rates of energy dissipation within the volume of the mixer. The impact that various constituents present in fermentation broths have on bubble breakage/coalescence and mass transfer was simulated by Azizi and Al Taweel by adding trace quantities of a cationic surfactant (up to 20 ppm of SDS). In spite of the well-known adverse effect that surfactants have on the value of the liquid-side mass transfer coefficient k_L, [24, 35], volumetric mass transfer

Figure 2: Axial variation in local interphase mass transfer coefficient.

coefficients as high as $4.0\,s^{-1}$ were obtained thanks to the ability of screens/sieves to efficiently generate large interfacial areas of contact.

It is however very interesting to note that whereas static mixers are typically characterized as having very high local energy dissipation rates (with ε values of up to $1,000\,kW/tonne$ being reported), the power needed to pump the fermentation broth through the bioreactor can be rather low. Thus whereas Azizi and Al Taweel [34] obtained mass transfer coefficients as high as $4.0\,s^{-1}$ using average energy dissipation rates within the contactor volume, ε, of 320 W/kg, the amount of energy used to pump a unit mass of the liquid through the 560 mm long static mixer, E_M, was found to be as low as 0.02 kWh/tonne. This is mainly attributable to the low residence times spent within the static mixer. Much smaller values of E_M were obtained by Lemenand et al., [36], while using high-efficiency vortex static elements to disperse immiscible fluids.

The aforementioned very high volumetric mass transfer coefficients were obtained by using relatively small interscreen spacing (70 mm) and high superficial velocities, factors which resulted in reducing the efficiency by which energy is utilized to promote mass transfer between the phases (0.1–$0.6\,kgO_2/kWh$, depending on the operating conditions and the interfacial characteristics of the system). These values are an order of magnitude smaller than those reported by Al Taweel et al. [9] using similar mixing elements placed far apart (with interscreen spacing of 700–1,200 mm) where the emphasis was on achieving high oxygen transfer efficiencies by taking advantage of the coalescence retardation effect of the contaminants.

In the present analysis, it is envisaged that the approach recommended by Turunen and Haario [32] will be adopted. Short sections containing a relatively small number of static-mixing elements will be used to disperse the gas into small bubbles. Each of these sections will then be followed by relatively long sections of empty pipes which are used to provide the loop reactor with the desired residence time. Unfortunately, the fine bubbles formed by the static mixers will tend to coalesce into bigger ones as the dispersion flows into the regions of lower local energy dissipation rates. The overall outcome of these processes is schematically depicted in Figure 2 which presents the axial variation of the local mass transfer coefficient predicted by CFD simulation for two superficial velocities.

The achievement of high interphase mass transfer rates allows for supplying the high oxygen demands associated with the use of high cell loadings, and for the stripping of

the CO_2 that tends to dissolve in the broth particularly at elevated pressures.

3. Converting Hydrocarbons into SCP

In this section, the impact of multiphase mixing (and the associated impact on interphase mass transfer) on the performance of forced-flow pipe-loop bioreactors is illustrated using the important industrial biotechnology case where hydrocarbons and hydrocarbon-based products are converted into single-cell protein. This technology is well-established and has been practiced for many years [37]. Initially, attention focused on the use of waxy n-paraffins, a byproduct from oil refineries with the primary use of the product being poultry and cattle feed. Because of the abundance of relatively low-cost natural gas, and the fast conversion rates achievable at lower hydrocarbon molecular weights, emphasis has recently shifted towards using several methanotrophic microorganisms in a continuous process that simply uses methane, oxygen, ammonia, minerals, and water as raw materials. This approach was so successful that a joint venture between Statoil and DuPont (Norferm A/S) constructed a 10,000 tpa plant in Norway that utilized circulating loop reactors with both horizontal and vertical sections in which static mixers were introduced to enhance gas/liquid mass transfer. Commercial-scale production began in May 2003, but was shut down after 3 years presumably because of the low production rate per unit volume of the reactor and the relatively high cost of natural gas supply.

3.1. Pipe-Loop Bioreactors for SCP Production. The continuous manufacture of proteins by the biochemical oxidation of gaseous hydrocarbons in the presence of a nitrogenous nutrient has been achieved using horizontal and vertical closed-loop reactors, vertical airlift reactors, as well as vertical U-loop reactors [10, 11, 27, 38]. These investigations, as well as many others, identified that the productivity of this process is influenced by a wide range of parameters such as the liquid phase concentration of oxygen, methane and CO_2, the biomass concentration, temperature, and pH.

Although the process is relatively simple, the reactor design methodology is rather complex as it deals with a multiphase system (gas/liquid/solid) in which the gaseous reactants have to dissolve into the aqueous medium where a highly exothermic heterogeneous biochemical reaction takes place.

The model presented in this paper takes into account the most critical components affecting the various processes taking place within the bioreactor used for converting natural gas into SCP. It can be used to design and evaluate the performance of vertical and horizontal tubular loop reactors, as well as the riser section of an Air-Lift Reactor where most of the interphase mass transfer takes place. The model calculates the spatial variation in biomass production as the multiphase reacting mixtures flow along the length of the pipe-loop reactor and can therefore be used for

(i) identifying the operating conditions under which the overall production rate is mass transfer limited or reaction rate limited,

(ii) identifying the optimum design and operating conditions such as reactor length, superficial liquid velocity and the gas to liquid flow ratio, and optimum biomass concentration in the recycle stream,

(iii) determining the impact of promoting interphase mass transfer by preconcentrating the oxygen in the gas stream (by switching from air to cryogenic oxygen), operating at elevated pressures, and the insertion of static mixers at various locations along the reactor length,

(iv) calculating the impact of the various design and operating conditions on the energy dissipation rates in the various components of the process, thereby enabling the identification of the optimum balance between capital and operating costs,

(v) identifying the optimum oxygen to methane ratio and the conditions under which it is necessary to recycle and reuse unconsumed raw materials (natural gas, methanol, oxygen, and ammonia).

Better understanding of the interaction between those parameters is needed in order to develop sustainable means for converting natural gas and methanol into SCP.

3.2. Specific Conditions for M. capsulatus SCP Production. Bioreaction stoichiometry can vary significantly depending on the value of a host of parameters that include growth media optimization, temperature, and pressure of the reaction. The SCP produced by the biooxidation of natural gas using mostly *M. capsulatus* contains about 70% crude protein, 10% crude fat, 10% nucleic acid, and 7% ash and can be represented by the elemental analysis $CH_{1.8}O_{0.5}N_{0.2}$. Nielsen et al. [39] presented the following stoichiometry for the biooxidation of natural gas (mainly methane) with ammonia and oxygen using the aforementioned microorganism:

$$CH_4 + 0.104NH_3 + 1.45O_2 \longrightarrow 0.52CH_{1.8}O_{0.5}N_{0.2}$$
$$+ 0.48CO_2 + 1.69H_2O \tag{1}$$
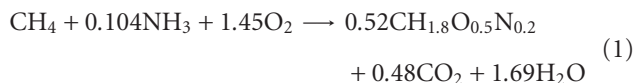
The corresponding reaction yield coefficients are given in Table 1.

According to Joergensen and Degn [40] the specific growth rate of *M. capsulatus*, μ_S, during the biooxidation of methane at 45°C, can be described by the following *Monod* equation with the saturation constant values given in Table 1:

$$\mu_S = \frac{\mu_{\max}C_{S,l}}{K_{SM} + C_{S,l}}. \tag{2}$$

4. Modeling the Performance of Forced-Circulation Loop Bioreactors

Analysis of a bioreactor performance requires a model for the flow field, a model for the biomass reactions taking

TABLE 1: Baseline parameters used in simulations.

Parameter	Value	Units	Parameter	Value	Units
μ_{max}	0.37	hr^{-1}	T_{STP}	25	°C
K_S	$1.3\,e^{-6}$	mol CH$_4$/L	P_T	3	atm
Y_{SX}	1.93	(mol CH$_4$/mol Cell)	P_{STP}	1	atm
Y_{OX}	2.80	(mol O$_2$/mol Cell)	$U_{G,0}$	0.043	m/s
Y_{CX}	0.92	(mol CO$_2$/mol Cell)	U_L	0.5	m/s
H_{CH_4}	1,000.9	L·atm/mol	$y_{CH_4,0}$	0.40	[—]
H_{O_2}	1,100.81	L·atm/mol	$y_{O_2,0}$	0.58	[—]
H_{N_2}	2,023.6	L·atm/mol	$y_{N_2,0}$	0.02	[—]
H_{CO_2}	47.39	L·atm/mol	$y_{CO_2,0}$	0.00	[—]
T	45	°C	Z	15	m

place in the liquid phase, and a model for the mass transfer between phases (from gas to liquid and from the liquid to biomass). Despite the fact that biological reactions are conditioned by the mass transfer between the liquid and the biomass, hydrodynamics and bioreactions are generally coupled through conservation equations for the dissolved species.

For properly designed forced-circulation loop reactors operating at the relatively high Reynolds numbers encountered in large-scale operations, the tendency of bubbles to segregate under the action of gravity can be neglected particularly when static mixers are inserted to counteract the tendency for phase segregation and to redisperse the gas phase into finer bubbles [33, 41, 42]. The bioconversion taking place in such reactors can then be well represented by the simple plug-flow multiphase reactor loop in which the microorganisms can be considered as fully dispersed into the liquid phase (Figure 3).

The rate of interphase mass transfer that can be achieved in such a reactor depends on the type of static mixer used, the spacing between mixing elements, the superficial velocity of the liquid, the interfacial characteristics of the system, and the volume fraction occupied by the gas in the two-phase flowing system [17, 20, 27, 31–34]. In this investigation, emphasis is therefore placed on developing better understanding of the role that interphase mass transfer plays in determining the overall bioreaction rate, and how it interacts with different design and operating conditions. Subsequent publications will address means by which optimum mixing conditions can be achieved in pipe-loop bioreactors.

The characteristics of the bubbly flow system passing through the control element depicted in Figure 3 is determined by the physical properties of the two phases, their respective flow rates, and the extent to which the gas phase is dispersed through the liquid. The microorganisms suspended in the liquid phase usually have a density that is close to that of water and their volumetric flow rate can, at present, be incorporated as a part of the liquid phase. At relatively low volumetric concentrations (up to 30 g cells/L dry weight) the presence of bacteria in water will exert little influence on its characteristics but, the rheology of the microbial suspensions can become more complex at
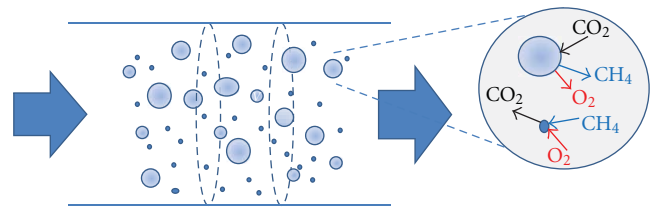
FIGURE 3: Schematic representation of the bubbly flow and interphase mass transfer, taking place in pipe-loop bioreactor.

high-volumetric solid loadings of interacting and flocculated microorganisms [43].

The operational characteristics of the multiphase bioreactor are usually based on the volumetric flow rate of the liquid phase to be processed (which includes the suspended microorganisms as an integral part of it) and the gas to liquid volumetric flow ratio, G/L. The latter is usually taken at STP (25°C, Pressure 1 atm) and does therefore not necessarily reflect the actual conditions present in the reactor which can operate over a wide range of temperatures and pressures.

The total number of gaseous molecules introduced to the reactor is therefore given by

$$N_{G0} = \sum_{i=1}^{i=n} \frac{F_{G,i}P_{STP}}{RT_{STP}}, \tag{3}$$

where $F_{G,i}$ is the gas flow rate (at STP) for each of the ith gases introduced to the reactor and n is the total number of gaseous species encountered in the bioreactor.

Consequently, the volumetric flow rate of the gas phase at any particular point along the reactor length, Q_G, can be determined from

$$Q_G = \frac{N_{G0}RT}{P_T}. \tag{4}$$

And the superficial velocity of the gas phase flowing through the control element, U_G, can be expressed by,

$$U_G = \frac{Q_G}{A_c}, \tag{5}$$

where A_c is the cross-sectional area of the loop reactor.

Similarly, the superficial velocity of the liquid phase flowing through the element, U_L, can be expressed by

$$U_L = \frac{Q_L}{A_c}. \tag{6}$$

The superficial velocity of the two-phase system can therefore be expressed as

$$U_T = U_G + U_L. \tag{7}$$

Neglecting the slip velocity between the phases, a reasonable assumption in finely dispersed bubble flows, the volume fraction of the gas phase (i.e., the gas holdup) can be expressed as

$$\varepsilon_G = \frac{Q_G}{Q_G + Q_L}. \tag{8}$$

The total number of gas molecules flowing through the control element is determined by the flow rate of the various gaseous constituents fed into the reactor, minus those quantities that have been transferred into the liquid phase, as well as by the various gaseous products that evolve as a result of the biochemical reaction taking place. Parts of the latter gases dissolve into the liquid phase with the remainder being transferred into the bubbly flow gas phase (including water vapour which can play a significant role at relatively high operating temperatures).

Since there is no biochemical reaction taking place in the gas phase, the axial evolution of the reactant concentrations (in the gas and liquid phases) along the length of the reactor can be described by

$$\frac{dC_{CH_4,G}}{dz} = \frac{-(k_L a/\varepsilon_G)\left(C^*_{CH_4} - C_{CH_4,L}\right)}{U_T}, \tag{9}$$

$$\frac{dC_{CH_4,L}}{dz} = \frac{(k_L a/(1-\varepsilon_G))\left(C^*_{CH_4} - C_{CH_4,L}\right) - Y_{SX}\mu C_X}{U_T}, \tag{10}$$

$$\frac{dC_{O_2,G}}{dz} = \frac{-(k_L a/\varepsilon_G)\left(C^*_{O_2} - C_{O_2,L}\right)}{U_T}, \tag{11}$$

$$\frac{dC_{O_2,L}}{dz} = \frac{(k_L a/(1-\varepsilon_G))\left(C^*_{O_2} - C_{O_2,L}\right) - Y_{OX}\mu C_X}{U_T}, \tag{12}$$

$$\frac{dC_{CO_2,G}}{dz} = \frac{-(k_L a/\varepsilon_G)\left(C^*_{CO_2} - C_{CO_2,L}\right)}{U_T}, \tag{13}$$

$$\frac{dC_{CO_2,L}}{dz} = \frac{(k_L a/(1-\varepsilon_G))\left(C^*_{CO_2} - C_{CO_2,L}\right) + Y_{CX}\mu C_X}{U_T}. \tag{14}$$

The values of the yield coefficients Y_{SX}, Y_{OX}, and Y_{CX} are given in Table 1 for the case when *Methylococcus capsulatus* is used to convert methane into SCP.

In addition to the reactants, the gases introduced to the bioreactor usually contain an amount of inerts (nitrogen and

rare gases) the value of which depends on the composition of the oxygen source as well as that of the natural gas. Although these gases do not take part in the biooxidation reaction, they partially dissolve in the liquid stream circulated through the loop reactor and their presence in the gas phase results in reducing the concentration of the reactants present in that phase and can, therefore, adversely affect the mass transfer rates. The same applies to the case of the CO_2 produced as a result of the biochemical reaction.

The axial variation of the inert gas concentration in the gaseous and liquid phases is given by

$$\frac{dC_{Inert,G}}{dz} = \frac{-(k_L a/\varepsilon_G)\left(C^*_{Inert} - C_{Inert,L}\right)}{U_T}, \tag{15}$$

$$\frac{dC_{Inert,L}}{dz} = \frac{(k_L a/(1-\varepsilon_G))\left(C^*_{Inert} - C_{Inert,L}\right)}{U_T}. \tag{16}$$

Although the mass transfer coefficient for the various gases can be significantly different, they are assumed to be equal for the purpose of this investigation. The equilibrium concentrations present at the gas/liquid interface used in (9)–(16) were computed using Henry's law,

$$C^*_i = \frac{y_i \cdot P}{H_i}, \tag{17}$$

where the values of Henry's constant for the various gases are based on the standard values reported in Table 1 but corrected for the bioreactor operating temperature using a van't Hoff equation. The vapour pressure of water present at the interface was estimated using the Antoine equation.

5. Results and Discussion

The system of nonlinear ODE describing the fermentation of *M. capsulatus* in a single pass, (3)–(17), was solved using MATLAB's ODE solvers. The impact of various design and operating parameters on the performance of the reactor was numerically determined with the objective of identifying optimum design and operating conditions using the productivity per unit volume as a preliminary indicator. Pressure losses due to the flow through the static mixers and along the reactor length was neglected at this stage of analysis.

Throughout the present investigation, the oxygen to methane ratio was kept at the stoichiometric value of 1.45. The 15 m long loop bioreactor was assumed to operate at the optimum temperature of 45°C by providing means for removing the heat released through the biooxidation reaction. The oxygen stream is also assumed to be from cryogenic distillation (97% O_2 with 3% inerts) except where the effect of using different oxygen enrichment methods was assessed. In cases where the methane and oxygen are completely consumed prior to leaving the tubular reactor, the set of differential equations reduces to only the liquid phase for the remainder of the reactor. This was necessitated because a singularity in the gas phase equations occurs as the gas fraction approaches zero.

To reduce the computational effort associated with the analysis of this complex process at this early stage of process
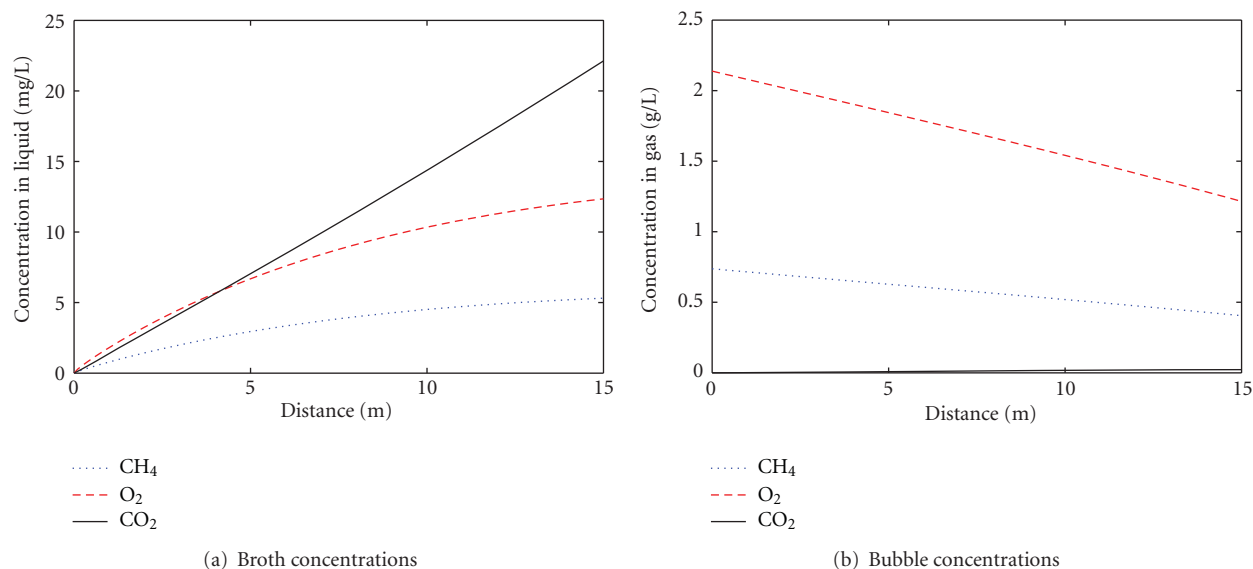
(a) Broth concentrations

(b) Bubble concentrations

Figure 4: Startup concentration profiles in the liquid and gas phases ($P_T = 3$ atm, $k_L a = 0.05$ s^{-1}, $C_{X0} = 5$ g/L, $G/L = 0.20$, and $U_L = 0.5$ m/s).

assessment, it was assumed that the dissolved gases are flushed out from the recycled liquid stream which is then returned to the reactor after it is presaturated by the reactants (95% of max achieved at the operating temperatures pressures).

5.1. Startup Operations. In the liquid phase, where the biooxidation reaction takes place, the axial variation of the reactants (CH_4 and O_2) and product (CO_2) concentrations is controlled by the relative magnitude of the rate at which the reactants are supplied to the liquid phase (through interphase mass transfer) and the rate at which they are consumed through the biooxidation microbial activity. During the startup stage, the bioreaction is initiated by introducing a small amount of the bacterial inoculums to the recirculating liquid followed by the introduction of the reactant gases at the desired pressure. To accurately simulate this transient stage, the concentration of the reactants in the liquid phase entering the loop was set at zero but was found to increase along the reactor length due to the absorption and/or gas evolution associated with the microbial growth (Figure 4).

On the other hand, the concentration of the reactants in the gas phase decreases as the dispersion progresses along the reactor length with very low concentrations of CO_2 appearing in the gas phase due to its progressive accumulation in the liquid phase where it is very soluble at the relatively high pressures used in this case. Due to the low biomass loadings used at startup, the gaseous reactants (CH_4 and O_2) are not fully consumed in the bioreactor and large quantities of the gaseous reactants may need to be flared or recirculated until sufficient biomass loadings have been built up.

This transit situation continues with complete recirculation of the liquid at progressively higher concentration of the microorganisms until a quasi-steady state is reached in which the SCP can be harvested. Since harvesting is typically conducted at atmospheric pressure, most of the gases dissolved in that liquid stream will flash out before the liquid is returned back to the reactor (Figure 1).

5.2. Effect of Mixing and Promotion of Interphase Mass Transfer. The relative importance of interphase mass transfer and reaction rates is clearly shown in Figure 5. At relatively low volumetric mass transfer coefficients, the average productivity of the bioreactor is limited by the rate at which the gaseous reactants are transported into the liquid phase. On the other hand, the reactor productivity is controlled by the intrinsic biooxidation rate at high mass transfer coefficients with the transition point between the two regimes being a function of the different design and operating conditions.

The length of reactor needed to achieve >99% utilization of the reactants was found to decrease as the value of the interphase mass transfer coefficient and biomass loadings are increased. This suggests that the process can be operated at somewhat higher gas/liquid ratios, or that shorter reactor lengths can be used, in order to ensure maximum utilization of the reactor volume. Both of these options can have significant impact on enhancing process sustainability.

The importance of using a combination of high cell loading and high volumetric mass transfer coefficients is demonstrated in Figure 6. For the design and operating conditions tested, the fraction of reacting gases that get converted in a single pass through the loop was found to increase from about 20% up to about 100% as the cell loading is increased from 3 to 15 g/L provided that the mixing intensity is high enough to supply the microorganisms with the nutrients they need to grow. The overall complexity of the conversion process becomes much simpler if practically all the reactants are consumed within a single pass, thus avoiding need for the complex and costly operations needed to separate and recycle the unused reactants. There is, however, some indications that it is necessary to maintain a minimum level of oxygen
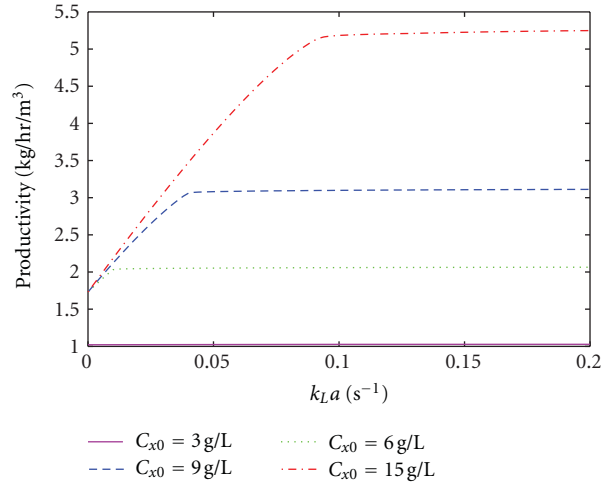
FIGURE 5: Effect of the volumetric mass transfer coefficient on the reactor productivity ($P_T = 3$ atm, $G/L = 0.20$, and $U_L = 0.5$ m/s).

(a) Bubble oxygen concentration

(b) Bubble methane concentration
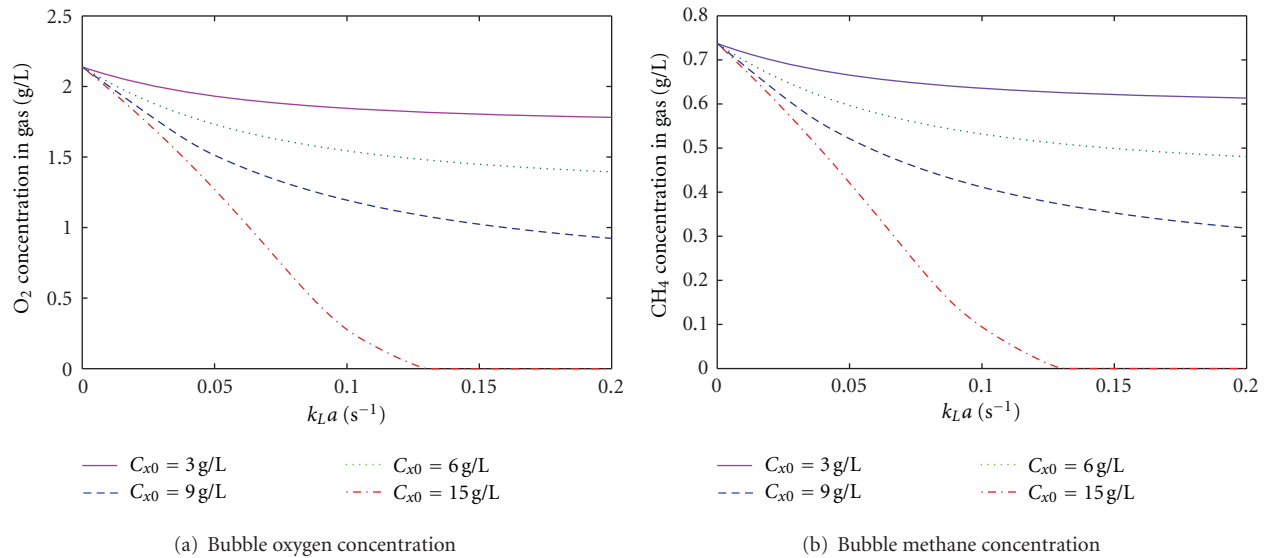
FIGURE 6: Effect of the volumetric mass transfer coefficient on the concentration of oxygen and methane in the gas phase exiting the reactor ($P_T = 3$ atm, $G/L = 0.20$, and $U_L = 0.5$ m/s).

concentration within the reactor to maintain a vigorous and healthy microorganism population.

The high-mass transfer coefficients needed to maintain a high level of reactor productivity cannot always be achieved, particularly in the case of shear-sensitive microorganisms. The use of high-operating pressures to promote mass transfer has been proposed as a mean for overcoming such difficulties. As can be seen from Figure 7, the production-rate per unit volume of the reactor was found to increase linearly with increasing operating pressure but tends to flatten off beyond a certain pressure the value of which depends on the cell loading. Operating the reactors at pressures higher than those optimal values is wasteful of energy, whereas the full productivity potential of the reactor will not be achieved by operating at pressures lower than the optimal. It is, however,

important to remember that the volumetric flow rate of the gases flowing through the reactor decreases in proportion to the operating pressure, thereby making it more difficult to achieve and maintain elevated volumetric mass transfer coefficients at high pressures.

An extensive analysis of the results obtained revealed that productivity of the pipe-loop bioreactor is controlled mainly by the magnitude of the interphase mass transfer and the cell loading in the fermentation broth being introduced into the reactor. The combined effect of these two highly interactive parameters is given in Figure 8 which clearly illustrates the regions of mass transfer limitations, regions where the kinetics of microbial growth controls the overall performance, and the conditions where both of these parameters play an important role.

FIGURE 7: Effect of pressure on the reactor productivity for different cell loadings ($k_L a = 0.025\,\text{s}^{-1}$, $G/L = 0.20$, and $U_L = 0.5\,\text{m/s}$).

FIGURE 9: Effect of superficial liquid velocity and mass transfer coefficient on the productivity of the bioreactor ($P_T = 3$ atm, $C_{x0} = 15\,\text{g/L}$, and $U_{G,0} = 0.043\,\text{m/s}$).

FIGURE 8: Effect of initial cell loading and volumetric mass transfer coefficient on the productivity of the bioreactor ($P_T = 3$ atm, $G/L = 0.20$, and $U_L = 0.5\,\text{m/s}$).
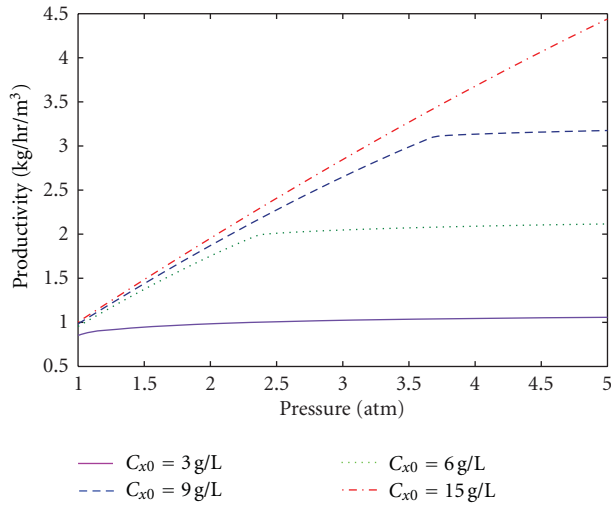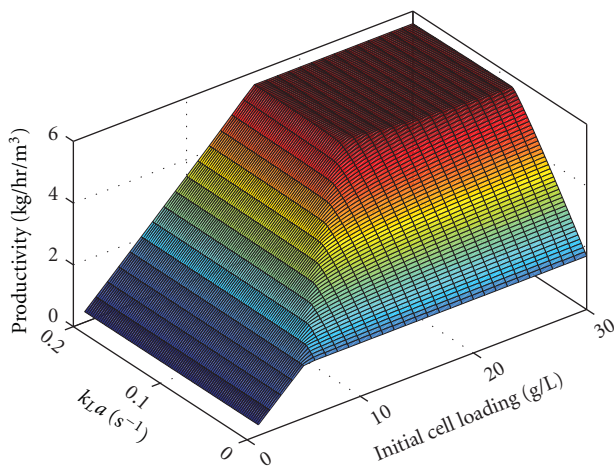
A plateau in reactor productivity was observed to occur under conditions where both high biomass loadings, and elevated interphase mass transfer coefficients, can be achieved. In this region, an increase in the value of either parameter does not appear to enhance the productivity of the loop-bioreactor mainly because the reactants are exhausted before reaching the end of the fixed length bioreactor (15 m). On the other hand, one can use shorter bioreactor length to match that where the bioactivity takes place, thereby reducing the capital cost of the bioreactor and increasing the productivity of the bioactive parts of the reactor.

Figure 8 clearly shows that bioreactor productivity as high as $4\,\text{kg/h m}^3$ can be achieved using average mass transfer coefficients as low as $0.05\,\text{s}^{-1}$, a feat that can be easily achieved using pipe-loop bioreactors that are equipped with appropriately designed static mixers. However, considering

that there are in excess of 40 commercially available static mixers designs that can be used for that purpose, the detailed analysis/design of the gas liquid contact in such units is beyond the scope of the present investigation.

One of the most commonly used means for controlling the level of the interphase mass transfer coefficient in the case of gas/liquid dispersions flowing through static mixers is by increasing the superficial velocity of the liquid phase. The impact of such action on the productivity of the loop bioreactor is shown in **Figure 9** for a fixed biomass loading of $15\,\text{kg/m}^3$ and a constant inlet superficial gas velocity of $U_G = 0.043\,\text{m/s}$.

Since we are dealing with a fixed length reactor, an increase in superficial gas velocity will lead to reducing the residence time in the bioreactor. It is therefore interesting to see that for $k_L a$ values $0.08\,\text{s}^{-1}$, a plateau in the bioreactor productivity was observed to occur for superficial liquid velocities of 0.4 m/s or higher. Under such conditions, all the reactants are converted within the specified reactor length and any changes in the residence time, $k_L a$, and G/L ratio are not reflected in the productivity but in the length of the reactor needed to achieve conversion. The slight reduction in productivity observed at U_L values lower than 0.4 m/s is caused by the incomplete conversions of the reactants at the elevated G/L ratios associated with the low liquid superficial velocities.

Under conditions where low $k_L a$ values are expected to prevail, it was found that the use of high liquid superficial velocities results in increasing the productivity of the reactor to some extent. This unexpected finding stems from the increased importance of the reactant feed rates associated with the elevated influx of presaturated liquid feed. This, in turn, resulted in the average concentration across the reactor length being higher the larger the liquid superficial velocity is, with the consequent increase in average bioreaction rate. It is, however, not desirable to operate the bioreactor outside of the plateau region because of the large reactant fraction that remains unutilized at the end of the reactor, and

the consequent need to establish a costly reactant recovery system to maintain the sustainability of the operation.

6. Conclusions and Recommendations

The impact that mixing has on the productivity of growing microorganisms in loop bioreactors has been investigated using the bioconversion of natural gas into Single-Cell Protein as a case in point. A computer-aided design and simulation model capable of analyzing the factors affecting this process was developed which is capable of accounting for the impact that a wide range of operating and design conditions can have on the productivity of the tubular loop-reactors used in industry.

The results obtained in this investigation suggest that it is possible to operate the process in a manner by which more than 99% of the reactants can be utilized in a once-through operation provided that proper biomass loadings and reactor lengths are used, and adequately high interphase mass transfer coefficients are achieved. Average bioreactor productivities in excess of $4 \, \text{kg/h} \, \text{m}^3$ are predicted to be achieved using average mass transfer coefficients as low as $0.05 \, \text{s}^{-1}$, a feat that can be easily achieved using pipe-loop bioreactors that are equipped with appropriately designed static mixers.
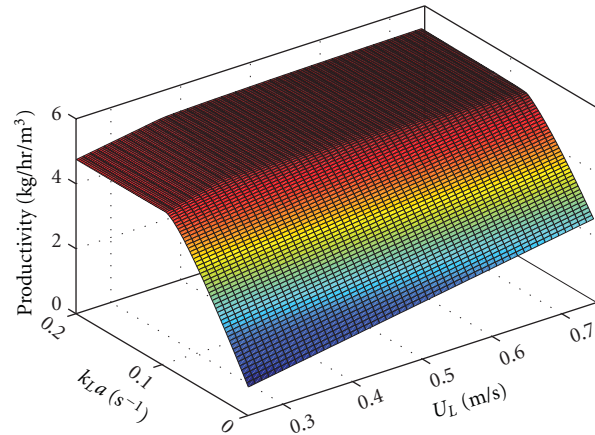
However, that model does not yet address the physical means by which the desired interphase mass transfer coefficients can be achieved, a deficiency that is presently being addressed.

Nomenclature

a: Interfacial area of contact $[\text{m}^2/\text{m}^3]$
A_c: Cross-sectional area of the loop reactor pipe $[\text{m}^2]$
C: Bulk concentration $[\text{mol/L}]$ and Constant in Van't Hoff equation $[\text{L}\cdot\text{atm/mol}]$
C^*:   Equilibrium concentration at the interface $[\text{mol/L}]$
D: Pipe diameter $[\text{m}]$
E: Energy consumption rate $[\text{kW}]$
E_m: Energy consumed per unit mass of the liquid $[\text{kW/tonne}]$
H: Henry's constant $[\text{L}\cdot\text{atm/mol}]$
k_L: Mass transfer coefficient in liquid phase $[\text{m s}^{-1}]$
$k_L a$:   Volumetric mass transfer coefficient $[\text{s}^{-1}]$
L: Pipe length $[\text{m}]$
P: Pressure at any particular point along the reactor length $[\text{atm}]$
Q: Volumetric flow rate $[\text{m}^3/\text{s}]$
R: Universal gas constant $[\text{L}\cdot\text{atm/K}\cdot\text{mol}]$
Re: Pipe Reynolds number
t: Residence time $[\text{s}]$
T: Temperature $[^\circ\text{C}]$
U: Superficial velocity $[\text{m/s}]$
V: Volume $[\text{m}^3]$
y: mole fraction in gas phase

Y_{ij}:   Stoichiometric yield coefficient of component i relative to component j (e.g., Y_{SX}, mol CH_4/mol Cells)$[\text{mol } i/\text{mol } j]$.

Greek Symbols

ε: Local turbulent kinetic energy dissipation rate $[\text{kW/tonne}]$
ε_G: Volumetric fraction of dispersed phase $[—]$
ρ: Density $[\text{kg/m}^3]$
σ: Surface tension $[\text{N/m}]$
τ: Total residence time in the reactor $[\text{s}]$
μ: Viscosity $[\text{cP}]$ and Specific growth rate of the microorganisms $[\text{h}^{-1}]$
ϕ: Volumetric fraction of dispersed phase $[—]$.

Subscript

0:   Initial conditions
CH_4:   Methane
CO_2:   Carbon dioxide
G: Gas
H_2O: Water vapour
i: Component i in yield coefficient either produced or consumed (e.g., S for substrate or C for carbon dioxide)
Inert: Nonreactive gases
j: Component j in yield coefficient (e.g., X)
L: Liquid
Max: Maximum
ref: Reference conditions
STP: Standard temperature and pressure (25°C, 1 atm)
T: Total
X: Cell biomass.

Acknowledgment

References

[1] J. C. Merchuk and J. A. Asenjo, "The maned equation and mass transfer," *Biotechnology and Bioengineering*, vol. 45, no. 1, pp. 91–94, 1995.

[2] OECD, *The Application of Biotechnology to Industrial Sustainability*, OECD Publications, Paris, France, 2001.

[3] C. U. Ugwu, J. C. Ogbonna, and H. Tanaka, "Improvement of mass transfer characteristics and productivities of inclined tubular photobioreactors by installation of internal static mixers," *Applied Microbiology and Biotechnology*, vol. 58, no. 5, pp. 600–607, 2002.

[4] P. L. Rogers, Y. J. Jeon, and C. J. Svenson, "Application of biotechnology to industrial sustainability," *Process Safety and Environmental Protection*, vol. 83, no. 6B, pp. 499–503, 2005.

[5] J. Villadsen, "Innovative technology to meet the demands of the white biotechnology revolution of chemical production,"

Chemical Engineering Science, vol. 62, no. 24, pp. 6957–6968, 2007.

[6] M. Gavrilescu, R. V. Roman, and R. Z. Tudose, "Hydrodynamics in external-loop airlift bioreactors with static mixers," *Bioprocess Engineering*, vol. 16, no. 2, pp. 93–99, 1997.

[7] H. Eriksen, K. Strand, and L. Jorgenson, "Method of fermentation," GB Patent 0120025.2, Assigned to Statoil, Stavanger Norway, 2001.

[8] E. B. Larsen, "U-shaped and/or nozzle U-loop fermentor and method of carrying out a fermentation process," US Patent 6, 492, 135, 2002.

[9] A. M. Al Taweel, J. Yan, F. Azizi, D. Odedra, and H. G. Gomaa, "Using in-line static mixers to intensify gas-liquid mass transfer processes," *Chemical Engineering Science*, vol. 60, no. 22, pp. 6378–6390, 2005.

[10] F. Yazdian, S. A. Shojaosadati, M. Nosrati, M. R. Mehrnia, and E. Vasheghani-Farahani, "Study of geometry and operational conditions on mixing time, gas hold up, mass transfer, flow regime and biomass production from natural gas in a horizontal tubular loop bioreactor," *Chemical Engineering Science*, vol. 64, no. 3, pp. 540–547, 2009.

[11] D. F. Olsen, J. B. Jorgensen, J. Villadsen, and S. B. Jorgensen, "Optimal operating points for SCP production in the U-loop reactor," in *Proceedings of the 9th International Symposium on Dynamics and Control of Process Systems (DYCOPS '10)*, M. Kothare, M. Tade, A. Vande Wouwer, and I. Smets, Eds., Leuven, Belgium, July 2010.

[12] A. Amanullah, B. C. Buckland, and A. W. Nienow, "Mixing in the fermentation and cell culture industries," in *Handbook of Industrial Mixing Science and Practice*, E. L. Paul, V. A. Atiemo-Obeng, and S. M. Kresta, Eds., John Wiley & Sons, New York, NY, USA, 2004.

[13] M. Douaire, J. Morchain, and A. Liné, "Mini review: relationship between hydrodynamic conditions and substrate influx toward cells," in *Proceedings of the 13th European Conference on Mixing*, London, UK, April 2009.

[14] Y. K. Lee, "Microalgal mass culture systems and methods: their limitation and potential," *Journal of Applied Phycology*, vol. 13, no. 4, pp. 307–315, 2001.

[15] B. H. Um and Y. S. Kim, "Review: a chance for Korea to advance algal-biodiesel technology," *Journal of Industrial and Engineering Chemistry*, vol. 15, no. 1, pp. 1–7, 2009.

[16] C. Y. Chen, K. L. Yeh, R. Aisyah, D. J. Lee, and J. S. Chang, "Cultivation, photobioreactor design and harvesting of microalgae for biodiesel production: a critical review," *Bioresource Technology*, vol. 102, no. 1, pp. 71–81, 2011.

[17] A. Heyouni, M. Roustan, and Z. Do-Quang, "Hydrodynamics and mass transfer in gas-liquid flow through static mixers," *Chemical Engineering Science*, vol. 57, no. 16, pp. 3325–3333, 2002.

[18] I. Reynolds, "Laboratory protocol PI," in *Proceedings of the 14th Process Intensification Network Meeting*, BHR Group, Cranfield UK, November 2002.

[19] B. Weyand, M. Israelowitz, H. von Schroeder, and P. Vogt, "Fluid dynamics in bioreactor design: considerations for the theoretical and practical approach," in *Bioreactor Systems for Tissue Engineering*, C. Kasper, M. van Griensven, and R. Portner, Eds., pp. 251–268.

[20] R. Munter, "Comparison of mass transfer efficiency and energy consumption in static mixers," *Ozone: Science & Engineering*, vol. 32, no. 6, pp. 399–407, 2010.

[21] A. Arwa, S. Baup, N. Gondrexon, J. P. Magnin, and J. Willison, "Enhancement of mass transfer characteristics and phenanthrene degradation in a two-phase partitioning bioreactor equipped with internal static mixers," *Biotechnology and Bioprocess Engineering*, vol. 16, no. 2, pp. 413–418, 2011.

[22] C. Zhong and Y. J. Yuan, "Responses of Taxus cuspidata to hydrodynamics in bubble column bioreactors with different sparging nozzle sizes," *Biochemical Engineering Journal*, vol. 45, no. 2, pp. 100–106, 2009.

[23] S. Schmalzriedt, M. Jenne, K. Mauch, and M. Reuss, "Integration of physiology and fluid dynamics," *Advances in Biochemical Engineering/Biotechnology*, vol. 80, pp. 19–68, 2003.

[24] F. Garcia-Ochoa and E. Gomez, "Bioreactor scale-up and oxygen transfer rate in microbial processes: an overview," *Biotechnology Advances*, vol. 27, no. 2, pp. 153–176, 2009.

[25] C. Lu, F. G. Acién Fernández, E. Cañizares Guerrero, D. O. Hall, and E. Molina Grima, "Overall assessment of Monodus subterraneus cultivation and EPA production in outdoor helical and bubble column reactors," *Journal of Applied Phycology*, vol. 14, no. 5, pp. 331–342, 2002.

[26] A. H. Scragg, A. M. Illman, A. Carden, and S. W. Shales, "Growth of microalgae with increased calorific values in a tubular bioreactor," *Biomass and Bioenergy*, vol. 23, no. 1, pp. 67–73, 2002.

[27] F. Yazdian, M. P. Hajiabbas, S. A. Shojaosadati, M. Nosrati, E. Vasheghani-Farahani, and M. R. Mehrnia, "Study of hydrodynamics, mass transfer, energy consumption, and biomass production from natural gas in a forced-liquid vertical tubular loop bioreactor," *Biochemical Engineering Journal*, vol. 49, no. 2, pp. 192–200, 2010.

[28] R. K. Thakur, C. Vial, K. D. P. Nigam, E. B. Nauman, and G. Djelveh, "Static mixers in the process industries—a review," *Chemical Engineering Research and Design*, vol. 81, no. 7, pp. 787–826, 2003.

[29] L. Oshinowo and D. C. S. Kuhn, "Turbulence decay behind expanded metal screens," *Canadian Journal of Chemical Engineering*, vol. 78, no. 6, pp. 1032–1039, 2000.

[30] F. Azizi and A. M. Al Taweel, "Population balance simulation of gas-liquid contacting," *Chemical Engineering Science*, vol. 62, no. 24, pp. 7436–7445, 2007.

[31] A. W. M. Roes, A. J. Zeeman, and F. H. J. Bukkems, "High intensity gas/liquid mass transfer in the bubbly flow region during co-current upflow through static mixers," vol. 87 of *Institution of Chemical Engineers Symposium Series*, pp. 231–238, 1984.

[32] I. Turunen and H. Haario, "Mass transfer in tubular reactors equipped with static mixers," *Chemical Engineering Science*, vol. 49, no. 24, pp. 5257–5269, 1994.

[33] A. R. Toader, P. Hamersma, and R. F. Mudde, "Mass transfer in static mixers," in *Proceedings of the 10th International Gas Liquid Solid Reactor Engineering Conference*, Praga, Portugal, June 2011.

[34] F. Azizi and A. M. Al Taweel, "Intensifying gas-liquid mass transfer operations," in *Proceedings of the 8th European Congress of Chemical Engineering*, Berlin, Germany, September 2011.

[35] G. Hebrard, J. Zeng, and K. Loubiere, "Effect of surfactants on liquid side mass transfer coefficients: a new insight," *Chemical Engineering Journal*, vol. 148, no. 1, pp. 132–138, 2009.

[36] T. Lemenand, P. Dupont, D. Della Valle, and H. Peerhossaini, "Turbulent mixing of two immiscible fluids," *Journal of Fluids Engineering, Transactions of the ASME*, vol. 127, no. 6, pp. 1132–1139, 2005.

[37] C. Israelidis, "Nutrition—Single Cell Protein, Twenty Years Later," 2006, http://www.biopolitics.gr/BIOPOLITICS/HTML/PUBS/VOL1/isreali.htm.

[38] K. Rostami, M. T. Moazed, D. Zareh, and A. Kheirolomoom, "Single cell protein production using airlift reactor containing static mixer," in *Journal of Bioscience and Bioengineering*, vol. 108, pp. 1389–1723, 2009.

[39] J. Nielsen, J. Villadsen, and G. Liden, *Bioreaction Engineering Principles*, Kluwer Academic/Plenum Publishers, 2003.

[40] L. Joergensen and H. Degn, "Growth rate and methane affinity of a turbidostatic and oxystatic continuous culture of Methylococcus capsulatus (Bath)," *Biotechnology Letters*, vol. 9, no. 1, pp. 71–76, 1987.

[41] K. S. Jun and S. C. Jain, "Oxygen transfer in bubbly turbulent shear flow," *Journal of Hydraulic Engineering*, vol. 119, no. 1, pp. 21–36, 1993.

[42] K. Podila, A. M. Al Taweel, M. Koksal, A. Troshko, and Y. P. Gupta, "CFD simulation of gas-liquid contacting in tubular reactors," *Chemical Engineering Science*, vol. 62, no. 24, pp. 7151–7162, 2007.

[43] J. Klein, J. Maia, A. A. Vicente, L. Domingues, J. A. Teixeira, and M. Juraščík, "Relationships between hydrodynamics and rheology of flocculating yeast suspensions in a high-cell-density airlift bioreactor," *Biotechnology and Bioengineering*, vol. 89, no. 4, pp. 393–399, 2005.

Research Article

Investigation of the Pulsed Annular Gas Jet for Chemical Reactor Cleaning

Zvegintsev Valery Ivanovich, Nalivaichenko Denis Gennadievich, and Chirkashenko Vladimir Fedorovich

Khristianovich Institute of Theoretical and Applied Mechanics, Siberian Branch, Russian Academy of Sciences, Novosibirsk 630090, Russia

Correspondence should be addressed to Zvegintsev Valery Ivanovich, zvegin@itam.nsc.ru

The most economical technology for production of titanium dioxide pigment is plasma-chemical syntheses with the heating of the oxygen. The highlight of the given reaction is formation of a solid phase as a result of interactions between two gases, thus brings the formation of particle deposits on the reactor walls, and to disturbing the normal operation of the technological process. For the solving of the task of reactor internal walls cleaning the pulsed gaseous system was suggested and investigated, which throws circular oxygen jet along surfaces through regular intervals. Study of aerodynamic efficiency of the impulse system was carried by numerical modeling and experimentally with the help of a specially created experimental facility. The distribution of the pulsed flow velocity at the exit of cylindrical reactor was measured. The experimental results have shown that used impulse device creates a pulsed jet with high value of the specified flow rate. It allows to get high velocities that are sufficient for the particle deposits destruction and their removal away. Designed pulsed peelings system has shown high efficiency and reliability in functioning that allows us to recommend it for wide spreading in chemical industry.

1. Introduction

The most technologically advanced and economical method of production of titanium dioxide pigment is a plasma-chemical synthesis of oxygen with heating to 3500 K in an arc plasma torch [1–3]. In this process, titanium dioxide is formed by the oxidation of atomized liquid titanium tetrachloride, which interacts with an oxygen plasma. Chemical reactor, which implements the technology in question, represents a cylindrical tube with an inner diameter of 200–300 mm and a length of 1,000–2,000 mm. At the entrance to the reactor, a torch is installed, which creates a high subsonic jet of oxygen and feeder tetrachloride into the jet. At the reactor outlet, gas stream is obtained with particles of titanium dioxide, which are separated in a certain way from the gas phase.

A feature of this reaction is the formation of a solid phase as a result of the interaction of two gaseous components.

Originally appearing particles of titanium dioxide are in gaseous state, then the condensation of the molecular-dispersed titanium dioxide formed aerosols. As the particles pass the reactor space as their size increases due to condensation of titanium dioxide from the gas phase on the particle surface and by coalescence of individual particles into larger agglomerates, resulting in particle sizes reach 0.1–0.4 microns. This raises the problem of sticking of particles on water-cooled walls of the reactor [4]. Buildup begins at 150–200 mm from the place of tetrachloride supply. The resulting scull can completely fill the workspace of the reactor and disrupt the process. Cleaning the inside surface of the reactor from the sticky particles by stationary slit jet of oxygen was recognized ineffective because of the low speed jet.

To ensure that effective cleaning is necessary to significantly increase the speed of the flow near the wall of the reactor. This problem can be solved by using a pulsed
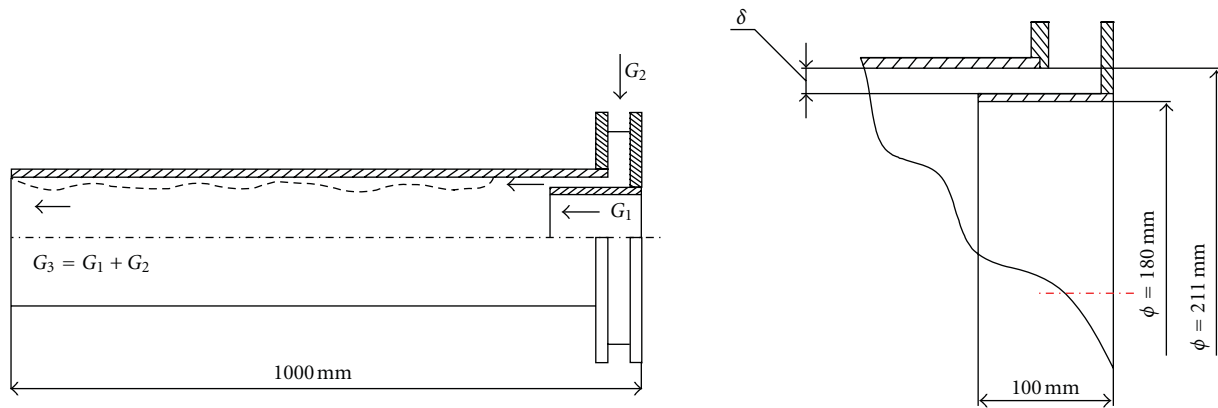
FIGURE 1: Proposed scheme of pulse cleaning system.
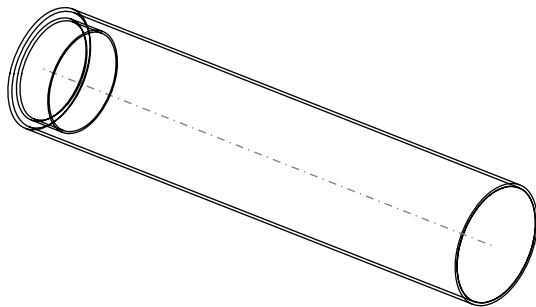
FIGURE 2: Scheme of the reactor with open entrance.

FIGURE 3: Isolines of the velocity V. (a) $\delta = 12$ mm; (b) $\delta = 6$ mm; (c) $\delta = 6$ mm; (d) $\delta = 2.5$ mm.

annular gas jet, which is released periodically along the inner wall of the reactor in the direction of flow [5–8]. Pulse mode provides the highest value of specific flow rate and, accordingly, the highest value of flow velocity. In addition, annular jet configuration provides displacement of the velocity maximum near the surface being cleaned. The proposed scheme of pulse cleaning system is shown in Figure 1.

In the central part, as before, continuously operating high-flow oxygen is fed together with a mixture of titanium tetrachloride. Consumption of gas components at the entrance G_1. With the help of a special ring around the inner wall of the reactor, periodically pulsed jet of oxygen is supplied at room temperature with high pressure. Flow rate of this jet will denote as G_2. The jet should create such a flow in the channel of the reactor, which breaks and removes the accumulating deposits on the reactor walls. It is natural that during the time of the pulsed jet creating the flow rate of the gas phase at the reactor outlet G_3 is the sum of flow rates of incoming gases G_1 and G_2.

From the technological conditions, the next additional requirements to the cleaning system follow. Produced gaseous jet should have a sufficiently high speed (20–40 m/s) needed for deposit breaking, and a small total flow rate (not more than 10% of the basic flow of oxygen through the reactor). In the process of pulse jet forming, a pressure in the flow at the inlet of the reactor should not be increased,

to avoid disruption of the arc plasma torch. In addition, a device for creating a pulsed jet should be simple in design and reliable in operation.

2. Mathematical Model and Numerical Simulation Results

Gas dynamics of flow in the reactor at different variants of the annular jet and entraining conditions at the inlet was studied

(a)

(b)

(c)
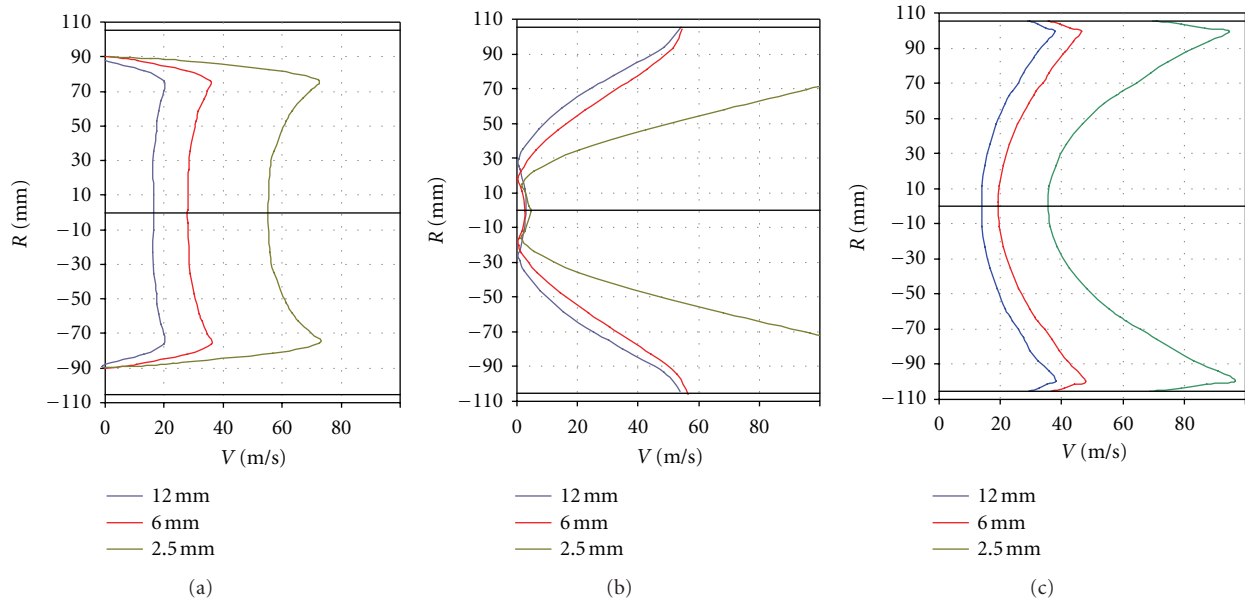
FIGURE 4: The velocity V distribution in the cross-sections ($X = 2$ mm, 500 mm, and 1000 mm).

(a)

(b)

(c)

(d)
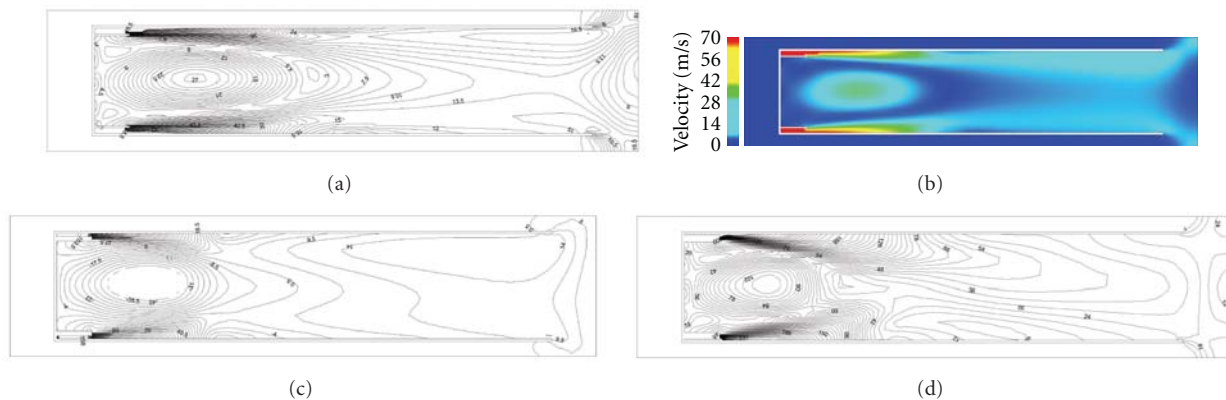
FIGURE 5: Isolines of the velocity V. (a) $\delta = 12$ mm; (b) $\delta = 12$ mm; (c) $\delta = 6$ mm; (d) $\delta = 2.5$ mm.

primarily by theoretical analysis [9] and then by means of numerical simulations. Calculations were performed using an integrated software package SolidWorks + ANSYS. Preparation of a geometric 3D model of the reactor was carried out in the program SolidWorks, then the model was imported in the computer module ANSYS, where the gas-dynamic calculations were performed. The specified computer software involves finite-volume method and time-dependent Navier-Stokes equations for computations. The program automatically analyzes the body geometry and forms the computational grid on the surface of the body and released into the field of computing. In the process of solving, the grid was optimized in the areas of large flow parameter gradients.

The configuration of the calculated cases determined by the following terms and conditions. The hole diameter of 180 mm at the entrance of the reactor is opened or closed. The initial conditions in the reactor corresponded to ambient conditions. We considered three values of the height of the annular slot for gas injection: 2.5 mm, 6 mm, and 12 mm. In all cases, the flow rate of the annular jet remained constant with the value of 0.7 kg/s. Produced annular jet was either parallel to the axis of the reactor, or twisted in the tangential direction.

2.1. Entrance Is Opened: The Jet Is Parallel to the Axis. The scheme is shown in Figure 2. Figure 3 shows a typical velocity distribution inside the reactor under consideration at different heights ejecting slit. Figure 4 shows a comparison of the diagrams of velocities in the cross-sections at a distance of 2 mm, 500 mm, and 1000 mm from the entrance.

As seen from Figure 3 in the considered range of slot heights, an annular jet injects air through the open entrance and expands in the propagation through the channel. The region of conical shape is formed inside the channel. The velocity in this region decreases from a maximum at the

(a)

(b)

(c)
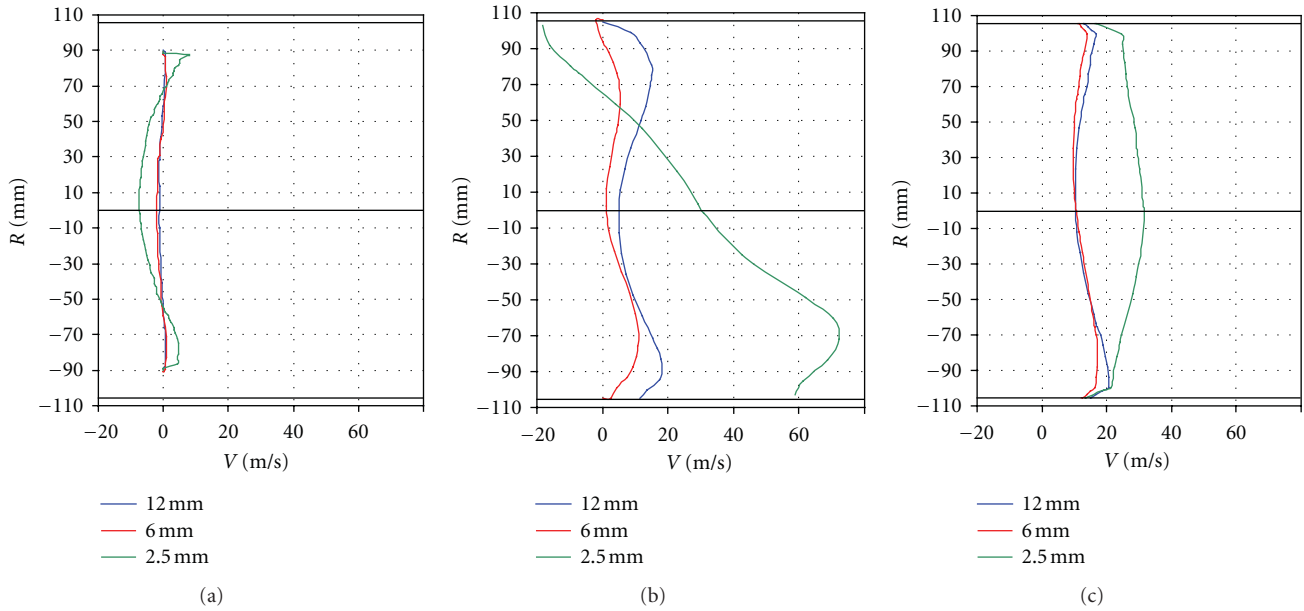
FIGURE 6: The velocity V distribution in the cross-sections ($X = 2$ mm, 500 mm, and 1000 mm).
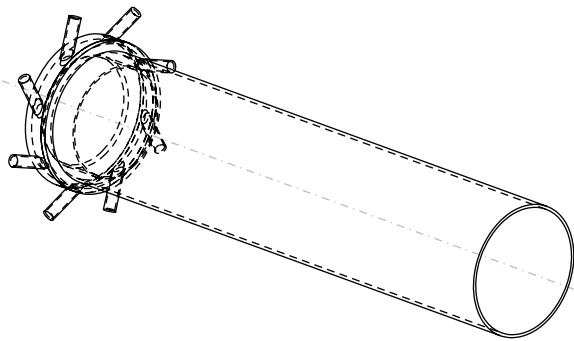
FIGURE 7: Scheme of the reactor with swirling ejecting jet.

entrance to almost zero in the middle of the channel. From these data, it is seen that the greatest velocity at the reactor walls creates a jet with a height of 2.5 mm slit (see Figure 4). This means that a maximum possible value of the dynamic pressure acts on deposits along the walls, which is required to accomplish the cleanup task.

2.2. Entrance Is Closed: The Jet Is Parallel to the Axis.

The results of calculations of gas-dynamic parameters in the reactor with a closed entrance showed significant time-dependent nature of the flow. In these calculations, we could not get a picture of the stationary distribution of velocities and flow parameters inside the reactor. Therefore, the figures below show the unsteady random velocity distribution in different sections.

The data presented (see Figures 5 and 6) show that the recirculation zone with reduced pressure is formed due to the action of the annular jet in the channel near the closed entrance. Implemented asymmetric velocity distribution in
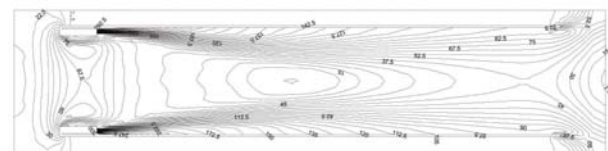

(a)

(b)

(c)

(d)
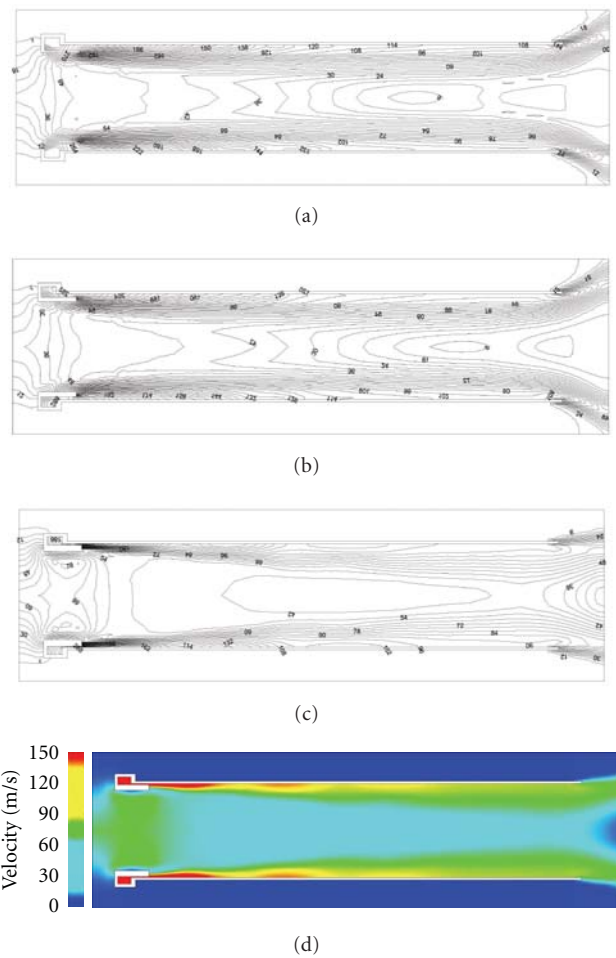
FIGURE 8: Isolines of the total velocity V. (a) $\delta = 12$ mm; (b) $\delta = 6$ mm; (c) $\delta = 2.5$ mm; (d) $\delta = 2.5$ mm.

(a)

(b)

(c)
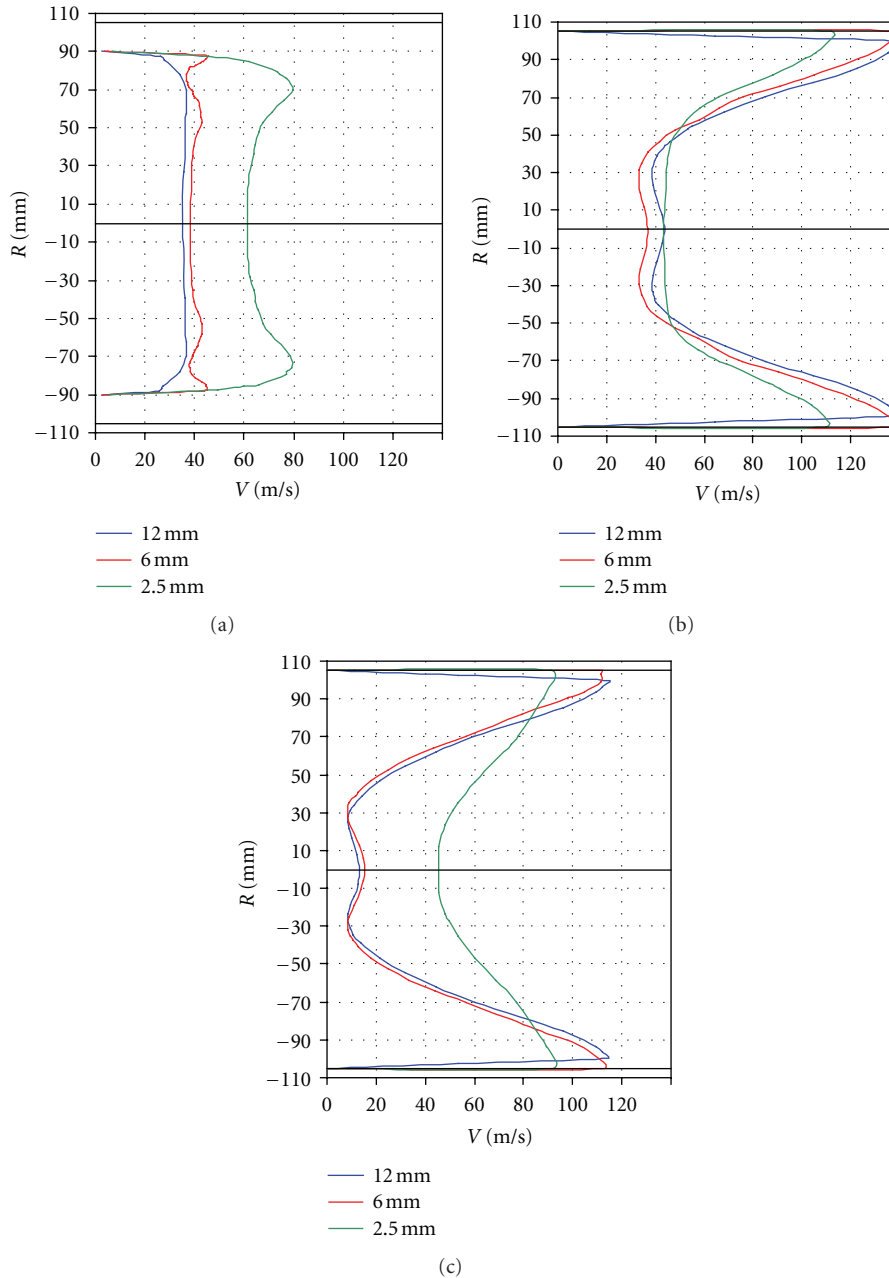
Figure 9: The total velocity V distribution in the cross-sections ($X = 2$ mm, 500 mm, and 1000 mm).

the channel is explained by unsteady interaction of the recirculation zone with the annular jet.

The values of flow velocities in the annular jet inside the channel are substantially less than in the case of open-channel input. The main reasons of this situation are the low flow rate of ejected gas and the formation of low-pressure zone near to closed entrance.

2.3. Entrance Is Opened: Twisted Jet. The scheme is shown in Figure 7. The adopted computational technology allows us to calculate swirling flow in the channel of the reactor in the presence of the initial vorticity of ejecting jet. The

typical distributions of the absolute values of velocity in the longitudinal and cross-sections are shown in Figures 8 and 9. It is seen that, at sufficiently high altitude the annular gap ($\delta = 12$ mm, 6 mm), a decisive role in the jet parameters have dimensions of supplying pipes. With a decrease in the height of the slit, when its area becomes commensurate with the area of supplying pipes, the effect of vorticity the ejecting jet decreases, and the effect of the height of the annular gap on the parameters of the formed flow becomes crucial.

The data show that the swirling flow significantly affected the structure of the flow in the channel. Absolute flow velocity in the annular jet, and the inside of the channel
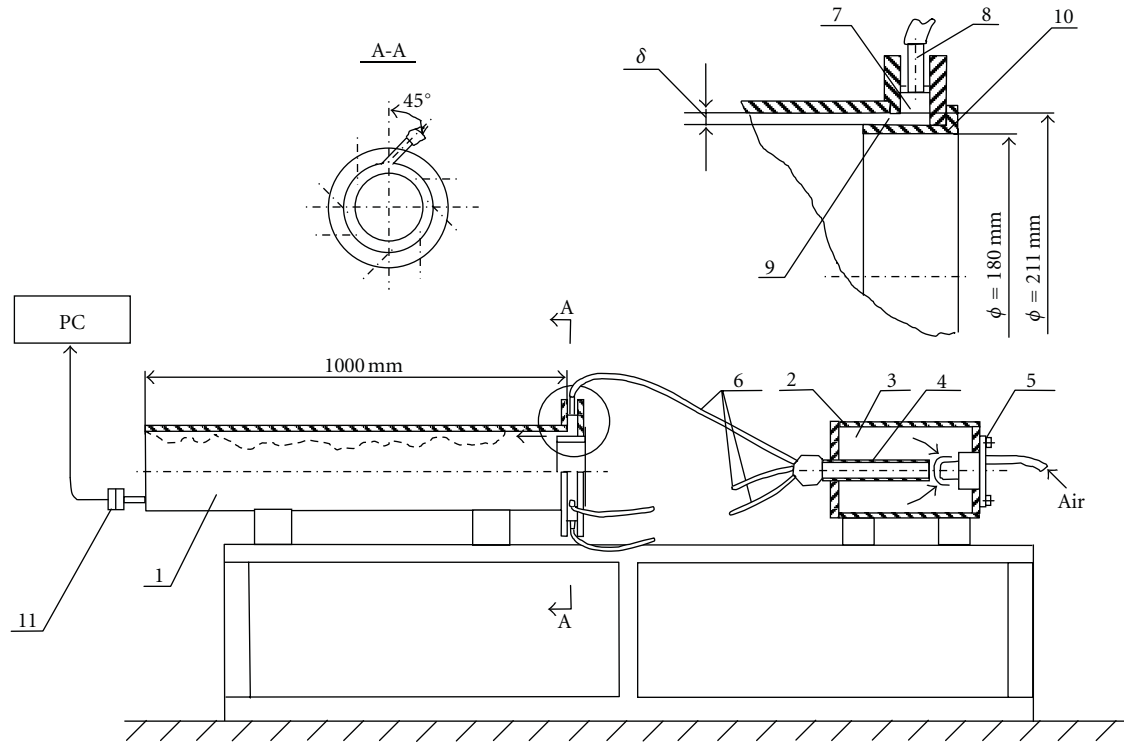
FIGURE 10: The experimental setup. (1) model of a chemical reactor, (2) pnevmopulse generator, (3) storage chamber, (4) exhaust nozzle, (5) high-speed valve, (6) rubber hose, (7) circular prechamber, (8) fitting, (9) slotted nozzle, (10) the input cylinder, and (11) total pressure probe.
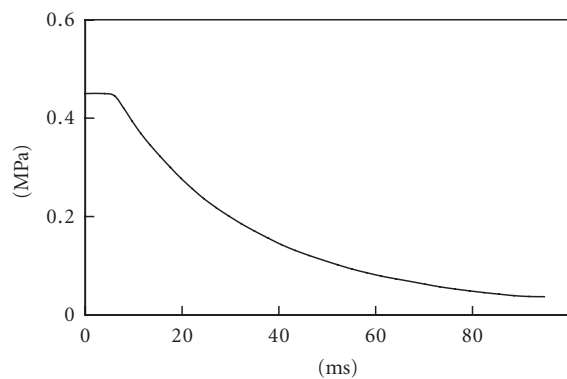
FIGURE 11: Total pressure of the air flow at the reactor entrance.
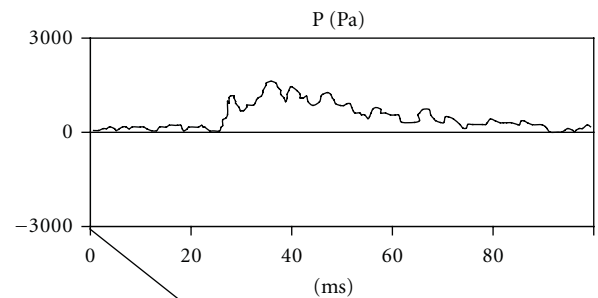
FIGURE 12: Total pressure of the air flow at the reactor exit.

increased markedly relative to the situation with longitudinal blowing (see Figures 3 and 4). Inside the channel, in contrast to the longitudinal blowing, a uniform flow with velocity of 40 m/s is forming almost at entire length.

Deceleration of the flow (up to 10 m/s) occurs only near the channel exit. It should be noted that the twisted blowing from the ring nozzle with a slit height of 2.5 mm leads to a decrease in flow velocity within the channel from 60 m/s at the entrance up to 40 m/s in the middle of the channel, and again increases at the outlet of the channel. At the same time, the flow velocity at the channel walls reaches 120 m/s. Typical peculiarities of vortex flow in velocity profiles in the transverse and longitudinal sections of the channel indicate that the twist flow is saved along the entire length of the channel. The increase in ejection of air with open entrance of the reactor caused by the intensification of the mixing process for swirling annular jet due to additional azimuthal velocity component.
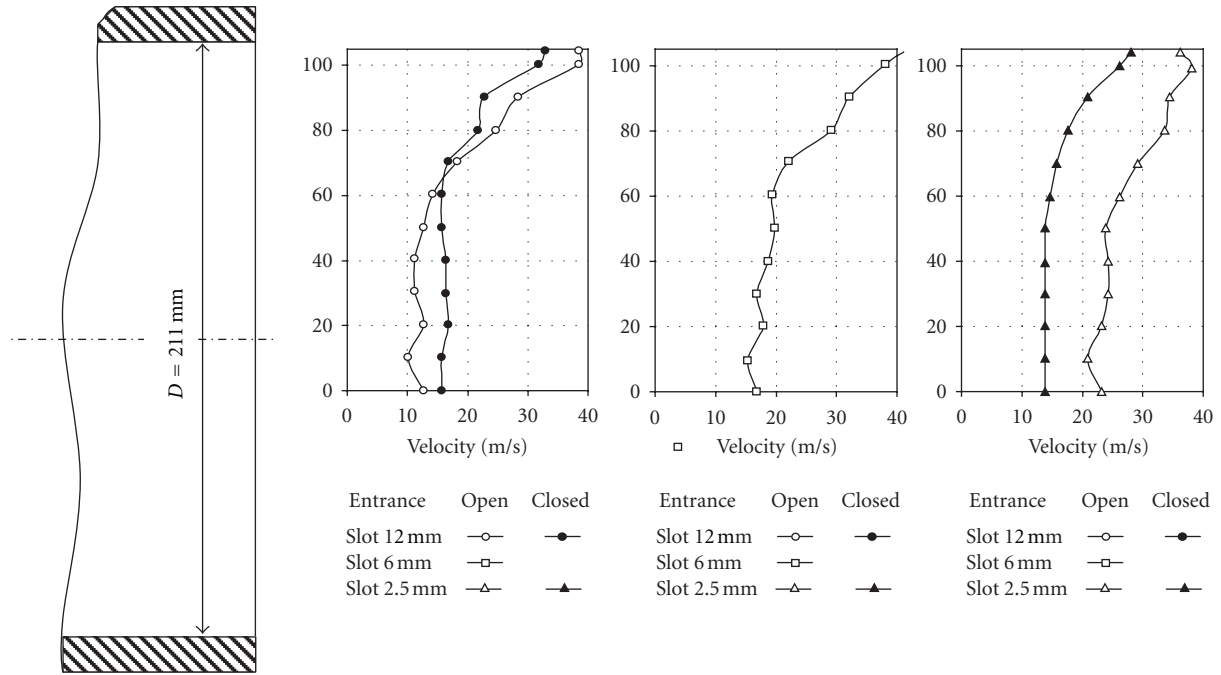
FIGURE 13: Distribution of mean velocity at the outlet of the reactor model.
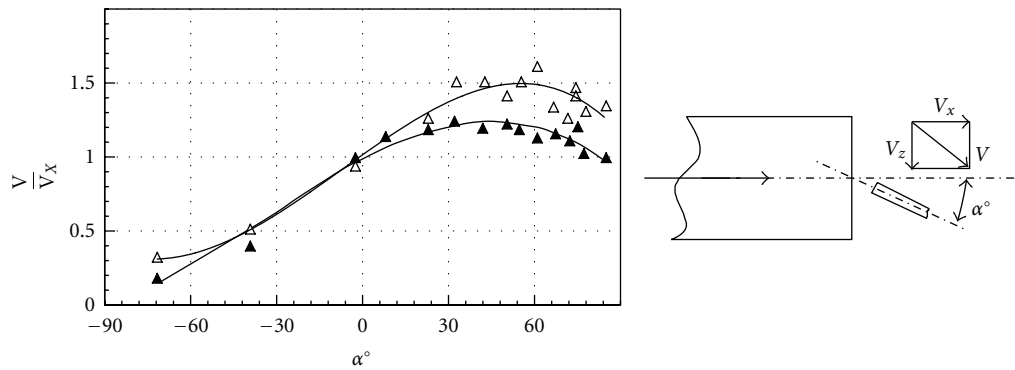
FIGURE 14: Measurement of twist angle of the annular jet (notation as in Figure 13).

TABLE 1: Experimental results.

Width of the annular gap		12 mm	6 mm	2.5 mm
	Entrance is opened experiment	0.92	1.07	1.23
	Entrance is opened calculations	1.19	1.61	2.51
Mass flow rate at the outlet, kg/s	Entrance is closed experiment	0.87	—	0.73
	Entrance is closed calculations	0.70	0.70	0.70
	Entrance is opened swirling jet calculations	1.62	1.52	2.83
	Entrance is opened experiment	0.35	0.57	0.81
	Entrance is opened calculations	0.75	1.37	2.69
Ejection coefficient $(G_3 - G_1)/G_1$	Entrance is closed experiment	0.28	—	0.07
	Entrance is closed calculations	0.00	0.00	0.00
	Entrance is opened swirling jet calculations	1.31	1.17	3.04

3. Experimental Study of Pulse Cleaning System

Investigation of the aerodynamic efficiency of the developed system cleaning was conducted on a specially designed experimental model of the reactor (see Figure 10), which preserves the basic dimensions of the real reactor.

The model of the reactor was a cylindrical tube 1 with an inner diameter of 211 mm and a length of 1000 mm. At the entrance of the reactor model is hosted a unit forming an annular jet for cleaning, which consists of an annular chamber (prechamber) 7 with a volume of 0.6-0.7 dm^3, tubes 8 with a diameter of 16 mm for the air supply and slotted nozzle 9 as an annular gap formed by the inner wall of the pipe 1 and the outer wall of the input cylinder 10. The gap width δ can vary from 2 to 12 mm. Air supply tubes located at an angle of 45° to the radius of the tube, which reduces the total pressure loss at the entrance to the prechamber and forms a twisted flow inside the reactor. To create circular pulsed jet, we use the air at room temperature (instead of oxygen under actual conditions). In the central part of the reactor input, it is a cylinder 10 with diameter of 180 mm, through which the pulse annular jet sucked the air from the atmosphere.

As a source of pulse gas flow, a pnevmopulse generator 2 developed by the authors [10] was used. The generator consists of storage tank 3 with a volume 9.4 dm^3, designed for pressures up to 1.0 MPa , exhaust nozzle 4 with diameter of 41 mm and high-speed valve 5. Pnevmopulse generator was connected to the reactor by rubber hoses 6 of 18 mm in diameter and 1 m in a length.

To carry out the time-dependent measurements of pulse pressure at the reactor outlet special high-speed digital test equipment, which included initial pressure transducer 11, and a registration system based on PC was implemented. In each experiment, 4096 samples were recorded during 0.65 s with the help of 10-bit ADC. The absolute error of pressure measurements did not exceed 70 Pa.

Experiments were carried out as follows. First of all Pitot probe with a diameter of 3 mm was mounted at the reactor outlet. The recording apparatus was set in a state of readiness.

Pressured air is filled storage volume 3 for 3–5 seconds until the pressure in the network, then automatically activated high-speed valve 5 (time of full opening of 3-4 ms) and a release of working gas through the slotted nozzle 4 for 50–60 ms (see Figure 11). At this time we recorded the total pressure at a given point of the outlet plane of the reactor model. A typical oscillogram of the total pressure recording is shown in Figure 12.

From each oscillogram, a section length of 100 ms was cut out for further analysis. It began after the arrival of the perturbation to the pressure transducer. Integral of this region was calculated during the time of the positive phase pulse from signal being recorded. Dividing the received pulse at the expiration of the time scale of the pnevmopulse generator (60 ms), we obtain the mean value of the total pressure in this experiment. This value is used to calculate the average speed of subsonic flow during the period in the assumption that the static flow pressure and atmospheric pressure are equal.

All experiments were performed at an initial pressure of air in generator of 0.46 MPa and a temperature of 285 K. At these parameters, storage chamber of pnevmopulse generator implies 0.0406 kg of air. Maximum flow rate at the beginning of the exhaust is 1.06 kg/s or 0.9 m^3/s. Average mass flow rate during 0.060 s will be 0.68 kg/s and 0.57 m^3/s. For comparison, that the stationary compressor providing the same air flow rate (0.8 m^3/s), has a drive power of 140 kW [11]. High values of specific flow productivity are a distinctive feature of pulse systems and allow relatively easy to solve the problems of industrial cleaning systems from deposits.

The width of the annular gap in the experiments was δ = 12.0, 6.0, and 2.5 mm. According to the calculations the initial jet velocity was 66, 133, and 266 m/s (for slots with δ = 12 mm, 6 mm and 2.5 mm, resp.). To evaluate the ability of ejecting annular jet for cleaning, experiments were carried out with open and closed section of the input cylinder 10. The obtained profiles of mean velocity at the outlet of the reactor are shown in Figure 13. Light symbols correspond to an open entrance into a reactor, the dark to closed entrance. It is seen that at the reactor outlet air velocity is slowed down, but remains at least 30–40 m/s, which ensures the effective destruction of the deposits on the walls. In a length of 1000 mm, there is no alignment of the flow, and the maximum velocity is near the walls. This confirms the correctness of our choice of annular injection scheme for cleaning the reactor at a specified length.

The mass of flowing air at the outlet of the reactor under different input conditions, obtained by integrating the axial velocity distribution over the area is shown in Table 1. It also shows the coefficient of ejection as the ratio of the mass of air ejected from the environment to the mass of the ejecting gas flowing from pnevmopulse generator in the form of an annular jet. We see that when the open entrance takes place a visible ejection of gas occurs, and its magnitude increases with decreasing size of the annular gap. In the experiment, the maximum ejection coefficient (80%) provides an annular jet, which follows from the gap of 2.5 mm. In calculating the coefficient of ejection exceeds the experimental values of 2-3 times and reaches 250%. The gap 12 mm in experiment generates ejection coefficient of 35%, and the calculation of up to 70%. It is interesting to note that even with a closed entrance gas mass addition is observed up to 26%. This indicates the presence of backflow through the central portion of the output section of the reactor, where the measurements were made with low accuracy. The presence of back flow in the central part of the output section at the closed entrance and width of the gap of 2.5 mm was observed visually in the experiments. In this case, the ejection is a negative factor because it implies additional disturbances in the gasdynamic flow pattern and can lead to a breach of the technological process in the reactor. From this point of view, it is preferable to use a larger gap (e.g., 12 mm), which performs the task of cleaning and does not create problems with ejection. In the calculations with the swirling jet an

ejection coefficient is further enhanced for all values of the slot heights.

In Figure 14 the values of flow velocity, referred to the velocity measured along the tube axis for open and closed entrance with gap width of 2.5 mm are shown. It is seen that the maximum velocity reached at the orientation of Pitot probe at an angle of 40–50° to the axis in the direction of the expected tangential velocity component. Accordingly, the same direction has an absolute velocity vector of the swirling flow. It means that original angle of twist of 45° has not changed over a length of 1000 mm. Taking it into account, the values of the axial component of jet velocity, shown in Figure 13 shall be increased by 25–50%, so the real value of the flow velocity relative to the tube walls reaches up to 60 m/s.

4. Conclusion

The results of the studies have shown that the annular pulse jet ensures the gas flow velocity (up to 60 m/s) sufficient to clean over the whole length of the inner wall of a chemical reactor under consideration. In accordance with the experimental and theoretical results of this study unique pulse cleaning system was designed, manufactured, and installed on a real existing chemical reactor. Experience in continuous operation showed that the system has a high cleaning efficiency and reliability, so it is possible to recommend similar cleaning systems for widespread use in the chemical industry.

References

[1] N. N. Rykalin et al., "Thermodynamics of the syntheses of the dioxide of titanium at the incineration of the tetrachloride of titanium in the oxygen," *FCHOM*, vol. 4, p. 53, 1977 (Russian).

[2] B. Karlemo, P. Koukkari, and J. Paloniemi, "Formation of gaseous intermediates in titanium(IV) chloride plasma oxidation," *Plasma Chemistry and Plasma Processing*, vol. 16, no. 1, pp. 59–77, 1996.

[3] J.-G. Li, M. Ikeda, R. Ye, Y. Moriyoshi, and T. Ishigaki, "Control of particle size and phase formation of TiO_2 nanoparticles synthesized in RF induction plasma," *Journal of Physics D*, vol. 40, no. 8, pp. 2348–2353, 2007.

[4] A. D. Zimon, *Adhesion of Dust and Powders*, Khimia (Chemistry), Moscow, Russia, 1976, (Russian).

[5] N. Y. Bulatov and M. P. Sharygin, *Pulse Aerodynamic Cleaning of Surfaces in Chemical Technology*, Alma-Ata.Gylym, 1990, (Russian).

[6] Y. M. Shchelokov, A. M. Avvakumov, and Y. K. Sazykin, *Cleaning of Heating Surfaces of Heat-Recovery Boilers*, Energoatomizdat, Moscow, Russia, 1984, (Russian).

[7] E. S. Shchetinkov, *Physics of Gases Combustion*, Nauka (Science), Moscow, Russia, 1965, (Russian).

[8] A. A. Gurin, P. S. Maliy, and S. K. Savenko, *Air Shock Waves in the Mines*, Nedra (Subsoil), Moscow, Russia, 1983, (Russian).

[9] G. N. Abramovich, *Applied Gas Dynamics. Part 1*, Nauka (Science), Moscow, Russia, 1991, (Russian).

[10] V. I. Zvegintsev, "Claim of Russian Federation," no. 2023228, 1992.

[11] Z. Z. Rahmilevich, *Compressor Units*, Khimiya (Chemistry), Moscow, Russia, 1989, (Russian).

Research Article

The Effects of Mixing, Reaction Rates, and Stoichiometry on Yield for Mixing Sensitive Reactions—Part I: Model Development

Syed Imran A. Shah,[1] Larry W. Kostiuk,[2] and Suzanne M. Kresta[1]

[1] *Department of Chemical & Materials Engineering, University of Alberta, 7th Floor,*
 Electrical & Computer Engineering Research Facility (ECERF), 9107-116 Street, Edmonton, AB, Canada T6G 2V4
[2] *Department of Mechanical Engineering, University of Alberta, 4-9 Mechanical Engineering Building,*
 Edmonton, AB, Canada T6G 2G8

Correspondence should be addressed to Suzanne M. Kresta, suzanne.kresta@ualberta.ca

There are two classes of mixing sensitive reactions: competitive-consecutive and competitive-parallel. The yield of desired product from these coupled reactions depends on how fast the reactants are brought together. Recent experimental results have suggested that the mixing effect may depend strongly on the stoichiometry of the reactions. To investigate this, a 1D, dimensionless, reaction-diffusion model at the micromixing scale was developed. Assuming constant mass concentration and mass diffusivities, systems of PDE's were derived on a mass fraction basis for both types of reactions. Two dimensionless reaction rate ratios and a single general Damköhler number emerged from the analysis. The resulting dimensionless equations were used to investigate the effects of mixing, reaction rate ratio, and reaction stoichiometry. As expected, decreasing either the striation thickness or the dimensionless rate ratio maximizes yield, the reaction stoichiometry has a considerable effect on yield, and all three variables interact strongly.

1. Introduction

Mixing and apparent reaction rate are intrinsically related: reactions involving multiple reactants cannot occur without the reactants being contacted intimately at a molecular level. In a reactor, reactants are added at the macro- or meso-scale. For the reaction to occur, the pure reactants need to be homogenized at the molecular scale so that molecules can collide. If the mixing is fast enough, the intrinsic chemical kinetics governs the rate of production of new species. This requires a reduction of scale and of differences in concentration, which is the very definition of mixing as it pertains to chemical reactions.

In two known classes of reaction, the progress of the reaction depends heavily on how quickly the reactants are brought together. These reactions consist of two or more competitive reactions either occurring in parallel, where two or more reactions involving the same reactants take place at the same time, or in a consecutive sequence, where the desired product of one of the reactions participates in a second undesired reaction with the original reactants. Both types of reaction schemes can involve considerable production of unwanted by-product despite the desired reaction being as much as a million times faster than the undesired reaction.

Typical representations of these reaction schemes are given in Table 1. For both cases, $k_1' \gg k_2'$, P is the desired product, and S is the undesired by-product. Therefore, for a perfectly homogeneous mixture of reactants present in a stoichiometric ratio of one ($A : B = 1 : 1$), the yield of by-product S should be very small. It is well established (Baldyga and Bourne [1], Patterson et al. [2]) that the yield of byproduct can indeed be quite significant: an effect which is due to imperfect mixing. These classical stoichiometries have been extensively studied (Baldyga and Bourne [1, 3], Baldyga et al. [4], Cox et al. [5], Clifford et al. [6], Cox [7], and Patterson et al. [2]). The primary aim of this paper is to study the effect of a different overall reaction stoichiometry on the yield of desired product and the diffusive mass transfer limitations that are associated with this difference.

TABLE 1: Classic mixing sensitive reaction schemes.

Competitive-consecutive (C-C)	Competitive-parallel (C-P)
$A + B \xrightarrow{k_1'} P$	$A + B \xrightarrow{k_1'} P$
$P + B \xrightarrow{k_2'} S$	$C + B \xrightarrow{k_2'} S$

The Damköhler number is the dimensionless number used to scale the rate of mixing to the rate of reaction for any given mixing sensitive reaction. There are several forms of the Damköhler number, with the mixing Damköhler number (Da) given by (Patterson et al. [2]):

$$ \text{Da} = \frac{\tau_M}{\tau_R} = \text{mixing time} \cdot \text{reaction rate} \qquad (1) $$

where τ_M is the characteristic mixing time and τ_R is the characteristic reaction time. The academic and industrial mixing communities have proposed several definitions of τ_M, τ_R, and Da with respect to the reacting flow problem, and some of those efforts are summarized in the following sections.

2. Literature Review

The literature review is structured as follows. First, a review of the chemical engineering literature that focuses on competitive-consecutive and competitive-parallel reaction schemes is presented. This is followed by a review of the nonlinear reaction dynamics literature that has focused on the same reaction schemes but from an applied mathematics perspective.

2.1. Mixing Models. Investigations of yield from homogeneous reactions have been investigated by chemical engineers for quite some time starting with Danckwerts [8, 9] and Levenspiel [10] who provided analytical solutions for the yield of any reaction provided it is perfectly mixed. Since perfect instantaneous mixing is almost impossible to realise in practice, there have also been a number of investigations into the effect of imperfect mixing on the final yield of desired product (e.g., Patterson et al. [2], Baldyga and Bourne [1, 3], Baldyga et al. [4], and Bhattacharya [11]).

In the fine chemicals industry, reactions are frequently carried out in semi-batch stirred tanks. Mixing and turbulence are very closely related and the rate of mixing is greatly influenced by the turbulence intensity within the tank, which can vary by orders of magnitude in different regions of the tank. The maximum intensity is usually at the impeller, and the minimum is mostly in the bulk of the tank. Therefore, for most mixing sensitive reactions, the reactants are injected at the impeller.

From the more theoretical side, the focus is on a simple geometry with Lagrangian micro-mixing models by Baldyga, Bourne, and others (Baldyga and Pohorecki [12], Baldyga and Bourne [1], and Villermaux and Falk [13]). These are very inexpensive computationally and, in some cases, have analytical solutions. The micro-mixing models have evolved from early alternating striations of reactants to the

Engulfment Model (Baldyga and Bourne [1]) which is widely regarded as the best micro-mixing model currently available. The scales of these models are usually at or below the Kolmogorov scale of turbulent eddies, therefore they are assumed to be independent of the large scale fluid mechanics. The Generalized Mixing Model proposed by Villermaux and Falk [13] is a similar model extended to take into account meso-mixing effects.

There have also been attempts to integrate computational fluid dynamics (CFD) with micro-mixing models. Fox [14, 15] combined Villermaux and Falk's [13] Generalized Mixing Model and CFD for turbulent mixing simulations. Muzzio and Liu [16] took a similar approach, integrating a micro-mixing model and CFD for laminar mixing.

The reacting flow problem for multiple competing reactions has also caught the eye of physicists and mathematicians, since it presents interesting non-linear behaviour. A summary of their efforts is given in the next section.

2.2. Review of the Non-Linear Reaction Dynamics Literature. The C-C reaction provides an interesting non-linear problem that has been extensively investigated by physicists and chaos mathematicians like Cox, Clifford, and others (Clifford [17], Clifford and Cox [18], Clifford et al. [6, 19–21], Cox [7], and Cox et al. [5]). The C-P reaction scheme has been of less interest to the mathematics and physics communities and there is a smaller body of work attached to it (Hecht and Taitelbaum [22], Sinder [23], Sinder et al. [24], and Taitelbaum et al. [25]).

Mixing sensitive reactions exhibit interesting behaviour at reactant interfaces. There are several studies investigating these behaviours for reactions. Cornell and Droz [26] is an example of such a study, where the behaviour of the reaction front for the general single step reaction $mA + nB \rightarrow$ Products was investigated. Cox et al. [5] and later Cox and Finn [27] investigated the reaction interface for the classic C-C reaction extensively. They provided figures and analytical expressions for the profiles of each species at the reaction interface using a model consisting of 1-D alternating reactant striations of varying thickness. The striations had uniform initial concentrations for which they wrote mole balance partial differential equations (PDEs) for each of the species participating in the reaction.

In the long time investigations, Cox et al. [5] first started with stationary and segregated stripes of alternating reactants, that is, "Zebra Stripes," with uniform initial concentrations of reactants across the striations. They performed a mole balance and derived the equations in molar concentrations. Their equations were made dimensionless using the rate constant and concentrations, and the striation thickness was avoided. Their dimensionless equations are:

$$ T = t \cdot (k_1 c_{B_0}) \qquad X = x \cdot \left(\frac{k_1 c_{B_0}}{D} \right)^{1/2} \qquad I' = \frac{c_{I'}}{c_{B_0}} \qquad (2) $$

where $(t, x, c_{I'})$ and (T, X, I') are dimensional and dimensionless time, space, and concentration for species I' respectively. k_1 is the rate constant for the desired reaction, c_{B_0} is the initial concentration of the limiting reagent, and D is

the diffusivity, which was assumed to be equal for all four species (A, B, R, S) involved. Their R is equivalent to P in Table 1. They used striations of unequal thickness within the same domain so the striation thickness could not be used as a non-dimensionalizing parameter. Since they looked at only one type of stoichiometry, their rate expressions are constant and are the obvious choice for non-dimensionalization.

Initially they looked at a model which had a single striation thickness of initially segregated reactants (Cox et al. [5]). They investigated the effects of initial scale of segregation, that is, striation thicknesses, and the reaction rate ratio for the classic competitive consecutive reaction scheme. They found that decreasing the scale of segregation, that is, striation thickness and the reaction rate ratio (k_2/k_1) was favourable. The formulations of the Damköhler number and reaction rate ratio that they found were as follows:

$$\text{Da}_{\text{II}} = \frac{k_1 c W^2}{D} \qquad \varepsilon = \frac{k_2}{k_1} \qquad (3)$$

where W represents the initial striation thickness of the reactants, k_1 is the reaction rate of the desired reaction, c is the molar concentration, D is the diffusivity, and ε is the reaction rate ratio. Using this model, they investigated the yield from zebra stripes of equal thicknesses (Clifford et al. [6]) and confirmed that decreasing the scale of segregation can have a significant favourable effect on the yield of desired product. They also included a parameter to allow for non-stoichiometric initial concentrations of reactants and investigated the effects of having more A than B, less A than B, and a stoichiometric mixture quite extensively. They also found that if the initial ratio of reactants $(A : B)$ is less than 1, the yield will go to zero and only if the initial ratio is above 1 can there be a significant yield of desired product.

Clifford [17] and Clifford and Cox [18] took the constant striation thickness model further by assuming a more realistic Gaussian distribution of concentration of reactants within the striations. They compared the full partial differential equations (PDEs) of the Gaussian model with the uniform concentration model and an ordinary differential equation (ODE) model. The uniform concentration model was found to overpredict the yield and the ODE model agreed quite well with the full PDE solution results. This was somewhat of a departure from the rest of the literature on the subject, but provides an interesting perspective on the problem.

The next step Clifford, Cox, and Roberts took was to introduce multiple initial striation thicknesses into the model, the so called "Bar Code" model (Clifford et al. [20, 21]). This gives a closer representation of striation distribution in a chaotic mixing situation. They varied the total number and the arrangement of the striations and found that grouping similar-sized striations together maximized the yield of desired product. Using an average striation thickness for the system over-predicted yield for a small sample, but increasing the number of striations in the model brought the two values closer together.

Clifford et al. [20] investigated the effect of arrangement of striations of alternating reactants $(A \text{ and } B)$ with varying thicknesses on the yield. The arrangements were chosen such that the widths of the alternating reactants were positively correlated, negatively correlated or placed randomly. Because of the large computational requirements, they applied the Gaussian method developed by Clifford [17]. They found that a positive correlation between the thicknesses of the striations, that is, striations of similar thicknesses grouped together, provided the highest yield of desired product for intermediate times but that there is a crossover at large times where in fact the random arrangement provides the largest final yield of desired product. The negatively correlated case, that is, alternating "thick" and "thin" striations, provided the worst yield. The final step in Clifford, Cox, and Roberts' quest for simulation of reality was to include a stretching parameter to take the reaction-diffusion model to a reaction-diffusion-advection model (Clifford et al. [19]). Cox summarizes these efforts to reduce a chaotic mixing field to a 1D model, a 2D model and other reduced models, including various chaotic mixing models, such as the Baker Map model for simulating stretching and folding in [7]. He found that the yield of desired product in a C-C reaction is underestimated by a 1D lamellar model that ignores the effects of fluid mixing but overestimated by the two other lamellar models (continuous stretching and discrete stretching and folding (Baker Map)) that include the fluid mixing.

All this work was done for the C-C reaction scheme and the classic stoichiometry. The C-P reaction scheme has a considerably smaller body of work with most publications concentrating on the reaction front behaviour (Taitelbaum et al. [25], Sinder [23], Sinder et al. [24], and Hecht and Taitelbaum [22]) and the classical stoichiometry.

A Damköhler number for the classic C-C reaction was suggested by Cox et al. [5], but there is no such suggestion for a C-C reaction scheme with a general stoichiometry. There is a similar lack of definition for the C-P reaction scheme.

2.3. Mixing and Reaction Rate Ratio. Perfect mixing for reactions is defined as the instant reduction to a homogeneous concentration field. This also corresponds to the perfectly micro-mixed mixing condition (Levenspiel [10]). Good mixing rapidly approaches this perfectly homogeneous condition and hence approaches the maximum yield of desired product.

At the other end of the spectrum is complete segregation of reactants without diffusion and with a minimum surface area for contact. In this case the reaction can occur only at the interface and then comes to a complete halt, so the yield of desired product is minimized. In the absence of diffusion, the only way to increase the yield is to increase the area of contact between reactants, in which case the extent of the reaction is completely dependent on the scale of segregation. The situation is vastly improved with the introduction of diffusion because then reactants away from the interfaces are granted access to one another. Diffusion is the final agent of mixing at the smallest scales of segregation. When the scale of segregation is varied by adjusting the initial striation thickness of the reactants, the limit of perfectly mixed is the case where striation thickness goes to zero, and the limit of perfectly segregated occurs when there is only one interface.

The second aspect of the model is the reaction kinetics. The faster the desired reaction is, compared to the undesired

reaction, the larger the final yield of desired product will be (Levenspiel [10] and Fogler [28]). Since the objective is to maximize the yield of desired product, a very small k_2/k_1 is favourable and a very large k_2/k_1 is undesirable.

The goal of this paper is to provide some insight to the chemical engineering practitioner who is designing a reactor for a previously uninvestigated mixing sensitive reaction. Prediction of the yield for mixing sensitive reactions has been particularly difficult, as documented in *Chapter 13* of the *Handbook of Industrial Mixing* [2], owing mostly to a lack of information about the reaction schemes, reaction rate ratios, mixing requirements, and so forth. Much of the work on mixing sensitive reactions is for specific known reactions, so the results are not directly transferable to a new reaction, and any general treatment has been restricted to specific stoichiometries, all with coefficients of one. Designs involving more complex reactions often rely on experience and trial and error, or on extensive pilot scale testing.

From the more theoretical point of view, there has been quite a bit of debate on the formulation of the Damköhler number for two stage reactions: does one use the rate of the first reaction, the second reaction, or the reaction for which the information is available? What is the appropriate mixing time? Once a standard Damköhler number can be determined it will be possible to develop a framework around which charts or figures predicting yield for mixing sensitive reactions can be produced, thus making it easier for the practicing chemical engineer to deal with complex reaction systems involving multiple interacting parameters. Even if the model does not serve to predict the yield exactly, it will at least serve to provide a framework for the analysis of new reaction schemes. This paper will improve understanding of the design requirements of reactors for mixing sensitive reactions by clarifying the dominant variables and the interactions between them.

The rest of this paper presents the derivation of a model of the effects of initial mixing condition, reaction rate ratio, and stoichiometry on two types of mixing sensitive reactions: the Competitive-Consecutive (C-C) reaction and Competitive-Parallel (C-P) reaction.

The key results are:

(1) Development of a model which has a general Damköhler number for any mixing sensitive reaction with a variable stoichiometry.

(2) Tools which allow investigation of the effects of stoichiometry, mixing and relative reaction rates on the final yield of desired product for mixing sensitive reactions of both types: C-C and C-P.

(3) Simulations of the transient behaviour of the reaction interface for short and long times.

3. Model and Governing Equations

The model that has been developed is based on an idealized one-dimensional geometry of initially alternating layers of reactants at the micro-mixing scale with a cross section as shown in Figure 1(a). Figure 1(b) depicts an isolated segment

of the overall structure in the vicinity of $x = 0$, which is placed at the interface between the generic reactant mixtures Y and Z, thereby creating a domain of interest bounded by the symmetric zero-flux boundaries at the mid-planes of these layers. In this formulation, the mixtures Y and Z are allowed to take on different species compositions depending on the reaction scheme being considered and the imposed stoichiometry. Figure 1(c) shows the geometry for the specific case of pure striations of A and B.

A system of dimensionless reactive-diffusive partial differential equations (PDEs) based on a mass balance was developed for each of the species in the reaction system. It is assumed that the fluid in the system remains homogeneous in phase and is at a constant temperature, as well as being quiescent. Given these assumptions, the general unsteady 1D species mass balance reaction-diffusion equation is given by:

$$\frac{\partial (\rho_i)}{\partial t} = D_i \frac{\partial^2 (\rho_i)}{\partial x^2} + R_i \qquad (4)$$

where ρ_i is the individual species mass concentration, D_i is the individual species diffusivity with respect to the mixture, and R_i represents the reaction source/sink terms. x and t are the space and time coordinates, respectively. The model assumes that the initial striation thicknesses of the reactant mixtures are equal, L_Z, as shown in Figure 1(b) with $L_Y = L_Z$. One of the objectives of this model is to allow for the investigation of initial mixing conditions by varying the initial striation thicknesses. Space (x) and time (t) are made dimensionless using the initial striation thickness and the molecular diffusivity:

$$x^* = \frac{x}{L_Z} = \frac{x}{L_B} \qquad t^* = \frac{t \, D_Z}{L_Z^2} = \frac{t \, D_B}{L_B^2} \qquad (5)$$

The choice of D_Z and L_Z for making the equations dimensionless was made because later on in this paper the composition for the Z layer is to be restricted to a mixture containing only an inert I and/or the limiting reagent B, which is always assumed to be the limiting reagent of the reaction regardless of the scheme, effectively making $D_Z = D_B$ and $L_Z = L_B$, as shown in (5). The properties of the limiting reagent were used for non-dimensionalization. Species mass concentrations (ρ_i) were converted to mass fractions (w_i) using:

$$\rho_T = \sum \rho_i \qquad w_i = \frac{\rho_i}{\rho_T} \qquad (6)$$

Using (5)-(6) to modify (4), the dimensionless general species equation for the unsteady 1-D, stationary, reactive-diffusive system is given by:

$$\frac{\partial (w_i)}{\partial t^*} = \frac{D_i}{D_B} \frac{\partial^2 (w_i)}{\partial x^{*2}} + \frac{L_B^2}{\rho_T D_B} R_i \qquad (7)$$

The assumption of all the species having the same diffusivities was also applied, hence making the coefficient of the elliptical term in (7) unity and giving:

$$\frac{\partial (w_i)}{\partial t^*} = \frac{\partial^2 (w_i)}{\partial x^{*2}} + \frac{L_B^2}{\rho_T D_B} R_i \qquad (8)$$
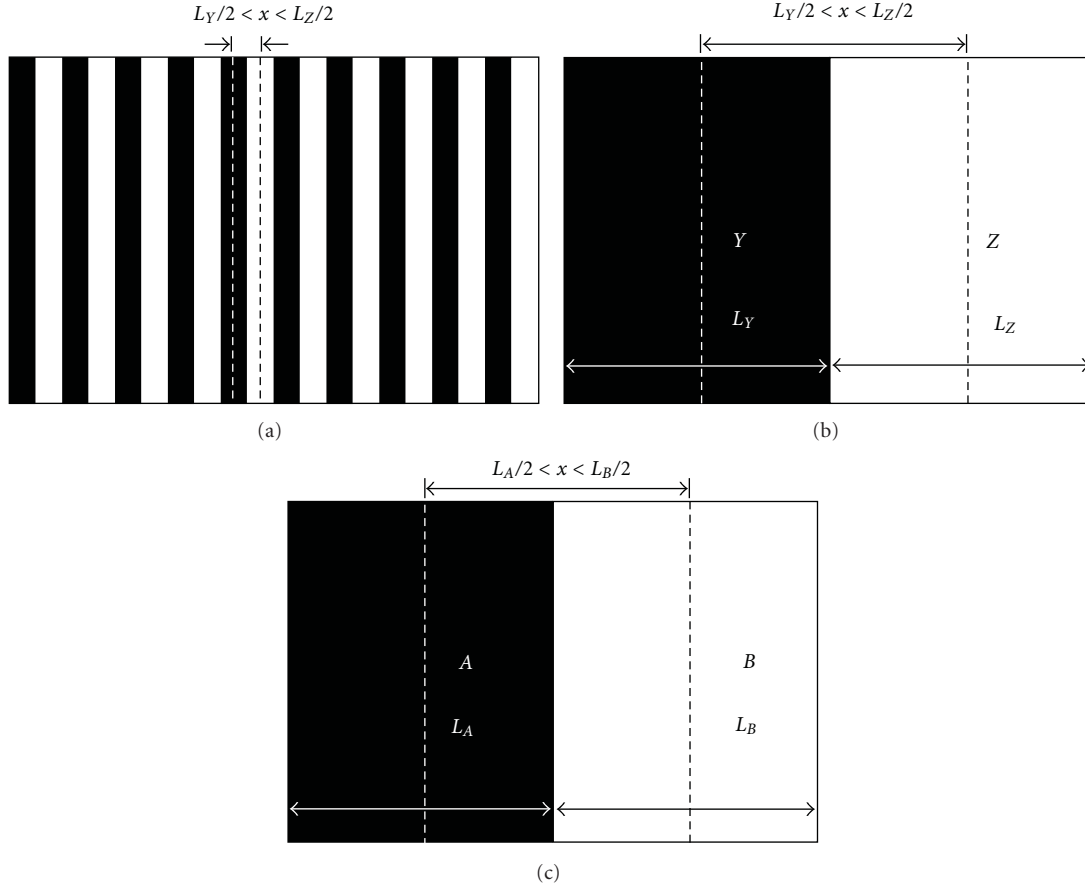
$L_Y/2 < x < L_Z/2$

(a)

$L_Y/2 < x < L_Z/2$

Y

Z

L_Y

L_Z

(b)

$L_A/2 < x < L_B/2$

A

B

L_A

L_B

(c)

FIGURE 1: Geometry for proposed mixing model at time $t = 0$.

TABLE 2: General mixing sensitive reaction schemes.

Competitive-consecutive (C-C)	Competitive-parallel (C-P)
$A + \epsilon B \xrightarrow{k_1'} \alpha P$	$A + \epsilon B \xrightarrow{k_1'} P$
$\beta P + \gamma B \xrightarrow{k_2'} S$	$C + \gamma B \xrightarrow{k_2'} S$

Equation (8) represents the reaction-diffusion equation for some arbitrary reaction, represented by the source/sink term R_i. The particulars of this term define themselves once a reaction scheme is specified. For the purposes of this paper, the reaction scheme will be specified as either a generalized Competitive-Consecutive (C-C) or Competitive-Parallel (C-P) reaction between the two layers. For these purposes, layer Z was assumed to be composed of a homogeneous mixture of limiting reagent, B, and an inert, I, while layer Y was composed of either a single reactant, A, or two reactants, A and C, again with an inert species mixed into this layer. Table 2 shows the generalized reaction schemes for the two types of mixing sensitive reactions that will be investigated. The effect of species diffusivity was not investigated in this paper.

A and B represent the initial reactants for the C-C scheme. A, B, and C represent the initial reactants for the C-P scheme. P is the desired product and S the undesired product for both reaction schemes. An inert, I, is also present, but it does not participate in the reaction. k_1' and k_2' represent the rate constants for the desired and undesired reactions, respectively, and α, β, γ, ϵ are the stoichiometric coefficients.

If it is assumed that the reactions are elementary, expressions for R_i can be written a priori as molar rate expressions. In order to be used in (8), these molar-based expressions are converted to mass fraction rate expressions using the molecular masses of each species. To keep the focus on the effects of stoichiometry, It was further assumed that the molecular masses of A, B, and C were identical (M). As an example, the source term for species A for both C-C and C-P is given by:

$$R_A \left[\frac{\text{mass}}{m^3 s} \right] = -k_1' [A][B]^\epsilon M_A = -k_1' \frac{\rho_A}{M_A} \left(\frac{\rho_B}{M_B} \right)^\epsilon M_A$$

$$= -k_1' \frac{\rho_T^{1+\epsilon}}{M_B^\epsilon} w_A w_B^\epsilon \qquad (9)$$

These mass fraction rate expressions are then placed in (8). The molecular masses of P and S depend on the stoichiometry and are derived using the law of mass action. For example, the molecular mass of P for the C-P scheme would be:

$$M_P = M_A + \epsilon M_B = (1 + \epsilon)M \qquad (10)$$

Expressions for the source and sink terms for all participating species can be written as illustrated for species A in (9). It should be noted that the source/sink terms contain all the information for the reaction scheme of interest. The R_i terms for the other species are significantly different for the C-C and C-P reaction scheme. The systems of partial differential equations (PDE's) are developed separately in the following subsections.

3.1. Competitive-Consecutive (C-C) Reaction Scheme. The C-C reaction scheme is the reaction scheme in which the desired product (P), once formed, participates in an undesired reaction with one of the original reactants (in this case, B). The species that participate in the reaction are A, B, and P. The desired product is P and the undesired by-product is S. The general stoichiometry for this type of reaction scheme is given in Table 2. The source and sink term expressions for A, B, P, S, and inert I for the C-C reaction scheme are developed by a procedure similar to that shown in (9). Once these expressions are substituted in (8) and simplified, the following system of equations is obtained:

$$A: \frac{\partial(w_A)}{\partial t^*} = \frac{\partial^2(w_A)}{\partial x^{*2}} - \left[k_1' \left(\frac{\rho_T}{M}\right)^{\epsilon} \frac{L_B^2}{D_B} w_A w_B^{\epsilon} \right]$$

$$B: \frac{\partial(w_B)}{\partial t^*} = \frac{\partial^2(w_B)}{\partial x^{*2}} - \epsilon \left[k_1' \left(\frac{\rho_T}{M}\right)^{\epsilon} \frac{L_B^2}{D_B} w_A w_B^{\epsilon} \right]$$

$$- \frac{\alpha \gamma}{\beta} \left[\frac{\alpha^{\beta-1} \beta}{(1+\epsilon)^{\beta}} k_2' \left(\frac{\rho_T}{M}\right)^{\beta+\gamma-1} \frac{L_B^2}{D_B} w_P^{\beta} w_B^{\gamma} \right]$$

$$P: \frac{\partial(w_P)}{\partial t^*} = \frac{\partial^2(w_P)}{\partial x^{*2}}$$

$$+ (1+\epsilon) \left[\begin{array}{c} k_1' \left(\frac{\rho_T}{M}\right)^{\epsilon} \frac{L_B^2}{D_B} w_A w_B^{\epsilon} \\ - \frac{\alpha^{\beta-1} \beta}{(1+\epsilon)^{\beta}} k_2' \left(\frac{\rho_T}{M}\right)^{\beta+\gamma-1} \frac{L_B^2}{D_B} w_P^{\beta} w_B^{\gamma} \end{array} \right]$$

$$S: \frac{\partial(w_S)}{\partial t^*} = \frac{\partial^2(w_S)}{\partial x^{*2}} + \left(1 + \epsilon + \frac{\alpha \gamma}{\beta}\right)$$

$$\times \left[\frac{\alpha^{\beta-1} \beta}{(1+\epsilon)^{\beta}} k_2' \left(\frac{\rho_T}{M}\right)^{\beta+\gamma-1} \frac{L_B^2}{D_B} w_P^{\beta} w_B^{\gamma} \right]$$

$$I: \frac{\partial(w_I)}{\partial t^*} = \frac{\partial^2(w_I)}{\partial x^{*2}}$$

$$(11)$$

In order to compare the effect of the relative rates of the desired and undesired reactions while allowing for different reaction stoichiometries, it is necessary to provide a dimensionless expression for the reaction rate ratio of the desired and undesired reactions. Using the ratio k_2'/k_1' is insufficient, since this ratio would have different dimensions for each reaction stoichiometry, making comparison difficult. An ideal dimensionless ratio should give relative rates of the desired reaction to the undesired reaction while retaining a

physical meaning that can be intuitively understood. This can be accomplished by comparing the mass conversion rates associated with the first and second reactions. For the C-C scheme this was done by comparing the mass rate of consumption of desired product P in the second reaction to the mass rate of production of P in the first reaction:

$$\frac{k_2}{k_1} = \frac{\text{mass rate of consumption of } P \text{ by undesired reaction}}{\text{mass rate of production of } P \text{ by desired reaction}}$$

$$(12)$$

The objective is to make this ratio as small as possible to maximize the amount of P produced. By using mass rate expressions to replace the statements in (12) and then simplifying the resulting expression, the dimensionless reaction rate ratio for the general C-C reaction scheme becomes:

$$\frac{k_2}{k_1} = \left[\frac{\beta}{\alpha} \left(\frac{\alpha}{1+\epsilon}\right)^{\beta} \left(\frac{\rho_T}{M}\right)^{\beta+\gamma-\epsilon-1} \right] \frac{k_2'}{k_1'}$$

$$(13)$$

This physically meaningful k_2/k_1 captures both the effect of stoichiometry and the effect of the reaction rate constants of the two reactions, as well as having the benefit of significantly simplifying (11) to give:

$$A: \frac{\partial(w_A)}{\partial t^*} = \frac{\partial^2(w_A)}{\partial x^{*2}} - \left[\left(k_1' \left(\frac{\rho_T}{M}\right)^{\epsilon} \frac{L_B^2}{D_B}\right) w_A w_B^{\epsilon} \right]$$

$$B: \frac{\partial(w_B)}{\partial t^*} = \frac{\partial^2(w_B)}{\partial x^{*2}} - \epsilon \left[\left(k_1' \left(\frac{\rho_T}{M}\right)^{\epsilon} \frac{L_B^2}{D_B}\right) w_A w_B^{\epsilon} \right]$$

$$- \frac{\alpha \gamma}{\beta} \left[\left(k_1' \left(\frac{\rho_T}{M}\right)^{\epsilon} \frac{L_B^2}{D_B}\right) \frac{k_2}{k_1} w_P^{\beta} w_B^{\gamma} \right]$$

$$P: \frac{\partial(w_P)}{\partial t^*} = \frac{\partial^2(w_P)}{\partial x^{*2}}$$

$$+ (1+\epsilon) \left[\begin{array}{c} \left(k_1' \left(\frac{\rho_T}{M}\right)^{\epsilon} \frac{L_B^2}{D_B}\right) w_A w_B^{\epsilon} \\ - \left(k_1' \left(\frac{\rho_T}{M}\right)^{\epsilon} \frac{L_B^2}{D_B}\right) \frac{k_2}{k_1} w_P^{\beta} w_B^{\gamma} \end{array} \right]$$

$$S: \frac{\partial(w_S)}{\partial t^*} = \frac{\partial^2(w_S)}{\partial x^{*2}}$$

$$+ \left(1 + \epsilon + \frac{\alpha \gamma}{\beta}\right) \left[\left(k_1' \left(\frac{\rho_T}{M}\right)^{\epsilon} \frac{L_B^2}{D_B}\right) \frac{k_2}{k_1} w_P^{\beta} w_B^{\gamma} \right]$$

$$I: \frac{\partial(w_I)}{\partial t^*} = \frac{\partial^2(w_I)}{\partial x^{*2}}$$

$$(14)$$

Examination of (14) shows that there is an expression common to all four of the equations involving reactions, which takes the form of a Damköhler number (Da) given by:

$$\text{Da} = k_1'\left(\frac{\rho_T}{M}\right)^\epsilon \frac{L_B^2}{D_B} = \frac{k_1'\left(\rho_T/M\right)^\epsilon}{\left(D_B/L_B^2\right)}$$

$$= \frac{\text{rate of desired fast reaction}}{\text{rate of diffusion}}$$

$$= (\text{rate of desired fast reaction}) * (\text{diffusion time})$$

(15)

This Da depends on the rate constant of the desired reaction and the initial striation thickness of the reactants. It scales the rate of diffusion at the smallest scale of mixing with the desired reaction rate. The effect of the second reaction rate is included through the rate ratio k_2/k_1. Looking at (15), a small Damköhler number indicates that diffusion in the smallest striation is fast compared to the desired/fast reaction and a large Damköhler number indicates that diffusion is slow compared to the fast reaction. A small Da is expected to give a high yield.

Cox et al.'s [5] formulations of Damköhler number and dimensionless reaction rate ratio for the classic C-C reaction scheme are obtained from our general forms of the Damköhler number (15), and dimensionless reaction rate ratio (13). Setting α, β, γ, and ϵ equal to 1 gives the classic C-C reaction scheme. A factor of 0.5 appears in the k_2/k_1 ratio because we used a mass balance in the derivation of the equations and Cox et al. used a mole balance.

Substituting (15) into (14) gives the final set of equations:

$$A: \frac{\partial(w_A)}{\partial t*} = \frac{\partial^2(w_A)}{\partial x*^2} - \left[\text{Da } w_A w_B^\epsilon\right]$$

$$B: \frac{\partial(w_B)}{\partial t*} = \frac{\partial^2(w_B)}{\partial x*^2} - \epsilon\left[\text{Da}w_A w_B^\epsilon\right] - \frac{\alpha\gamma}{\beta}\left[\text{Da}\frac{k_2}{k_1}w_P^\beta w_B^\gamma\right]$$

$$P: \frac{\partial(w_P)}{\partial t*} = \frac{\partial^2(w_P)}{\partial x*^2} + (1+\epsilon)\left[\text{Da}w_A w_B^\epsilon - \text{Da}\frac{k_2}{k_1}w_P^\beta w_B^\gamma\right]$$

$$S: \frac{\partial(w_S)}{\partial t*} = \frac{\partial^2(w_S)}{\partial x*^2} + \left(1+\epsilon+\frac{\alpha\gamma}{\beta}\right)\left[\text{Da}\frac{k_2}{k_1}w_P^\beta w_B^\gamma\right]$$

$$I: \frac{\partial(w_I)}{\partial t*} = \frac{\partial^2(w_I)}{\partial x*^2}$$

(16)

Using (16), the effect of reaction rates and striation thickness on C-C reactions can be investigated using the dimensionless reaction rate ratio (k_2/k_1) and the Damköhler number (Da).

3.2. Competitive-Parallel (C-P) Reaction Scheme. In the C-P reaction scheme one of the original reactants (in this case, B) participates in two reactions simultaneously. The general stoichiometry for this type of reaction is shown in Table 2. The source and sink terms for A, B, C, P, S, and inert I for the C-P reaction scheme were developed following the same procedure as shown for the C-C reaction scheme above and then replaced in (8) to get a set of PDE's for the C-P reaction scheme.

As with the C-C reaction scheme, variable stoichiometry requires the introduction of a physically meaningful, dimensionless reaction rate ratio for the C-P scheme. Since the C-P reaction scheme has only one reagent (B) which participates in both reactions, the dimensionless reaction rate ratio for the C-P scheme becomes:

$$\frac{k_2}{k_1} = \frac{\text{mass rate of consumption of } B \text{ by undesired reaction}}{\text{mass rate of consumption of } B \text{ by desired reaction}}$$

(17)

which, on substitution of rate expressions, can be written as:

$$\frac{k_2}{k_1} = \left[\frac{\gamma}{\epsilon}\left(\frac{\rho_T}{M}\right)^{\gamma-\epsilon}\right]\frac{k_2'}{k_1'}$$

(18)

As with the k_2/k_1 ratio defined for the C-C reaction scheme, minimization of this ratio would yield the maximum desirable product (P). This k_2/k_1 also includes the effects of stoichiometry and reaction rate constants for the two reactions. Substitution of (18) into the C-P PDEs and simplifying gives the same Damköhler number that appeared in the C-C reaction equations, giving the C-P equations for numerical simulations:

$$A: \frac{\partial(w_A)}{\partial t*} = \frac{\partial^2(w_A)}{\partial x*^2} - \left[\text{Da}w_A w_B^\epsilon\right]$$

$$B: \frac{\partial(w_B)}{\partial t*} = \frac{\partial^2(w_B)}{\partial x*^2} - \epsilon\left[\text{Da}w_A w_B^\epsilon\right] - \epsilon\left[\text{Da}\frac{k_2}{k_1}w_c w_B^\gamma\right]$$

$$C: \frac{\partial(w_C)}{\partial t*} = \frac{\partial^2(w_C)}{\partial x*^2} - \frac{\epsilon}{\gamma}\left[\text{Da}\frac{k_2}{k_1}w_c w_B^\gamma\right]$$

$$P: \frac{\partial(w_P)}{\partial t*} = \frac{\partial^2(w_P)}{\partial x*^2} + (1+\epsilon)\left[\text{Da}w_A w_B^\epsilon\right]$$

$$S: \frac{\partial(w_S)}{\partial t*} = \frac{\partial^2(w_S)}{\partial x*^2} + \left(\epsilon+\frac{\epsilon}{\gamma}\right)\left[\text{Da}\frac{k_2}{k_1}w_c w_B^\gamma\right]$$

$$I: \frac{\partial(w_I)}{\partial t*} = \frac{\partial^2(w_I)}{\partial x*^2}$$

(19)

This formulation for both C-C and C-P schemes allows the use of one Damköhler number to describe the mixing relative to the desired reaction rate. It also provides a physically meaningful dimensionless reaction rate ratio to describe the relative rates of reaction. While there is no explicit expression for the effect of stoichiometry, both of the dimensionless measures include stoichiometric coefficients, showing that both the mixing and the relative reaction rates are affected by the stoichiometry of the reaction scheme.

4. Numerical Solution of Equations

The two systems of equations for the C-C (16) and the C-P (19) reaction schemes were solved using COMSOL Multiphysics 3.4, a commercial finite element PDE solver. The 1-D transient convection and diffusion mass transport model was used with the mass fractions for each species specified as independent variables. Elements were specified as Lagrange-quadratic. A 1-D geometry line of unit length equally split

Table 3: General initial conditions for C-C and C-P reaction schemes at $t^* = 0$.

	C-C			C-P	
	$-1/2 \leq x^* < 0$	$0 \leq x^* \leq 1/2$		$-1/2 \leq x^* < 0$	$0 \leq x^* \leq 1/2$
A	w_{A_0}	0	A	w_{A_0}	0
B	0	w_{B_0}	B	0	w_{B_0}
C	—	—	C	w_{C_0}	—
P	0	0	P	0	0
S	0	0	S	0	0
I	$1 - w_{A_0}$	$1 - w_{B_0}$	I	$1 - w_{A_0} - w_{C_0}$	$1 - w_{B_0}$

Table 4: Stoichiometric initial conditions based on w_{B_0} for C-C and C-P reaction schemes.

	C-C			C-P	
	$-1/2 \leq x^* < 0$	$0 \leq x^* \leq 1/2$		$-1/2 \leq x^* < 0$	$0 \leq x^* \leq 1/2$
A	$(1/\epsilon)(w_{B_0})$	0	A	$(1/\epsilon)(w_{B_0})$	0
B	0	w_{B_0}	B	0	w_{B_0}
C	—	—	C	$(1/\gamma)(w_{B_0})$	0
P	0	0	P	0	0
S	0	0	S	0	0
I	$1 - (1/\epsilon)(w_{B_0})$	$1 - w_{B_0}$	I	$1 - (1/\epsilon + 1/\gamma)(w_{B_0})$	$1 - w_{B_0}$

into two domains ($-1/2 \leq x^* < 0$ and $0 \leq x^* \leq 1/2$), and a mesh of 2048 equally spaced elements was generated. Boundary conditions (BCs) for all cases were specified as

$$\frac{\partial(w_i)}{\partial x^*} = 0 \quad \text{at } x^* = -\frac{1}{2}, \ x^* = \frac{1}{2} \tag{20}$$

$$\forall t^*, i = A, B, C, P, S, I$$

The general initial conditions for the two reaction schemes are shown in Table 3. The initial conditions were chosen to replicate the segregated striation condition of the model.

A final constraint imposed on the simulations is that the reactants need to be present in stoichiometric quantities. Using this constraint, it is possible to express the initial mass fractions as a function of the initial mass fraction of the limiting reagent $B(w_{B_0})$, as shown in Table 4. For the C-C case, the only reactants present initially are A and B. Therefore, the alternating striations would have mass fractions of unity for A and unity for B. For the C-P cases, however, there are three initial reactants present. In this model, it is assumed that reactants A and C are well mixed and present in the Y striation and that the limiting reagent B is in the Z striation. The inert species I was allowed to be present in both Y and Z striations as required to maintain constant mass concentrations in the striations and was assumed to be well mixed with the other reactants. Another condition specified for the C-P case is that the ratios of A, B, and C are such that either A or C could consume all of the available B, so B is always the limiting reagent.

Simulations for both reaction schemes were run until the equivalent of $t^* = 500$ in the case of Da = 1. Since the simulations are solved in time, the dimensionless times to which the simulations were run were scaled according to the Damköhler number. Therefore, $t^* = 500$ for Da = 1 is equal

to $t^* = 50000$ for Da = 0.01 and $t^* = 0.05$ for Da = 10000, that is, the values of Da $\cdot$ t^* are equal for all cases. In fact, Da $\cdot$ t^* is equivalent to a dimensionless reaction time where Da $\cdot$ $t^* = t/\tau_R$. Therefore, running the simulations to Da $\cdot$ $t^* = 500$ is the same as the simulations being run for 500 reaction times. All these dimensionless times are in fact equal in real time. For most of the cases, it was seen that all of the limiting reagent B is consumed by $t^* = 500$ or equivalent. COMSOL returned profiles of mass fraction for the various species over the dimensionless space x^* for each dimensionless time step t^*.

5. Results and Discussion

The results and discussion are presented as follows. First, the time evolution of species profiles across individual striations is presented and discussed for the competitive-consecutive and competitive-parallel reactions. This discussion includes the effects that mixing and reaction rate ratio have on the species profiles. After that, the definition of yield of desired product is presented, and results showing the time evolution of the yield of desired product for both reaction schemes are shown. This is followed by a discussion of the effects of mixing and reaction rate ratio on the yield of desired product for both reaction schemes.

5.1. Competitive-Consecutive (C-C) Reaction. In order to test the model for the C-C reaction, values were assigned to Da and k_2/k_1 as given in Table 5. The stoichiometric coefficients were all set to 1 in order to match the classic reaction scheme used by Cox and others (Muzzio and Liu [16], Clifford et al. [6, 19–21], Clifford [17], Clifford and Cox [18], and Cox [7]). This allows comparison of results for the effect of

TABLE 5: Numerical values for simulated C-C test cases. Stoichiometric coefficients α, β, γ, and ϵ were set to 1, representing the reaction: $A + B \xrightarrow{k_1'} P, P + B \xrightarrow{k_2'} S$, and the initial mass fraction of species B was always 1 ($w_{B_0} = 1$).

C-C case	$k_2/k_1 = (1/2)(k_2'/k_1')$	$Da = k_1'(\rho_T/M)(L_B^2/D_B)$
1	10^{-5}	1
2	10^{-5}	10000
3	1	1
4	1	10000

striation thickness and reaction rates with their data. The initial conditions were chosen such that only pure A and B are present in the system.

Looking at the C-C cases in Table 5, the values of k_2/k_1 and Da for Case 1 are favourable conditions for a high yield of P, that is, $k_2/k_1 \ll 1$ and Da = 1. For Case 4, the yield of P should be small, that is, $k_2/k_1 = 1$ and Da $\gg 1$. The two cases are meant to represent the two extremes of very favorable reaction rate ratio and perfect mixing and very unfavorable kinetics and poor mixing conditions. Cases 2 and 3 have good k_2/k_1 with bad mixing and bad k_2/k_1 with good mixing. The solutions COMSOL returns are the profiles of mass fraction for the various species over the dimensionless space x^* for each time step t^*. Figure 2 shows the spatial and temporal evolution of species over a single dimensionless striation. Before discussing the profiles in detail, it is important to note a couple of points about the profiles. A vertical line represents a sharp interface. A curved line represents a gradient in the concentration. Finally, a horizontal line represents uniform concentration across the space.

Looking at Figures 2(a) and 2(c), one can see that all of the species are uniformly distributed for all time steps greater than $t^* = 0$. This is not the case for Figures 2(b) and 2(d). This can be attributed to the smaller striation thicknesses, that is, the lower Damköhler number, for Cases 1 and 3. As the striations are thinner for those cases, the species can completely diffuse across in a shorter amount of time than for Cases 2 and 4 where the striations are 100 times thicker. The thicker striations allow for spatial inhomogeneity of the species. The thinner striation thicknesses allow for differences only in temporal distribution of species and not spatial distribution. The thicker striations cause differences in both temporal and spatial distributions. Figures 2(b) and 2(d) also exhibit an interface between reactants whereas Figures 2(a) and 2(c) do not.

Despite the fact that there is complete mixing for both Cases 1 and 3, there is a very large difference in the yield of P for the two cases. For Case 1, which has both good mixing and a favourable reaction rate ratio, the majority of the mass present is that of P, the desired product (Figure 2(a)-(iii)). For Case 3, however, the mass fraction of the undesired product is always higher than that of the desired product (Figure 2(c)-(iii)). There is a significant drop in mass fraction of P from 0.99 to 0.25, showing the dramatic effect of reaction rate ratio for the same mixing conditions.

Looking at Figures 2(b)-(iii) and 2(d)-(iii), the same reversal of P and S is observed. The reaction rate ratio has a profound effect on the yield of desired product that is independent of mixing. When the reaction rate ratio is good, the undesired reaction does not participate. All of the product P forms at the interface of A and B, making the profile of mass fraction of P symmetric about the mid-plane, $x^* = 0$, as shown in Figures 2(b)-(ii) and 2(b)-(iii). When the undesirable by-product reaction occurs at a comparable rate to that of the desired reaction, a significant asymmetry in the profiles of mass fraction for all species is visible (Figures 2(d)-(ii) and 2(d)-(iii)). This can be attributed to the fact that the second reaction occurs only on the right hand side of $x^* = 0$ where P is in contact with B. This causes P to react to form S when it is exposed to B on one side.

The key results are as follows: first, a small striation thickness allows for uniform concentrations of species, that is, perfect mixing, whereas larger striations can cause spatial inhomogeneities in species mass fraction. Second, the reaction rate ratio is an independent factor which can significantly alter the yield of desired product regardless of the mixing condition. This effect is predictable in the sense that if the ratio is good the yield is good, and if the ratio is poor the yield is poor. Finally, for the larger striation thicknesses, a good reaction ratio causes symmetric concentration profiles of desired product P, while a bad ratio causes the product profiles to skew towards the B side of the striation. Perfect mixing simplifies the reaction analysis and shortens the reaction time. Having favourable kinetics improves the yield significantly.

Changing the stoichiometry did not affect the species profiles in the case of good reaction rate ratio ($k_2/k_1 = 10^{-5}$) for both good and bad mixing conditions ($1 < Da < 10000$). The profiles of all the species were identical to those presented above. The species profiles for the different stoichiometries with the bad reaction rate ratio ($k_2/k_1 = 1$) and good mixing (Da = 1) look similar to those shown here, but the amount of P and S produced changes. The case of both bad rate ratio ($k_2/k_1 = 1$) and poor mixing (Da = 10000) always resulted in a larger amount of S produced than P, and all the profiles were skewed towards B. The amount of S and P produced varies with stoichiometry, and the profiles are skewed more or less depending on the stoichiometry.

5.2. Competitive-Parallel (C-P) Reaction. Table 6 shows the variable settings for the C-P simulations. The four cases are identical to the ones used for the C-C simulations with the exception of the definition of k_2/k_1. The stoichiometry illustrated is the classic C-P reaction scheme with all stoichiometric coefficients set to 1. The initial conditions were chosen such that $w_{B_0} = 0.5$, and the initial amounts of A, C, and I present in the system were calculated using the formulae in Table 4. The solutions COMSOL returns are the profiles of mass fraction for the various species over the dimensionless space x^* for each time step t^*. Figure 3 shows the spatial and temporal evolution of species including the inert.
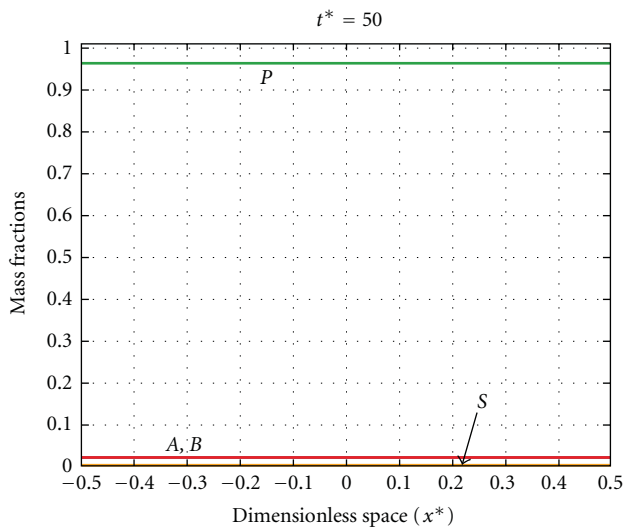
The C-P case profiles show many of the same characteristics as the C-C cases. Cases 1 and 3, with the thinner initial striations, once again show spatial homogeneity for
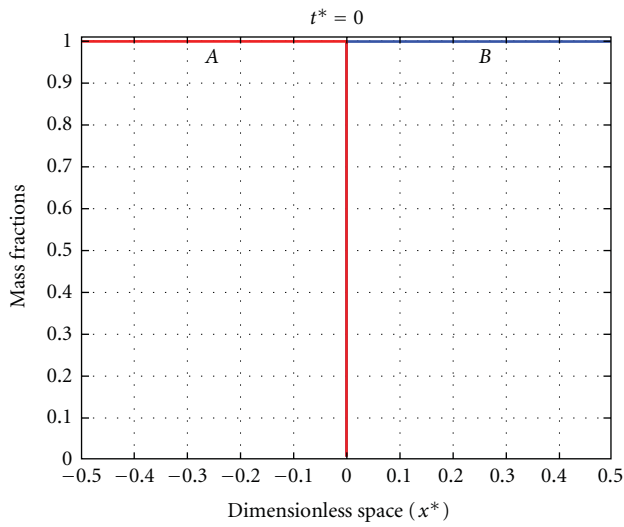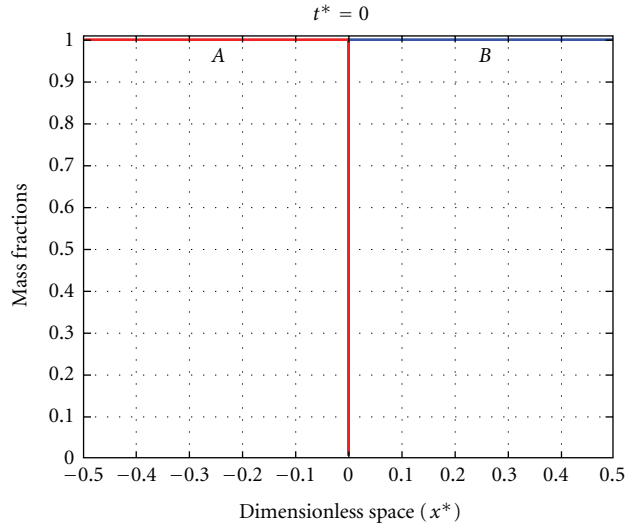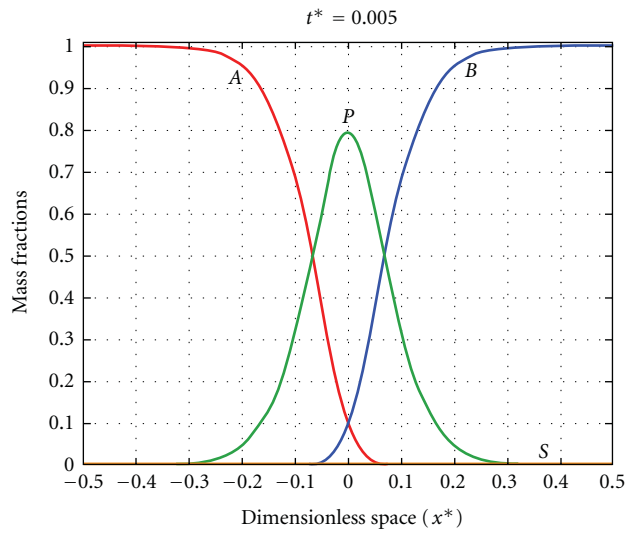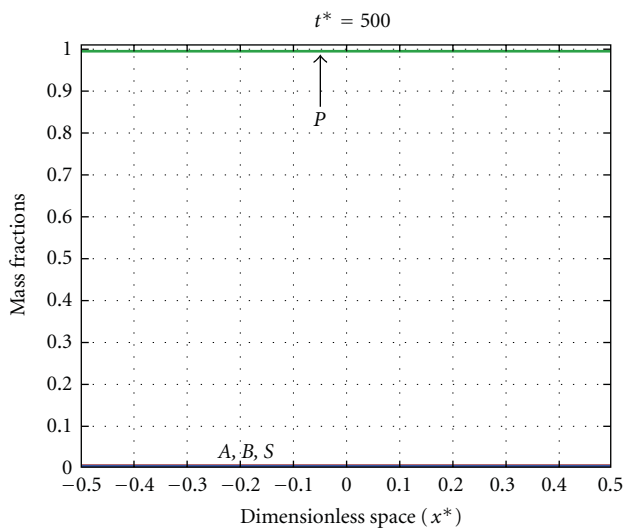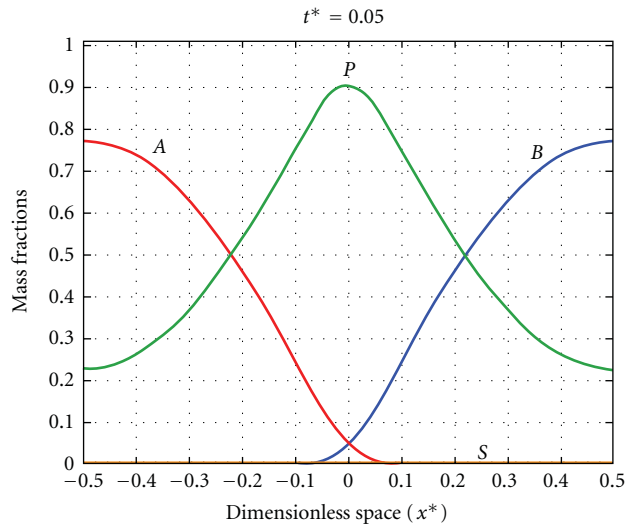
(a) Case 1, $k_2/k_1 = 10^{-5}, \mathrm{Da} = 1$

(b) Case 2, $k_2/k_1 = 10^{-5}, \mathrm{Da} = 10000$

Figure 2: Continued.
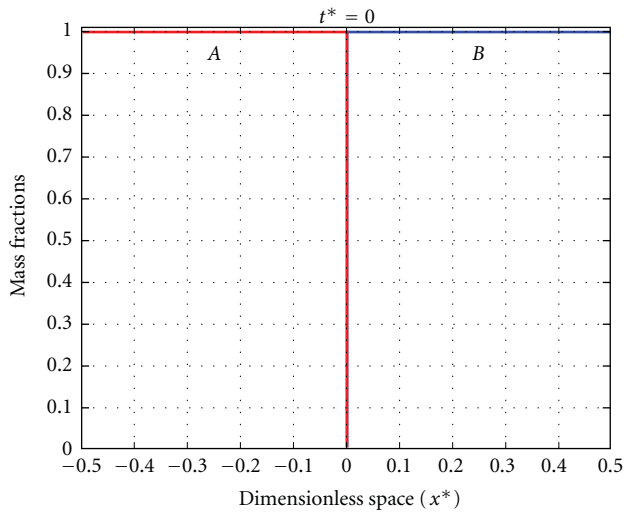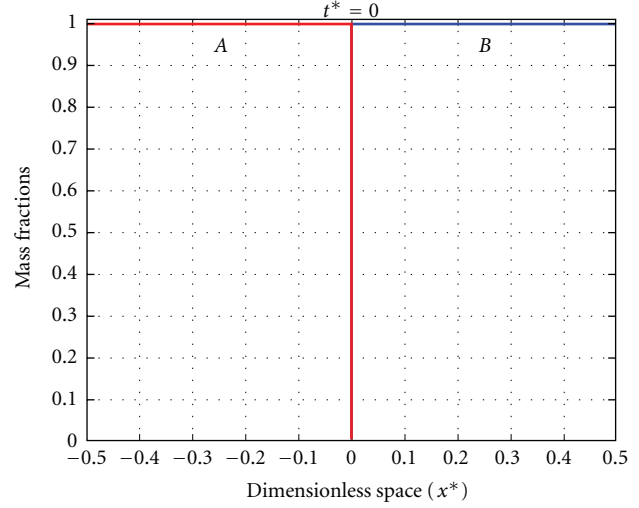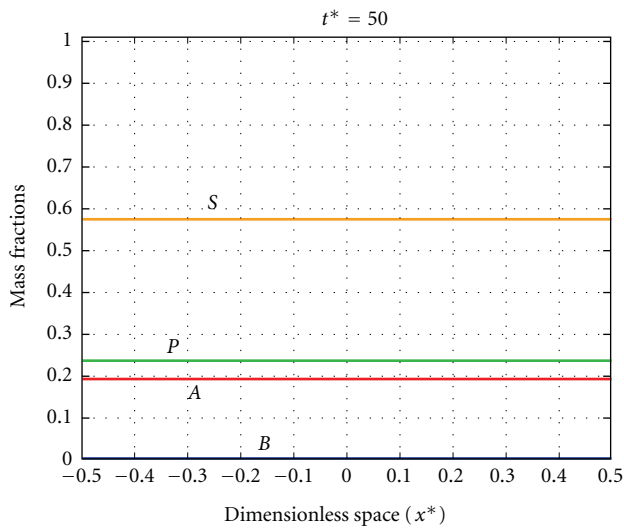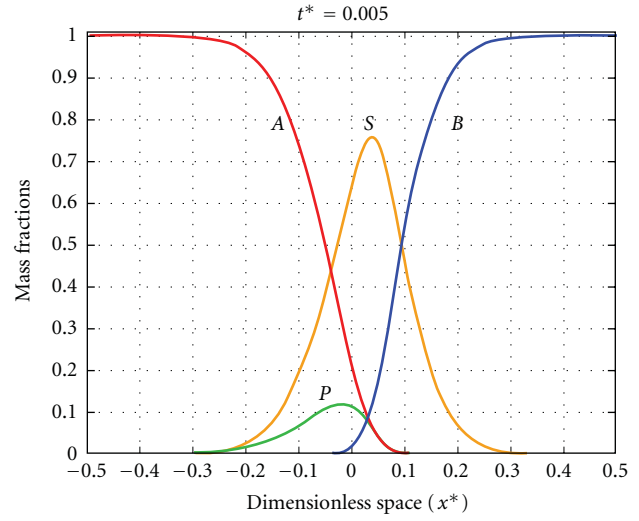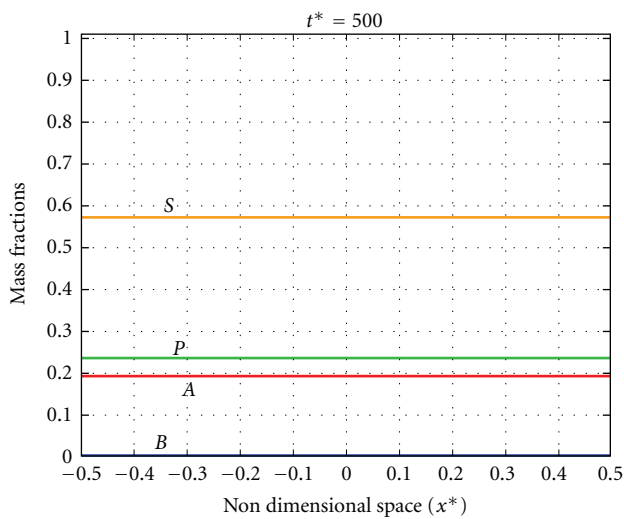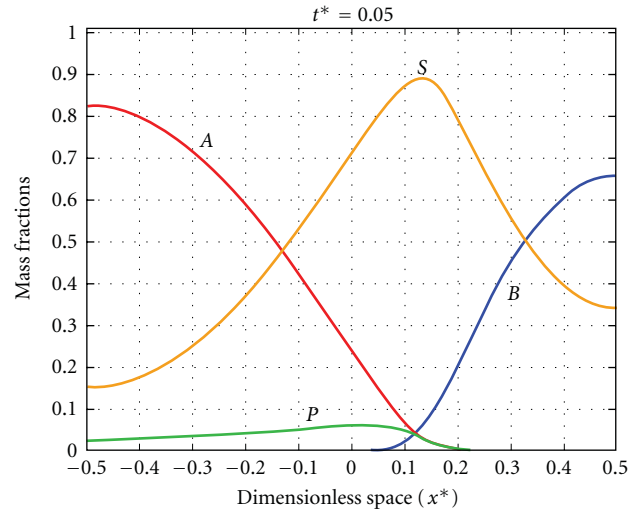
(c) Case 3, $k_2/k_1 = 1$, Da $= 1$

(d) Case 4, $k_2/k_1 = 1$, Da $= 10000$

FIGURE 2: Spatial and temporal evolution of mass fractions for C-C cases (a) Case 1 ($k_2/k_1 = 10^{-5}$, Da $= 1$); (b) Case 2 ($k_2/k_1 = 10^{-5}$, Da $= 10000$); (c) Case 3 ($k_2/k_1 = 1$, Da $= 1$); and (d) Case 4 ($k_2/k_1 = 1$, Da $= 10000$).
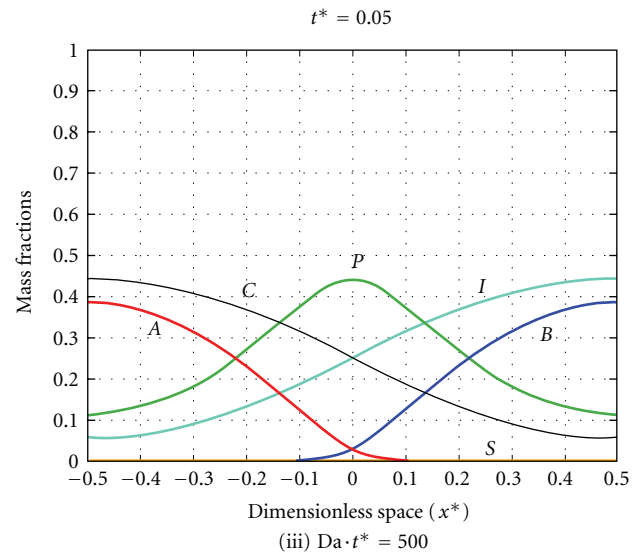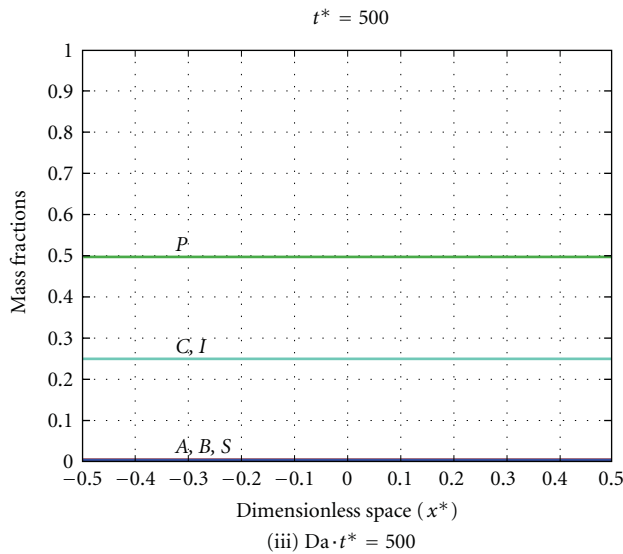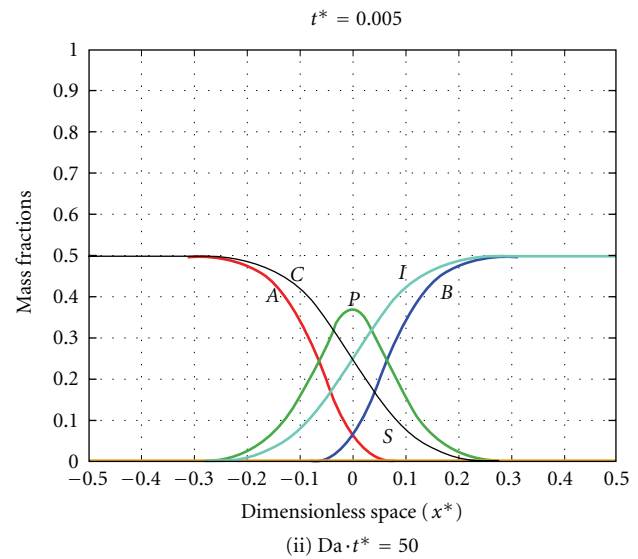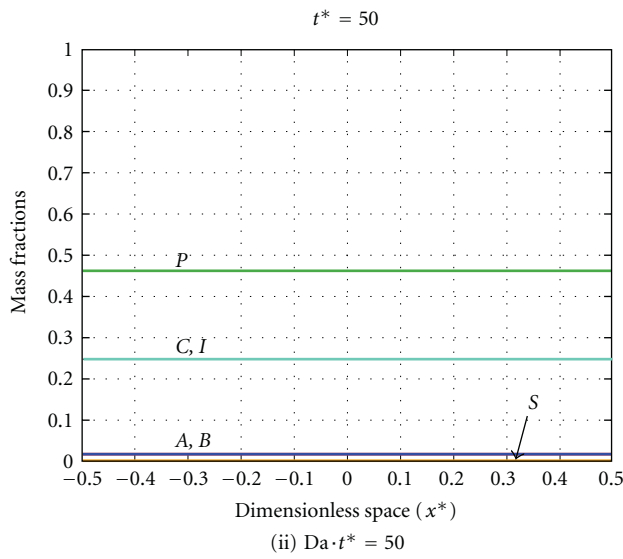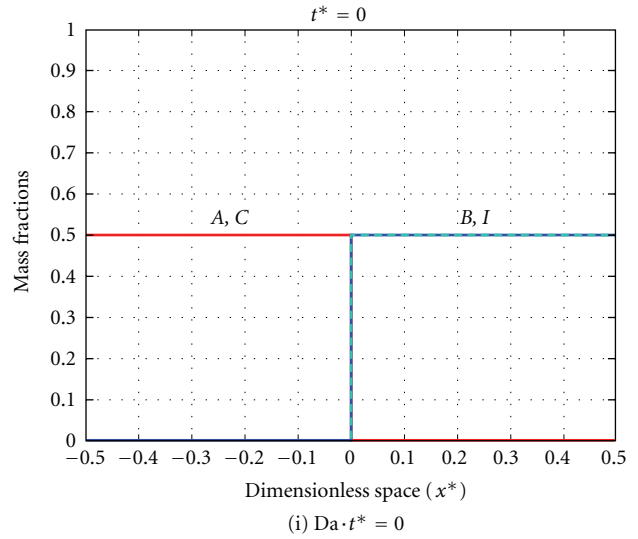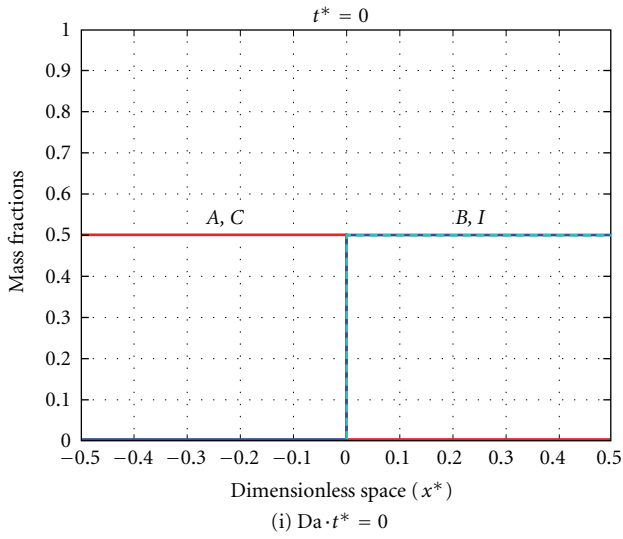
(a) $k_2/k_1 = 10^{-5}, \mathrm{Da} = 1$

(b) $k_2/k_1 = 10^{-5}, \mathrm{Da} = 10000$

FIGURE 3: Continued.
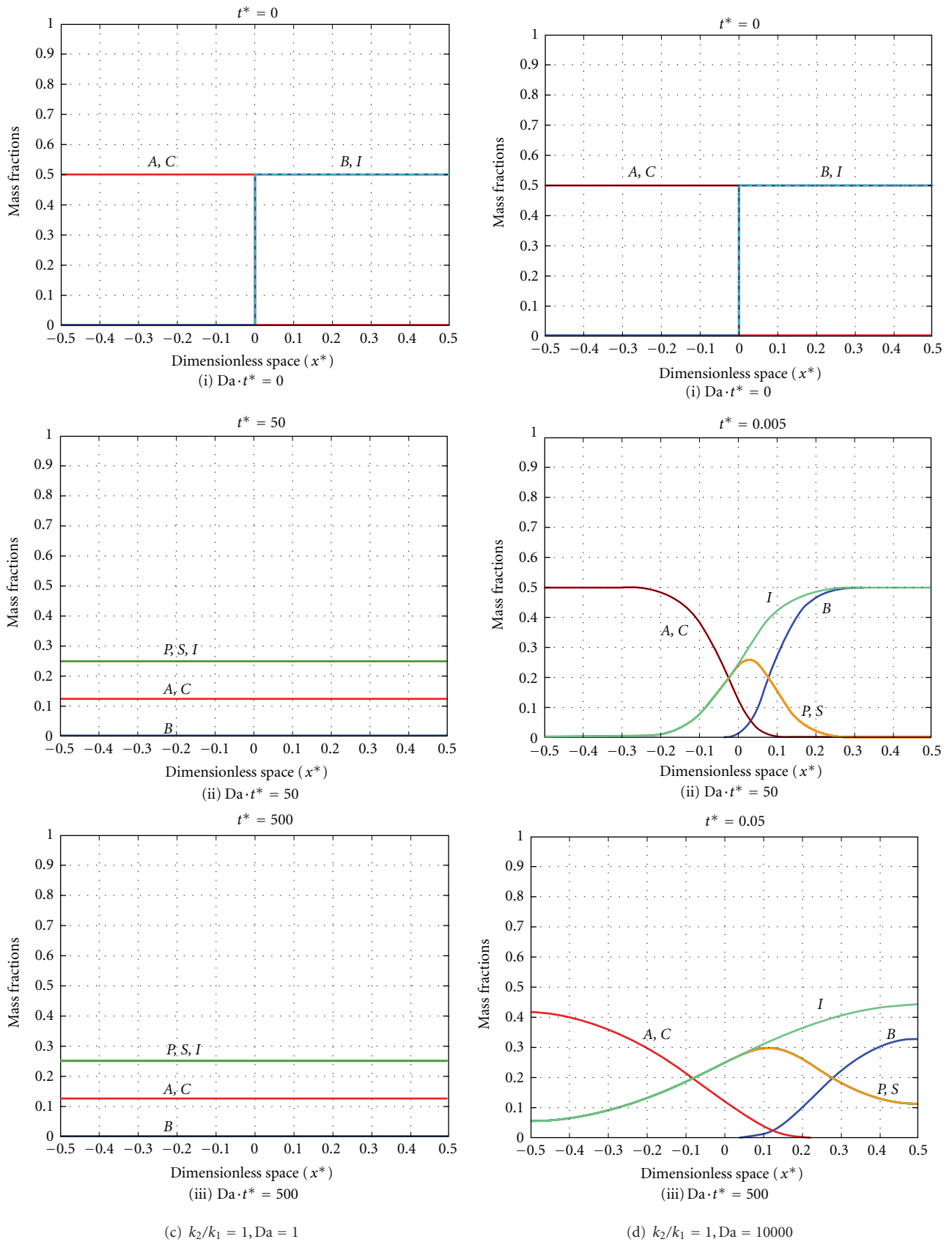
Figure 3: Spatial and temporal evolution of mass fractions for C-P cases (a) Case 1 ($k_2/k_1 = 10^{-5}$, Da = 1); (b) Case 2 ($k_2/k_1 = 10^{-5}$, Da = 10000); (c) Case 3 ($k_2/k_1 = 1$, Da = 1); and (d) Case 4 ($k_2/k_1 = 1$, Da = 10000).

TABLE 6: Numerical values for simulated C-P test cases. Stoichiometric coefficients γ and ϵ were set to 1, representing the reaction: $A + B \xrightarrow{k_1'} P, C + B \xrightarrow{k_2'} S$, and the initial mass fraction of species B was always 0.5 ($w_{B_0} = 0.5$).

C-P case	$k_2/k_1 = k_2'/k_1'$	$Da = k_1'(\rho_T/M)(L_B^2/D_B)$
1	10^{-5}	1
2	10^{-5}	10000
3	1	1
4	1	10000

all the species across the entire striation thickness, whereas Cases 2 and 4 show spatial variations in mass fraction for all the species across the striations. The yields of P and S change when the reaction ratio is varied from favourable ($k_2/k_1 = 10^{-5}$) to unfavourable ($k_2/k_1 = 1$). Cases 1 and 2 have a high yield of P; Cases 3 and 4 have an equal yield of P and S. The cases with the large striation thicknesses ($Da = 10000$) show symmetry in product mass fraction profiles about $x^* = 0$ when the second reaction is insignificant ($k_2/k_1 = 10^{-5}$) and significant asymmetry when it is actively participating in the reaction ($k_2/k_1 = 1$). The main difference between the C-C and C-P reactions is that once the product P is formed in the C-P reaction, it does not get consumed by a side reaction. Therefore, in terms of measuring the yield of P, the C-P reaction scheme is a lot less mixing sensitive than the C-C reaction scheme. For the C-C reaction, the longer that P sits in contact with B, the higher the chance that the yield of P will decrease.

Changing the stoichiometry for the C-P reactions resulted in some non-linear profile changes. While the profiles for the well-mixed cases remained uniform across the striation, the magnitudes of desired and undesired product produced changed. The profiles for the poorly mixed cases look different from the profiles presented here owing partly to the different initial conditions required when the stoichiometry was changed and also because of the stoichiometries themselves. In a second paper [29], the yield of P is used to capture all of these changes for both the C-P as well as the C-C reaction schemes.

*5.3. Yield of Desired Product P.* In order to to assess yield for the non-uniform profiles of mass fraction, the profiles of P were integrated to obtain the total mass of P present in the system at an instant in time:

$$Y_P = \frac{\text{mass of species } P \text{ at } t^*}{\text{max mass of } P \text{ obtainable}} = \frac{\int_{-0.5}^{0.5} w_P dx^*(t^*)}{0.5 w_{B_0}(1 + (1/\epsilon))} \quad (21)$$

Following Y_P over time gives the progression of yield over time. Figure 4 shows the yield of P over time as the reaction progresses for the four C-C cases, and Figure 5 shows the same results for the four C-P cases. Plotting $Da \cdot t^*$ on the x-axis allows all four curves to be displayed on the same figure. These figures confirm the conclusions drawn above that good mixing and a good reaction rate ratio will maximize the yield of desired product (Case 1 in both Figures 4 and 5), and poor mixing with an unfavourable reaction rate
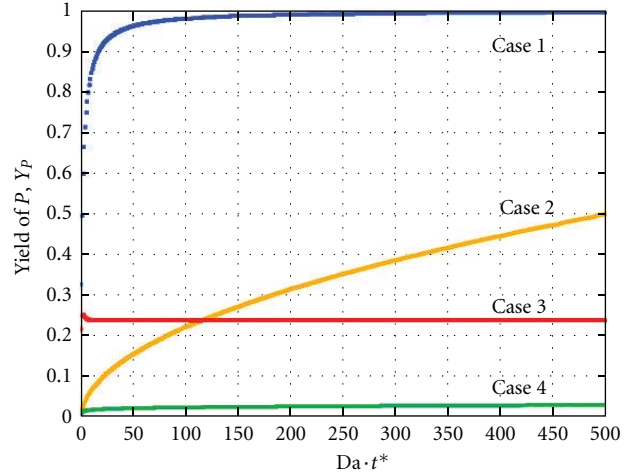
FIGURE 4: Yield of P versus time for the C-C cases.

ratio minimizes the yield of desired product (Case 4 for both Figures 4 and 5). This also confirms the notion that minimization of the Damköhler number and reaction rate ratio is desirable. Clifford et al.'s [6] conclusions for the classic C-C stoichiometry are the same as ours. Quantitative comparison is not possible because our characteristic length and time scale choices are different from theirs.

5.4. Effect of Reaction Rate Ratio on Yield of P. Figures 4 and 5 show that the reaction rate ratio affects how much product is formed regardless of the mixing condition. This is evident in the comparison of Cases 1 and 3, which are both well mixed, and Cases 2 and 4, which are both poorly mixed. The favourable reaction rate ratio (Cases 1 and 2) always provides a higher final yield of P. It is impossible to get a good yield of desired product if the reaction rate ratio is unfavourable, regardless of the mixing condition (Cases 3 and 4). Clifford et al. [6] came to the same conclusion for the effect of reaction rate ratio. A smaller reaction rate ratio is favourable for maximizing the yield of desired product.

5.5. Effect of Mixing on Yield of P. There is a significant effect of mixing on Y_P evident in Figures 4 and 5. When the reaction rate ratio is favourable, having good mixing can cause a substantial increase in yield of desired product, as seen by comparing Cases 1 and 2 in both the figures ($Y_P = 0.5$ to 1 for C-C and $Y_P = 0.5$ to 1 for C-P). If the reaction rate ratio is unfavourable, a similar favourable effect of mixing is seen by comparing Cases 3 and 4, though it is not as profound as when the reaction rate ratio is good ($Y_P = 0.03$ to 0.24 for C-C and $Y_P = 0.33$ to 0.5 for C-P). This illustrates that the effect of mixing is limited by the reaction rate ratio, that is, the reaction rate ratio determines the final yield and good mixing helps one to realise that asymptotic value of yield. For the well-mixed cases (Cases 1 and 3) the final yield of P is attained much faster, so mixing also determines the pace of the reaction. In the C-C case, due to the nature
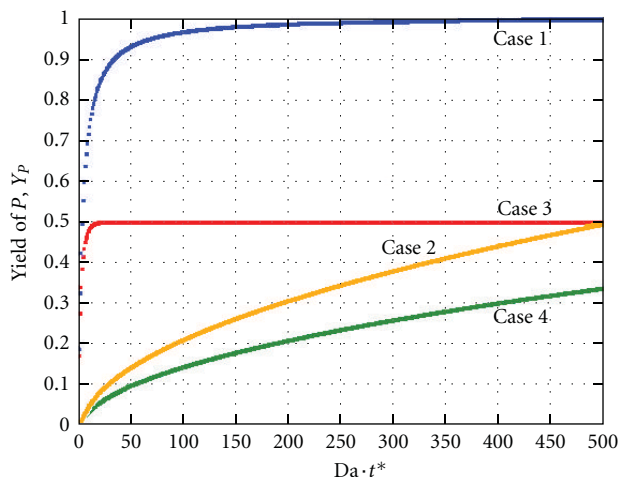
FIGURE 5: Yield of *P* versus time for the C-P cases.

of the reaction, this has a significant positive effect on the final yield of *P*. Cox and others came to a similar conclusion (Cox et al. [5] and Clifford et al. [6]): minimizing the Damköhler number leads to an increase in the yield of desired product.

6. Conclusions

New definitions of Damköhler number (Da) and dimensionless reaction rate ratio (k_2/k_1) were derived to investigate the effects of stoichiometry, mixing, and reaction rate ratio for competitive-consecutive and competitive-parallel reactions with a general stoichiometry. The model development deals with both reaction schemes, something that was not previously available. A single Damköhler number was found for both kinds of mixing sensitive reactions. This is encouraging, since there has previously been a lot of debate on the formulation of the Damköhler number for these competing reactions, for example, whether it should be based on the first or the second reaction. Having just one expression to describe mixing is more physical, since mixing should be independent of the reaction scheme. The general expression for the Damköhler number, when applied to the classic reaction schemes, collapses to the expressions used in previous investigations, Cox et al. [5] in particular. The C-C and C-P reaction schemes, however, are very different and these differences are reflected in the specific reaction rate ratios for the two types of reaction stoichiometries that are to be used in the model.

The effects of mixing and reaction rate ratios on the yield of desired product were investigated for the classic competitive-consecutive and competitive-parallel reaction schemes. The reaction rate ratio ultimately limits the final yield of desired product. Mixing determines whether that yield is achieved, and the rate at which the final yield is reached. The reaction rate ratio and the Damköhler number both need to be minimized to achieve the maximum yield of product. The results from the model agree with the expected

results and with the results of previous investigations where both mixing and reaction rate ratio were varied. Improving the mixing and chemistry by minimizing the Damköhler number and the reaction rate ratio is desirable and leads to improvements in yield of desired product.

This confirmation of the model allows for future work where the effects of stoichiometry, mixing and k_2/k_1 ratios on yield will be investigated for a general mixing sensitive reaction with varying stoichiometry.

While the model allows for the investigation of the effects of initial concentrations of reactants, this was not done in the current study and this is another possible avenue for further exploration. It is also acknowledged that the 1D model is not an accurate depiction of real turbulent mixing, but this investigation was meant to be a first foray into the effect of stoichiometry of mixing sensitive reactions, so simplicity was desirable. Added complexities include introducing fluid flow into the model, such as taking into account laminar stretching of the striations, 2D deformation and eventually 3D deformation, similar to the works of Cox [7] and Baldyga and Bourne [1]. The eventual goal would be to integrate the reaction diffusion equations into the Engulfment model of Baldyga and Bourne [1]. This model could also be integrated into 3D meso-mixing models to better approximate the real industrial situation.

Nomenclature

c : Molar concentration in Cox et al. [5] [kmol/m^3]
c_{B_0}: Initial concentration of limiting reagent in Cox et al. [5] [kmol/m^3]
Da: Damköhler Number [−]
Da$_{II}$: Damköhler Number in Cox et al. [5] [−]
D: Diffusivity, [m^2/s]
I': Dimensionless concentration of species *I* in Cox et al. [5] [−]
k_1: Rate constant 1 in Cox et al. [5] [m^3/kmol s]
k_2: Rate constant 2 in Cox et al. [5] [m^3/kmol s]
k_1': Rate constant 1 [m^3/kmol s]
k_2': Rate constant 2 [varies]
k_2/k_1: Dimensionless reaction rate ratio [−]
L: Striation thickness [m]
M: Molecular weight [kg/kmol]
R: Reaction term [kg/m^{3}s]
t: Time [s]
t^*: Dimensionless time [−]
T: Dimensionless time in Cox et al. [5] [−]
w: Mass fraction [−]
W: Striation thickness in Cox et al. [5] [m]
x: Distance [m]
x^*: Dimensionless distance [−]
X: Dimensionless distance in Cox et al. [5]
Y_P: Yield of desired product *P* [−].

Greek Letters

$\alpha, \beta, \gamma, \epsilon$: Stoichiometric Coefficients [−]
ε: Reaction rate ratio in Cox et al. [5] [−]
ρ: Mass concentration [kg/m^3]

τ_M: Mixing time [s]
τ_R: Reaction time [s].

Subscripts

A: Species A (reactant)
B: Species B (reactant)
C: Species C (reactant)
i: Species A, B, C, I, P or S
I: Species I (inert)
I': Any species I' in Cox et al. [5]
0: Initial value
P: Species P (product)
S: Species S (by-product)
T: Total
Y, Z: Species mixtures.

Acknowledgments

References

[1] J. Baldyga and J. R. Bourne, *Turbulent Mixing and Chemical Reactions*, Wiley, Chichester, UK, 1999.

[2] G. K. Patterson, E. L. Paul, S. M. Kresta, and A. W. Etchells III, "Mixing and chemical reactions," in *Handbook of Industrial Mixing—Science and Practice*, E. L. Paul, V. A. Atiemo-Obeng, and S. M. Kresta, Eds., Wiley, Hoboken, NJ, USA, 2004.

[3] J. Baldyga and J. R. Bourne, "Interactions between mixing on various scales in stirred tank reactors," *Chemical Engineering Science*, vol. 47, no. 8, pp. 1839–1848, 1992.

[4] J. Badyga, J. R. Bourne, and S. J. Hearn, "Interaction between chemical reactions and mixing on various scales," *Chemical Engineering Science*, vol. 52, no. 4, pp. 457–466, 1997.

[5] S. M. Cox, M. J. Clifford, and E. P. L. Roberts, "A two-stage reaction with initially separated reactants," *Physica A*, vol. 256, no. 1-2, pp. 65–86, 1998.

[6] M. J. Clifford, E. P. L. Roberts, and S. M. Cox, "The influence of segregation on the yield for a series-parallel reaction," *Chemical Engineering Science*, vol. 53, no. 10, pp. 1791–1801, 1998.

[7] S. M. Cox, "Chaotic mixing of a competitive-consecutive reaction," *Physica D*, vol. 199, no. 3-4, pp. 369–386, 2004.

[8] P. V. Danckwerts, "The definition and measurement of some characteristics of mixtures," *Applied Scientific Research, Section A*, vol. 3, no. 4, pp. 279–296, 1952.

[9] P. V. Danckwerts, "The effect of incomplete mixing on homogeneous reactions," *Chemical Engineering Science*, vol. 8, no. 1-2, pp. 93–102, 1958.

[10] O. Levenspiel, *Chemical Reaction Engineering*, Wiley, New York, NY, USA, 2nd edition, 1972.

[11] S. Bhattacharya, *Performance improvement of stirred tank reactors with surface feed [Ph.D. thesis]*, University of Alberta, Edmonton, Canada, 2005.

[12] J. Baldyga and R. Pohorecki, "Turbulent micromixing in chemical reactors—a review," *The Chemical Engineering Journal and The Biochemical Engineering Journal*, vol. 58, no. 2, pp. 183–195, 1995.

[13] J. Villermaux and L. Falk, "A generalized mixing model for initial contacting of reactive fluids," *Chemical Engineering Science*, vol. 49, no. 24, pp. 5127–5140, 1994.

[14] R. O. Fox, "On the relationship between Lagrangian micromixing models and computational fluid dynamics," *Chemical Engineering and Processing*, vol. 37, no. 6, pp. 521–535, 1998.

[15] R. O. Fox, *Computational Models for Turbulent Reacting Flows*, Cambridge University Press, Cambridge, UK, 2003.

[16] F. J. Muzzio and M. Liu, "Chemical reactions in chaotic flows," *Chemical Engineering Journal and the Biochemical Engineering Journal*, vol. 64, no. 1, pp. 117–127, 1996.

[17] M. J. Clifford, "A Gaussian model for reaction and diffusion in a lamellar structure," *Chemical Engineering Science*, vol. 54, no. 3, pp. 303–310, 1999.

[18] M. J. Clifford and S. M. Cox, "A simple model for a two-stage chemical reaction with diffusion," *IMA Journal of Applied Mathematics*, vol. 63, no. 3, pp. 307–318, 1999.

[19] M. J. Clifford, S. M. Cox, and E. P. L. Roberts, "Lamellar modelling of reaction, diffusion and mixing in a two-dimensional flow," *Chemical Engineering Journal*, vol. 71, no. 1, pp. 49–56, 1998.

[20] M. J. Clifford, S. M. Cox, and E. P. L. Roberts, "Reaction and diffusion in a lamellar structure: the effect of the lamellar arrangement upon yield," *Physica A*, vol. 262, no. 3-4, pp. 294–306, 1999.

[21] M. J. Clifford, S. M. Cox, and E. P. L. Roberts, "The influence of a lamellar structure upon the yield of a chemical reaction," *Chemical Engineering Research and Design*, vol. 78, no. 3, pp. 371–377, 2000.

[22] I. Hecht and H. Taitelbaum, "Perturbation analysis for competing reactions with initially separated components," *Physical Review E*, vol. 74, no. 1, Article ID 012101, 2006.

[23] M. Sinder, "Theory for competing reactions with initially separated components," *Physical Review E*, vol. 65, no. 3, Article ID 037104, pp. 037104/1–037104/4, 2002.

[24] M. Sinder, J. Pelleg, V. Sokolovsky, and V. Meerovich, "Competing reactions with initially separated components in the asymptotic time region," *Physical Review E*, vol. 68, no. 2, Article ID 022101, 4 pages, 2003.

[25] H. Taitelbaum, B. Vilensky, A. Lin, A. Yen, Y. E. L. Koo, and R. Kopelman, "Competing reactions with initially separated components," *Physical Review Letters*, vol. 77, no. 8, pp. 1640–1643, 1996.

[26] S. Cornell and M. Droz, "Exotic reaction fronts in the steady state," *Physica D*, vol. 103, no. 1–4, pp. 348–356, 1997.

[27] S. M. Cox and M. D. Finn, "Behavior of the reaction front between initially segregated species in a two-stage reaction," *Physical Review E*, vol. 63, no. 5 I, pp. 511021–511027, 2001.

[28] H. S. Fogler, *Elements of Chemical Reaction Engineering*, Prentice Hall, Upper Saddle River, NJ, USA, 3rd edition, 1999.

[29] S. I. A. Shah, L. W. Kostiuk, and S. M. Kresta, "The effects of mixing, reaction rates and stoichiometry on yield for mixing sensitive reactions, Part II: design protocols," *International Journal of Chemical Engineering*. In press.

Research Article

Characterization of Minimum Impeller Speed for Suspension of Solids in Liquid at High Solid Concentration, Using Gamma-Ray Densitometry

Rouzbeh Jafari, Philippe A. Tanguy, and Jamal Chaouki

Department of Chemical Engineering, École Polytechnique de Montréal, P.O. Box 6079, Station Centre-Ville, Montreal, QC, Canada H3C 3A7

Correspondence should be addressed to Jamal Chaouki, jamal.chaouki@polymtl.ca

The successful design and operation of Liquid-Solid (LS) and Gas-Liquid-Solid (GLS) stirred tank reactors requires an accurate determination of the level of solid suspension needed for the process at hand. A poor design of the stirred tank to achieve optimum conditions and maintain the system under these conditions during operation may cause significant drawbacks concerning product quality (selectivity and yield) and cost. In this paper, the limitations of applying conventional measurement techniques for the accurate characterization of critical impeller speed for just off-bottom suspension (N_{JS}) at high solid concentrations are described. Subsequently, the Gamma-Ray Densitometry technique for characterizing N_{JS} is introduced, which can overcome the limitations of previous experimental techniques. The theoretical concept of this method is explained, and experimental validation is presented to confirm the accuracy of the Gamma-Ray Densitometry technique. The effects of clearance, scale, and solid loading on N_{JS} for several impellers are discussed. Experimental N_{JS} values are compared with correlations proposed in the literatures, and modifications are made to improve the prediction. Finally, by utilizing the similarity to the incipient movement of solid particles in other systems, a theoretical model for N_{JS} prediction is presented.

1. Introduction

Maximum solid-liquid contact is essential for the optimization of many chemical processes. Contact modes include solid dispersion, dissolution, leaching, crystallization, precipitation, adsorption, ion exchange, solid-catalyzed reaction, and suspension polymerization. In many processes (especially dissolution, leaching and solid-catalyzed reactions), the main objective of liquid-solid contacting is to maximize the surface area of the solid particles available for reaction or transport processes (heat and/or mass transfer). This can only be achieved by optimizing hydrodynamic conditions where solid particles move freely and do not accumulate at any point in the vessel. Under these conditions, the system can be described to be under "just off-bottom suspension or just-suspended" conditions.

Inside a reaction vessel, solid particles in a liquid medium tend to settle towards the bottom as their density is usually higher than that of the liquid. In this scenario, an external force is necessary to lift the solids and retain them in a suspended state. Depending on the unit operation at hand, this force can be provided through various techniques such as agitation in stirred tanks or gas sparging in three-phase fluidized beds. The energy input creates a turbulent flow field that lifts the solid particles from the vessel base and disperses them throughout the liquid. Solids pickup from the vessel base is achieved by a combination of (1) the drag and lift forces of the moving fluid on the solid particles and (2) the burst of turbulent eddy created in the flow bulk.

Stirred tanks have been used in the chemical process industry for decades. The energy input provided by the rotating impeller enhances mass and heat transfer rate compared to other types of contactors. For liquid-solid (LS) stirred tank, mass transfer rate is increased by increasing impeller speed. However, two contrasting trends can be observed; at impeller speeds lower than just-suspended condition, mass

transfer clearly increases with higher impeller speeds. On the other hand, the observed rate may not increase significantly with impeller speed or mixing intensity beyond the just-suspended condition. This indicates that operating at just-suspended conditions is the minimum requirement for processes where mass transfer is controlling the process [1]. It is, therefore, important to define what level of suspension is required versus the desired process results. While just-suspended condition is optimal condition for many processes, a high degree of suspension is required for crystallization or slurry feed system. For the dissolution of highly soluble solids, partial suspension is sufficient. Failure to operate at optimal condition due to uncertainty in predicting the impeller speed required to achieve and maintain the just-suspended condition leads to considerable drawbacks. If a mixing system operates above the minimum speed for solid suspension, the degree of suspension will be improved and the mass transfer rate will be enhanced. Higher speed, however, yields a higher turbulence shear rate, which for some processes, that is, biological processes, may cause undesirable particle attrition or cell mortality. Obviously, there is also a practical economic limit on the maximum speed of agitation. For example, in the gold cyanidation process, where a high concentration slurry (up to 50% wt/wt) is processed to achieve a high production rate of gold, operating at an impeller speed lower than the just-suspended condition will generate fillets in the vessel, thereby detrimentally affecting the reaction selectivity and yield. In some cases, a small proportion of particles may be allowed to accumulate in corners or on the bottom in relatively stagnant regions to form fillets. This condition may offer advantages from the practical point of view because of a large savings in energy consumption compared to what is required for complete suspension. This energy savings may be more than the effect of the loss of active solids. However, it is important to quantitatively define what portion of solid is left unsuspended. On the other hand, overprediction of N_{JS} causes significant economical drawbacks. For example, in the gold cyanidation process, 5 to 50% overprediction of N_{JS} leads to \$150,000 to \$2,200,000/year in supplementary energy expenses. Also, the added cost for the purchase, installation, and maintenance of larger mechanical parts should be considered. This extra capital and operating costs cannot be compensated by additional gold recovered from the process. Furthermore, comprehensive knowledge about the effect of different factors (physical properties, geometrical and operational parameters) is central to the proper design and operation of LS-stirred tank reactors. Although characterizing N_{JS} was the subject of much research and many published scientific contributions, the subjectivity of conventional measurement techniques leads to a high degree of uncertainty in the prediction of N_{JS}. It was shown that a significant variance appears in the prediction of N_{JS}, and there is no correlation with universal validity. Bohnet and Niesmak [2] calculated the critical impeller speed of the suspension using nine correlations and found that the reported values were in the range of -56% to $+250\%$ from their own values. In addition, only a few studies deal with high concentration solid suspensions in stirred tanks and current

experimental methods show their limitations in terms of accuracy. For the design of concentrated systems, it is important to develop more reliable techniques for characterizing just-suspended speed. In this work, the Gamma-Ray Densitometry technique is proposed. It will be shown that this new technique minimizes the subjectivity of N_{JS} characterization techniques and is not affected by the mixing system.

2. Background

At constant loading of solid particles, if the impeller speed is increased incrementally, bottom particles become increasingly suspended and the fraction of settled solids decreases. Upon reaching a specific impeller speed, all settled particles are continuously in motion on the tank bottom before becoming suspended. The bottom motion prior to suspension may involve a fraction of the settled solids coming to a brief rest before departing from the bottom into suspension. With a slight increase in impeller speed, this stoppage of solid particles is eliminated and particle-bottom contact time is shortened. The impeller speed at which this phenomenon occurs is defined as the critical impeller speed required for solid suspension (N_{JS}). The earliest and most common method for characterizing N_{JS} is the visual technique. Zwietering [3] proposed a visual observation method to determine N_{JS}. The motion of the solid particles was observed through the wall and bottom of transparent tank using a mirror placed directly underneath it. N_{JS} was defined as the impeller speed at which no solids remain on the tank bottom for more than 1 or 2 seconds. This method allows determining N_{JS} with an accuracy of $\pm 5\%$ for the same observer.

However, only with careful observation it is possible to achieve $\pm 5\%$ reproducibility in a diluted suspension. Furthermore, visual methods require a transparent vessel, which is feasible for most laboratory-scale studies, but rather complicated for large-scale vessels. To overcome the limitations of the visual technique, other methods have been proposed. In Table 1, experimental methods for characterizing N_{JS} have been listed. Their limitations and advantages have been explained and they are ranked based on their accuracy and applicability. Those experimental techniques were applied to numerous empirical and semiempirical investigations on solid suspension, whose results were critically reviewed in the literature (e.g., [6, 12]). To provide more insight about the suspension mechanism, researchers have introduced theoretical models to predict N_{JS}. These models are generally classified into different categories. The first category describes particle pickup by turbulent eddies [13], while with the second category, particles are assumed to be picked up by fluid flow [14]. There also exists a third category in which a suspension model is based on analogy to other multiphase systems, like minimum fluidization of the gas-liquid-solid fluidized beds [15, 16]. Theoretical methods are listed and explained in Table 2. Although these theoretical methods are applicable for a first estimation of operating conditions, most of these methods still require empirical characterization of some parameters. There have been few efforts to predict N_{JS} by means of commercial CFD codes

TABLE 1: Experimental methods for characterizing N_{JS} (adapted from [1, 4]).

Method proposed by	Concept	Advantages	Disadvantages	Applicability	Accuracy
Zwietering [3]	Visual observation of particles that do not rest at the vessel bottom for more than 1-2 sec	Simplicity, nonintrusive	Not applicable for opaque system, high uncertainty for high solid loading systems, careful and skilled observation is necessary	1	3
Mersmann et al. [5]	Visual observation of the height of the slurry compared to the total height	Nonintrusive, Simplicity	Small particles suspended, come to the top of the tank, results in vanishing interface while larger particles are still resting at the bottom	1	5
Rewatkar et al. [6]	Variation of impeller power consumption by increasing the amount of solid suspended	Nonintrusive, can be used for opaque systems	Requires accurate measurement of power consumption, expensive for large scale vessels, the criteria are not clear	3	5
Rewatkar et al. [6]	Variation of liquid phase mixing time by increasing amount of solid suspended	Can be used for opaque system	Requires accurate measurement of mixing time, not applicable for large-scale vessels, the criteria are not clear, in high solid loading or three-phase systems, accurate measurement of mixing time is challenging	3	5
Rewatkar et al. [6]	Decrease in count rate recorded from radioactive tracer inside the vessel by increasing impeller speed	Nonintrusive can be used in opaque system	Decrease in recorded count rate could be because of tracer dispersion not just off-bottom suspension The criteria are not clear	5	5
Musil et al. [7]	Discontinuity in solid concentration close to the bottom of the vessel by increasing impeller speed	Can be used in opaque system	Intrusive, accurate measurement of concentration is challenging	3	4
Chapman et al. [8]	Peak in solid concentration measured close to the bottom of the vessel by increasing impeller speed	Can be used in opaque system	Intrusive accurate measurement of concentration is difficult	3	4
Buurman et al. [9]	Use of Doppler effect at vessel bottom	Independent of material and scale, nonintrusive	Applying the technique is challenging, ultrasound sensor must be installed inside the vessel otherwise signals are scattered by wall	4	2
Micale et al. [10, 11]	Change in the pressure recorded at the bottom of the vessel by increasing impeller speed	Independent of material, nonintrusive	Proper selection of pressure recording port is important, method proposed to eliminate effect of dynamic pressure head is not accurate	2	3

Accuracy: 1: most accurate, 5: least accurate, Applicability: 1: easiest to apply, 5: most difficult to apply.

[17–21]. CFD tools could provide a valuable opportunity for studying solid suspension phenomena and characterizing N_{JS} but the validity of computational methods in highly concentrated turbulent flow is still questionable.

Prediction of just suspended speed was the subject of few CFD studies [19, 21–23]. CFD simulations, if successfully applied, can be more quantitative and predictive than the empirical or theoretical correlations.

Lea [23] used a CFD-assisted design approach to study the effectiveness of mixing tank geometrical configurations to suspend particles. He developed a design heuristic that can be applied in process industries. Murthy et al. [19] used CFD simulation to study the effect of different parameters on just suspended speed in LS and GLS systems. Their study covers solid loading up to 15% (wt/wt). Fletcher and Brown [22] studied the influence of the choice of turbulence

TABLE 2: Theoretical methods for predicting N_{JS}.

Reference	Concept	Remarks
Kolar [29]	Energy necessary to suspend particles equals the energy dissipated by the particle moving at its terminal velocity in a still fluid	In a turbulent fluid, the settling velocity of a particle is different from that in a still fluid. Very simple model, unable to precisely predict N_{JS} Assumptions are more likely similar to homogenous suspension rather than just-suspended conditions
Baldi et al. [13]	Particles are picked up and kept suspended by turbulent eddies	Cannot describe the effect of viscosity nor the effect of solid concentration. Cannot describe why the impeller that creates mass circulations (PBT) is more effective for suspending particles than impeller which creates a lot of turbulence
Narayanan et al. [30]	Balance of vertical forces acting on particles	Assumption of no slip between solid and liquid and homogenous distribution of solid particles is questionable. Proposed for very diluted solid concentrations
Subbarao and Taneja [31]	Balance of forces acting on particles	Particle settling velocity was estimated from a correlation for the porosity of a liquid fluidized bed as a function of liquid velocity
Ditl and Rieger [32]	Same concept as Baldi et al. [13], solid particles are picked up by different sizes of eddies	Cannot describe the effect of viscosity nor the effect of solid concentration Cannot describe why the impeller that creates mass circulations (PBT) is more effective for suspending particles than impeller which creates a lot of turbulence
Musil and Vlk [33]	Balance between liquid and particle kinetic energy	The approach followed by them was rejected by Ditl and Rieger [34] because of mathematical mistakes
Ayazi Shamlou and Zolfagharian [14]	Proposed a model for estimation necessary conditions for incipient motion of solid particles based on average velocity of the liquid near the bottom of the vessel and forces acting on particles, like lift, drag, buoyancy, and weight resting at the bottom of the vessel	Model does not need any experimental adjustment, but the parameter describing solid arrangement is unknown
Molerus and Latzel [15, 35]	Solid suspension governed by two different mechanisms based on Archimedes number. Region responsible for solid suspension is the wall boundary layer of the vessel	Requires accurate correlation for predicting shear rate at the boundary layer of the vessel
Wichterle [36]	Difference between the terminal settling velocity of particle and velocity of the liquid	The ratio between N_{JS} and settling velocity allows predicting N_{JS} easily
Mersmann et al. [5]	Power input dissipated by two phenomena: consumption of power to avoid settling and generating discharge flow for suspension	Values for N_{JS} calculated by this method are highly underpredicted compared to experimental data. This could be because the correlations for fluctuating velocity at the bottom of the vessel are not accurate

models on the prediction of solid suspension by means of commercial CFD codes. Kee and Tan [18] presented a new CFD approach for predicting N_{JS} and characterized effect of D/T and *C/T* on N_{JS}. Ochieng and Lewis [20] provided qualitative and quantitative insight into solid suspension by simultaneous investigations using CFD and LDV. In their work suspension studies have been carried out in a Nickel precipitation process and best simulation results were obtained for solid loading lower than 6% [24]

studied three different criteria to determine N_{JS} based on CFD simulation results. Comparing simulation results with empirical correlation predictions is reasonable, yet they suggested examining solid velocity at the bottom of the vessel as proper criteria [25] provided a complete review on the CFD simulation of solid suspension in a stirred tank. They have explained important parameters to achieve accurate simulation and discussed different models and simulation approaches. Although extensive efforts have been

1: Impeller   5: Radioactive tracer
2: Torque meter   6: Computer
3: DC motor   7: Detector
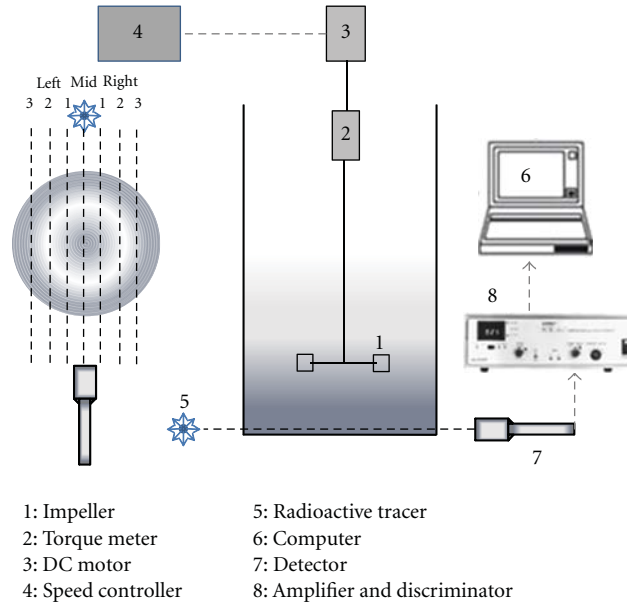4: Speed controller 8: Amplifier and discriminator

FIGURE 1: Experimental setup and gamma-ray densitometry data acquisition system.

made to apply CFD simulation to predict hydrodynamic parameters and the state of solid suspension in solid-liquid and gas-liquid-solid stirred tank reactors, it is commonly believed that turbulent models, which are being used for modeling a turbulent flow field in stirred tank reactors, have considerable uncertainties even in the single phase. Recently, [26] demonstrated that even in the single phase with current turbulent models, CFD results show errors up to 20% of the time. There are numbers of CFD works for liquid-solid stirred tank reactors, but they rarely have been validated for high solid concentration.

3. Materials and Methods

3.1. Experimental Setup. Experiments were conducted in 14 L and 58 L transparent polycarbonate cylindrical-stirred vessels with standard baffles, an open top and a flat bottom (Figure 1). Three different impellers were tested, mounted on a central shaft, namely, a six-blade Rushton turbine (RT), a concave blade turbine (CBT), and a four-blade pitched blade turbine in down-pumping mode (PBT-D). The vessel, impeller dimension, and geometrical details of the mixing system are given in Table 3. Water was used as the liquid phase and sand as the solid phase (density of 2650 kg/m^3). Particle size distribution of sand was measured by the Horiba laser scattering particle size distribution analyzer (model: LA-950). The mean particle size was 277 μm. The operating slurry height was set equal to the vessel diameter.

3.2. Methods. The use of radioactive sources (radioisotopes) to characterize the fluid dynamics and hydrodynamics of single-phase and multiphase systems has an extensive history. A detailed review of these methods can be found in Chaouki et al. [27]. In the present work, we use the concept of densitometry described and applied above [27, 28] to

TABLE 3: Design details of a mechanically stirred tank.

Parameter	Value
Vessel diameter (m)	0.2
H/T	1
Baffle with	T/10
Number of baffles	4
Material of construction	Plexiglass
Geometry	Cylindrical with flat bottom
Impeller clearance from the bottom	Varies between 0.5T to 0.2T
Impellers	RT (6 blade), D:T/3, W/D: 1/5 CBT (6 blade), D:T/3, W/D: 1/5 PBT (4 blade @ 45°), D:T/3, W/D: 1/5

propose a new technique for characterizing N_{JS}. If a radioactive source is placed on one side of the vessel and a detector on the other side, based on the material between them the detector receives a specific amount of gamma ray. This phenomenon can be modeled by the Beer-Lambert's law that describes the decay in intensity of the emitted gamma ray by passing through the medium: $I = I_0 \cdot \exp(-\rho\mu l)$. Changes in the density or phase of the medium lead to corresponding changes in the gamma-ray intensity recorded by the detector. In multiphase systems, the ray intensity is related to the volume fraction of each phase. This gamma-ray emission-obstruction-detection framework could be the basis of a useful tool for characterizing solid suspension in stirred tanks.

In practice, a source of gamma ray (a 2 mm glass bead filled with scandium oxide) was activated in the Slowpoke nuclear reactor of Ecole Polytechnique of Montreal. The source activity was between 100–200 μCi, and the half-life

time of the tracer was 84 days. The tracer was placed in the holder where it was completely shielded by lead. Emitted gamma rays from this source were collimated by lead support. It passed through a 5 mm hole on the protection shield and went through the vessel. A NaI scintillation detector (Teledyne Isotope, Model S-1212-I) was placed on the other side of the vessel and coupled to an amplifier (EG&G ORTEC Model: 925-SCINT) and a data acquisition system (TOMO MSC plus-17)—See Figure 1. Both tracer and detector were positioned in order to be able to scan the region about 0.5 cm from the bottom of the vessel. The signals were recorded for 2 minutes with a 200 msec sampling time at each impeller speed (varied between 0 to 1000 rpm with different step sizes). Counts were recorded at each impeller speed, and they were converted and processed by home-made codes. It was verified that changing the sampling time and recording period as well as the background noise did not alter the experimental results. The original recorded count rates were related to the solid volume fraction. For this purpose, the same region was scanned without solids (pure water (1)). According to this procedure, the following equations can be established. Equation (4) relates the measured intensity to solid hold-up

$$I_{\text{water only}} = I_0 \exp(-\rho_{\text{water}}\mu_{\text{water}}L) \cdot \exp(-A), \qquad (1)$$

$$I_{\text{liquid-solid}(N=0)} = I_0 \exp(-\rho_{\text{water}}\mu_{\text{water}}L(1 - \epsilon_{s,0})$$
$$-\rho_{\text{solid}}\mu_{\text{solid}}L(\epsilon_{s,0})) \cdot \exp(-A), \qquad (2)$$

$$I_{\text{liquid-solid}(N>0)} = I_0 \exp(-\rho_{\text{water}}\mu_{\text{water}}L(1 - \epsilon_s)$$
$$-\rho_{\text{solid}}\mu_{\text{solid}}L(\epsilon_s)) \cdot \exp(-A), \qquad (3)$$

$$\epsilon_s = \epsilon_{s,0} \frac{\ln\left(I_{\text{liquid-solid}(N>0)}/I_{\text{water only}}\right)}{\ln\left(I_{\text{liquid-solid}(N=0)}/I_{\text{water only}}\right)} \qquad (4)$$

N_{JS} was also characterized by two conventional techniques for comparison: the visual technique and the pressure gauge technique. For characterizing N_{JS} with the visual technique, the vessel base was illuminated and the bottom was observed while increasing the impeller speed with a low step size of 10 rpm. N_{JS} was determined according to the Zwietering criteria. For characterizing N_{JS} by the pressure gauge technique, a calibrated pressure transducer (Lucas Schaevitz Model P3061-20wg) was connected to the vessel bottom. LabView software (National Instruments) was used for data acquisition. Signals were recorded with a sampling time of 1 sec for 5 minutes. The recorded signals were then processed based on the procedure explained by Micale et al. [10, 11]. In the experiments, various solid loading and impeller clearance conditions were investigated. The effect of the gas flow rate on solid suspension was studied as well. Different scale-up procedures were evaluated to identify which procedure may provide proper scale-up conditions. All experiments were repeated at least three times to ascertain the reproducibility. All experiments have been done in ambient conditions.
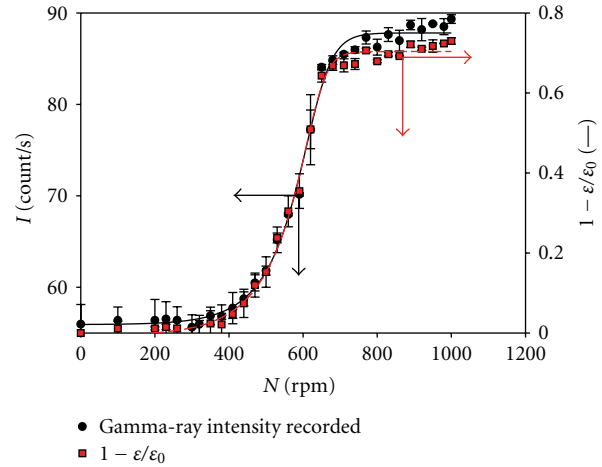

Figure 2: Variation of recorded count rate and average solid hold-up by increasing impeller speed at the bottom of the vessel. Impeller: RT, X: 20%, d_p: 277 μm, C/T: 0.33.

4. Results and Discussion

4.1. Main Features of Solid Suspension. Typical results of the densitometry technique are shown in Figure 2. This figure shows variation of count rate recorded by detector versus impeller speed. At $N = 0$ (rpm), when all the solid particles settled on the bottom of the vessel, the recorded intensity by the detector $I_{N=0}$ is constant. By increasing the impeller speed and as solid particles in the scanning region commence motion and are lifted by the liquid, the recorded intensity increases. At higher impeller speeds, when all the solid particles are experiencing random motion and no solid rests on the bottom of the vessel, the recorded intensity is expected to stabilize. In practice, a slight intensity increase can be observed, which is related to the change in solid particle speed and a decrease of the residence time of the solid in the scanning zone.

Solid hold-up can be calculated from recorded count rates by employing (1), (2), (3), and (4). Figure 2 also illustrates the variation of solid hold-up at the bottom of the vessel by increasing impeller speed.

As many researchers have mentioned (e.g., [7]) solid concentration at the bottom of the vessel at just-suspended conditions exhibits a discontinuity. As shown in Figure 2, based on densitometry data, a discontinuity in solid concentration can be noticed at the bottom of the vessel by increasing impeller speed and passing N_{JS}. The starting point of this discontinuity is considered as N_{JS}. ϵ/ϵ_0 represents the normalized solid volume fraction at the bottom of the vessel. By plotting $1 - \epsilon/\epsilon_0$ vsersus impeller speed the discontinuity in solid concentration at the bottom of the can be identified clearly. As illustrated in Figure 2, for low impeller speed, all solid particles rest on the bottom of the vessel base. Upon increasing impeller speed, a fraction of the solid particles commences lifting and reaches suspension at a certain height. Partial suspensions correspond to the situation where some solids rest on the bottom of the tank. Since the particles are
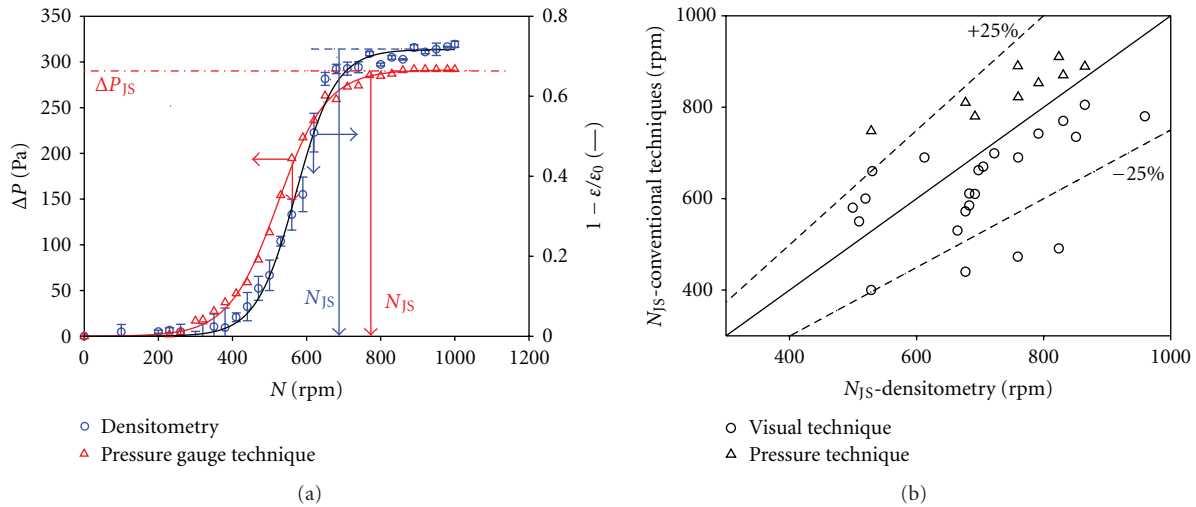
FIGURE 3: (a) Comparison of gamma-ray densitometry technique with pressure technique. (b) Comparison of gamma-ray densitometry technique with two conventional methods.

in constant contact with the bottom of the vessel, not all the surface area of particles is available for chemical reaction, mass, or heat transfer.

As the impeller speed is increased, the partially suspended solid yields three distinct zones: a clear liquid layer at the top, a nonsuspended solid layer at the bottom; and a region with a suspended mixture in between. The relative size of the three zones depends on how easily particles can be picked up by the fluid and how efficiently the impeller is agitating the liquid. Increasing impeller speed results in conditions where no particle stagnates at the bottom of the vessel. Although virtually all solid particles are suspended, the system is not yet homogeneous, with a clear interface between the solid-rich and solid-lean regions. By increasing impeller speed beyond the just-suspended condition, the degree of homogeneity increases.

4.2. Comparing Densitometry with the Pressure-Gauge and Visual Observation Techniques.
Results of the gamma-ray densitometry technique were compared with those of the two conventional techniques in Figures 3(a) and 3(b).

As illustrated in Figure 3(a), the pressure-gauge technique quite systematically overestimates the just-suspended speed compared to the densitometry technique. This could be related to the fact that the method for eliminating the dynamic head effect is not valid for high solid concentration and for axial flow impellers. As discussed by Micale [10, 11], the dynamic head effect can perturb experimental data significantly. At low solid loading, N_{JS} determined by the pressure-gauge technique, and the visual method are in good agreement. Differences in N_{JS} values obtained using the different methods do not exceed 5%. This difference is well within the range of experimental uncertainty. However, for high solid loading and special cases like an axial flow impeller or low off-bottom impeller clearance, both conventional techniques exhibit larger differences compared to the new method.

4.3. Effect of Impeller Type.
The degree of solid suspension in stirred tanks is strongly related to the specific power, pumping capacity and flow pattern. The main source of power dissipation and pumping is the impeller rotation. Researchers have studied a variety of impellers for solid suspension. The choice of a given impeller to achieve maximum solid suspension with minimum power requirement is the key for the technical and economic viability of the process. N_{JS} is affected significantly by the region of the vessel where the final portion of settled solid particles is brought into suspension. This region varies for different impeller types and vessel geometry.

Three types of impellers have been studied in this paper: Rushton Turbine (RT), Pitched Blade Turbine in down-pumping mode (PBT-D), and Concave Blade Turbine (CBT). Axial flow impellers (like PBT-D) are more favorable for liquid-solid mixing processes since they can provide a good quality of solid suspension at lower impeller speed compared to radial flow impellers [1, 37], but their instability for being applied in a three-phase system (Gas-liquid-solid) leads us to study RT and CBT as well.

There are two zones on the tank base where recirculation loops are weak: underneath the impeller and at the junction of the tank base and wall. As illustrated in Figure 4(a) for the Rushton turbine, the final settled solids were suspended from underneath the impeller at the centre of the tank. At the same impeller speed, more solids were suspended from other regions compared to the centre. There are many characterization studies regarding the flow pattern of radial and axial flow impellers (e.g., [38–40]). The radial flow generated with radial flow impeller first hits the wall and change direction, moving upward and downward [40, 41]. Downward jet hits bottom of the vessel and is redirected to the center. Thus, the radial flow impeller sweeps particles toward the center of the vessel bottom and lifts them from an annulus around the center of the vessel bottom. As illustrated in Figure 4(a), solid concentration is lower at third scanning
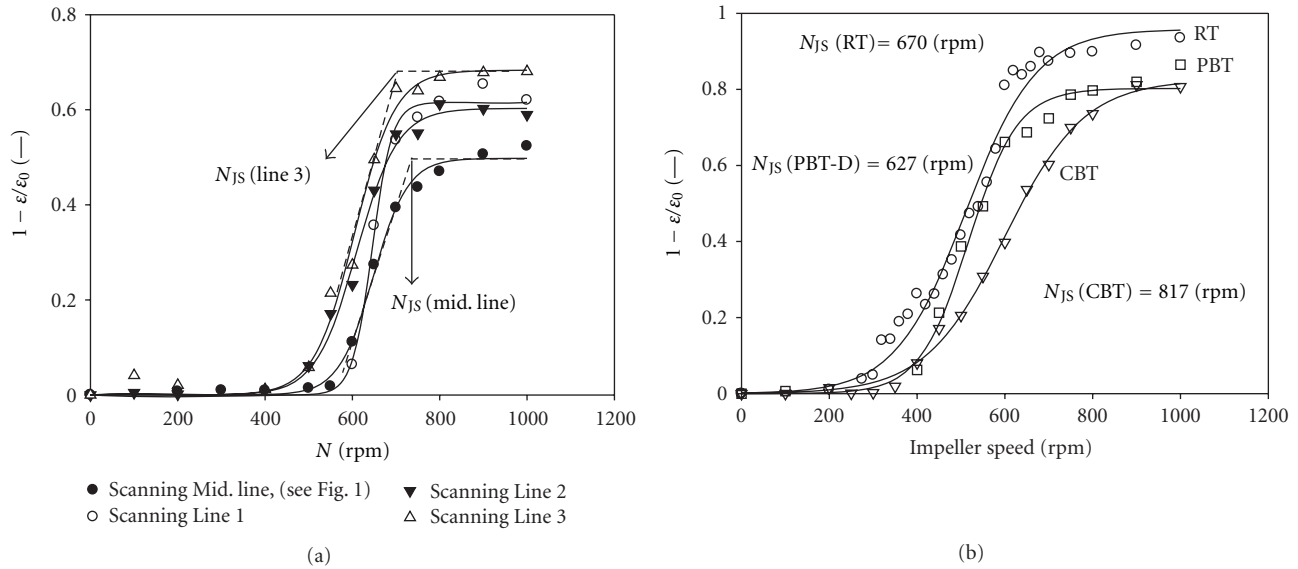
FIGURE 4: (a) Solid hold-up variation at the bottom of the vessel by increasing impeller speed, for 4 different scanning lines, impeller: RT, X: 30%, dp: 277 μm, C/T: 0.33. (b) Comparison of just-suspended speed for different impellers. X: 10% wt/wt, C/T: 0.33.

line, which corresponds to periphery of the vessel, compared to Mid. line.

On the other hand, axial flow impellers tend to suspend solid particles from the periphery of the vessel bottom. The flow generated by axial flow impeller (in down pumping mode) first hits the bottom of the vessel. It is then redirected to the wall and generates liquid wall jet moving upward, which could push solid particle forward and lift them from the periphery of the vessel [39, 42–44]. Wall jet generated by axial flow impeller at the wall is stronger than the one generated by radial flow impeller. Accordingly, it is more difficult to lift particles from the center than drive them toward the corner. The flow pattern of axial flow impellers facilitates suspension in comparison to radial flow impellers. As shown in Figure 4(b), radial flow impellers require higher impeller speeds for solid suspension compared to axial flow impellers.

4.4. Effect of Solid Loading. The effect of solid concentration on N_{JS} has also been studied. As shown in Figure 5(a), higher solid loading causes an increase in required N_{JS}. Upon increasing solid loading, more power is required to suspend large portions of solid. In the plateau region (Figure 5(a)), solid hold-up at the bottom of the vessel is higher at $X = 40$ (% wt/wt) compared to the other case, because the power draw of the impeller is not high enough to disperse the solid. The effect of solid loading on N_{JS} for the various impellers is summarized in Figure 5(b).

4.5. Effect of Impeller Clearance. The effect of the impeller clearance on the just-suspended speed is illustrated in Figures 6(a) and 6(b). Experimental results show that the clearance has a substantial effect on solid suspension especially for PBT-D. Critical impeller speed for off-bottom suspension increases as the clearance is increased. Based on impeller

clearance and type of impeller two radically different flow patterns could be observed: (1) a double-loop shape in which two recirculation loops circulate above and below the impeller and (2) a single-loop shape in which the lower recirculation loop is suppressed. Single-loop flow is typical for axial flow impellers, while double-loop is typical for radial flow impellers. Variation of the flow pattern leads to different solid suspension regimes, which, in turn, affect N_{JS} as discussed previously. Energy transfer from the impeller to the particles is maximized in configurations where the impeller operates close to the tank base [37]. When the impeller is placed close to the vessel base, the particles trapped at the bottom of the vessel underneath the impeller are initially driven toward the corners. This centre-to-corner motion faces minimal resistance while accumulating sufficient momentum to lift into suspension after sliding to the junction of wall and vessel base. By increasing the impeller off-bottom clearance, the stagnant zone underneath the impeller increases, more solid particles are trapped in that region as less momentum is transferred to the particles. A higher speed (more power) is necessary to force particles to move toward the tank corner from where they become suspended. Figure 6(b) illustrates the variation of solid hold-up at the bottom of the vessel for radial flow and axial flow impellers at two different impeller clearances.

The variation of N_{JS} as a function of impeller clearance is shown in Figure 6(b). Sharma and Shaikh [45] have defined three regions in the N_{JS} versus impeller clearance plot. In the first region, N_{JS} remains constant by increasing impeller clearance. This corresponds to the configuration where the impeller is located very close to the vessel base. This phenomenon is related to the local energy dissipated at the tank base, which remains constant when the impeller operates very close to the vessel base [13]. Impellers exhibit a high efficiency for suspending solid particles in this region.
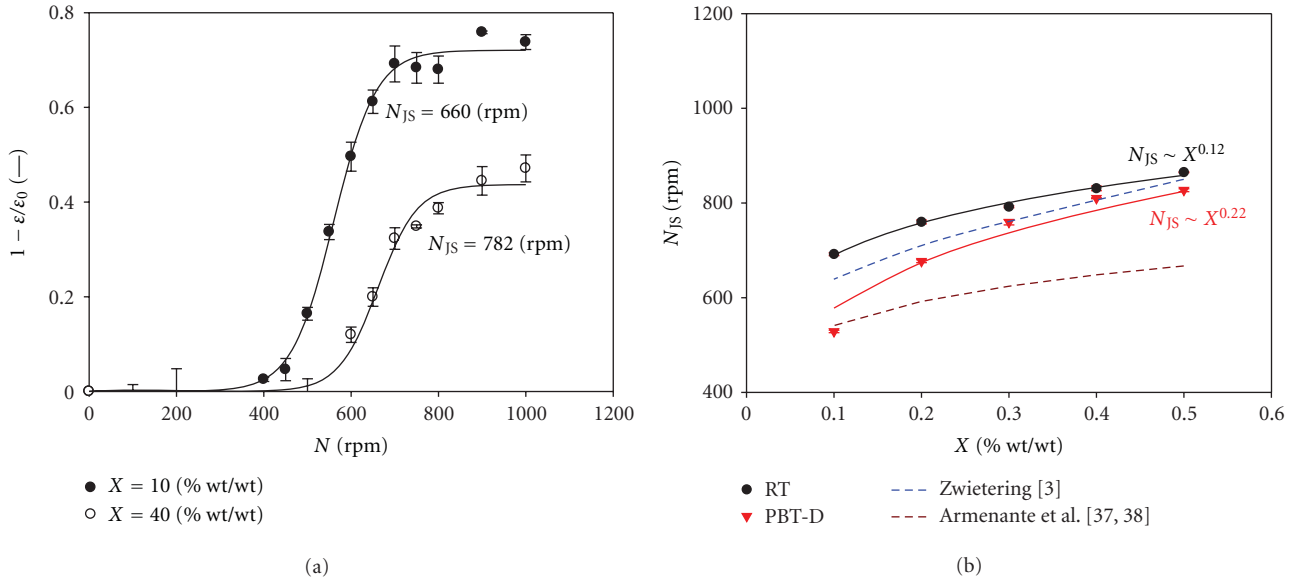
(a)

(b)

FIGURE 5: (a) Variation of solid hold-up at the vessel bottom for low and high solid concentration, impeller: RT, $C/T = 0.33$. (b) Variation of N_{JS} by increasing solid concentration, C/T: 0.33.
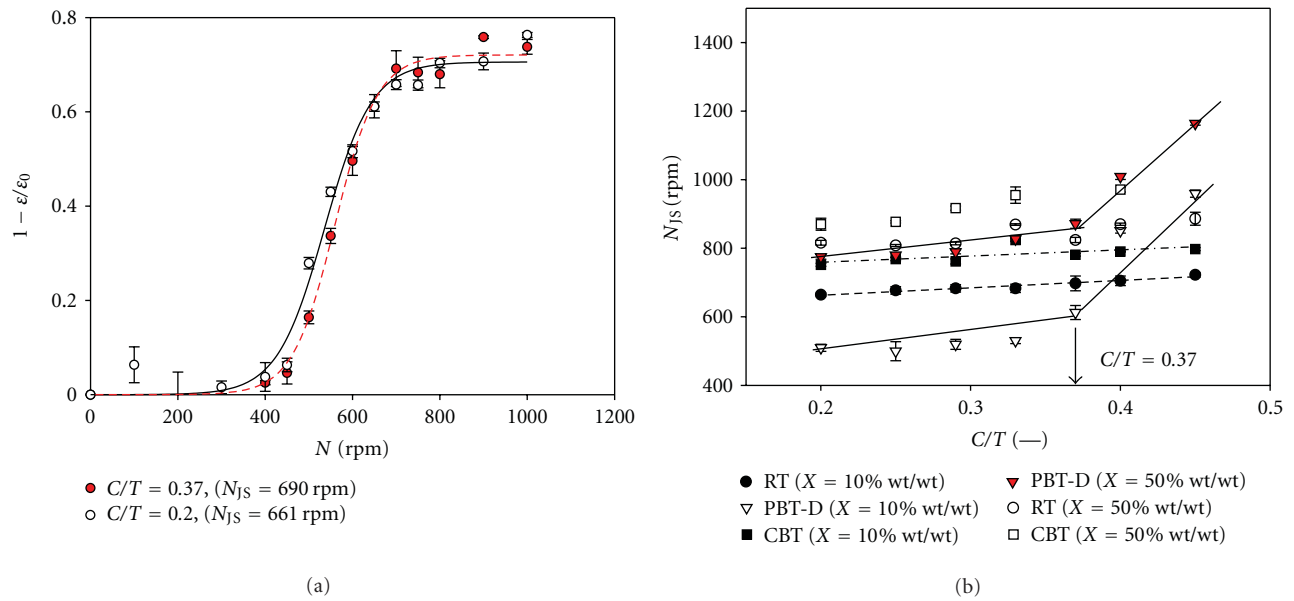

(a)

(b)

FIGURE 6: (a) Variation of solid hold-up at the vessel bottom for low and high impeller clearance, Impeller: RT. (b) Variation of N_{JS} by impeller clearance.

According to Sharma and Shaikh [45], this phenomenon can be observed only in conditions where $C/T < 0.1$. All impellers with very low clearance ($C/T < 0.1$) behave as axial flow impellers and generate a single-eight loop flow. This low-clearance range is the most efficient condition for the impellers.

The difference between N_{JS} for different impellers is related to the amount of power dissipated by the impeller in the vessel. As illustrated in Figure 6(b), at impeller clearances higher than 0.2, N_{JS} increases only slightly with increasing clearance. For radial flow impellers, the flow pattern changes

from single-loop to double-loop [46] and, as discussed before, this changes the mechanism of solid suspension. At higher impeller clearance, the trend is similar. Impeller efficiency decreases by increasing the impeller clearance and, as a result, N_{JS} increases.

For the axial flow impeller, a different behavior is observed. At impeller clearances lower than 0.37, N_{JS} increases slightly as the clearance increases. This is observed for the same reason as with radial flow impellers with the added feature that at clearances higher than 0.37, N_{JS} becomes a strong function of the impeller clearance and the slope in

this region is higher compared to other regions. This increase in N_{JS} is related to the modification of the flow pattern. At clearances higher than 0.37, flow lines originating from the impeller hit the wall before they hit the vessel base. After hitting the wall, they slide downward or upward along the wall. This is typical of the double-eight flow pattern generated by radial flow impellers. It means that the axial flow impeller converts to a radial flow impeller. Such an increase cannot be observed for radial flow impellers (RT and CBT). For radial flow impellers N_{JS} slightly increases since the power available for solid suspension decreases by increasing impeller clearance.

Flow visualization can provide more insight about this phenomenon. As reported in different articles [39, 46, 47], flow transitions occur by increasing impeller clearance for both radial and axial flow impellers. In case of radial flow impeller (RT) transition from double-eight flow patter to single eight happens at $C/T = 0.15$ [46]. When the clearance value is less than or equal to 0.15 T, the strong inclination of impeller stream can be utilized to promote solid suspension from bottom of the vessel. With clearance higher than 0.15T a double eight flow pattern is produced (e.g., [41]) and it was shown that an annular wall jet exists at the wall of the tank. By increasing the impeller clearance, downward wall jet weakens, which explains the higher impeller speed required for off-bottom suspension.

For axial flow impeller, at critical value of impeller clearance, impeller's discharge flow will impinge on the vessel wall rather than the base, which leads to two flow loops in the vessel. The primary flow loop moves upward the wall. The secondary flow loop is characterized by low-velocity, radially inward flow at the base of the vessel, which returns to the impeller via up-flow at the center of the vessel. This flow pattern that is known as reveres flow is not well suited for solid suspension. Different values have been reported for clearance at which axial impeller undergoes a distinct transition. It is strongly affected by type of impeller, D/T ratio, and impeller blade angle [39, 47]. The critical value for PBT-D reported as $C/T = 0.37$ (Figure 6(b)) in this work.

4.6. Comparing with Correlations.

Different correlations have been proposed for predicting N_{JS} (with general format of (5)). However, no correlations with global agreement have been presented so far. As illustrated in Figure 7, the agreement between the prediction and experimental data is not good, which means there is no equation with global validity

$$N_{JS} = Sv^\alpha \left[\frac{g_c (\rho_{s-}\rho_l)}{\rho_l} \right]^\beta d_p^\gamma D^\delta X^\theta. \quad (5)$$

The subjectivity of conventional experimental techniques causes significant differences between predicted values for the same system. Most of the studies resulted in modifications of model parameters in the Zwietering correlation. Values determined for the model parameters (α, β, γ, δ, and θ in (5)) in different studies are almost similar to each other, but in Figure 7 high differences between measured and predicted values can be seen. Therefore, it can be concluded that
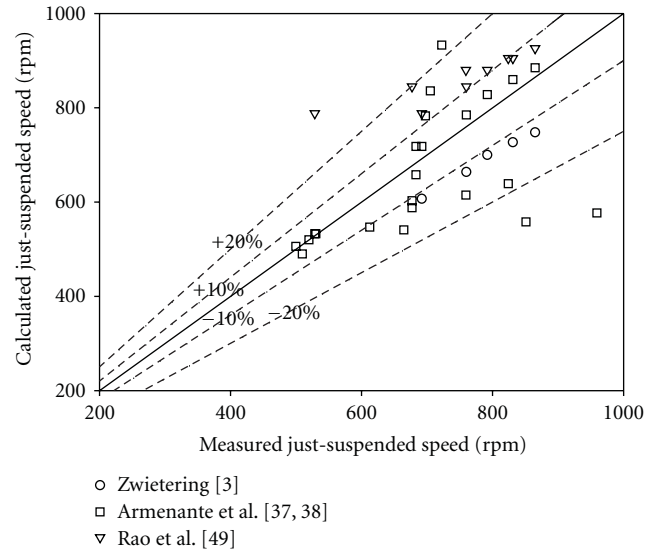

Figure 7: Comparing measured values for just-suspended speed by densitometry technique and predicted ones with different models [3, 37, 49].

Table 4: Values for a and b parameters in equation 3 for different impellers.

Impeller	a	b
RT ($0.1 < C/T$)	4.7	1.1
PBT-D ($0.1 < C/T < 0.35$)	3.47	1.35
CBT ($0.1 < C/T$)	5.4	0.98

the difference between measured values and predicted ones can be related to variations of the dimensionless number S in Zwietering's correlation, which is a function of impeller size, type, and clearance. The value of S changes linearly for radial impellers with increasing impeller clearance. For axial impellers, however, S is significantly affected by impeller clearance beyond the critical point [37]. As a result, the Zwietering correlation can be modified as follows:

$$N_{JS} = \left(a + b\frac{C}{T} \right) v^\alpha \left[\frac{g_c (\rho_{s-}\rho_l)}{\rho_l} \right]^\beta d_p^\gamma D^\delta X^\theta, \quad (6)$$

where $\theta = 0.12$ and 0.22 for RT and PBT-D, respectively, $\delta = -0.85$, $\gamma = 0.2$, $\beta = 0.45$, $\alpha = 0.1$. Values for a and b for different impellers are given in Table 4.

In Figure 7, comparison between predicted values by new model and previous published models [3, 37, 48] are illustrated.

4.7. Effect of Scale.

The effect of scale on N_{JS} was also evaluated by the gamma-ray densitometry technique. For this purpose, experiments were repeated in a larger vessel ($T = 0.4$ m) at different solid concentrations for PBT-D and RT. Results are reported in Figure 8. Different scale-up methods have been proposed for N_{JS}. These scale-up methods are divided into two categories. The first category includes two common approaches used by engineers to scale-up stirred
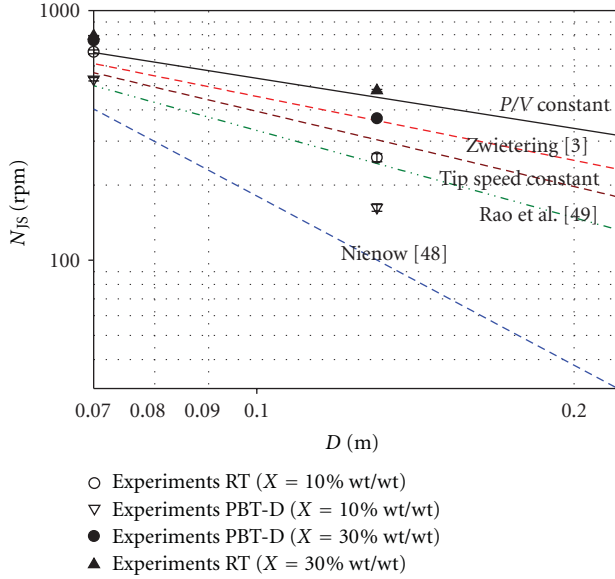
FIGURE 8: Variation of N_{JS} by increasing scale and comparison with different scale-up procedures [3, 48, 49].

FIGURE 9: Variation of ΔN_{JS} in gas-liquid-solid system by increasing gas flow rate: experimental data compared with correlations [50–52].

tanks, that is, constant specific power (P/V) and constant tip speed. The second category includes the scale-up procedure developed based on empirical studies or theoretical concepts. As it was shown in **Figure 8**, applying different scale-up rules leads to significant differences in predicting N_{JS} for larger scale. The reader should note that even a small difference in the exponent of D can have large effect on power consumption when N_{JS} is scaled-up. At high solid loading, for RT, constant P/V seems a promising method but for PBT-D, at same solid loading, tip speed constant may provide better prediction. At low solid loading, the criterion proposed by Nienow [19] is more accurate. Clearly, there is no scale-up procedure with global validity, and appropriate operating condition at large scale, for any mixing system, should be determined independently.

4.8. Application of the Gamma-Ray Densitometry Technique in a Three-Phase System.
Solid suspension is also a key factor in three-phase (GLS) stirred tanks. In a three-phase system, the presence of gas makes the solid suspension a more complex phenomenon. It is common knowledge [1] that the presence of gas decreases the ability of the impeller for solid suspension due to (1) decreasing the power dissipation in the system and (2) affecting the flow pattern of the liquid phase resulting in reducing the liquid-solid slip velocity. Reduction of slip velocity decreases the interphase forces (drag and lift), which are responsible for solid pickup from the vessel base. As illustrated in **Figure 9** by increasing the gas flow rate, a higher impeller speed is required to achieve just off-bottom suspension. The differences between literature data and densitometry technique are considerable.

The use of the visual technique in the presence of gas is more difficult. Gas flow (at very low values) could help the suspension of solid particles, but as reported in the
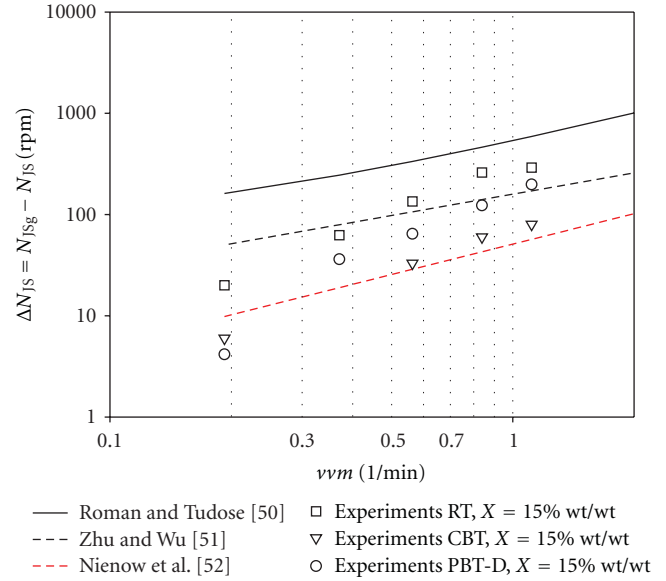
illustrated in **Figure 9**, increasing the gas flow rate directly affects the impeller performance. Accordingly, ΔN_{JS} (= $N_{JSg} - N_{JS}$) increases by increasing the gas flow rate. Radial and axial flow impellers show different behavior in the GLS system. As can be seen in **Figure 9**, performance of CBT is less affected by presence of gas compared to two other impellers.

4.9. Theoretical Prediction of N_{JS}.
The empirical correlations for predicting N_{JS}, which typically take the form of (6), do not facilitate the understanding of the particle suspension mechanism, and theoretical models may provide more insight about the suspension mechanism. The method considered here is based on a force balance acting on a single particle resting at the bottom of the vessel. If we consider a solid particle resting at the bottom of the vessel in liquid, which is under turbulent agitation, by increasing impeller speed particles may start to move by rolling, sliding or lifting. Once particles have lifted up from bottom of the vessel they can be carried away due to the sedimentation-dispersion mechanism. Different forces may act on a single spherical particle when it moves in turbulent media [53]. Based on what is reported in the literatures for solid motion in a stirred tank (e.g., [53]), also by considering an analogy with particle minimum pickup velocity in pipes (e.g., [54, 55]), for the particle resting at the bottom of the vessel and at the moment of dislodgment, the force balance on single particle can be written as

$$\frac{1}{2}A_P\rho_l C_D v_{l\text{-JS}}^2 - gV_P(\rho_s - \rho_l) - \rho_{Sl}gHA_P = 0, \quad (7)$$

which on solving for velocity yields

$$v_{l\text{-JS}} = \sqrt{\frac{4gdp(\rho_s - \rho_l)}{3\rho_l C_D} + \frac{\rho_{ls}Hg}{\rho_l C_D}}. \quad (8)$$

$v_{l\text{-}js}$ is the minimum velocity of fluid required to initiate the just-suspended condition of solid particles. Equation (7) assumes complete "wet-ability" of solids by the liquid and also assumes no slip between particles and fluid. It also assumes spherical particles. Equation (8) describes the minimum liquid velocity required at the bottom of the vessel for pick-up particles at conditions close to just-suspended speed, and it is sensitive to liquid and solid physical properties (dp, ρ_s, ρ_l, ν) and solid concentration (through slurry density and C_D). It is necessary to find an appropriate approach for relating the impeller speed to this minimum liquid velocity. If such a relation exists, it would be possible to determine N_{JS} theoretically for any mixing system by knowing physical properties of the liquid and solid phase and solid loading. In light of the lack of accurate data concerning local liquid velocity at the bottom of the vessel for dense liquid-solid systems [56, 57], local liquid velocity could be determined from circulation time in a single-phase stirred tank. McManamey [58] proposed that the time required for the liquid to circulate once through the flow path should be equal to the maximum length of the circulation path divided by the average liquid velocity in the circulation path ($t = $ (liquid circulation path)/(liquid velocity)). The liquid circulation path can calculated from the geometry of the vessel and impeller type. For a PBT-D impeller the liquid circulation path is *2H+T/2* [59] and for an RT impeller it is *3T-2C* [30]. Accordingly, we will have $t_c = (3T - 2c)/v_l$ for RT and $t_c = 3T/v_l$ for PBT-D. The circulation time can be expressed as a function of impeller speed, liquid properties, and tank and impeller geometry [60]. In stirred tanks, mixing time can be assumed to be some multiple of the circulation time [16, 61, 62]. In this case, accurate correlations for predicting mixing time in dense liquid-solid mixing systems may help to predict the correct N_{JS} values. However, by applying this approach, the calculated N_{JS} values were highly different compared to current experimental results. This leads to the conclusion that the minimum liquid velocity at the bottom of the vessel required for off-bottom suspension is much lower than the average circulation velocity.

Van der Molen and Van Maanen [63], based on investigations with a laser-Doppler velocimeter, have found that the average velocity at the wall of the stirred tank could be calculated as $v_l = C_1 U_{\text{tip}}(D/T)^{7/6}$. At just-suspended conditions, we can rewrite this equation as

$$v_{l\text{-JS}} = C_1 U_{\text{tip-JS}}\left(\frac{D}{T}\right)^{7/6} \text{ or}$$

$$v_{l\text{-JS}} = C_1 N_{JS}\pi D\left(\frac{D}{T}\right)^{7/6}. \tag{9}$$

For the system used in this study, minimum liquid velocity at the bottom of the vessel at just-suspended condition ($v_{l\text{-JS}}$) was calculated from (8). Calculated $v_{l\text{-JS}}$ and experimental values for N_{JS} were replaced in equation (9) and C_1 defined for RT and PBT-D. For RT, at constant solid loading, C_1 increases very slightly by increasing impeller clearance (average value = 0.05); however, it shows linearly increases by increasing solid loading (slope: 0.18). For PBT-D, C_1 increases linearly by increasing solid loading
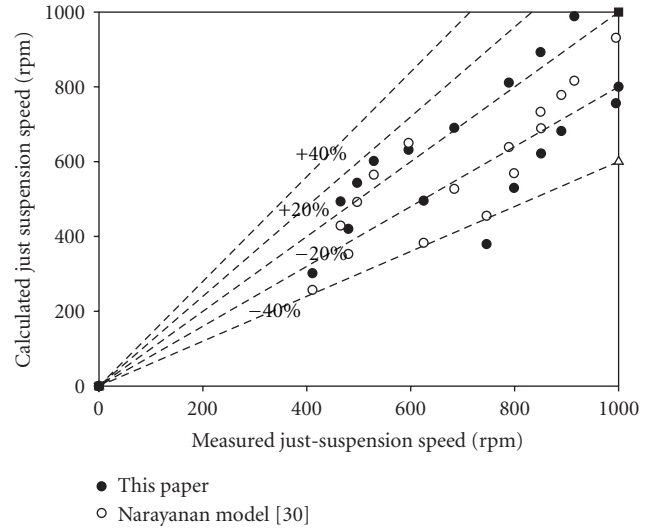

FIGURE 10: Comparing N_{JS} calculated from semitheoretical model proposed in this work with model and experimental data proposed by Narayanan et al. [30].

(slope: 0.13). It is constant for low impeller clearances that is, $C/T < 0.37$ ($C_1 = 0.07$). Results of the theoretical prediction of N_{JS} using the current method were compared with experimental data reported by Narayanan [33] and the model they have proposed in Figure 10. Narayanan et al. [33] have done experiments in systems where clearance is 0.5 and solid loading varies between 5% and 20%. Both models exhibit almost same accuracy. The combination of (8) and (9) provides a very simple and semitheoretical approach for predicting just-suspended impeller speed. The uncertainty of predicted N_{JS} could be decreased by modifying (9) based on local measurement of the liquid velocity at the bottom of the vessel [51, 52].

5. Summary and Conclusions

To overcome limitations of conventional techniques for characterizing just-suspended speed in liquid-solid mixing systems, a novel technique was developed based on gamma-ray densitometry. This technique represents an original approach and a convenient means of measuring just-suspended speed in systems where visual observation is not possible. Even in the systems where other methods are applicable, the densitometry technique can provide more accurate measurement. It was clearly observed that, based on impeller clearance, axial and radial impellers operate differently. All impellers are efficient at low clearance. However, there exists a critical clearance where the flow pattern of the axial flow impeller changes. It was also shown that correlations for predicting N_{JS} do not have universal validity. Correlation for predicting N_{JS} was modified based on gamma-ray densitometry results. Finally, a theoretical approach was proposed based on the analogy between solid suspension in stirred tanks and the incipient movement of solid particles in pipes. This model shows good agreement

with experimental data collected from the literature. However, model accuracy could be improved by local solid-liquid characterization close to the bottom of the vessel.

Nomenclatures

a : Constant of equation (6)(−)
A: Surface area (m^2), attenuation of vessel, and environment (−)
A_p: Particle surface area (m^2)
b: Constant of equation (6) (−)
C: Impeller clearance (m)
C_D: Drag coefficient (−)
D: Impeller diameter (m)
dp: Average particle diameter (m)
g: Gravity acceleration (m/s^2)
H: Liquid height (m)
I: Count rate (count/sec)
P: Pressure (Pa)
ΔP: Pressure difference in pressure gauge technique, $P_{N>0} - P_{N=0}$, (Pa)
L: Scanning length (m)
N: Impeller speed (1/sec)
S: Zwietering correlation constant (−)
t_c: Circulation time (sec)
$v_{l\text{-JS}}$: Liquid velocity at the bottom of the vessel at just-suspended condition (m/s)
vp: Particle volume (m^3)
vvm: Volume of gas per unit volume of liquid per minute (1/min)
W: Blade width (m)
X: Solid loading $Ms/Mt \times 100$ (% wt/wt-).

Greek Letters

$\alpha, \beta, \gamma, \delta, \theta$: Constants of equation(6)
ΔN_{JS}: $N_{JSg} - N_{JS}$ (rpm)
ρ: Density (kg/m^3)
μ: Mass attenuation coefficient (kg/m^2)
ε : Solid hold-up or volume fraction (−)
ν: Liquid dynamic viscosity.

Subscripts

i: Representation of scanningsection
imp: Impeller
js: Just-suspended, liquid-solid system
jsg: Just-suspended, gaz-liquid-solid
l: Liquid
s: Solid
ls: Slurry
0: Initial condition (N = 0 rpm).

Acknowledgments

References

[1] V. A. Atieme-Obeng, W. R. Penney, and P. Armenante, "Solid-liquid mixing," in *Handbook of Industrial Mixing, Science and Practice*, E. L. Paul, V. A. Atiemo-Obeng, and S. M. Kresta, Eds., pp. 543–584, John Wiley & Sons, Hoboken, NJ, USA, 2004.

[2] M. Bohnet and G. Niesmak, "Distribution of solid in stirred suspension," *German Chemical Engineering*, vol. 3, no. 1, pp. 57–65, 1980.

[3] T. N. Zwietering, "Suspending of solid particles in liquid by agitators," *Chemical Engineering Science*, vol. 8, no. 3-4, pp. 244–253, 1958.

[4] G. R. Kasat and A. B. Pandit, "Review on mixing characteristics in solid-liquid and solid-liquid-gas reactor vessels," *Canadian Journal of Chemical Engineering*, vol. 83, no. 4, pp. 618–643, 2005.

[5] A. Mersmann, F. Werner, S. Maurer, and K. Bartosch, "Theoretical prediction of the minimum stirrer speed in mechanically agitated suspensions," *Chemical Engineering and Processing*, vol. 37, no. 6, pp. 503–510, 1998.

[6] V. B. Rewatkar, K. S. M. S. Raghava Rao, and J. B. Joshi, "Critical impeller speed for solid suspension in mechanically agitated three-phase reactors. 1. Experimental part," *Industrial and Engineering Chemistry Research*, vol. 30, no. 8, pp. 1770–1784, 1991.

[7] L. Musil, J. Vlk, and H. Jiroudková, "Suspending solid particles in an agitated tank with axial-type impellers," *Chemical Engineering Science*, vol. 39, no. 4, pp. 621–628, 1984.

[8] C. M. Chapman, A. W. Nienow, M. Cooke, and J. C. Middleton, "Particle-gas-liquid mixing in stirred vessels—part I: particle-liquid mixing," *Chemical Engineering Research and Design*, vol. 61, pp. 71–81, 1983.

[9] C. Buurman, G. Resoort, and A. Plaschkes, "Scaling-up rules for solids suspension in stirred vessels," in *Proceedings of the 5th European Conference on Mixing*, 1985.

[10] G. Micale, V. Carrara, F. Grisafi, and A. Brucato, "Solids suspension in three-phase stirred tanks," *Chemical Engineering Research and Design*, vol. 78, no. 3, pp. 319–326, 2000.

[11] G. Micale, F. Grisafi, and A. Brucato, "Assessment of particle suspension conditions in stirred vessels by means of pressure gauge technique," *Chemical Engineering Research and Design*, vol. 80, no. 8, pp. 893–902, 2002.

[12] R. Jafari, P. A. Tanguy, and J. Chaouki, "Comprehensive review of just suspended speed in liquid-solid and gas-liquid-solid stirred tank reactors," *Chemical Engineering Journal*, vol. 10, no. 1, 2012.

[13] G. Baldi, R. Conti, and E. Alaria, "Complete suspension of particles in mechanically agitated vessels," *Chemical Engineering Science*, vol. 33, no. 1, pp. 21–25, 1978.

[14] P. Ayazi Shamlou and A. Zolfagharian, "Incipient solid motion in liquids in mechanically agitated vessels," in *Proceedings of the 3rd Fluid Mixing Conference*, pp. 195–208, September 1987.

[15] O. Molerus and W. Latzel, "Suspension of solid particles in agitated vessels—II. Archimedes numbers > 40, reliable prediction of minimum stirrer angular velocities," *Chemical Engineering Science*, vol. 42, no. 6, pp. 1431–1437, 1987.

[16] K. Saravanan, A. W. Patwardhan, and J. B. Joshi, "Critical impeller speed for solid suspension in gas inducing type mechanically agitated contactors," *Canadian Journal of Chemical Engineering*, vol. 75, no. 4, pp. 664–676, 1997.

[17] S. Hosseini, D. Patel, F. Ein-Mozaffari, and M. Mehrvar, "Study of solid-liquid mixing in agitated tanks through computational fluid dynamics modeling," *Industrial and Engineering Chemistry Research*, vol. 49, no. 9, pp. 4426–4435, 2010.

[18] N. C. S. Kee and R. B. H. Tan, "CFD simulation of solids suspension in mixing vessels," *Canadian Journal of Chemical Engineering*, vol. 80, no. 4, pp. 721–726, 2002.

[19] B. N. Murthy, R. S. Ghadge, and J. B. Joshi, "CFD simulations of gas-liquid-solid stirred reactor: prediction of critical impeller speed for solid suspension," *Chemical Engineering Science*, vol. 62, no. 24, pp. 7184–7195, 2007.

[20] A. Ochieng and A. E. Lewis, "CFD simulation of solids off-bottom suspension and cloud height," *Hydrometallurgy*, vol. 82, no. 1-2, pp. 1–12, 2006.

[21] R. Panneerselvam, S. Savithri, and G. D. Surender, "Computational fluid dynamics simulation of solid suspension in a gas-liquid-solid mechanically agitated contactor," *Industrial and Engineering Chemistry Research*, vol. 48, no. 3, pp. 1608–1620, 2009.

[22] D. F. Fletcher and G. J. Brown, "Numerical simulation of solid suspension via mechanical agitation: effect of the modelling approach, turbulence model and hindered settling drag law," *International Journal of Computational Fluid Dynamics*, vol. 23, no. 2, pp. 173–187, 2009.

[23] J. Lea, "Suspension mixing tank-design heuristic," *Chemical Product and Process Modeling*, vol. 4, no. 1, article 17, 2009.

[24] F. Wang, Z. Mao, and X. Shen, "Numerical study of solid-liquid two-phase flow in stirred tanks with Rushton impeller (II) Prediction of critical impeller speed," *Chinese Journal of Chemical Engineering*, vol. 12, no. 5, pp. 610–614, 2004.

[25] A. Ochieng and M. S. Onyango, "CFD simulation of solids suspension in stirred tanks: review," *Hemijska Industrija*, vol. 64, no. 5, pp. 365–374, 2010.

[26] H. Bashiri, J. Chaouki, F. Bertrand, and M. Heniche, "Cfd-based compartmental modelling of stirred tank reactors," in *Proceedings of the GLS10*, Braga, Portugal, 2011.

[27] J. Chaouki, F. Larachi, and M. P. Duduković, "Noninvasive tomographic and velocimetric monitoring of multiphase flows," *Industrial and Engineering Chemistry Research*, vol. 36, no. 11, pp. 4476–4503, 1997.

[28] B. Esmaeili, J. Chaouki, and C. Dubois, "An evaluation of the solid hold-up distribution in a fluidized bed of nanoparticles using radioactive densitometry and fibre optics," *Canadian Journal of Chemical Engineering*, vol. 86, no. 3, pp. 543–552, 2008.

[29] V. Kolar, "Suspensing solid particles in liquids by menas of mechanical agitation," *Collection of Czechoslovak Chemcial Communications*, vol. 26, pp. 613–627, 1961.

[30] S. Narayanan, V. K. Bhatia, D. K. Guha, and M. N. Rao, "Suspension of solids by mechanical agitation," *Chemical Engineering Science*, vol. 24, no. 2, pp. 223–230, 1969.

[31] D. Subbarao and V. K. Taneja, "Three phase suspensions in agitated vessels," in *Proceedings of the 3rd European Conference on Mixing*, York, UK, 1979.

[32] P. Ditl and F. Rieger, "Suspension of solids particle—relative velocity of particles in turbulent mixing," in *Proceedings of the 5th European Conf on Mixing*, Wurzburg, West Germany, 1985.

[33] L. Musil and J. Vlk, "Suspending solid particles in an agitated conical-bottom tank," *Chemical Engineering Science*, vol. 33, no. 8, pp. 1123–1131, 1978.

[34] P. Ditl and F. Rieger, "Suspension of solid particles—letter to the editors," *Chemical Engineering Science*, vol. 35, pp. 764–765, 1980.

[35] O. Molerus and W. Latzel, "Suspension of solid particles in agitated vessels—I. Archimedes numbers $\lesssim$ 40," *Chemical Engineering Science*, vol. 42, no. 6, pp. 1423–1430, 1987.

[36] K. Wichterle, "Conditions for suspension of solids in agitated vessels," *Chemical Engineering Science*, vol. 43, no. 3, pp. 467–471, 1988.

[37] P. M. Armenante and E. U. Nagamine, "Effect of low off-bottom impeller clearance on the minimum agitation speed for complete suspension of solids in stirred tanks," *Chemical Engineering Science*, vol. 53, no. 9, pp. 1757–1775, 1998.

[38] P. M. Armenante and C. C. Chou, "Velocity profiles in a baffled vessel with single or double pitched-blade turbines," *AIChE Journal*, vol. 42, no. 1, pp. 42–54, 1996.

[39] S. M. Kresta and P. E. Wood, "Mean flow field produced by a 45° pitched blade turbine: changes in the circulation pattern due to off bottom clearance," *Canadian Journal of Chemical Engineering*, vol. 71, no. 1, pp. 42–53, 1993.

[40] T. Kumaresan and J. B. Joshi, "Effect of impeller design on the flow pattern and mixing in stirred tanks," *Chemical Engineering Journal*, vol. 115, no. 3, pp. 173–193, 2006.

[41] S. M. Kresta, K. J. Bittorf, and D. J. Wilson, "Internal annular wall jets: radial flow in a stirred tank," *AIChE Journal*, vol. 47, no. 11, pp. 2390–2401, 2001.

[42] Z. Jaworski, A. W. Nienow, and K. N. Dyster, "An LDA study of the turbulent flow field in a baffled vessel agitated by an axial, down-pumping hydrofoil impeller," *Canadian Journal of Chemical Engineering*, vol. 74, no. 1, pp. 3–15, 1996.

[43] M. Schäfer, M. Yianneskis, P. Wächter, and F. Durst, "Trailing vortices around a 45° pitched-blade impeller," *AIChE Journal*, vol. 44, no. 6, pp. 1233–1246, 1998.

[44] G. Zhou and S. M. Kresta, "Impact of tank geometry on the maximum turbulence energy dissipation rate for impellers," *AIChE Journal*, vol. 42, no. 9, pp. 2476–2490, 1996.

[45] R. N. Sharma and A. A. Shaikh, "Solids suspension in stirred tanks with pitched blade turbines," *Chemical Engineering Science*, vol. 58, no. 10, pp. 2123–2140, 2003.

[46] G. Montante, K. C. Lee, A. Brucato, and M. Yianneskis, "An experimental study of double-to-single-loop transition in stirred vessels," *Canadian Journal of Chemical Engineering*, vol. 77, no. 4, pp. 649–659, 1999.

[47] K. J. Myers, A. Bakker, and R. R. Corpstein, "The effect of flow reversal on solids suspension in agitated vessels," *Canadian Journal of Chemical Engineering*, vol. 74, no. 6, pp. 1028–1033, 1996.

[48] A. W. Nienow, "Suspension of solid particles in turbine agitated baffled vessels," *Chemical Engineering Science*, vol. 23, no. 12, pp. 1453–1459, 1968.

[49] K. S. M. S. Raghava Rao, V. B. Rewatkar, and J. B. Joshi, "Critical impeller speed for solid suspension in mechanically agitated contactors," *AIChE Journal*, vol. 34, no. 8, pp. 1332–1340, 1988.

[50] R. V. Roman and R. Z. Tudose, "Studies on transfer processes in mixing vessels: effect of gas on solid- liquid hydrodynamics using modified Rushton turbine agitators," *Bioprocess Engineering*, vol. 17, no. 1, pp. 55–60, 1997.

[51] Y. Zhu and J. Wu, "Critical impeller speed for suspending solids in aerated agitation tanks," *Canadian Journal of Chemical Engineering*, vol. 80, no. 4, pp. 682–687, 2002.

[52] A. W. Nienow, M. Konno, and W. Bujalski, "Studies on three-phase mixing: a review and recent results," in *Proceedings of the*

5th European Conference on Mixing, Wurzburg, West Germany, 1985.

[53] J. J. Derksen, "Numerical simulation of solids suspension in a stirred tank," *AIChE Journal*, vol. 49, no. 11, pp. 2700–2714, 2003.

[54] E. Rabinovich and H. Kalman, "Incipient motion of individual particles in horizontal particle-fluid systems—B. Theoretical analysis," *Powder Technology*, vol. 192, no. 3, pp. 326–338, 2009.

[55] P. Stevenson, R. B. Thorpe, and J. F. Davidson, "Incipient motion of a small particle in the viscous boundary layer at a pipe wall," *Chemical Engineering Science*, vol. 57, no. 21, pp. 4505–4520, 2002.

[56] R. Fishwick, M. Winterbottom, D. Parker, X. Fan, and H. Stitt, "The use of positron emission particle tracking in the study of multiphase stirred tank reactor hydrodynamics," *Canadian Journal of Chemical Engineering*, vol. 83, no. 1, pp. 97–103, 2005.

[57] D. Guha, P. A. Ramachandran, and M. P. Dudukovic, "Flow field of suspended solids in a stirred tank reactor by Lagrangian tracking," *Chemical Engineering Science*, vol. 62, no. 22, pp. 6143–6154, 2007.

[58] W. J. McManamey, "Circulation model for batch mixing in agitated, baffled vessels," *Transactions of the Institution of Chemical Engineers*, vol. 58, no. 4, pp. 271–276, 1980.

[59] J. B. Joshi, A. B. Pandit, and M. M. Sharma, "Mechanically agitated gas-liquid reactors," *Chemical Engineering Science*, vol. 37, no. 6, pp. 813–844, 1982.

[60] D. B. Holmes, R. M. Voncken, and J. A. Dekker, "Fluid flow in turbine-stirred, baffled tanks-I. Circulation time," *Chemical Engineering Science*, vol. 19, no. 3, pp. 201–208, 1964.

[61] A. W. Nienow, "On impeller circulation and mixing effectiveness in the turbulent flow regime," *Chemical Engineering Science*, vol. 52, no. 15, pp. 2557–2565, 1997.

[62] A. W. Patwardhan and J. B. Joshi, "Relation between flow pattern and blending in stirred tanks," *Industrial and Engineering Chemistry Research*, vol. 38, no. 8, pp. 3131–3143, 1999.

[63] K. Van Der Molen and H. R. E. Van Maanen, "Laser-Doppler measurements of the turbulent flow in stirred vessels to establish scaling rules," *Chemical Engineering Science*, vol. 33, no. 9, pp. 1161–1168, 1978.

Research Article

Laminar Mixing in Stirred Tank Agitated by an Impeller Inclined

Koji Takahashi,[1] Yoshiharu Sugo,[1] Yasuyuki Takahata,[1] Hitoshi Sekine,[2] and Masayuki Nakamura[2]

[1] *Department of Chemistry and Chemical Engineering, Yamagata University, Yonezawa 992-8510, Japan*
[2] *Process Engineering Laboratory, Corporate R&D Department, Central Research Laboratories, DIC Co., Ltd., Sakura, Chiba 285-8668, Japan*

Correspondence should be addressed to Koji Takahashi, koji@yz.yamagata-u.ac.jp

The mixing performance in a vessel agitated by an impeller that inclined itself, which is considered one of the typical ways to promote mixing performance by the spatial chaotic mixing, has been investigated experimentally and numerically. The mixing time was measured by the decolorization method and it was found that the inclined impeller could reduce mixing time compared to that obtained by the vertically located impeller in laminar flow region. The effect of eccentric position of inclined impeller on mixing time was also studied and a significant reduction of mixing time was observed. To confirm the experimental results, the velocity profiles were calculated numerically and two novel numerical simulation methods were proposed.

1. Introduction

In recent years, many theoretical and experimental studies have been carried out for laminar chaotic mixing and have provided much beneficial information on how laminar mixing can be enhanced. However, it has also been recognized that the mixing in periodic flows is not necessarily complete, because such systems often display coexisting chaotic and nonchaotic regions. Fluids can neither penetrate nor leave these islands of unmixed fluids by regular motion. Therefore, the isolated mixing regions may become barriers to mixing.

In the pioneering studies in this field, Lamberto et al. [1] first attempted to solve this problem using time-dependent rotational velocity to enhance the mixing in a stirred tank equipped with ordinary small impellers. After that, several experimental studies have been also undertaken [2, 3] to demonstrate that the mixing performance can be improved markedly by increasing the chaotic degree in temporal terms. While the chaotic degree can be increased effectively by temporal terms, the approach is restricted to practical applications because of the restriction of the motor and the speed reducer machine to drive the impeller. In practice, the temporal approach has rarely been employed in the mixing industry except for washing machines.

In contrast, the chaotic degree can also be increased by spatial terms, for example, by reducing the circumferential symmetry and shifting the complexity in normal mixing equipment. While this spatial method does not improve the mixing performance as impressively as the temporal method, it places less demanding requirements on the machinery. Consequently, this approach has been widely used in industry.

The special measures employed in an agitated vessel related to spatial chaotic mixing include baffles, off-center impeller mounting, and uncircumferentially symmetrical tanks. The baffles can enhance the mixing performance remarkably and have been widely used, the off-center mounting has also been investigated thoroughly [4, 5] and the uncircumferentially symmetrical tanks have recently been studied [6–8]. However, the most desirable method is to know how to insert the traditional impeller into a vessel because it does not cost so much. Therefore, in the present study, the mixing performance is investigated in a vessel agitated by an impeller inclined itself, which has rarely been studied. The effectiveness of setting the impeller inclined is verified through the comparison of mixing time obtained for vertical setting impeller. Two novel numerical simulation
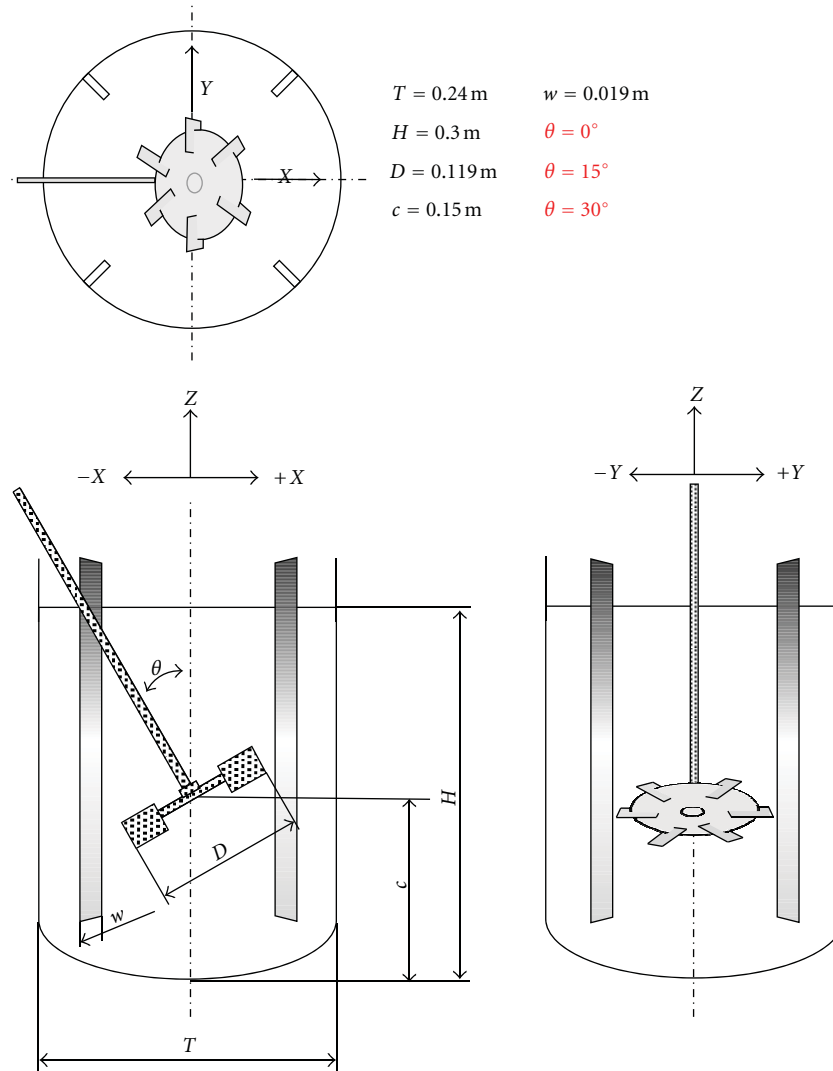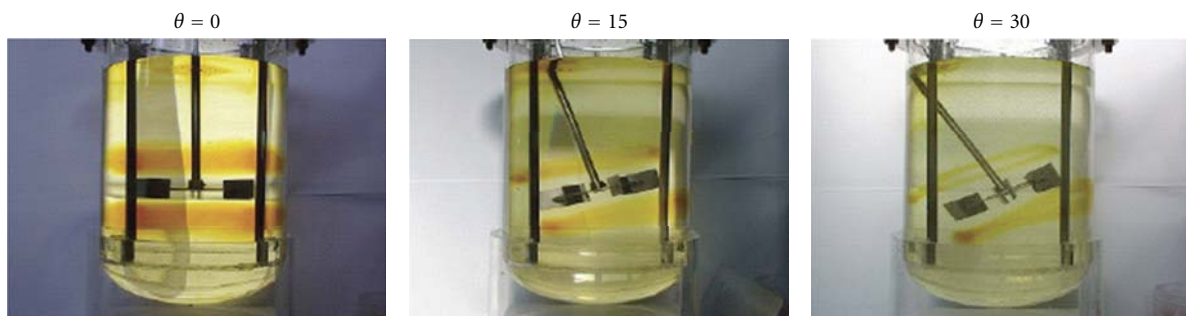
$T = 0.24$ m $w = 0.019$ m

$H = 0.3$ m $\theta = 0°$

$D = 0.119$ m $\theta = 15°$

$c = 0.15$ m $\theta = 30°$

FIGURE 1: Experimental setup.

$\theta = 0$ $\theta = 15$ $\theta = 30$

FIGURE 2: Isolated mixing regions observed (50 min^{-1}, DT), Re = 16.2.

methods were proposed to confirm the experimental results obtained in this work.

2. Mixing Time for Inclined Impeller

2.1. Experimental. The experimental setup consists of a cylindrical vessel with four baffles and an impeller, as shown in Figure 1. The experimental conditions conducted in this work are summarized in Table 1. The vessel was a transparent acrylic resin of 0.24 m inner diameter, T, with a liquid depth, H, of $1.25T$ and has a $2:1$ semiellipse dish shape bottom. The impellers used are a Rushton turbine (DT) and a 6 bladed pitched paddle rotated to create downward flow (PP). The impeller-to-vessel diameter ratio, D/T, was 0.5 and
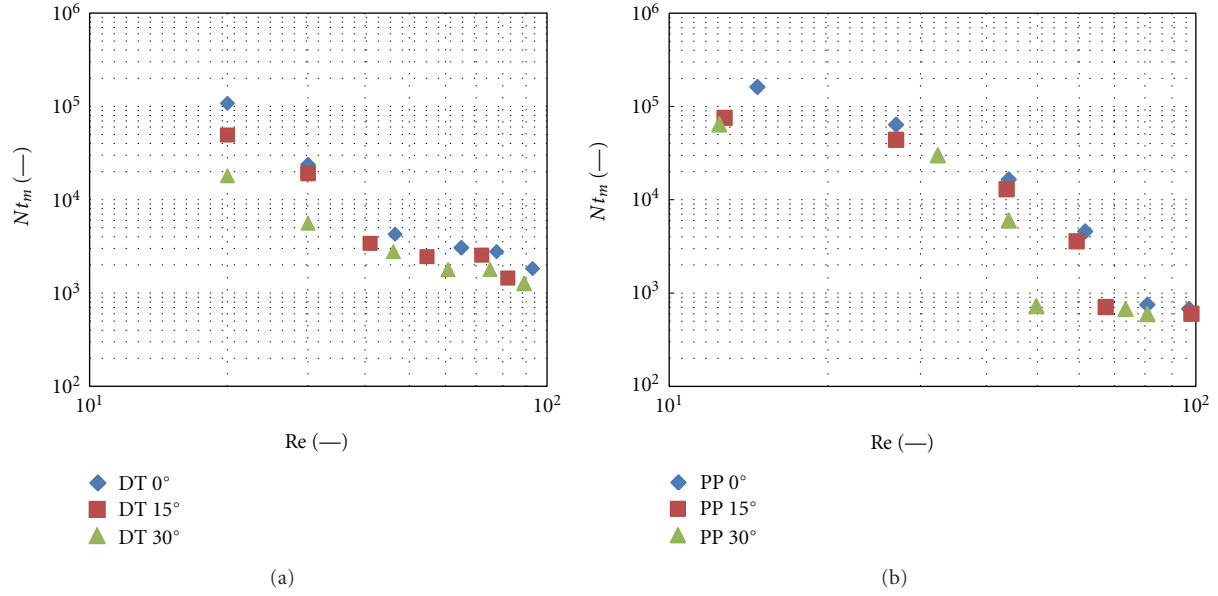
(a)

(b)

Figure 3: Relationship between dimensionless mixing time and Re number for disk turbine and pitched paddle.

Table 1: Experimental condition.

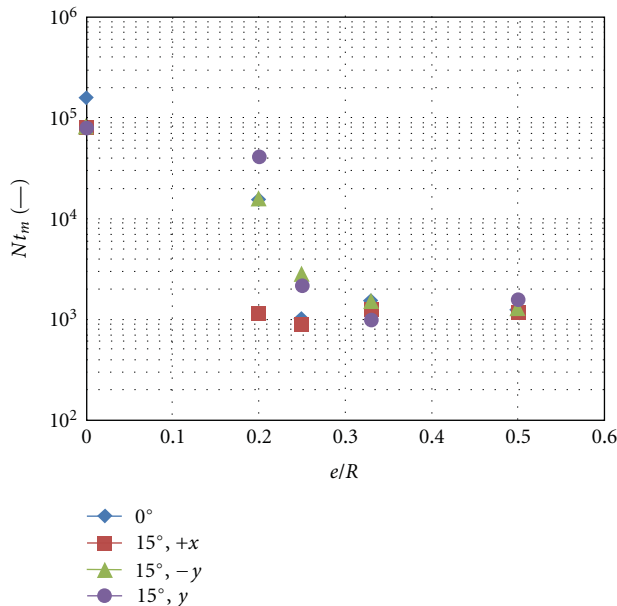| μ | [Pa·s] | 1.05~1.30 |
N	[min^{-1}]	50, 100, 150, 200, 250, 300
θ	[°]	0, 15, 30
e/R	[—]	0, 0.2, 0.25, 0.33, 0.5

Figure 4: Relationship between dimensionless mixing time and eccentric ratio.

the off bottom clearance of impeller was $0.5H$. Four baffles of width 0.19 m were set on the vessel wall. The impeller was set vertically and inclined at 15 or 30 degrees, so as to the center of impeller is consistent with the middle of vessel. Only for

Rushton turbine set vertical and inclined 15 degree, the effect of impeller eccentricity on mixing time was also investigated. In this case, the impeller was moved to front and back of inclined side (denoted $-x$ and $+x$) and to the perpendicular direction (denoted y), where the distance from center of impeller to the center line of tank was changed from 0 to 0.5 of radius of vessel. Newtonian aqueous solutions of corn syrup with viscosities of about 1 Pa s and water were used as test liquids. The mixing was carried out at the Reynolds number from 10 to 100.

The mixing time was measured by the decoloration method adopting the reaction between iodine and thiosulfate. The optimum equivalent ratio of thiosulfate to iodine 1.4 [9] is selected to measure the mixing times. The mixing time was defined as the time required to destroy the isolated mixing regions, where the streaks observed on the vessel wall at the end of mixing were ignored when determining the mixing time.

2.2. Mixing Time Measured

2.2.1. Effect of Inclination of Impeller on Mixing Time. Figure 2 shows the photographs of isolated mixing regions observed after 15 min for different inclined angles of impeller. It is well known that the doughnut rings are formed above and below the impeller at relatively low Reynolds numbers for ordinary small impellers [1, 5]. As expected, the doughnut rings were observed above and below the impeller not only for the vertical impeller ($\theta = 0$) but also inclined impellers ($\theta = 15$ or 30). However, the volume of the isolated regions reduces with an increase in the inclined angle of impeller.

The relationship between the dimensionless mixing time measured and the Reynolds number is shown in Figure 3, for impellers of different inclination. This figure shows that the
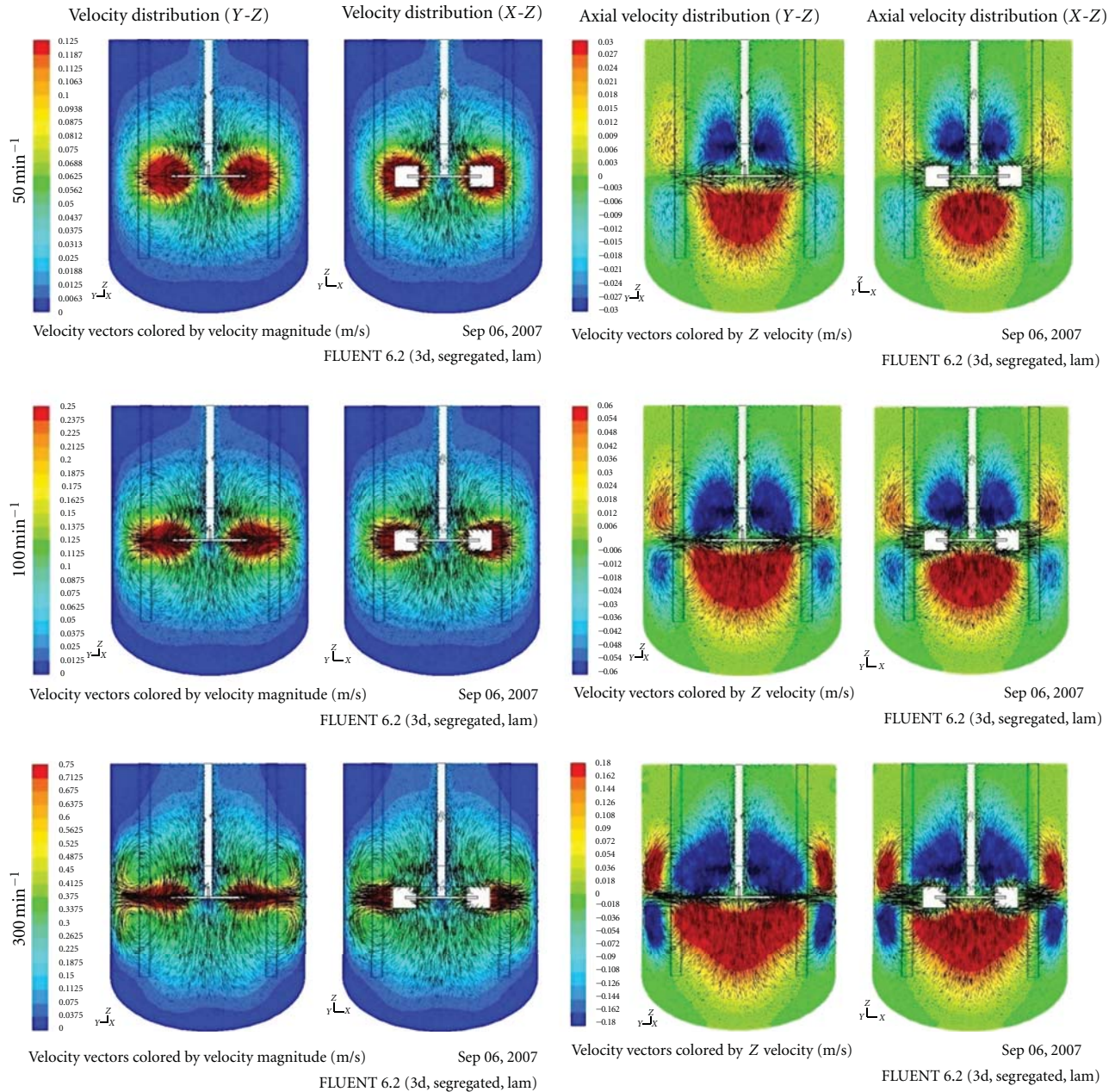
FIGURE 5: Three-dimensional flow velocity and axial velocity distribution (vertical located impeller). The rate vector was overlapped with each figure. The range of coloring was displayed in proportion to the rotational speed.

dimensionless mixing time decreases with an increase in Reynolds number for all impellers and with an increase in inclined angle of impeller. This result may indicate that the inclination of the impeller can promote the mixing performance in laminar flow regions. The effect of impeller inclination on mixing time is stronger for Rushton turbine than that for pitched paddle. A Rushton turbine creates radial flow to vessel wall but a pitched paddle axial one to bottom of vessel. Because of distance of impeller to vessel wall is shorter than that of impeller to bottom and the flow created by Rushton turbine is stronger than that by pitched paddle,

the more effective inclination on mixing time was obtained for a Rushton turbine than for a pitched paddle.

For both impellers, the power consumption was measured but there was no effect of impeller inclination on power.

2.2.2. Effect of Eccentricity on Mixing Time.
Figure 4 shows the relationship between the dimensionless mixing time measured and the Reynolds number for different eccentricities. It is clearly seen from the figure the promotion of mixing by eccentricity is more effective than that by inclination. For
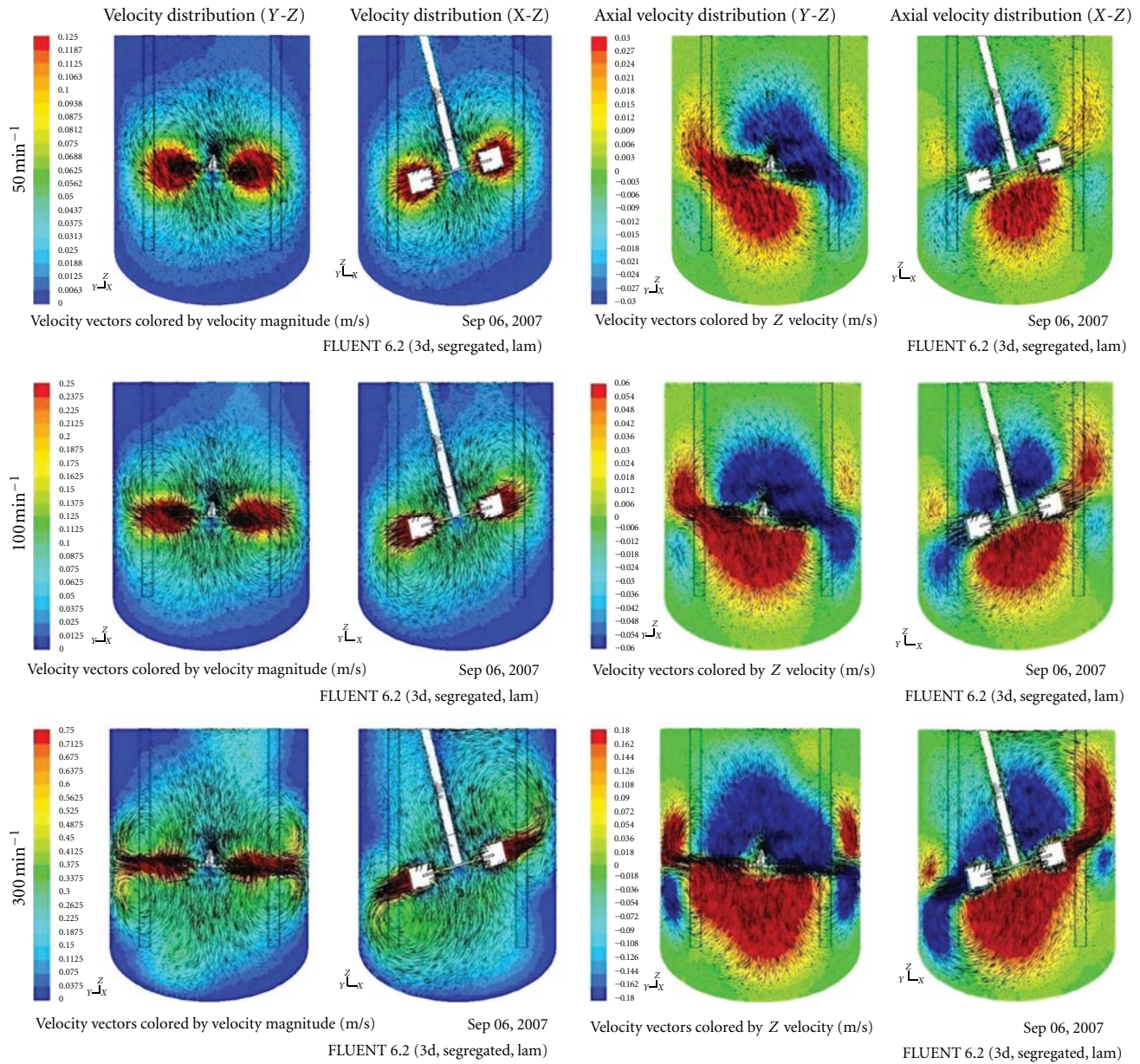
FIGURE 6: Three-dimensional flow velocity and axial velocity distribution (impeller inclined at 15°). The rate vector was overlapped with each figure. The range of coloring was displayed in proportion to the rotational speed.

vertical impeller, the mixing time decreases gradually with an increase in eccentricity as reported by Takahashi et al. [5]. For impeller inclined 15 degree moved to front of inclined side (denoted $-X$) and the perpendicular direction (denoted Y), the mixing times change with almost the same with those of vertical impeller. On the other hand, for impeller inclined moved to back of inclined side decreases drastically with a small change of eccentricity and then become constant at the eccentricity more than 0.25.

3. Flow Simulation

3.1. Simulation Method. In literature, there is no data on velocity profiles in a vessel agitated by an inclined impeller.

Thus, in order to get the information of the flow field in a vessel agitated by an inclined impeller, the flow simulation was carried out. The impeller simulated is a Rushton turbine because the more effective inclination on mixing was obtained for Rushton turbine than for pitched paddle, as is indicated in the previous section.

The geometries of mixing vessel and impeller provided for the numerical calculations are similar to those used in the experiment. The velocity profiles were calculated for the impeller inclined at 15 and 30 degrees to the vertical axis. For comparison, the velocity profiles created by vertically located impeller in a vertical vessel were also calculated. The simulation was conducted at the rotational speeds of 50, 100, and
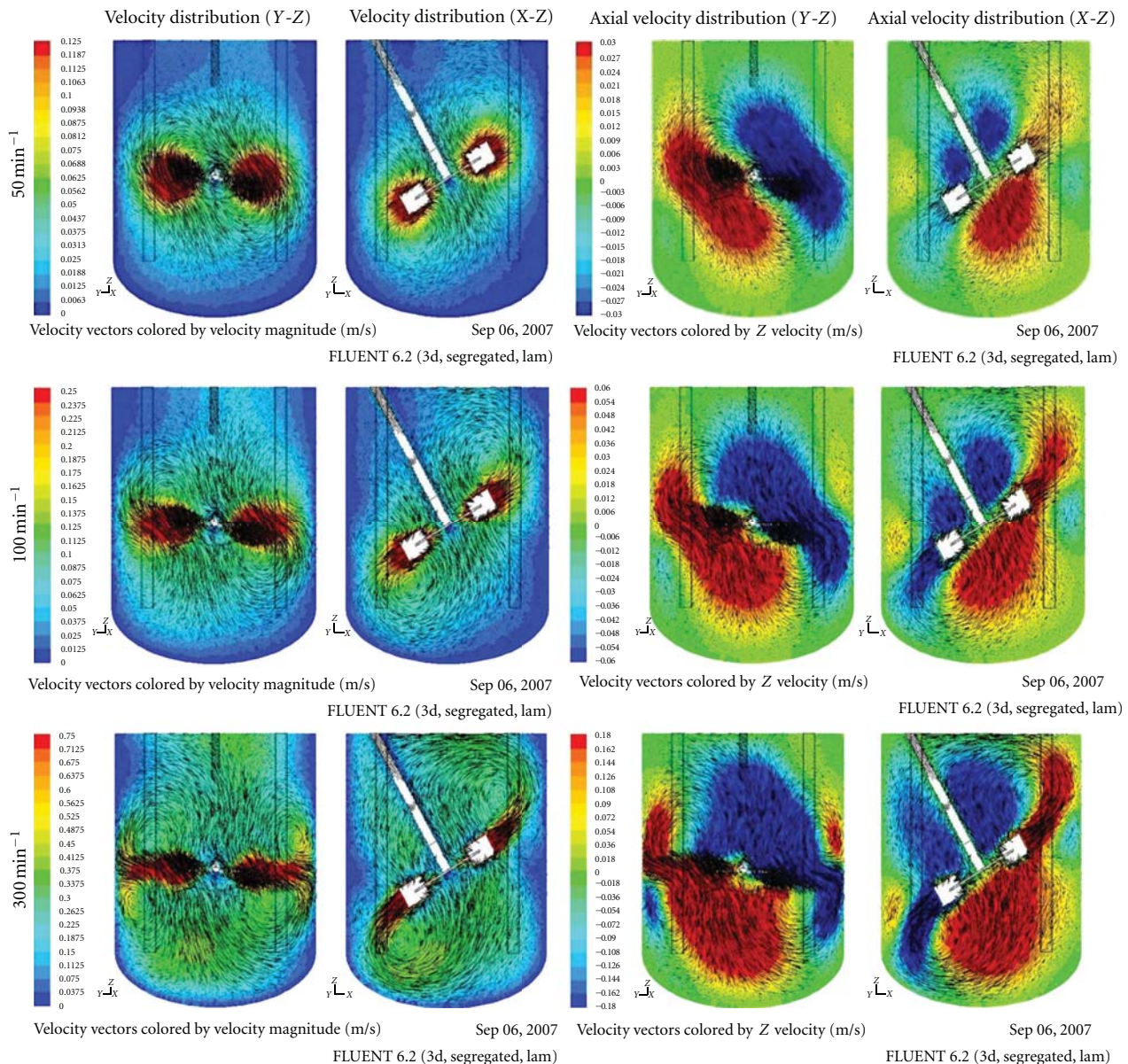
FIGURE 7: Three-dimensional flow velocity and axial velocity distribution (impeller inclined at 30°). The rate vector was overlapped with each figure. The range of coloring was displayed in proportion to the rotational speed.

300 rpm, which correspond to the Reynolds numbers of 16.5, 33.0, and 99.0, respectively. The viscosity and density of liquid was set at 1 Pa s and 1400 kg/m³. The fluid flow is solved using the three-dimensional finite-volume method software FLUENT developed by Fluent Inc. in the USA. A steady flow field on a rotating frame of reference fixed on the impeller is adopted.

3.2. Flow Field Simulated. Figures 5, 6, and 7 show the three-dimensional flow velocity distributions and the axial ones, those are the most important components to consider for the mixing, calculated in the *Y-Z* and *X-Z* cross sections (see Figure 1), where *Y-Z* cross section is perpendicular to and *X-Z* one parallel to impeller shaft. There is no difference in velocity distribution in *Y-Z* and *X-Z* cross sections for vertical impeller, regardless whether it is three-dimensional flow velocity or axial velocity distributions. For

inclined impellers, the three-dimensional flow velocity and the axial velocity distributions obtained for *Y-Z* and *X-Z* cross section are completely different from each other. It is clearly seen from these figures, with an increase in inclined angle of impeller and with an increase in rotational speed, the velocity becomes high and the area of high velocity regions increases, especially near free surface and bottom of vessel. The simulated results may indicate the higher the mixing performance, the larger the inclined angle of impeller.

4. Estimation of Mixing Performance by Numerical Simulation

In order to evaluate the dispersive mixing performance, two unique simulation methods were proposed based on the flow simulation results obtained above. One is the simulation of
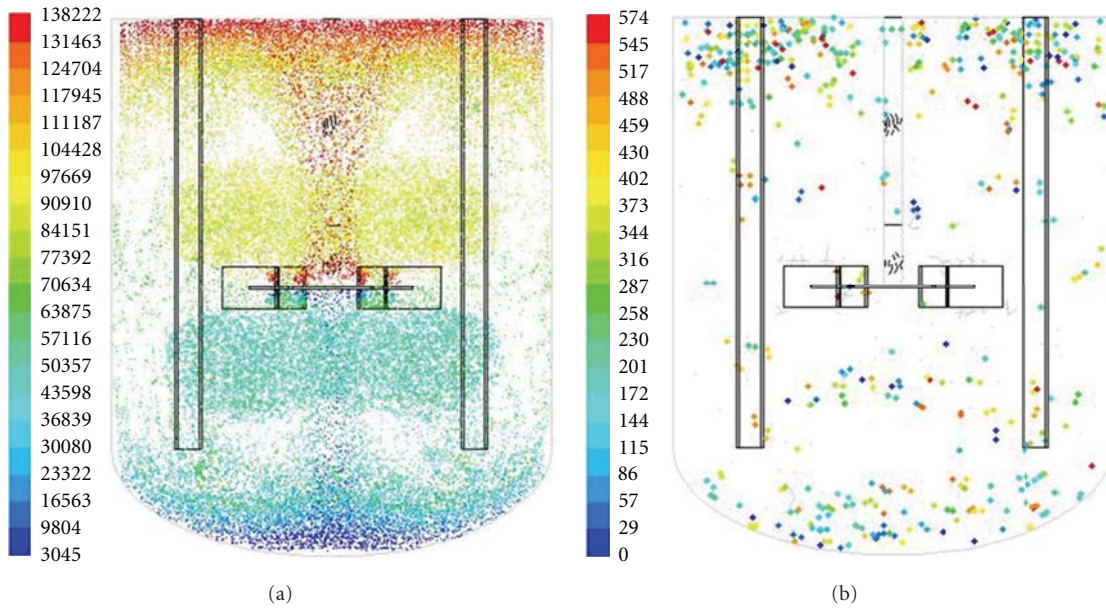
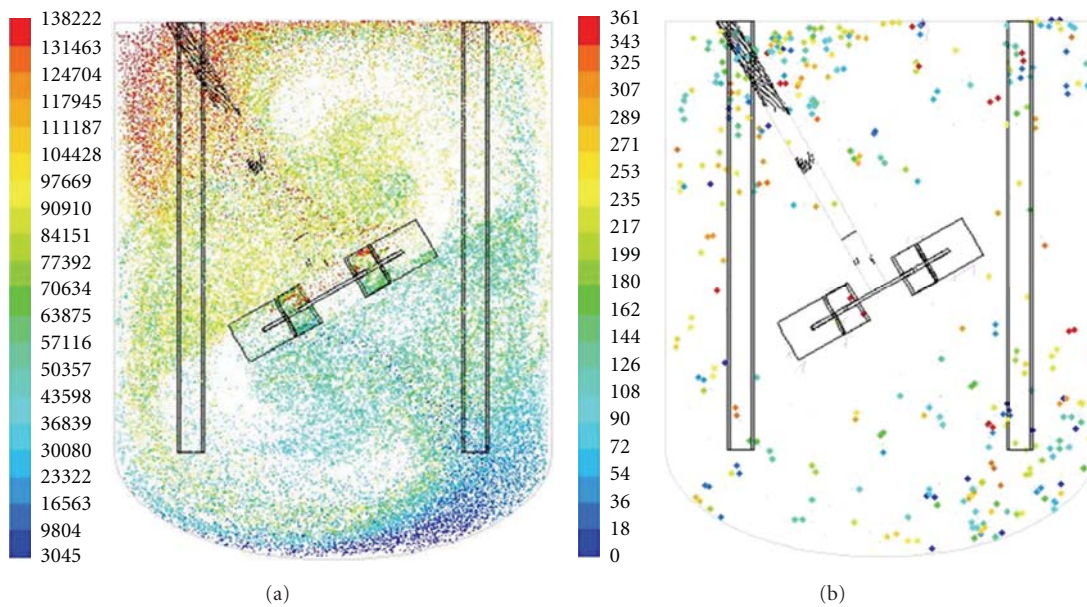FIGURE 8: Simulation result of particle dispersion ($\theta = 0°$).

FIGURE 9: Simulation result of particle dispersion ($\theta = 30°$).

particles dispersion and another is that of mixing of two miscible liquids.

4.1. Particle Dispersion. To quantify the mixing performance, the dispersion of particles is calculated for the vertical and 30 degree inclined impeller. If the flow is dispersive, the neighboring particles will be separated from each other. Based on this concept, the analysis was carried out according to the following procedure.

(1) Initially, the particles were positioned at all intersections of the X, Y, and Z lines at every 5 mm

intervals throughout the tank, where the particles are supposed to have the same density with the liquid.

(2) The movement of the particles was calculated according to the flow generated by impeller for 30 seconds after the start of agitation, where the particles are assumed to move exactly with liquid.

(3) For six particles placed adjacently from the marked particle (2 particles in each coordinate), the distances from the marked particle were calculated. If the distances become longer more than 7 mm (original distance of 5 mm + another 2 mm), the particles were removed from the image.
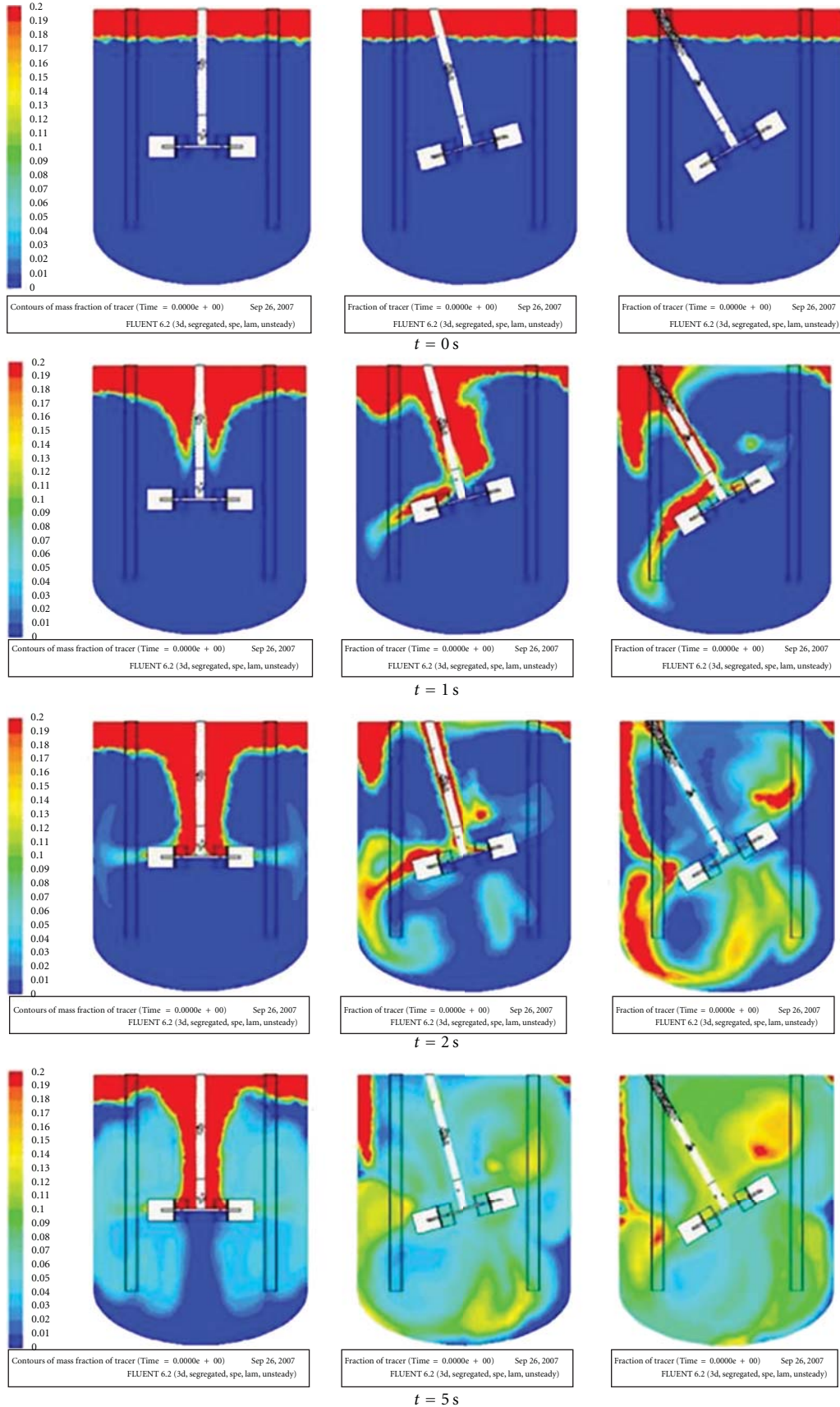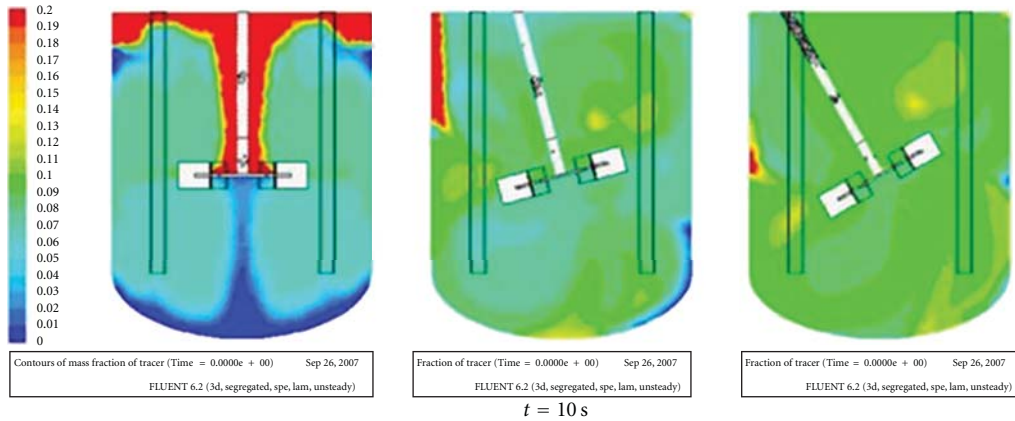
Figure 10: Continued.

$t = 10 \, s$

FIGURE 10: Simulation result of mixing of two miscible liquids.

(4) In order to get a clear image, 99% of remaining particle were also removed at random from the image.

(5) The number of remaining particles on the image was counted for both conditions.

The results of the simulations are shown in Figures 8 and 9. In these figures, the colors indicate the initial positions of the particles in axial direction, where red indicates top position and blue bottom one. Figures 8(a) and 9(a) are the results after removing the particles whose distances become longer than 7 mm and Figures 8(b) and 9(b) ones after eliminating 99% particles. In Figures 8(b) and 9(b), 574 particles remained in the vertical impeller condition, and 367 particles remained in the inclined impeller condition. The smaller number of particle, the higher the ability particle dispersion. Thus, it is confirmed that the inclined impeller condition exhibited a high dispersion ability.

4.2. Mixing of Two Miscible Liquids. Based on the flow simulation, the mixing process of two miscible liquids was simulated for the vertical and inclined 15 and 30 degree impellers. Two miscible liquids of same viscosity and density were set in a vessel: blue one 90% lower and red one 10% upper in a vessel. The calculation was conducted for 10 seconds.

The results are shown in Figure 10. It is clearly seen from the figure, with an increase in inclined angle, the mixing proceeds quickly throughout vessel. Especially, it should be noted that the entrainment of liquid near free surface has easily taken place for inclined impellers. In the process industries, solids lighter than liquid are commonly required to be dispersed into liquid [10]. For such purposes, the inclined impeller may be adequate to use.

5. Conclusions

The effects of impeller inclination angle on spatial chaotic mixing were investigated experimentally and numerically. The mixing pattern was observed and the mixing time was measured using the decoloration method. Agitation by an inclined impeller creates an effective flow pattern for mixing by reducing the size of the isolated mixing regions in the vessel. The results of the numerical simulations showed a complex flow and high ability of particle dispersion in the inclined impeller condition. Therefore, the flow control of the inclined impeller agitation introduced in this paper should be applicable to a wide range of processes.

Nomenclature

c: Off-bottom clearance of impeller [m]
D: Diameter of impeller [m]
e: Distance from shaft to center line of tank [m]
H: Liquid depth [m]
N: Impeller speed [s^{-1}]
R: Radius of tank [m]
Re: Reynolds number [—]
T: Tank diameter [m]
t_m: Mixing time [s]
w: Baffle width [m]
μ: Liquid viscosity [Pa s]
ρ: Liquid density [m s^{-3}]
θ: Inclined angle of impeller [—].

References

[1] D. J. Lamberto, F. J. Muzzio, P. D. Swanson, and A. L. Tonkovich, "Using time-dependent RPM to enhance mixing in stirred vessels," *Chemical Engineering Science*, vol. 51, no. 5, pp. 733–741, 1996.

[2] T. Nomura, T. Uchida, and K. Takahashi, "Enhancement of mixing by unsteady agitation of an impeller in an agitated vessel," *Journal of Chemical Engineering of Japan*, vol. 30, no. 5, pp. 875–879, 1997.

[3] W. G. Yao, H. Sato, K. Takahashi, and K. Koyama, "Mixing performance experiments in impeller stirred tanks subjected to unsteady rotational speeds," *Chemical Engineering Science*, vol. 53, no. 17, pp. 3031–3040, 1998.

[4] J. Karcz, M. Cudak, and J. Szoplik, "Stirring of a liquid in a stirred tank with an eccentrically located impeller," *Chemical Engineering Science*, vol. 60, no. 8-9, pp. 2369–2380, 2005.

[5] K. Takahashi, D. Shigihara, and Y. Takahata, "Laminar mixing in eccentric stirred tank with different bottoms," *Journal of Chemical Engineering of Japan*, vol. 44, pp. 931–935, 2011.

[6] H. Xiao and K. Takahashi, "Mixing characteristics in the horizontal non-baffled stirred vessel in low viscosity fluid," *Journal of Chemical Engineering of Japan*, vol. 40, no. 8, pp. 679–683, 2007.

[7] K. Takahashi, Y. Takahata, T. Imai, and K. Shisai, "Development of nobel equipment to produce bio-diesel fuel," *Kagaku Kogaku Ronbunshu*, vol. 37, pp. 852–858, 2011.

[8] T. Yang and K. Takahashi, "Effect of impeller blade angle on power consumption and flow pattern in horizontal stirred vessel," *Journal of Chemical Engineering of Japan*, vol. 43, no. 8, pp. 635–640, 2010.

[9] K. Takahashi, Y. Takahata, T. Yokota, and H. Konno, "Mixing of two miscible highly viscous newtonian liquids in a helical ribbon agitator," *Journal of Chemical Engineering of Japan*, vol. 18, no. 2, pp. 159–162, 1985.

[10] K. Takahashi and S. I. Sasaki, "Complete drawdown and dispersion of floating solids in agitated vessel equipped with ordinary impellers," *Journal of Chemical Engineering of Japan*, vol. 32, no. 1, pp. 40–44, 1999.

Research Article

Phosphorus Removal from Wastewater Using Oven-Dried Alum Sludge

Wadood T. Mohammed and Sarmad A. Rashid

Chemical Engineering Department, College of Engineering, University of Baghdad, Baghdad, Iraq

Correspondence should be addressed to Sarmad A. Rashid, sermed1972@yahoo.com

The present study deals with the removal of phosphorus from wastewater by using oven-dried alum sludge (ODS) as adsorbent that was collected from Al-Qadisiya treatment plant (Iraq); it was heated in an oven at $105°C$ for 24 h and then cooled at room temperature. The sludge particles were then crushed to produce a particle size of 0.5–4.75 mm. Two modes of operation are used, batch mode and fixed bed mode, in batch experiment the effect of oven-dried alum sludge doses 10–50 g/L, pH of solution 5–8 with constant initial phosphorus concentration of 5 mg/L, and constant particle size of 0.5 mm were studied. The results showed that the percent removal of phosphorus increases with the increase of oven-dried alum sludge dose, but pH of solution has insignificant effect. Batch kinetics experiments showed that equilibrium time was about 6 days. Adsorption capacity was plotted against equilibrium concentration, and isotherm models (Freundlich, Langmuir, and Freundlich-Langmuir) were used to correlate these results. In the fixed bed isothermal adsorption column, the effect of initial phosphorus concentration (C_o) 5 and 10 mg/L, particle size 2.36 and 4.75 mm, influent flow rate (Q) 6 and 10 L/hr, and bed depth (H) 0.15–0.415 m were studied. The results showed that the oven-dried alum sludge was effective in adsorbing phosphorus, and percent removal of phosphorus reaches 85% with increasing of contact time and adsorbent surface area (i.e., mass of adsorbent 50 g/L with different pH).

1. Introduction

Wastewater or contaminated water is a big environmental problem all over the world, in industrial plants; contaminants may be a result of side reactions, rendering the water stream an effluent status. These impurities are at low-level concentration but still need to be further reduced to levels acceptable by various destinations in the plant. Surface waters contain certain level of phosphorus (P) in various compounds, which is an important constituent of living organisms. In natural conditions the phosphorus concentration in water is balanced; that is, accessible mass of this constituent is close to the requirements of the ecological system. When the input of phosphorus to water is higher than it can be assimilated by a population of living organisms, the problem of excess phosphorus content occurs. Regulatory control on phosphorus disposal is evident all over the world recently [1–3]. Strict regulatory requirements decreased the permissible level of phosphorus concentration in wastewater at the point of disposal (i.e.,

1 mg/L). This has made it very important to find appropriate technological solution for treatment of wastewater prior to disposal.

Phosphorus removal is considered as a major challenge in wastewater treatment, particularly for small-scale wastewater treatment systems. Processes available for P-treatment are generally classified into three general categories: chemical, physical, or biological-based treatment systems. Among physical-chemical methods, phosphorus removal is achieved using ion exchange [4, 5], dissolved air flotation [6, 7], and membrane filtration [8, 9]. Filtration has been used either alone or in conjunction with a coagulation process as a means to remove phosphorus from wastewater [10, 11]. High-rate sedimentation has also been attempted in some studies [12, 13]. Among the various physical-chemical methods, coagulation with chemical precipitation and adsorption are the most common techniques being used for removing phosphorus. Enhanced biological methods for removing phosphorus are also used with success [14, 15]. For small-scale applications (e.g., aquaculture) biological methods may

not be appropriate for phosphorus removal because of the low carbon concentrations, which increases cost and time involved in biological methods [16]. Alternatively, physical-chemical methods can offer advantages for small industries because of lower initial costs involvement. These methods are also easier to use and do not require high level of expertise to maintain. Physical-chemical methods can also accommodate recycling sludge to reduce further costs involved in handling sludge. However, finding an effective and feasible material is a significant challenge in physical-chemical approach. This problem has not been addressed so far as a complete solution. The key problem is to find a suitable material, which is easily available and effective to remove phosphorus from small-scale wastewater applications.

Biosolid management is considered very important, as there are considerable amounts of biosolids generated due to anthropogenic reasons. Alum sludge, a biosolid generated in the coagulation process in a water treatment plant, is one such type.

Divalent and trivalent cation-based materials are known to be effective for phosphorus removal. Therefore, aluminum-based residuals (i.e., alum sludge) are a viable option for being an effective phosphorus removal material. Alum is typically effective in phosphorus removal in chemical precipitation process [17]. Therefore, use of alum sludge can be effective for phosphorus removal. Air-dried alum sludge has also been attempted in limited manner by some researchers with success [18]. However, the use of waste material (alum sludge) not only can provide low-cost appropriate technological alternative for small-scale applications but also reduce hazard and cost related to the disposal of large amount of alum sludge.

The aim of this work was to investigate the effectiveness of oven-dried alum sludge for adsorption of orthophosphate from deionized water and to compare the results with other conventional adsorbent (i.e., activated carbon).

1.1. Adsorption Isotherm. The most common forms of adsorption isotherms used in chemical-environmental engineering are the Langmuir and the Brunauer, Emmett and Teller (BET) besides the Freundlich empirical model [19–23]. The Langmuir model can be described as

$$\frac{X}{m} = \frac{(abC_e)}{(1 + aC_e)},\qquad(1)$$

where X = mass of solute adsorbed to the solid (mg), m = mass of adsorbent used (g), C_e = concentration of solute in solution at equilibrium (mg/L), a = Langmuir constant; the amount of solute adsorbed per unit weight of an adsorbent in forming a complete monolayer (L/mg), b = Langmuir constant (mg/g).

Assumptions made in developing the Langmuir model are as follows [19].

(a) The maximum adsorption corresponds to a saturated monolayer of solute molecules on the adsorbent surface.

(b) The energy of adsorbent is constant.

(c) There is no transmigration of adsorbate in the plane of the surface.

(d) The adsorption is reversible.

The Freundlich isotherm is an empirical model and was developed for heterogeneous surfaces. The Freundlich adsorption model is of the form [19]

$$\frac{X}{m} = kC_e^{1/n},\qquad(2)$$

where k = Freundlich equilibrium constant indicative of adsorptive capacity, n = Freundlich constant indicative of adsorption intensity.

Combination of Langmuir-Freundlich isotherm model, that is, the SIPS model for single component adsorption [24] is

$$q_e = \frac{\left(bqmC_e^{1/n}\right)}{\left(1 + bC_e^{1/n}\right)}.\qquad(3)$$

The BET isotherm model is of the form

$$\frac{X}{m} = \frac{(AC_eX_m)}{\left[(C_s - C_e)\left\{1 + (A-1)^{C_e/C_s}\right\}\right]},\qquad(4)$$

where A = a constant describing energy interaction between the solute and the adsorbent surface, X_m = amount of solute adsorbed in forming a complete monolayer (M/M), C_e = concentration of solute in solution at equilibrium, C_s = saturation concentration of solute in solution.

The BET isotherm model has been developed on the following assumptions [19].

(a) The model describes multilayer adsorption at the adsorbent surface.

(b) The Langmuir model applies to each layer.

(c) A given layer needs not complete formation prior to initiation of subsequent layers.

2. Experimental

2.1. Alum Sludge. Alum sludge is a waste material generated during the coagulation/sedimentation process in a drinking water treatment plant. Inorganic materials in alum sludge are presented in Table 1.

Alum sludge used in this research was heated in an oven at 105°C for 24 hours. The dried sludge was then cooled to room temperature. The sludge particles were then crushed to produce a particle size of (0.5, 2.36, and 4.75) mm. The physical properties are listed in Table 2.

2.2. Granulated Activated Carbon (GAC). Granulated activated carbon (GAC) is one of the most widely used adsorbents for organic, metallic, and inorganic contaminants in water. It was supplied by Unicarbo, Italians to the Iraqi local markets. The physical properties are listed in Table 3 [25].

2.3. Adsorbate. Orthophosphate (potassium dihydrogen orthophosphate KH_2PO_4) was used to prepare a phosphorus solution. Orthophosphate was chosen as it is the key species of phosphorus in most wastewaters. The physical properties of KH_2PO_4 are listed in Table 4.

TABLE 1: Inorganic materials in alum sludge.

Constituent	Weight percent
Aluminum	3.38%
Iron	0.819%
Manganese	0.16%
Chromium	0.013%
Vanadium	0.002%
Zinc	0.0098%
Lead	0.0001%
Barium	0.0001%
Arsenic	0.0002%

TABLE 2: Physical properties of oven dried alum sludge.

Item name	Oven dried alum sludge
Bulk density (kg/m^3)	786.7
Particle porosity	0.7
Bed porosity	0.65
BET surface area (m^2/g)	191

TABLE 3: Physical properties of activated carbon.

Item name	Granulated activated carbon
Base	Coconut shell
Apparent density (kg/m^3)	480–490
Bulk density (kg/m^3)	770
BET surface area (m^2/g)	1000
Particle porosity	0.5
Bed porosity	0.4
Ash content (%)	5 (max)
Iodine number (mg/g)*	1100–1130
pH**	10.2–10.6

*The iodine number refers to the milligrams of a 0.02 normal iodine solution per gram of GAC during a standard test (ASTM D4607).
**The pH of a solution of distilled water with a specific dosage of GAC according to a standard test (ASTM D3838).

TABLE 4: Main properties of adsorbate.

Name of component	Potassium dihydrogen orthophosphate
Chemical symbol	KH_2PO_4
Name of company	The British Drug Houses LTD/England
Molecular weight	136.09 kg/kg·mole
Assay (acidimetric)	99 to 101 per cent
Chloride (Cl)	Not more than 0.01 per cent
Sodium (Na)	Not more than 0.2 per cent
Sulphate (SO_4)	Not more than 0.05 per cent
pH (1 percent solution)	4.5 to 4.7

2.4. Wastewater. Deionized water was spiked with KH_2PO_4 to prepare a phosphorus solution of (5 and 10) mg/L; the masses used are listed in Table 5. The phosphorus concentration was chosen as typical phosphorus concentration in many wastewaters.

TABLE 5: Phosphorus solution.

Phosphorus concentration (mg/L)	KH_2PO_4 to be added (g)
5	0.00715
10	0.0143

2.5. Adsorption Column. The fixed bed adsorber studies were carried out in Q.V.F. glass column of 2 in. (50.8 mm) I.D. and (30 and 50) cm in height.

The oven-dried alum sludge was confined in the column by fine stainless steel screen at the bottom and a glass cylindrical packing at the top of the bed to ensure a uniform distribution of influent through the alum sludge. The influent solution was introduced to the column through a perforated plate, fixed at the top of the column.

2.6. Experimental Arrangements. The schematic representation of experimental equipment is shown in Figure 1.

3. Experimental Work

3.1. Batch Experiments. Batch experiments were used to obtain the equilibrium isotherm curves and then the equilibrium data. In batch mode the following experiments were carried out:

(i) effect of oven-dried alum sludge weight on adsorption process,

(ii) effect of pH of solution on adsorption process,

(iii) equilibrium isotherm experiments.

All experiments were carried out at 25°C ± 1. The desired pH was adjusted using 0.1 M NaOH and HCl.

Five 1 L flasks were used for each pH solution (i.e., 5, 6, 7, and 8). For experiments conducted with an initial phosphorus concentration of 5 mg/L, alum sludge was used in concentration of (10, 20, 30, 40 and 50) g/L. Samples were collected from the flasks and after 7.5 days tested for total orthophosphate phosphorus concentration. Phosphorus that was lost from the solution was assumed to be adsorbed onto the adsorbents. Data obtained from batch tests conducted on deionized water fitted to Freundlich, Langmuir, and Freundlich-Langmuir adsorption isotherm equations.

3.2. Fixed Bed Column Experiments. Column experiments were carried out to measure the breakthrough curves for the systems. Experiments were carried out at various pH, initial phosphorus concentrations (C_o), particle size, flow rate (Q), and bed depth (H).

4. Results

4.1. Batch Experiments

4.1.1. Effect of Mass of Oven-Dried Alum Sludge on the Adsorption Process. The results of the dependence of phosphorus on the mass of oven-dried alum sludge of size 0.5 mm at 25°C
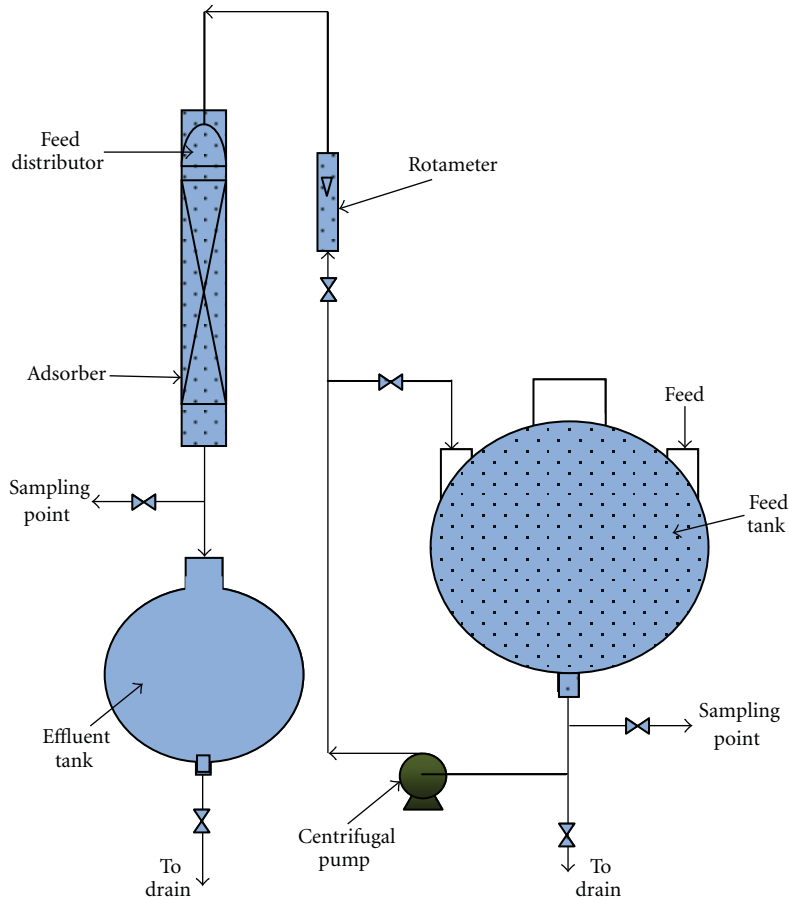
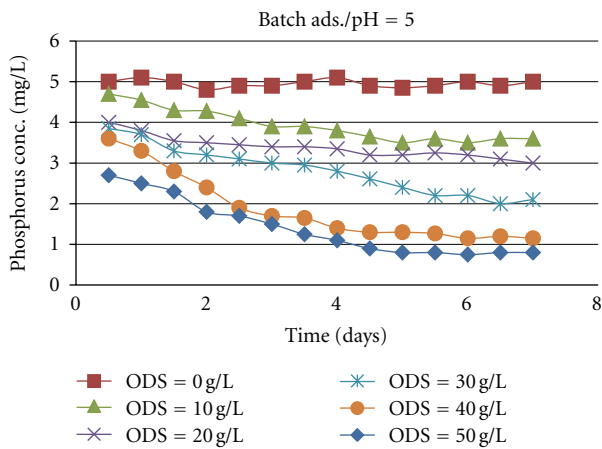FIGURE 1: Schematic representation of experimental equipment.

FIGURE 2: Change in phosphorus concentration with time of batch tests (C_o = 5 mg/L, pH = 5, Temp. = 25°C, particle size = 0.5 mm).
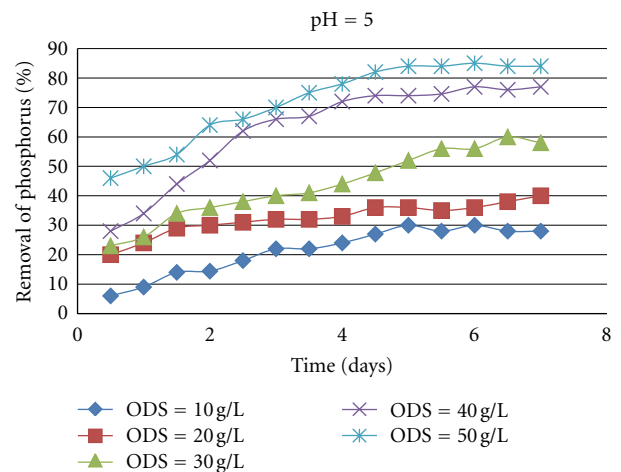
FIGURE 3: The effect of ODS on phosphorus removal (C_o = 5 mg/L, pH = 5, Temp. = 25°C, particle size = 0.5 mm).

are shown in Figures 2, 3, 4, 5, 6, 7, 8, and 9. These figures represent the plotting of the phosphorus concentration with time and the percentage removal of phosphorus against the mass of oven-dried alum sludge, respectively.

The percent removal of phosphorus increases with increasing weight of oven-dried alum sludge up to a certain value depending on adsorption sites. These figures can clearly show that the increase in the percent removal of phosphorus
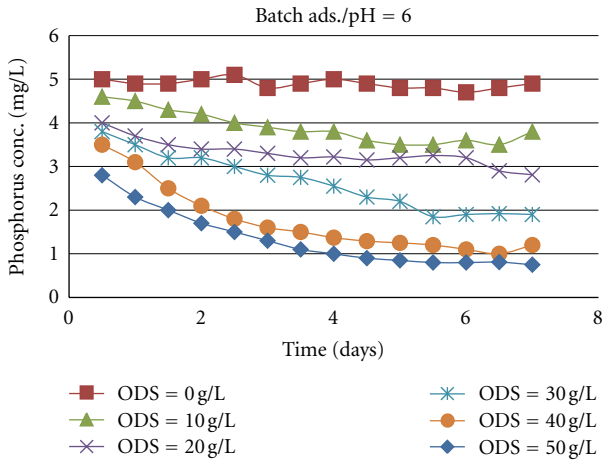
FIGURE 4: Change in phosphorus concentration with time of batch tests (C_o = 5 mg/L, pH = 6, Temp. = 25°C, particle size = 0.5 mm).
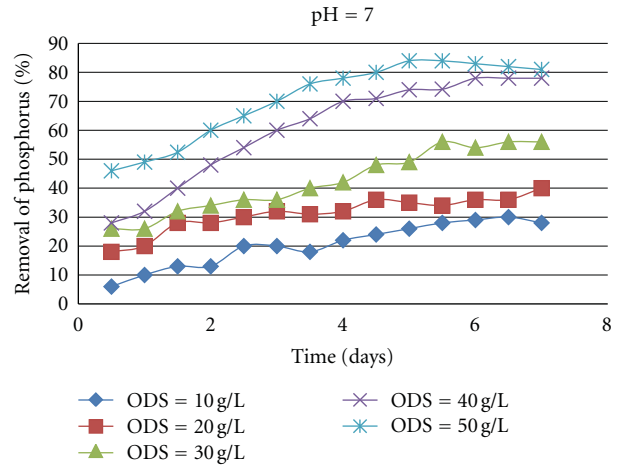
FIGURE 7: The effect of ODS on phosphorus removal (C_o = 5 mg/L, pH = 7, Temp. = 25°C, particle size = 0.5 mm).
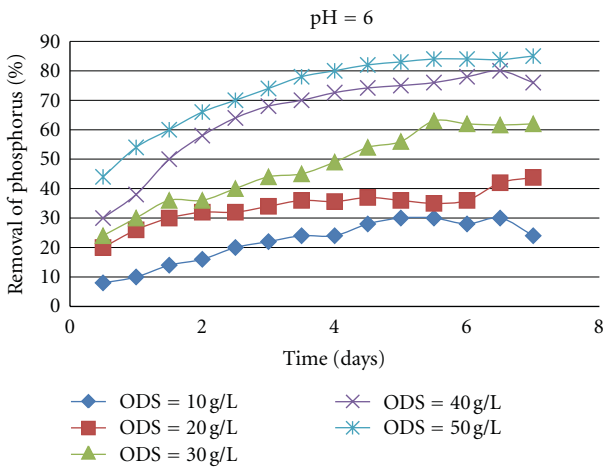
FIGURE 5: The effect of ODS on phosphorus removal (C_o = 5 mg/L, pH = 6, Temp. = 25°C, particle size = 0.5 mm).
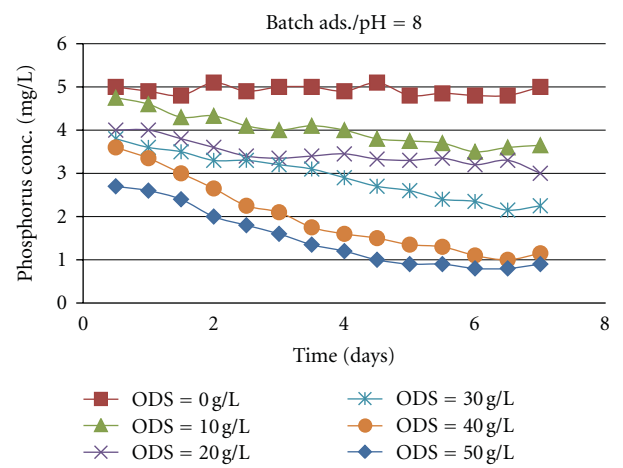
FIGURE 8: Change in phosphorus concentration with time of batch tests (C_o = 5 mg/L, pH = 8, Temp. = 25°C, particle size = 0.5 mm).
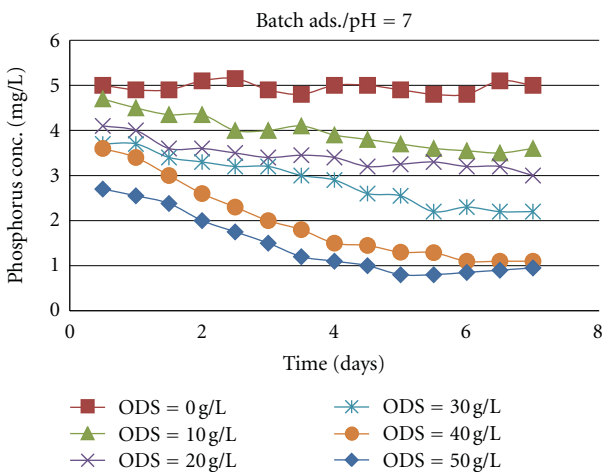
FIGURE 6: Change in phosphorus concentration with time of batch tests (C_o = 5 mg/L, pH = 7, Temp. = 25°C, particle size = 0.5 mm).
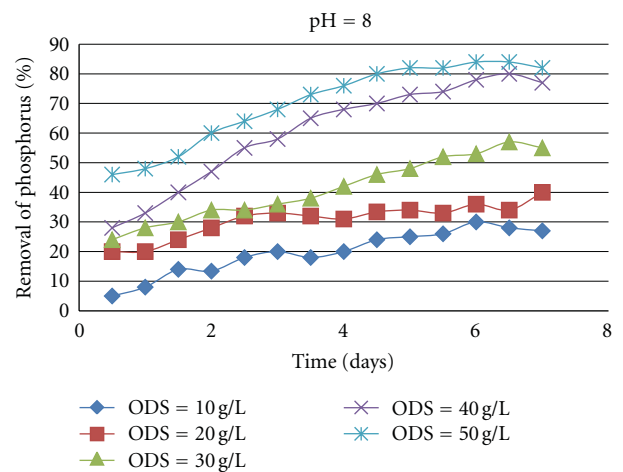
FIGURE 9: The effect of ODS on phosphorus removal (C_o = 5 mg/L, pH = 8, Temp. = 25°C, particle size = 0.5 mm).

FIGURE 10: The effect of pH on adsorption of phosphorus by ODS (C_o = 5 mg/L, mass of sludge = 10 g/L, Temp. = 25°C).
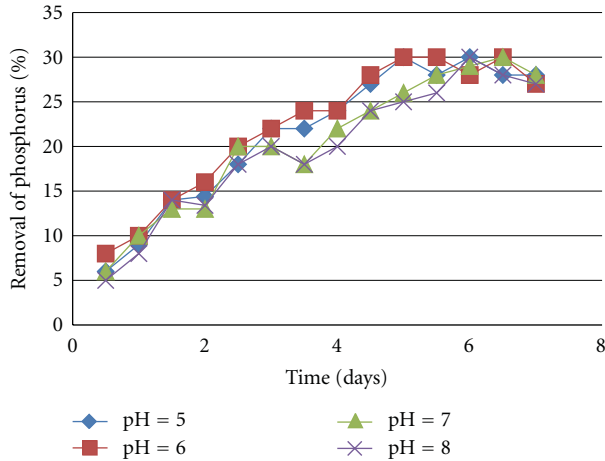

FIGURE 11: The effect of pH on adsorption of phosphorus by ODS (C_o = 5 mg/L, mass of sludge = 20 g/L, Temp. = 25°C).

is due to the greater availability of adsorption sites or surface area of adsorbent (oven-dried alum sludge).

4.1.2. Effect of pH on the Adsorption Process. The removal of phosphorus by using oven-dried alum sludge, as a function of pH, is presented in Figures 10, 11, 12, 13, and 14. Effect of pH, on the adsorption density is illustrated in Figure 15. pH had little effect on the adsorption density. However, solution pH of 6 appeared to produce maximum adsorption density in many of the experimental results.

The effluent pH was understandably dependent on the influent pH. An influent pH 5 produced effluent pH of (4.7–5.5). Similarly an influent pH 6 generated an effluent pH range (5.6–6.3), and an influent pH 7 generated an effluent pH range of (6.5–7.5). It was due to the adsorption and desorption of H$^+$ ions during the adsorption of phosphorus on alum sludge. An effluent pH below 4.5 is not suitable for disposal in surface water. The effluent pH can be increased prior to disposal in surface water. However, the cost of chemicals to reduce initial pH and to increase final pH and hazards of dealing with increased amount of sludge would pose negative interest for pH control.

In general, a pH value in the range of (6–9) is reasonable for wastewaters before disposal into surface water.

The removals of phosphorus on oven-dried alum sludge for all the pHs were more than (80)%.

4.2. Equilibrium Isotherm Experiments. The adsorption isotherm curves were obtained by plotting the weight of the solute adsorbed per unit weight of the adsorbent (q_e) against the equilibrium concentration of the solute (c_e). Figures 16, 17, 18, and 19 show the adsorption isotherm curves for phosphorus adsorption onto oven-dried alum sludge at 25°C. The obtained data of phosphorus was correlated with Langmuir, Freundlich, and Langmuir-Freundlich models. The parameters for each model were obtained from nonlinear statistical fit of the equation to the experimental
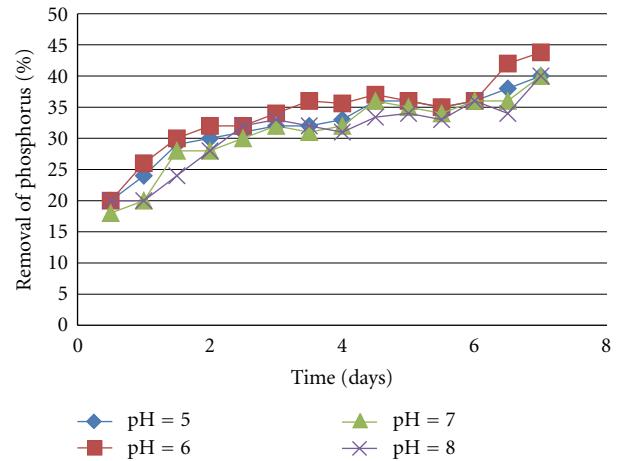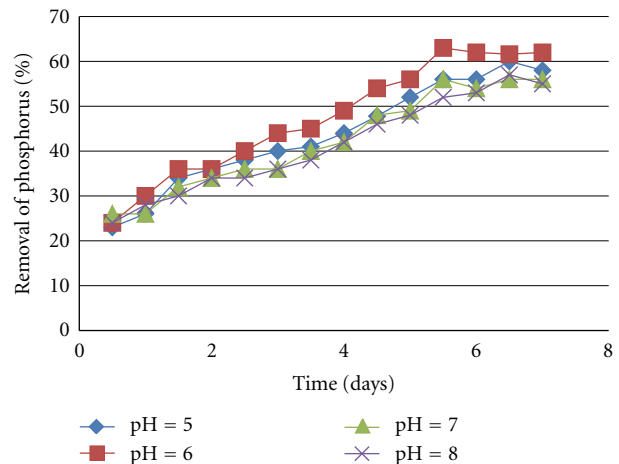

FIGURE 12: The effect of pH on adsorption of phosphorus by ODS (C_o = 5 mg/L, mass of sludge = 30 g/L, Temp. = 25°C).

data. All parameters with their correlation coefficients (R^2) are summarized in Table 6.

It is clear from the previous figures and table the following.

(i) The equilibrium isotherm is of favorable type, for being convex upward.

In order to assess the different isotherms and their ability to correlate with experimental results, the correlation coefficient was employed to ascertain the fit of each isotherm with experimental data. From Table 6, the correlation coefficient value was higher for Langmuir-Freundlich than other correlations. This indicates that the Langmuir-Freundlich isotherm is clearly the best fitting isotherm to the experimental data.
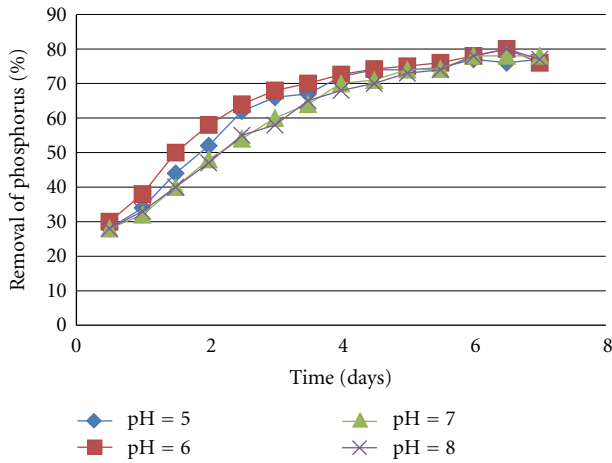
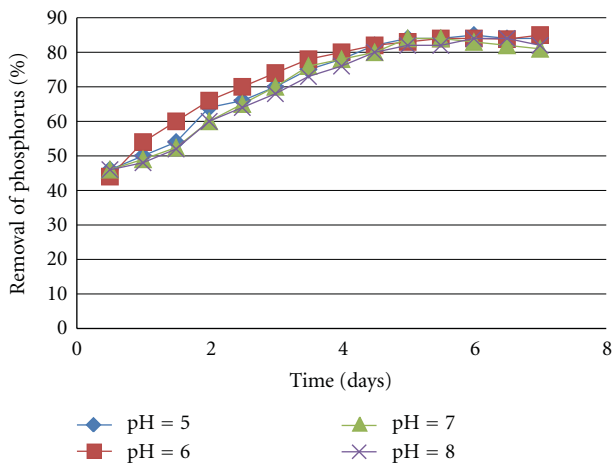FIGURE 13: The effect of pH on adsorption of phosphorus by ODS (C_o = 5 mg/L, mass of sludge = 40 g/L, Temp. = 25°C).

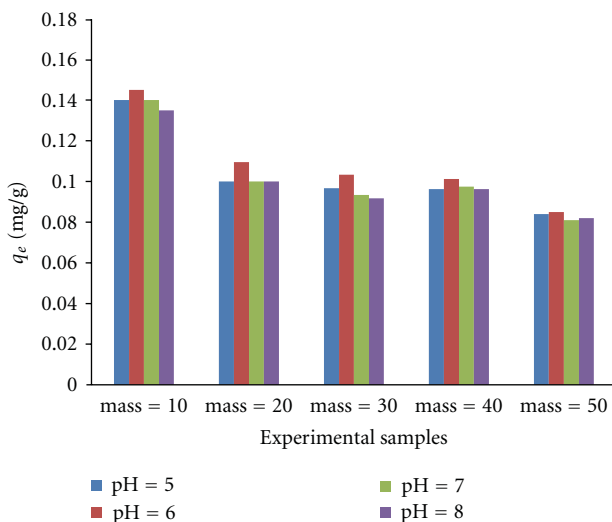FIGURE 14: The effect of pH on adsorption of phosphorus by ODS (C_o = 5 mg/L, mass of sludge = 50 g/L, Temp. = 25°C).

FIGURE 15: The effect of pH of solution on adsorption density.

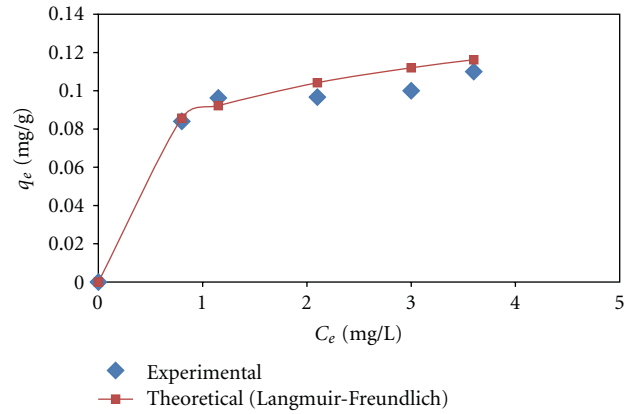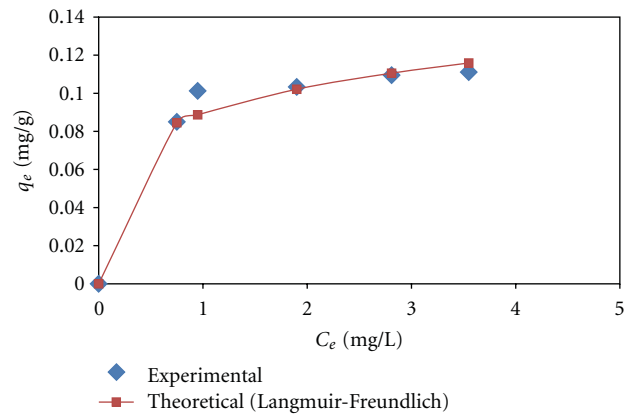FIGURE 16: Adsorption isotherm for phosphorus onto ODS (C_o = 5 mg/L, pH = 5, Temp. = 25°C).

FIGURE 17: Adsorption isotherm for phosphorus onto ODS (C_o = 5 mg/L, pH = 6, Temp. = 25°C).

4.3. Fixed Bed Experiments

4.3.1. Effect of Initial Concentration. Experimental data for adsorption of phosphorus onto ODS at flow rate of 6 L/hr, bed depth of 0.25 m, and particle size of 2.36 mm are shown in Figure 20. It is clear from the breakthrough curves that an increase in the initial concentration makes the breakthrough curves much steeper, which would be anticipated with the basis of the increases in driving force for mass transfer with increases in concentration of solute in solution. The breakpoint was inversely related to the initial concentration; that is, the time required to reach saturation decreases with increasing the inlet solute concentration. This may also be explained by the fact that since the rate of diffusion is controlled by the concentration gradient, it takes a longer contact time to reach saturation for the case of low value of initial solute concentration.

4.3.2. Effect of Particle Size. The breakthrough curves as shown in Figure 21 were obtained for different particle size at constant initial concentration of phosphorus (10 mg/L), bed depth of oven-dried alum sludge (0.25 m), and constant flow rate (6 L/hr). The experimental results showed that fine
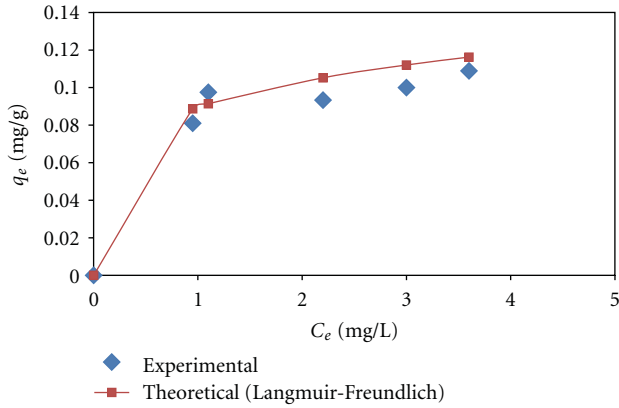
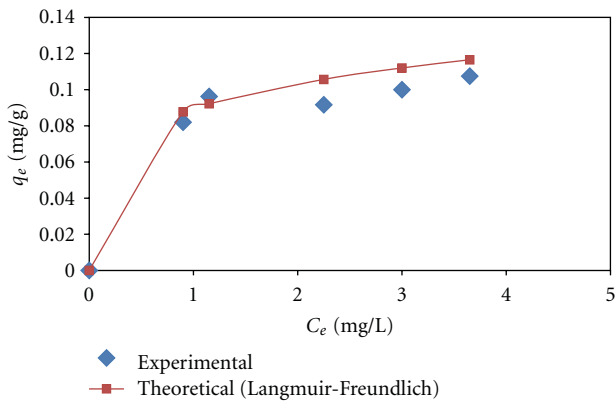FIGURE 18: Adsorption isotherm for phosphorus onto ODS (C_o = 5 mg/L, pH = 7, Temp. = 25°C).

FIGURE 19: Adsorption isotherm for phosphorus onto ODS (C_o = 5 mg/L, pH = 8, Temp. = 25°C).

TABLE 6: Isotherm parameters for phosphorus adsorption onto ODS with the correlation coefficient.

Model	Parameters	Values
	a,	2.437878
Langmuir (1)	b,	0.128524
	Correlation coefficient	0.977
	K,	0.090537
Freundlich (2)	n,	2.92948
	Correlation coefficient	0.9946
	q_m,	3.675591
Combination of	b,	0.025254
Langmuir-Freundlich (3)	n,	4.793108
	Correlation coefficient	0.995

particle sizes showed a higher phosphorus removal than coarse particle sizes as illustrated in the figure. This was due to large surface area of fine particles.

4.3.3. Effect of Flow Rate and Bed Depth. In the design of a fixed bed adsorption column, the contact time is the most significant variable, and therefore the bed depth

FIGURE 20: Experimental breakthrough curves for adsorption of phosphorus onto ODS at different initial concentration.
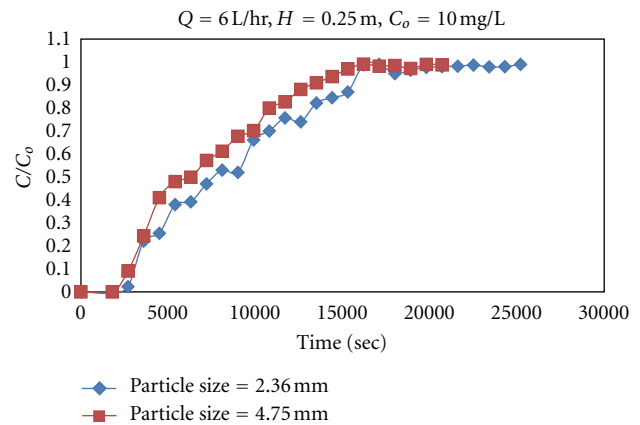
FIGURE 21: Experimental breakthrough curves for adsorption of phosphorus onto ODS at different particle size.

and the flow rate are the major design parameter. The effect of varying the volumetric flow rate was investigated. The experimental breakthrough curves are presented in Figure 22 in terms of C/C_o versus time at constant initial concentration of phosphorus (10 mg/L) and particle size (2.36 mm). Increasing the flow rate may be expected to make reduction of the surface film. Therefore, this will decrease the resistance to mass transfer and increase the mass transfer rate. Also, because the reduction in the surface film is due to the disturbance created when the film of the bed increased resulting from easy passage of the adsorbate molecules through the particles and entering easily to the pores, this decreased contact time between phosphorus and oven-dried alum sludge at high flow rate. The effect of bed depth was investigated for phosphorus adsorption onto oven-dried alum sludge; the experimental breakthrough curves are presented in Figure 23. The breakthrough curves were obtained for different bed depth of oven-dried alum sludge at constant flow rate and constant P concentration. It is clear that the increase in bed depth increases the breakthrough time and

FIGURE 22: Experimental breakthrough curves for adsorption of phosphorus onto ODS at different flow rates.

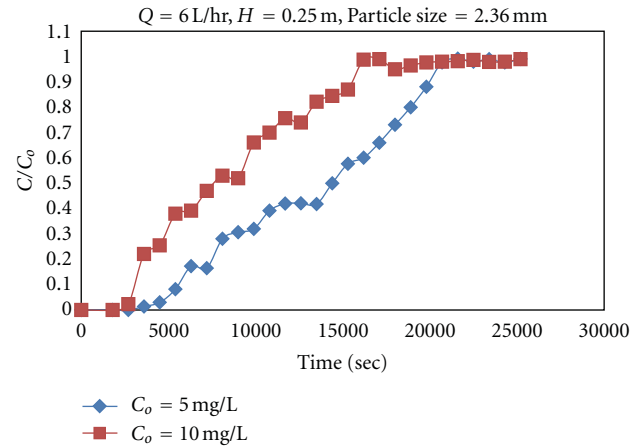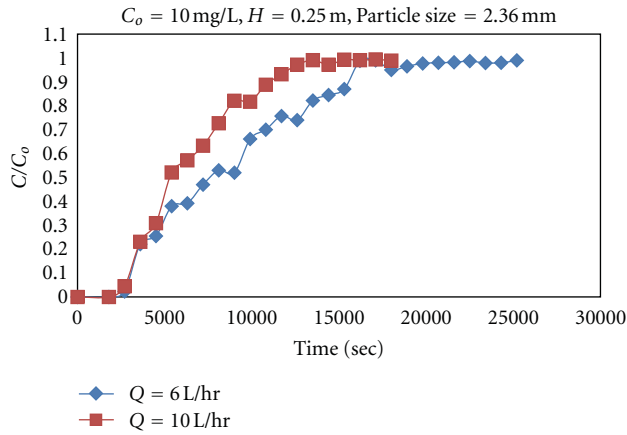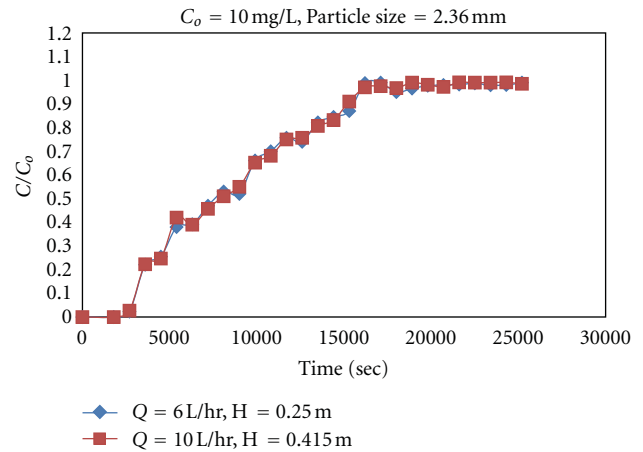FIGURE 24: Experimental breakthrough curves for adsorption of phosphorus onto ODS at different residence time.
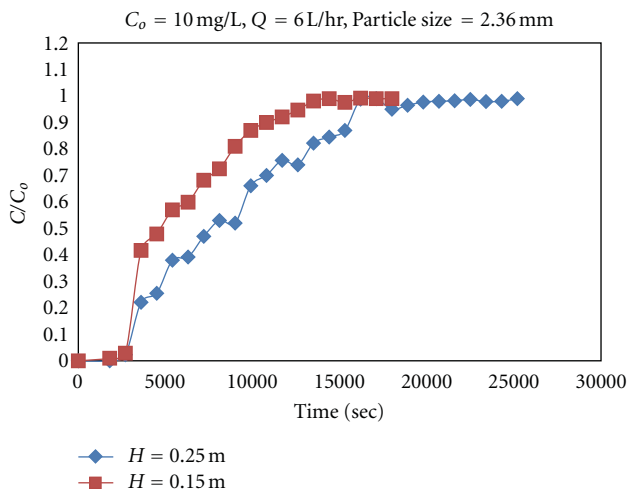
FIGURE 23: Experimental breakthrough curves for adsorption of phosphorus onto ODS at different bed depth.

FIGURE 25: Comparison between ODS and granular-activated carbon for phosphorus adsorption.

the residence time of the solute in the column. A comparison is shown in Figure 24, where bed depths are different but residence time was kept constant by changing the flow rate. These results show that increases of fluid velocity had no significant effect. Thus, the residence time in the column is more important than fluid velocity in improving the removal efficiency. The results are obtained, here.

4.3.4. Oven-Dried Alum Sludge Compared to Granular Activated Carbon. The results obtained, here, are presented in Figure 25. Granular-activated carbon (GAC) was used in this study as a reference by which to compare adsorption with oven-dried alum sludge. The results showed that granular-activated carbon had the best phosphorus removal capability due to its higher surface area. These results were on the contrary with the results obtained by Maruf et al., [26] due to higher surface area of alum sludge that was collected from the

Lake Major Water Treatment Plant, Halifax Regional Municipality, Canada with respect to granular-activated carbon; also this was probably because of other adsorbates competing with phosphorus in secondary municipal wastewater for adsorption sites.

5. Conclusions

The present study has led to the following conclusions.

(1) Oven-dried alum sludge was effective in adsorbing phosphorus from deionized water.

(2) In batch experiment the percent removal of phosphorus increases (85%) with increasing in the oven-dried alum sludge dose (i.e., 50 g/L at deferent pH).

(3) Batch kinetics experiments showed that equilibrium time was about 6 days without mechanical mixing.

(4) The results showed that the model (Langmuir-Freundlich) gave good fitting for adsorption capacity.

(5) In fixed bed experiment, the percent removal of phosphorus increases with increasing contact time and adsorbent surface area.

Nomenclature

a: Langmuir constant (L/mg)
b: Langmuir constant (mg/g)
C: Concentration of solute in solution (mg/L)
k: Freundlich equilibrium constant
n: Freundlich constant
m: Mass of solute adsorbent (g)
H: Bed depth (m)
pH: Acidity
Q: Flow rate (L/hr)
q: Amount of metal ion adsorbed (mg/g)
R^2:   Correlation coefficients
x: Mass of solute adsorbed (mg)
X_m: Amount of solute adsorbed in forming a complete monolayer (M/M).

Abbreviations

P: Phosphorus
ODS: Oven-dried alum
MTZ: Mass transfer zone
GAC: Granulated activated carbon
BET: The Brunauer, Emmett, and Teller
QVF: Quality vessels fabrication
ASTM: American society for testing and materials
USEPA: United states environmental protection agency
ID: Inner diameter.

Subscript

o: Initial
e: Equilibrium
s: Saturation.

References

[1] Environment Canada, "Proposed approach for wastewater effluent quality," Final Report, Environment Canada, 2000.

[2] USEPA, Environmental Assessment for the Final Effluent Limitations Guidelines, Pretreatment Standards for New and Existing Sources and New Source Performance Standards for the Centralized Waste Treatment, Prepared by Charles Tamulonis, 2000.

[3] Department of Justice, *Pollutant Substances Prevention Regulation*, Department of Justice, Ottawa, Canada, 2004.

[4] D. Zhao and A. K. Sengupta, "Ultimate removal of phosphate from wastewater using a new class of polymeric ion exchangers," *Water Research*, vol. 32, no. 5, pp. 1613–1625, 1998.

[5] L. Liberti, D. Petruzzelli, and L. De Florio, "REM NUT ion exchange plus struvite precipitation process," *Environmental Technology*, vol. 22, no. 11, pp. 1313–1324, 2001.

[6] R. G. Penetra, M. A. P. Reali, E. Foresti, and J. R. Campos, "Post-treatment of effluents from anaerobic reactor treating domestic sewage by dissolved-air flotation," *Water Science and Technology*, vol. 40, no. 8, pp. 137–143, 1999.

[7] P. Jokela, E. Ihalainen, J. Heinänen, and M. Viitasaari, "Dissolved air flotation treatment of concentrated fish farming wastewaters," *Water Science and Technology*, vol. 43, no. 8, pp. 115–121, 2001.

[8] K. C. Yu, J. S. Chang, I. P. Chen, D. J. Chang, C. Y. Chang, and S. H. Chen, "The removal of colloid and dissolved phosphorus by coagulation and membrane microfiltration," *Journal of Environmental Science and Health A*, vol. 35, no. 9, pp. 1603–1616, 2000.

[9] A. Dietze, R. Gnirß, and U. Wiesmann, "Phosphorus removal with membrane filtration for surface water treatment," *Water Science and Technology*, vol. 46, no. 4-5, pp. 257–264, 2002.

[10] W. Xie, M. Kondo, and Y. Naito, "Study on phosphorus removal using a new coagulation system," *Water Science and Technology*, vol. 30, no. 6, pp. 257–262, 1994.

[11] L. Jonsson, E. Plaza, and B. Hultman, "Experiences of nitrogen and phosphorus removal in deep-bed filters in the Stockholm area," *Water Science and Technology*, vol. 36, no. 1, pp. 183–190, 1997.

[12] F. Rogalla, G. Roudon, J. Sibony, and F. Blondeau, "Minimising nuisances by covering compact sewage treatment plants," *Water Science and Technology*, vol. 25, no. 4-5, pp. 363–374, 1992.

[13] S. Zeghal, N. Puznava, J. P. Subra, and P. Sauvegrain, "Process control for nutrients removal using lamella sedimentation and floating media filtration," *Water Science and Technology*, vol. 38, no. 3, pp. 227–235, 1998.

[14] D. G. Wareham, K. J. Hall, and D. S. Mavinic, "ORP screening protocol for biological phosphorus removal in sequencing batch reactors," *Canadian journal of civil engineering*, vol. 22, no. 2, pp. 260–269, 1995.

[15] N. R. Louzeiro, D. S. Mavinic, W. K. Oldham, A. Meisen, and I. S. Gardner, "Methanol-induced biological nutrient removal kinetics in a full-scale sequencing batch reactor," *Water Research*, vol. 36, no. 11, pp. 2721–2732, 2002.

[16] J. K. Park, J. Wang, and G. Novotny, "Wastewater characteristization for evaluation of biological phosphorus removal," Research Report 174, Department of Natural Resources, Wisconsin, Wis, USA, 1997.

[17] M. I. Aguilar, J. Sáez, M. Lloréns, A. Soler, and J. F. Ortuño, "Nutrient removal and sludge production in the coagulation-flocculation process," *Water Research*, vol. 36, no. 11, pp. 2910–2919, 2002.

[18] J. G. Kim, J. H. Kim, H. S. Moon, C. M. Chon, and J. S. Ahn, "Removal capacity of water plant alum sludge for phosphorus in aqueous solutions," *Chemical Speciation and Bioavailability*, vol. 14, no. 1–4, pp. 67–73, 2003.

[19] J. R. Weber and J. Walter, *Physicochemical Processes for Water Quality Control*, Wiley-Inter Science, New York, NY, USA, 1972.

[20] Metcalf and Eddy, *Waste Water Engineering Treatment, Disposal and Reuse*, McGrew Hill Book Company, New York, NY, USA, 1979.

[21] W. W. Eckenfelder Jr, *Application of Adsorption to Waste Water Treatment*, Enviro Press, Nashville, Tenn, USA, 1981.

[22] L. D. Benefield, J. L. Judkins, and B. L. Weanal, *Process Chemistry for Water and Wastewater Treatment*, Prentice Hall, New Jersey, NJ, USA, 1982.

[23] T. D. Reynolds and P. A. Richards, *Unit Operation and Processes in Environmental Engineering*, PWS publishing Co, Boston, Mass, USA, 1996.

[24] R. Sips, "Structure of a catalyst surface," *Journal of Chemical Physics*, vol. 16, pp. 490–495, 1984.

[25] S. E. Ebrahim, *Evaluation of mixture adsorption and glass bed for the removal of phenol and methylene blue from water [Ph.D. thesis]*, University of Baghdad, Baghdad, Iraq, 2008.

[26] M. Mortula, M. Gibbons, and G. A. Gagnon, "Phosphorus adsorption by naturally-occurring materials and industrial by-products," *Journal of Environmental Engineering and Science*, vol. 6, no. 2, pp. 157–164, 2007.

Research Article

Effect of Temperature Change on Geometric Structure of Isolated Mixing Regions in Stirred Vessel

Nor Hanizah Shahirudin, Alatengtuya, Norihisa Kumagai, Takafumi Horie, and Naoto Ohmura

Department of Chemical Science and Engineering, Kobe University, 1-1 Rokkodai, Nada, Hyogo, Kobe 657-8501, Japan

Correspondence should be addressed to Naoto Ohmura, ohmura@kobe-u.ac.jp

The present work experimentally investigated the effect of temperature change on the geometric structure of isolated mixing regions (IMRs) in a stirred vessel by the decolorization of fluorescent green dye by acid-base neutralization. A four-bladed Rushton turbine was installed in an unbaffled stirred vessel filled with glycerin as a working fluid. The temperature of working fluid was changed in a stepwise manner from 30°C to a certain fixed value by changing the temperature of the water jacket that the vessel was equipped with. The step temperature change can dramatically reduce the elimination time of IMRs, as compared with a steady temperature operation. During the transient process from an initial state to disappearance of IMR, the IMR showed interesting three-dimensional geometrical changes, that are, simple torus with single filament, simple torus without filaments, a combination of crescent shape and circular tori, and doubly entangled torus.

1. Introduction

Stirred vessels are frequently used to homogenize different substances, conduct chemical reactions, and enhance mass transfer between different phases. These vessels are versatile and they are available in a wide variety of sizes and impeller configurations for use in industrial processes. Although turbulent flow is efficient for mixing, laminar mixing is required in some cases such as for high-viscosity fluids and shear-sensitive materials. Koiranen et al. [1] proposed specific principles for effective mixing of highly viscous liquids or shear-sensitive materials in laminar flow mixing regimes. In these regimes, global mixing is inefficient due to the existence of isolated mixing regions (IMRs). Makino et al. [2] characterized IMRs in a stirred vessel using radial flow impellers and found that IMRs consisted of various Kolmogorov-Arnold-Moser (KAM) tori. Ohmura et al. [3] reported the existence of KAM tori as island structures in a phase-locked orbit that has a rational relation of the time period between the primary and secondary circulation flows. Noui-Mehidi et al. [4] found that the mechanism of IMR disappearance could be described by the formation of a period-doubling locus in the physical space when using a six-blade Rushton turbine impeller. Hashimoto et al. [5] successfully visualized a three-dimensional structure of thin filaments spirally wrapping around the core of toroidal region. They formulated and estimated the relation between mixing conditions and filament numbers and/or wire turns.

The elimination of IMR at low Reynolds numbers has also been studied extensively. Lamberto et al. [6] and Yao et al. [7] demonstrated that IMRs could be eliminated by using an unsteady rotation method. Takahashi and Motoda [8] proposed a method in which relatively large objects are introduced to the system in order to improve the mixing performance. Nishioka et al. [9] also found that small particles released at the liquid surface were captured within IMRs. Alatengtuya et al. [10] showed that the motion of small particles improves the material transfer between IMRs and the surrounding active mixing region (AMR).

Although research studies on IMRs in stirred vessels have been conducted extensively, few have paid attention to the effect of temperature change on laminar mixing. As industrial batch processes using stirred vessels are often conducted under nonisothermal conditions, it is crucial to
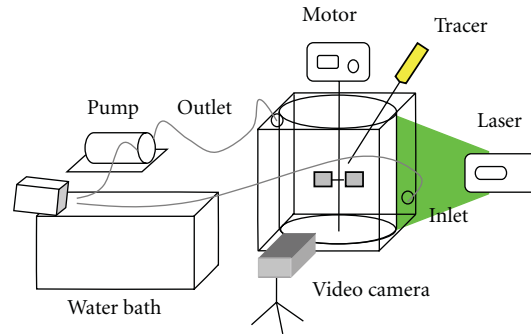
Figure 1: Experimental apparatus for flow visualization.

$A = 0.02\,\mathrm{m}$

$B = 0.035\,\mathrm{m}$

$C = 0.1\,\mathrm{m}$

$D = 0.1\,\mathrm{m}$

$T = 0.2\,\mathrm{m}$

$H = 0.18\,\mathrm{m}$

Four-bladed
Rushton impeller
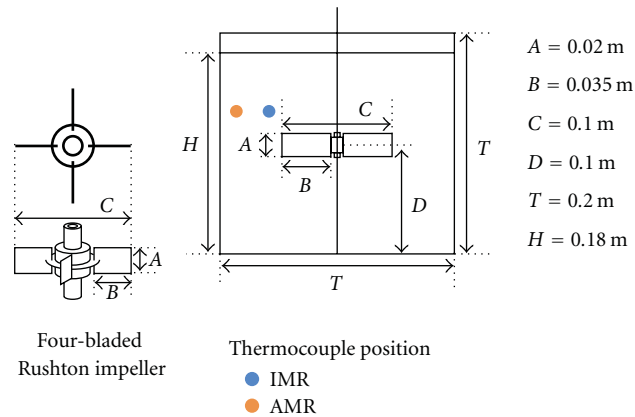
Thermocouple position
● IMR
● AMR

Figure 2: Configuration and location of a four bladed turbine impeller and position of thermocouples.

obtain knowledge of the effect of thermal unsteadiness on laminar mixing. This study, therefore, investigated transient behaviors of isolated mixing regions undergoing change of temperature in a stirred vessel.

2. Experimental

The mixing system consisted of a cylindrical flat-bottom vessel with the diameter of 0.1 m without a baffle and a four-bladed Rushton turbine, as shown in Figure 1. The cylindrical vessel was immersed in a square vessel of acrylic resin filled with water so that the temperature of glycerin solution was controlled by feeding water from a water bath, and photographic distortion was reduced. The dimensions and location of the impeller are shown in Figure 2. The impeller was installed 0.1 m from the bottom of the vessel. Hence, the ratio of impeller off-bottom clearance to the tank diameter, D/T, was 0.5.

The working fluid was glycerine ($\rho = 1260\,\mathrm{kg/m^3}$, where $\mu = 0.53\,\mathrm{Pa\,s}$ at 30°C). A fluorescent, pH sensitive and neutrally buoyant green dye, uranine, was used as a passive tracer to observe the mixing process. A small amount of basic solution made of 5 mL 1 N NaOH and 20 mL glycerin was added to the working fluid. After the impeller reached 67 rpm of rotational speed and glycerin temperature reached 30°C (the initial Reynolds number can be estimated at $Re = 27$), a small amount of acidic solution made of 5 mL 1 N HCl and

20 mL glycerin was injected approximately 1 cm away from the shaft and near to the center of impeller to decolorize the green dye by neutralization reaction. Then the feed of water was stopped for 30 minutes to maintain a stable IMR structure. While the glycerin temperature was kept at 30°C, the water bath temperature was changed to a fixed higher temperature (40, 50, 60°C). Then, the water was fed into the jacket after 30 minutes. The cross-sectional view of IMRs was visualized using a plane sheet of semiconductor laser light. The images of decolorization process were recorded by a digital video camera.

To measure the temperature in the upper IMR and its surrounding AMR, an experiment independent of the above flow visualization was conducted using two thermocouples. The positions of the two thermocouples were determined by the flow visualization experiment as shown in Figure 2 where the dots represent the thermocouples. One thermocouple was set in the upper IMR, and the other one was set in AMR.

3. Results and Discussion

3.1. Transition of IMR Structure. Figures 3 and 4 show overviews and cross-sectional views of IMR transition, respectively. One similarity in all of the experiments is that the upper torus is eliminated before the lower torus. Influence of the free liquid surface at the top of the stirred tank makes the volume of the upper torus structure smaller
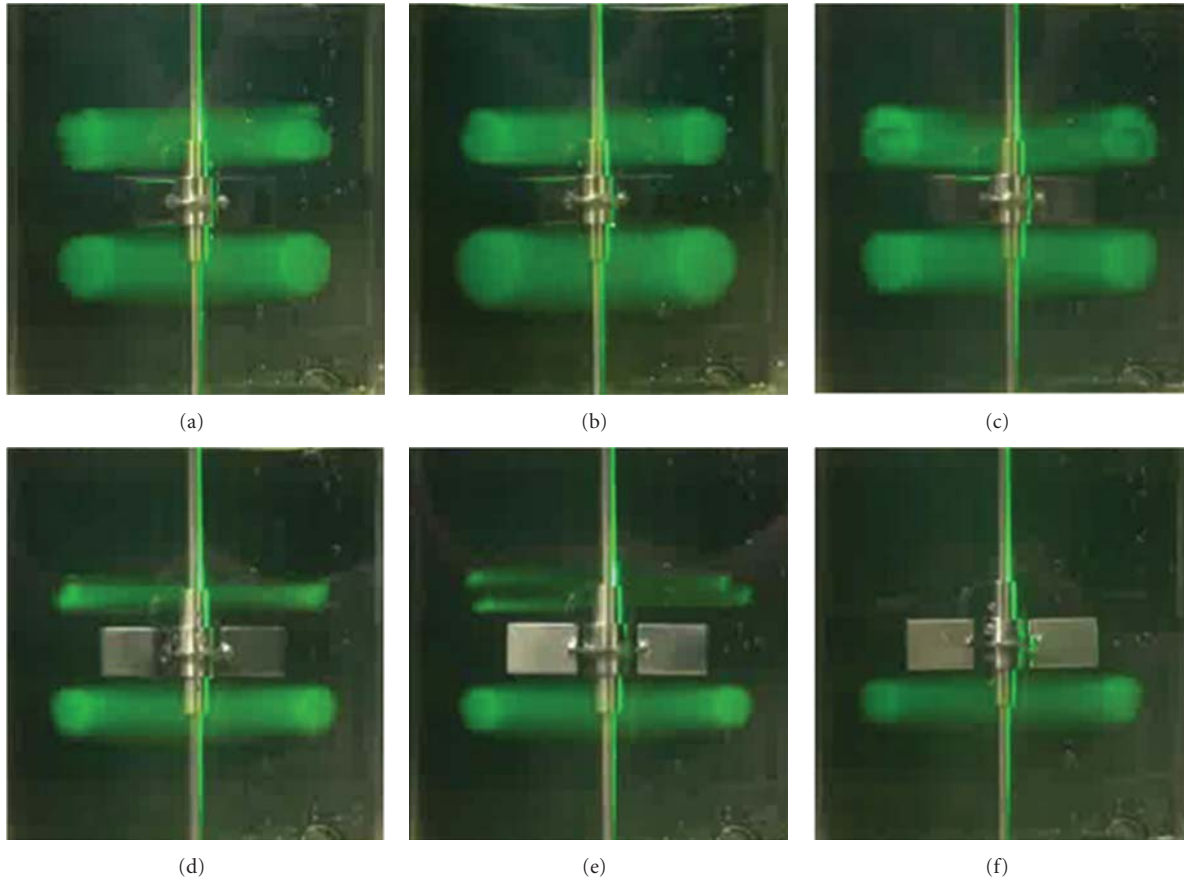
(a)   (b)   (c)

(d)   (e)   (f)

FIGURE 3: Overviews of IMR transition, $\Delta T = 10\,\mathrm{K}$.

than volume of the lower torus structure resulting in the elimination of the upper IMR first and later the lower IMR. Moreover, a larger temperature difference enhances the diffusion mechanism between IMR and AMR more easily. As illustrated in Figures 3(a) and 4(a), when the glycerin solution is maintained at 30°C, IMR is created above and below the impeller while it is preserved for 30 minutes to obtain a stable IMR structure. Since more acid is used compared to base, mixed regions of the stirred tank contain excess acid, causing the indicator in these regions to appear colorless. Segregated regions, on the other hand, contain unreacted base and display a green color. Lamberto et al. [6] explain that these regions remain segregated from the rest of the system and are not mixed by convective flow mechanisms. As time increases, single filament wrapped around the upper torus where the filament whose cross-section appears as islands formed small tori.

As temperature increases, the filament simultaneously disappear by diffusion and leave only the core torus as shown in Figures 3(b) and 4(b). After a few minutes, a large amount of fluid from the AMR penetrates into the coherent structure of IMRs resulting in combination of torus and crescent shape from the cross-section view. These shapes remain stable while the fluids inside both shapes rotate counterclockwise. Influence from the temperature difference between AMR and IMR enhances the erosion at the "outer" shells of the

toroidal regions, corresponding to Figures 3(c) and 4(c). This phenomenon continues for several minutes and returns to a stable toroidal shape. This toroidal shape becomes narrow, forming an ellipse as in Figures 3(d) and 4(d). Later, it continues to form a spiral structure of string IMR [11] that appeared as two islands from the cross-sectional view as in Figures 3(e) and 4(e). These islands' cross-sectional area decreases slowly and finally the string IMR gradually disappears, as shown in Figures 3(f) and 4(f). The above-mentioned results indicate that changing the temperature by steps can dramatically reduce the elimination time of IMRs, as compared with a steady temperature operation. This mixing enhancement might be attributed to dynamic change of flow structure due to decrease of viscosity when temperature increases. The changes of IMR structures occurred in both upper and lower IMR for different temperature variations.

3.2. Time Variations of Temperature of IMR and AMR. Figure 5 shows the time variation of temperature of IMR and AMR. Points notated from (c) to (f) in Figure 5 correspond to Figures 3 and 4. As can be seen from the graph, there is slight temperature difference between IMR and AMR for all of the temperature variations. With only 1°C to 2°C of temperature increase from the initial temperature, the changes of IMR structure started to occur. The curve in every graph for the upper IMR temperature is identical, where there is

(d)   (e)   (f)
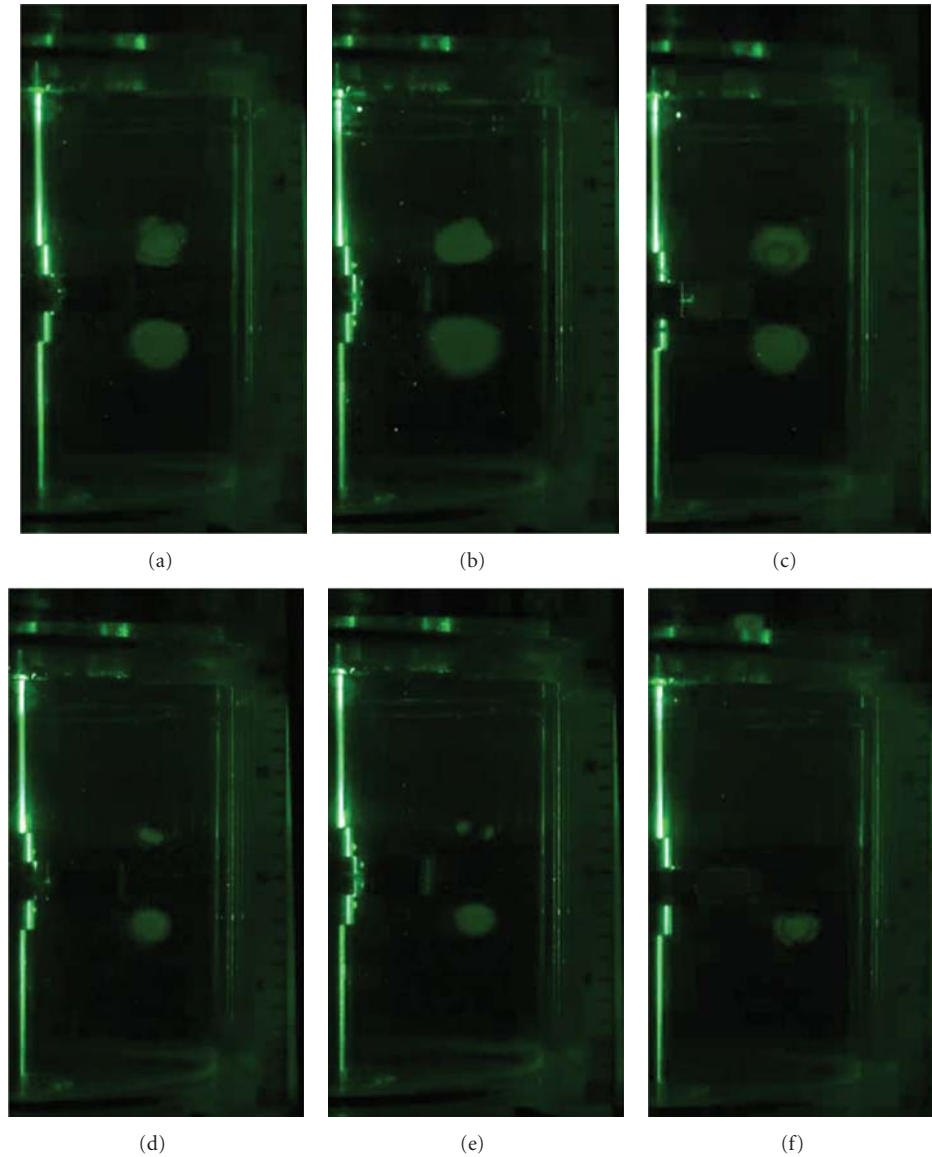
FIGURE 4: Cross-sectional views of IMR transition, $\Delta T = 10$ K.

a curve-step-like change. There is a unique characteristic indicated at (c) where the time is equivalent to the time during formation of torus and crescent shape. At point (d), as temperature increased continuously the formation of a narrow torus occurred and later a spiral structure of string IMR formed, at (e). During the elimination of the segregated region, there is no temperature difference between the two positions, as indicated at (f). Although the points in Figure 5 do not perfectly match the flow structures shown in Figures 3 and 4 because of the disturbance caused by a thermocouple in the IMR structure, nonetheless it can be seen that influence from the nonuniformity of temperature in the stirred tank allowed more interaction between IMR structure and AMR.

3.3. Dimensionless Time for Every Step of IMR Structure Transformation. Figure 6 displays the relation between dimensionless time against initial temperature difference for the upper and lower IMRs. The dimensionless time is defined as $t^* = t/t_e$, where t_e is the elimination time of IMRs, which is one criterion for mixing time. The t^* value when the combination of torus and crescent shape is formed can be considered constant while the t^* value during the formation of narrow torus and string IMR is proportional to the initial temperature difference. The dimensionless time in each step of IMR changes for 10 K temperature difference is the smallest compared to other temperature differences. The temperature step changes for 10 K temperature difference increase very slowly, which decreases the diffusive
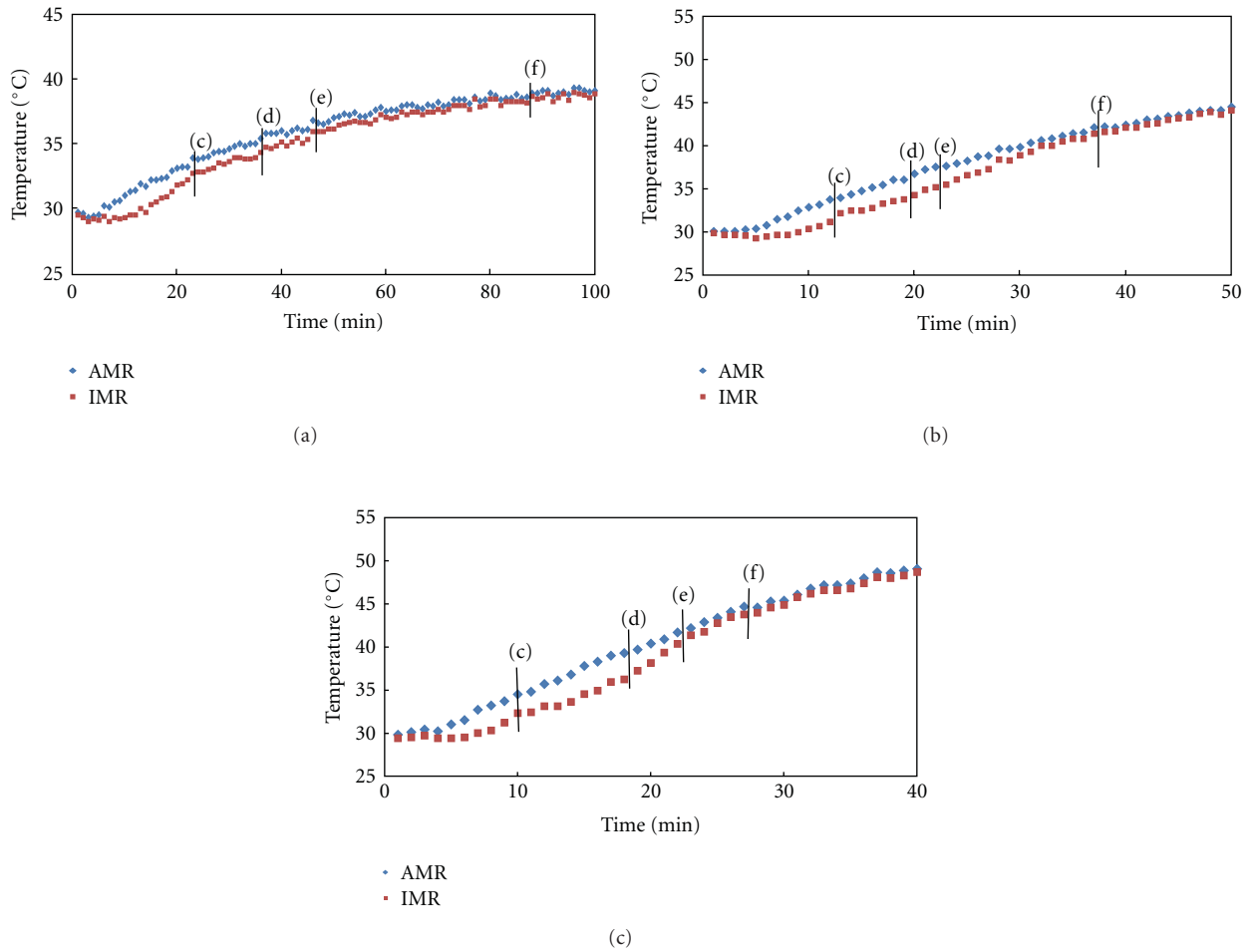
Figure 5: Time variation of temperature in the upper IMR and AMR: (a) $\Delta T = 10$ K, (b) $\Delta T = 20$ K, and (c) $\Delta T = 30$ K.
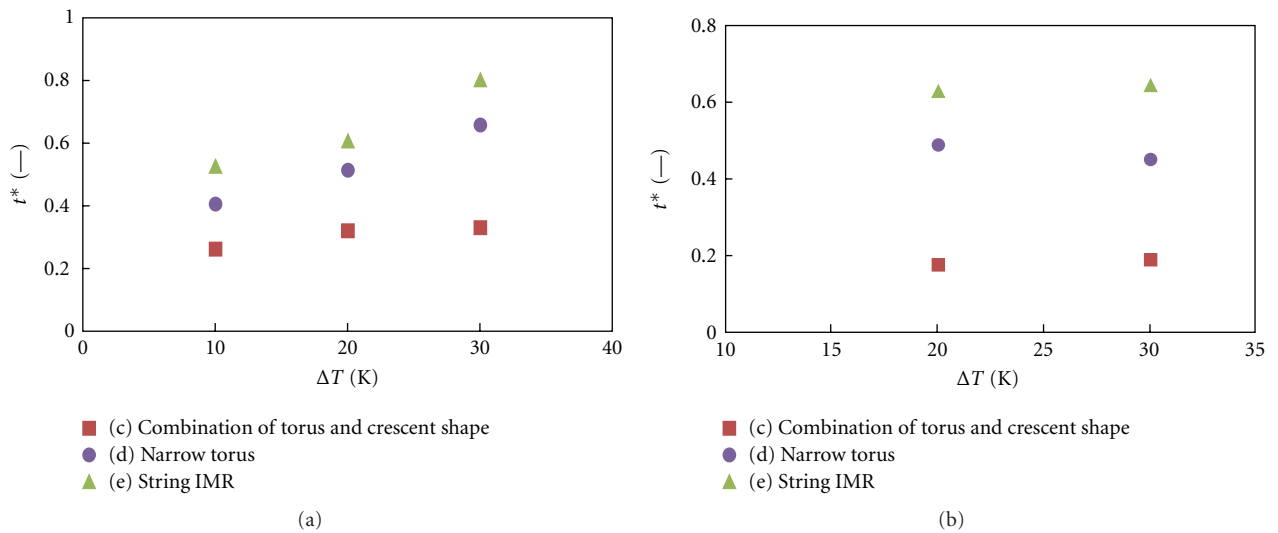

Figure 6: Dimensionless time as geometric structures of IMRs against temperature difference: (a) the upper IMR and (b) lower IMR.

mechanism between IMR and AMR. Therefore, the time for each process of IMR transformation needs to be lengthened. Moreover, it can also be considered that influence from the free surface liquid causes different trends in the results of upper IMR. Compared to the dimensionless time for upper IMR, dimensionless time for lower IMR is nearly constant for all steps of IMR structure changes. This is because the flow circulation in the lower region becomes weaker due to the existence of the bottom.

4. Conclusion

Presence of IMRs in a stirred vessel interrupts the process of achieving uniform mixing. Temperature changes from the jacket vessel can impact the structure of IMR. In this research, as the temperature started to change, the IMR structure transformed from a combination of crescent shape and torus, to narrow torus, to a spiral structure of string IMR, and finally the IMR disappeared. Influence from the step temperature change of the outer jacket enhances the elimination of IMR. Moreover, as the temperature difference increases, the time to eliminate IMR decreases by enhancing global mixing in the stirred vessel because a larger temperature difference enhances diffusion mechanism between IMR and AMR more easily.

Nomenclature

A: Height of turbine blade [m]
B: Length of turbine blade [m]
C: Impeller diameter [m]
D: Impeller off-bottom clearance [m]
H: Liquid height [m]
T: Diameter and height of vessel [m]
T: Temperature [K]
t: Time [min]
t_e: Elimination time of IMRs [min]
t^*: Dimensionless time ($=t/t_e$) [−].

Greek Letters

μ: Viscosity [Pa · s]
ρ: Density [kg · m^{-3}].

Acknowledgments

References

[1] T. Koiranen, A. Kraslawski, and L. Nyström, "Knowledge-based system for the preliminary design of mixing equipment," *Industrial and Engineering Chemistry Research*, vol. 34, no. 9, pp. 3059–3067, 1995.

[2] T. Makino, N. Ohmura, and K. Kataoka, "Observation of isolated mixing regions in a stirred vessel," *Journal of Chemical Engineering of Japan*, vol. 34, no. 5, pp. 574–578, 2001.

[3] N. Ohmura, T. Makino, T. Kaise, and K. Kataoka, "Transition of organized flow structure in a stirred vessel at low Reynolds numbers," *Journal of Chemical Engineering of Japan*, vol. 36, no. 12, pp. 1458–1463, 2003.

[4] M. N. Noui-Mehidi, N. Ohmura, J. Wu, B. Van Nguyen, N. Nishioka, and T. Takigawa, "Characterisation of isolated mixing regions in a stirred vessel," *International Journal of Chemical Reactor Engineering*, vol. 6, article no. A25, 2008.

[5] S. Hashimoto, H. Ito, and Y. Inoue, "Experimental study on geometric structure of isolated mixing region in impeller agitated vessel," *Chemical Engineering Science*, vol. 64, no. 24, pp. 5173–5181, 2009.

[6] D. J. Lamberto, F. J. Muzzio, P. D. Swanson, and A. L. Tonkovich, "Using time-dependent RPM to enhance mixing in stirred vessels," *Chemical Engineering Science*, vol. 51, no. 5, pp. 733–741, 1996.

[7] W. G. Yao, H. Sato, K. Takahashi, and K. Koyama, "Mixing performance experiments in impeller stirred tanks subjected to unsteady rotational speeds," *Chemical Engineering Science*, vol. 53, no. 17, pp. 3031–3040, 1998.

[8] K. Takahashi and M. Motoda, "Chaotic mixing created by object inserted in a vessel agitated by an impeller," *Chemical Engineering Research and Design*, vol. 87, no. 4, pp. 386–390, 2009.

[9] N. Nishioka, Y. Tago, T. Takigawa, N. M. Noui-Mehidi, J. Wu, and N. Ohmura, "Particle migration in a stirred vessel at low reynolds numbers," in *Proceedings of the 8th Italian Conference on Chemical and Process Engineering (AIDIC Conference Series)*, vol. 8, pp. 243–247, Milano, Italy, 2007.

[10] Alatengtuya, N. Nishioka, T. Horie, M. N. Noui-Mehidi, and N. Ohmura, "Effect of particle motion in isolated mixing regions on mixing in stirred vessel," *Journal of Chemical Engineering of Japan*, vol. 42, no. 7, pp. 459–463, 2009.

[11] Y. Inoue, H. Ito, Y. Nakata, and S. Hashimoto, "Theoretical analysis of isolated mixing regions in stirred vessels," *Kagaku Kogaku Ronbunshu*, vol. 36, no. 1, pp. 1–16, 2010.

Research Article

Correlation of Power Consumption for Several Kinds of Mixing Impellers

Haruki Furukawa,[1] Yoshihito Kato,[1] Yoshiro Inoue,[2] Tomoho Kato,[1] Yutaka Tada,[1] and Shunsuke Hashimoto[2]

[1] *Department of Life and Materials Engineering, Nagoya Institute of Technology, Gokiso-cho, Showa-ku, Nagoya-shi, Aichi 466-8555, Japan*

[2] *Division of Chemical Engineering, Graduate School of Engineering Science, Osaka University, 1-3 Machikaneyama-cho, Toyonaka-shi, Osaka 560-8531, Japan*

Correspondence should be addressed to Yoshihito Kato, kato.yoshihito@nitech.ac.jp

The authors reviewed the correlations of power consumption in unbaffled and baffled agitated vessels with several kinds of impellers, which were developed in a wide range of Reynolds numbers from laminar to turbulent flow regions. The power correlations were based on Kamei and Hiraoka's expressions for paddle and pitched paddle impellers. The calculated correlation values agreed well with experimental ones, and the correlations will be developed the other types of impellers.

1. Introduction

Mixing vessels is widely used in chemical, biochemical, food, and other industries. Recently scientific approaches were developed by Inoue and Hashimoto [1, 2]. On the other hand, the power consumption is the most important factor to estimate mixing performance and to design and operate mixing vessels.

To estimate the power consumption, the correlation of Nagata et al. [3] has traditionally been used. However, this correlation was developed for two-blade paddle impellers, which do not always have the same numerical values of power consumption as those of multiblade impellers. Kamei et al. [4, 5] and Hiraoka et al. [6] developed the new correlation of the power consumption of paddle impellers, which is more accurate than Nagata's.

However, the new correlation also cannot reproduce the power consumption for other types of impellers. The propeller- and Pfaudler-type impellers are used for low-viscosity liquid and solid-liquid suspensions, and the propeller type has been widely used in vessels ranging from portable type to large tanks. Kato et al. [7] developed a new correlation of power consumption for propeller- and Pfaudler-type impellers based on the correlations of Kamei and Hiraoka.

The power consumption for an anchor impeller was measured by Kato et al. [8, 9] in a wide range of Reynolds numbers from laminar to turbulent flow regions. In the laminar region, the power number of the anchor was reproduced by the correlations of Nagata and Kamei et al. by considering the anchor as a wide paddle impeller. In the turbulent region, it was reproduced by the correlation of Kamei et al. without the correction of the parameters.

In this paper, the authors reviewed the power correlations developed by authors in unbaffled and baffled mixing vessels with several kinds of impellers.

2. Experimental

Figure 1 shows a photograph of mixing impellers used in this work. Figure 2 shows the geometry of impellers with symbols. The mixing vessel used is shown in Figure 3. The vessels for the measurement of power consumption are flat-bottom cylindrical ones of inner diameter D = 185 and 200 mm.

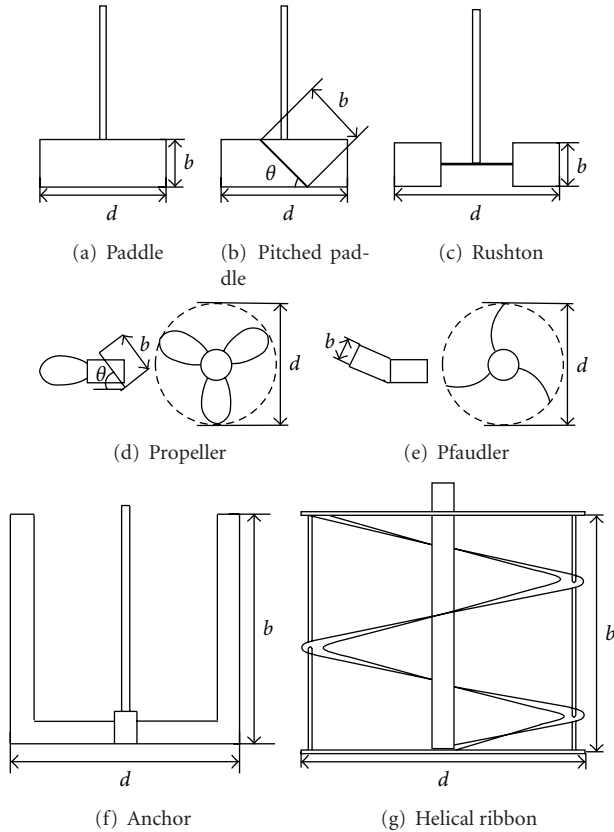FIGURE 1: Photograph of several kinds of mixing impellers.

(a) Paddle   (b) Pitched pad-   (c) Rushton
                   dle

(d) Propeller   (e) Pfaudler

(f) Anchor   (g) Helical ribbon

FIGURE 2: Geometry of mixing impellers.

FIGURE 3: Geometry of mixing vessel.

Three kinds of baffled conditions were mainly used: unbaffled, four baffles of $B_W = D/10$ (i.e., the standard baffled condition), and fully baffled. The baffles were plate type. The paddle, pitched paddle, Rushton turbine, propeller, and pfaudler impellers were symmetrically set up at one-half the level of the liquid depth ($C/H = 0.5$). The pfaudler, anchor, and helical-ribbon impellers were set up slightly above the bottom (bottom clearance of 1 mm).

For the measurement of the power consumption, the liquids used were desalted water and varying starch-syrup solutions ($\mu = 0.003$–13 Pa·s). The liquid was filled to the height equal to the vessel diameter ($H = D$).

The power consumption $P(= 2\pi nT)$ was measured with the shaft torque T and rotational speed n by using two types of torque meter (ST-1000 and ST-3000, Satake Chemical Equipment Mfg., Ltd.). The range of rotational speed was

from 60 to 540 rpm to avoid a large vortex at the center of the free surface of the liquid.

3. Results and Discussion

3.1. Paddle Impeller. The correlation equations of Table 1 were developed by Kamei et al. [4, 5] for paddle and Rushton turbine impellers. The comparison between experimental values and calculated values were shown in Figure 4. The correlation equations in Table 1 reproduced the experimental results better than Nagata's correlation equations for the wide range of impeller. The correlation equations for the pitched paddle impeller were shown in Table 2. The correlation equations also reproduced experimental values, which were not shown in a figure here.

3.2. Propeller and Pfaudler Impellers. The blades of the propeller and pfaudler impellers do not have sharp edges. The laminar term C_L in Table 1 can be used without modification. Because the deviation from correlations to measured values in the turbulent region was large, the turbulent terms C_t and m in Table 1 were modified by Kato et al. [7] based on fitting with the modified Reynolds number Re_G and the friction factor f, as follows:

$$C_t = \left[\left(3X^{1.5}\right)^{-7.8} + (0.25)^{-7.8} \right]^{-1/7.8},$$
$$m = \left[\left(0.8X^{0.373}\right)^{-7.8} + (0.333)^{-7.8} \right]^{-1/7.8}. \tag{1}$$

Figures 5 and 6 show the values correlated by the equations in Table 3 and the measured ones. The same equations can be used for the propeller- and the pfaudler-type impellers, regardless of the clearance between the vessel bottom and impeller.

FIGURE 4: Power diagram of paddle impeller (- - - [3]; — [4, 5]).
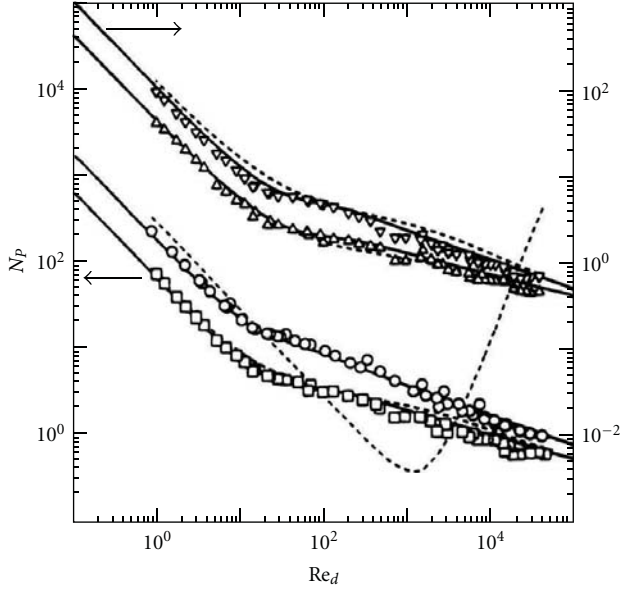
	d/D	b/D	n_p
▽	0.585	0.146	8
○	0.447	0.447	6
□	0.524	0.131	4
△	0.585	0.146	2

TABLE 1: Correlation equations of power number for paddle (a), Rushton turbine (c) and anchor (f).

Unbaffled condition

$N_{P0} = \{[1.2\pi^4\beta^2]/[8d^3/(D^2H)]\}f$

$f = C_L/\mathrm{Re}_G + C_t\{[(C_{tr}/\mathrm{Re}_G) + \mathrm{Re}_G]^{-1} + (f_{\curvearrowright}/C_t)^{1/m}\}^m$

$\qquad \mathrm{Re}_d = nd^2\rho/\mu$

$\qquad \mathrm{Re}_G = \{[\pi\eta\ln(D/d)]/(4d/\beta D)\}\mathrm{Re}_d$

$C_L = 0.215\eta n_p(d/H)[1 - (d/D)^2] + 1.83(b\sin\theta/H)(n_p/2\sin\theta)^{1/3}$

$C_t = [(1.96X^{1.19})^{-7.8} + (0.25)^{-7.8}]^{-1/7.8}$

$m = [(0.71X^{0.373})^{-7.8} + (0.333)^{-7.8}]^{-1/7.8}$

$C_{tr} = 23.8(d/D)^{-3.24}(b\sin\theta/D)^{-1.18}X^{-0.74}$

$f_{\curvearrowright} = 0.0151(d/D)C_t^{0.308}$

$X = \gamma n_p^{0.7}b\sin^{1.6}\theta/H$

$\beta = 2\ln(D/d)/[(D/d) - (d/D)]$

$\gamma = [\eta\ln(D/d)/(\beta D/d)^5]^{1/3}$

$\eta = 0.711\{0.157 + [n_p\ln(D/d)]^{0.611}\}/\{n_p^{0.52}[1 - (d/D)^2]\}$

Baffled condition

$N_P = [(1 + x^{-3})^{-1/3}]N_{P\max}$

$\qquad x = 4.5(B_w/D)n_B^{0.8}/N_{P\max}^{0.2} + N_{P0}/N_{P\max}$

Fully baffled condition

$N_{P\max} = \begin{cases} 10(n_p^{0.7}b/d)^{1.3} & (n_p^{0.7}b/d) \le 0.54 \\ 8.3(n_p^{0.7}b/d) & 0.54 < (n_p^{0.7}b/d) \le 1.6 \\ 10(n_p^{0.7}b/d)^{0.6} & 1.6 < (n_p^{0.7}b/d) \end{cases}$
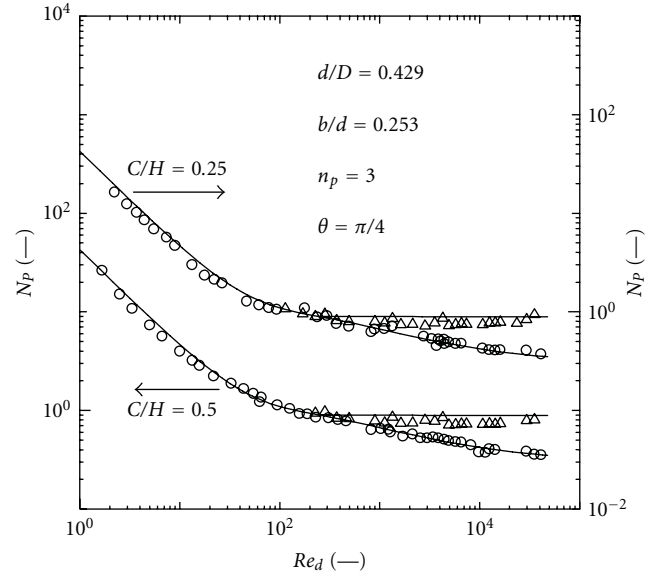
FIGURE 5: Power diagram of propeller impeller (— calc; ○ N_{P0}; △ N_P).
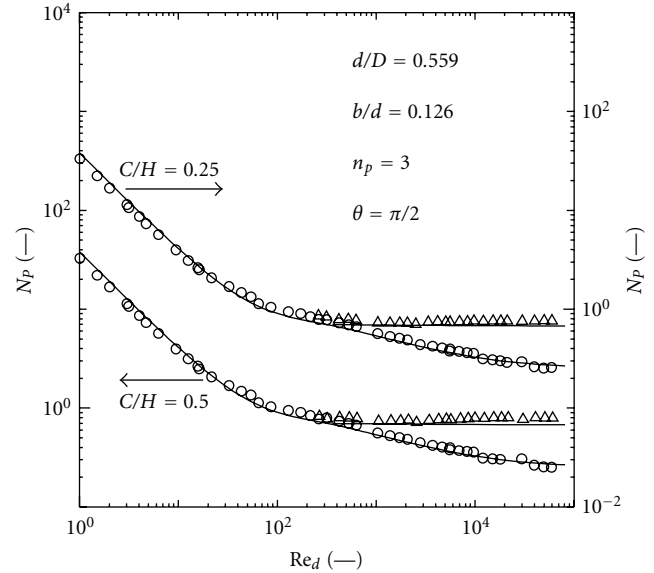
FIGURE 6: Power diagram of pfaudler-type impeller (— calc; ○ N_{P0}; △ N_P).

3.3. Anchor Impeller. The anchor impeller was used for the high-viscosity liquid normally. In this work, power consumption for an anchor impeller was measured in a wide range of Reynolds numbers from laminar to turbulent flow regions. In the laminar region, the power number of the anchor was reproduced by the correlations of Nagata and Kamei et al. by considering the anchor as a wide paddle impeller. In the turbulent region, it was reproduced by the correlation of Kamei et al. [4] without the correction of the parameters as shown in Figure 7 [8]. If a large vortex was generated in a turbulent mixing vessel, the experimental values of power number were larger than the calculated ones.
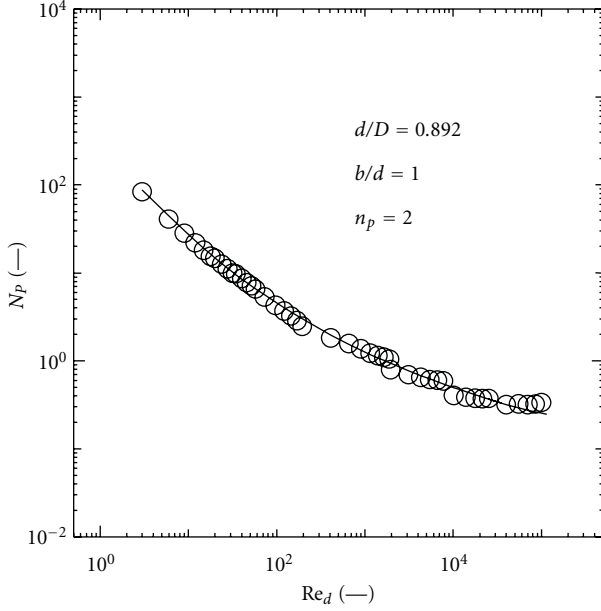
FIGURE 7: Power diagram of anchor impeller (— calc; $\circ$ N_{P0}).

TABLE 2: Correlation equations of power number for pitched paddle (b).

Unbaffled condition

$N_{P0} = \{[1.2\pi^4\beta^2]/[8d^3/(D^2H)]\}f$

$f = C_L/\mathrm{Re}_G + C_t\{[(C_{tr}/\mathrm{Re}_G) + \mathrm{Re}_G]^{-1} + (f_{\curvearrowleft}/C_t)^{1/m}\}^m$

$\qquad \mathrm{Re}_d = nd^2\rho/\mu$

$\qquad \mathrm{Re}_G = \{[\pi\eta\ln(D/d)]/(4d/\beta D)\}\mathrm{Re}_d$

$C_L = 0.215\eta n_p(d/H)[1 - (d/D)^2] + 1.83(b\sin\theta/H)(n_p/2\sin\theta)^{1/3}$

$C_t = [(1.96X^{1.19})^{-7.8} + (0.25)^{-7.8}]^{-1/7.8}$

$m = [(0.71X^{0.373})^{-7.8} + (0.333)^{-7.8}]^{-1/7.8}$

$C_{tr} = 23.8(d/D)^{-3.24}(b\sin\theta/D)^{-1.18}X^{-0.74}$

$f_{\curvearrowleft} = 0.0151(d/D)C_t^{0.308}$

$X = \gamma n_p^{0.7}b\sin^{1.6}\theta/H$

$\beta = 2\ln(D/d)/[(D/d) - (d/D)]$

$\gamma = [\eta\ln(D/d)/(\beta D/d)^5]^{1/3}$

$\eta = 0.711\{0.157 + [n_p\ln(D/d)]^{0.611}\}/\{n_p^{0.52}[1 - (d/D)^2]\}$

Baffled condition

$N_P = [(1 + x^{-3})^{-1/3}]N_{P\max}$

$\qquad x = 4.5(B_W/D)n_B^{0.8}/\{(2\theta/\pi)^{0.72}N_{P\max}^{0.2}\} + N_{P0}/N_{P\max}$

Fully baffled condition

$N_{P\max} = 8.3(2\theta/\pi)^{0.9}(n_p^{0.7}b\sin^{1.6}\theta/d)$

3.4. Helical-Ribbon Impeller.

As an example applied to a helical-ribbon impeller the correlation by Kamei et al. [4] was shown in Figure 8. Since it is the special case, the values of the equations for fitting the experimental values were shown in Table 4. It is the first time to show the power correlation of the helical-ribbon impeller over the wide range of Reynolds numbers.

TABLE 3: Correlation equations of power number for propeller (d) and pfaudler (f).

Unbaffled condition

$N_{P0} = \{[1.2\pi^4\beta^2]/[8d^3/(D^2H)]\}f$

$f = C_L/\mathrm{Re}_G + C_t\{[(C_{tr}/\mathrm{Re}_G) + \mathrm{Re}_G]^{-1} + (f_{\curvearrowleft}/C_t)^{1/m}\}^m$

$\qquad \mathrm{Re}_d = nd^2\rho/\mu$

$\qquad \mathrm{Re}_G = \{[\pi\eta\ln(D/d)]/(4d/\beta D)\}\mathrm{Re}_d$

$C_L = 0.215\eta n_p(d/H)[1 - (d/D)^2] + 1.83(b\sin\theta/H)(n_p/2\sin\theta)^{1/3}$

$C_t = [(3X^{1.5})^{-7.8} + (0.25)^{-7.8}]^{-1/7.8}$

$m = [(0.8X^{0.373})^{-7.8} + (0.333)^{-7.8}]^{-1/7.8}$

$C_{tr} = 23.8(d/D)^{-3.24}(b\sin\theta/D)^{-1.18}X^{-0.74}$

$f_{\curvearrowleft} = 0.0151(d/D)C_t^{0.308}$

$X = \gamma n_p^{0.7}b\sin^{1.6}\theta/H$

$\beta = 2\ln(D/d)/[(D/d) - (d/D)]$

$\gamma = [\eta\ln(D/d)/(\beta D/d)^5]^{1/3}$

$\eta = 0.711\{0.157 + [n_p\ln(D/d)]^{0.611}\}/\{n_p^{0.52}[1 - (d/D)^2]\}$

Baffled condition

$N_P = [(1 + x^{-3})^{-1/3}]N_{P\max}$

$\qquad x = 4.5(B_W/D)n_B^{0.8}/\{(2\theta/\pi)^{0.72}N_{P\max}^{0.2}\} + N_{P0}/N_{P\max}$

Fully baffled condition

$N_{P\max} = 6.5(n_p^{0.7}b\sin^{1.6}\theta/d)^{1.7}$

TABLE 4: Correlation equations of power number for helical ribbon (g).

$N_{P0} = \{[1.2\pi^4\beta^2]/[8d^3/(D^2H)]\}f = 16.0f$

$f = C_L/\mathrm{Re}_G + C_t\{[(C_{tr}/\mathrm{Re}_G) + \mathrm{Re}_G]^{-1} + (f_{\curvearrowleft}/C_t)^{1/m}\}^m$

$\qquad \mathrm{Re}_d = nd^2\rho/\mu$

$\qquad \mathrm{Re}_G = \{[\pi\eta\ln(D/d)]/(4d/\beta D)\}\mathrm{Re}_d = 0.0388\mathrm{Re}_d$

$\qquad C_L = 1.00, \ C_t = 0.100, \ m = 0.333, \ C_{tr} = 2500$

$\qquad f_{\curvearrowleft} = 0.00683$

$\qquad \beta = 2\ln(D/d)/[(D/d) - (d/D)] = 0.999$

$\qquad \eta = 0.538$

3.5. Pitched Paddle and Propeller Impellers with Partial Baffle.

The effects of the baffle length on the power consumption of a mixing vessel with several impellers were studied as shown in Figure 3. The power number was generally correlated with the baffle length, the number of baffles, and the baffle width [9]. The power number of the pitched paddle and the propeller impellers was correlated with only the correction as follows,

$$N_P = \left[(1 + x^{-3})^{-1/3}\right]N_{P\max}$$

$$x = \frac{4.5(B_W/D)n_B^{0.8}(h_B/H)}{\left\{(2\theta/\pi)^{0.72}N_{P\max}^{0.2}\right\}} + \frac{N_{P0}}{N_{P\max}}, \tag{2}$$

the results were shown in Figure 9.

3.6. Comparison of Power Number of Propeller Impeller with Rushton's Data.

Figure 10 shows the comparison of power number of a propeller impeller by Rushton et al. [10] with correlation in Table 3. The correlation equations in Table 3
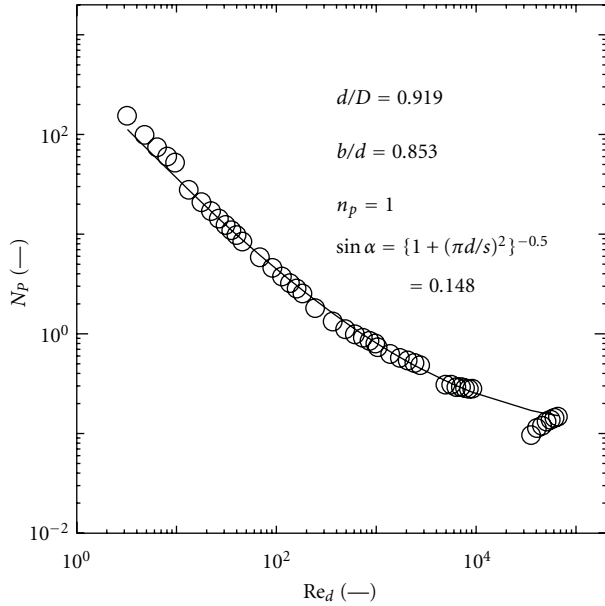
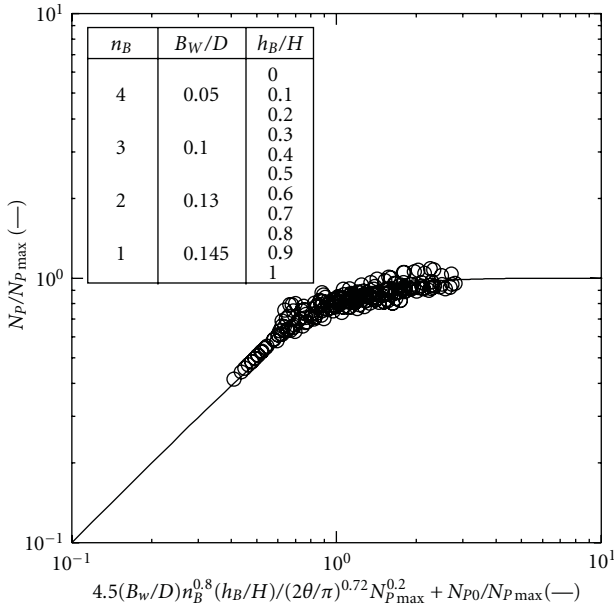FIGURE 8: Power diagram of helical ribbon-impeller (— calc; ○ N_{P0}).

FIGURE 9: Correlation of power number for propeller with partial baffle (— calc; ○ exp.).

also reproduced the data which other researchers measured well. As mentioned above, the correlation reproduced in this work has a possibility of correlating the power number of the mixing impellers of all geometry. It is the first time to compare between the data of Rushton's and the power correlation over the wide range of Reynolds number.

4. Conclusions

The authors reviewed the power correlations developed by authors. The new correlation equations of power number,
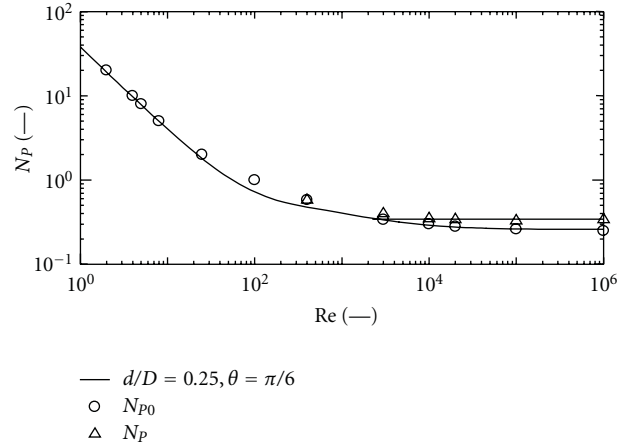
FIGURE 10: Comparison of power number for propeller with Rushton's data (— calc; ○, △ Rushton's).

based on the correlation of Kamei and Hiraoka, were developed for several kinds of mixing impellers, and it was shown that the calculated values of the power number agreed very closely with the measured ones. In future work, this correlation will be expanded to other impellers.

Nomenclature

b: Height of impeller blade (m)
C: Clearance between bottom and impeller (m)
D: Vessel diameter (m)
d: Impeller diameter (m)
f: Friction factor (—)
H: Liquid depth (m)
h_B: Baffle length (m)
N_P: Power number ($=P/\rho n^3 d^5$) (—)
N_{P0}:   Power number in unbaffled condition (—)
$N_{P\max}$:   Power number in fully baffled condition (—)
n: Impeller rotational speed (—)
n_B: Number of baffle plates (—)
n_p: Number of impeller blades (—)
P: Power consumption (W)
Re_d: Impeller Reynolds number ($=nd^2\rho/\mu$) (—)
Re_G: Modified Reynolds number (—)
T: Shaft torque (N·m)
θ: Angle of impeller blade (—)
μ: Liquid viscosity (Pa·s)
ρ: Liquid density (kg/m³).

References

[1] Y. Inoue and S. Hashimoto, "Analysis of mechanism of laminar fluid mixing in 3-D mixing tank based on streakline lobes," *Kagaku Kogaku Ronbunshu*, vol. 36, no. 4, pp. 355–365, 2010.

[2] Y. Inoue, "Invariant structure and variable properties in laminar fluid mixing model based on strealines," *Kagaku Kogaku Ronbunshu*, vol. 37, pp. 211–222, 2011.

[3] S. Nagata, T. Yokoyama, and H. Maeda, "Studies on the power requirement of paddle agitators in cylindrical vessels," *Kagaku Kogaku*, vol. 20, pp. 582–592, 1956.

[4] N. Kamei, S. Hiraoka, Y. Kato et al., "Power correlation for paddle impellers in spherical and sylindrical agitated vessels," *Kagaku Kogaku Ronbunshu*, vol. 21, pp. 41–48, 1995.

[5] N. Kamei, S. Hiraoka, Y. Kato et al., "Effects of impeller and baffle dimensions on power consumption under turbulent flow in an agitated vessel with paddle impeller," *Kagaku Kogaku Ronbunshu*, vol. 22, no. 2, pp. 255–256, 1996.

[6] S. Hiraoka, N. Kamei, and Y. Kato, "Power correlation for pitched blade paddle impeller in agitated vessels with and without baffles," *Kagaku Kogaku Ronbunshu*, vol. 23, no. 6, pp. 974–975, 1997.

[7] Y. Kato, Y. Tada, Y. Takeda, Y. Hirai, and Y. Nagatsu, "Correlation of power consumption for propeller and pfaudler type impellers," *Journal of Chemical Engineering of Japan*, vol. 42, no. 1, pp. 6–9, 2009.

[8] Y. Kato, N. Kamei, Y. Tada et al., "Power consumption of anchor impeller over wide range of reynolds number," *Kagaku Kogaku Ronbunshu*, vol. 37, pp. 19–21, 2011.

[9] Y. Kato, N. Kamei, A. Tada et al., "Effect of baffle length on power consumption in turbulent mixing vessel," *Kagaku Kogaku Ronbunshu*, vol. 37, pp. 377–380, 2011.

[10] J. H. Rushton, E. W. Costich, and H. J. Everett, "Power characteristics of mixing impellers part 1," *Chemical Engineering Progress*, vol. 46, no. 8, pp. 395–404, 1950.

Research Article

Effect of Impeller Agitation on Preparation of Tetra-*n*-Butyl Ammonium Bromide Semiclathrate Hydrate Slurries

Shunsuke Hashimoto, Hiroyuki Ito, Kazunari Ohgaki, and Yoshiro Inoue

Division of Chemical Engineering, Graduate School of Engineering Science, Osaka University, 1-3 Machikaneyama, Toyonaka, Osaka 560-8531, Japan

Correspondence should be addressed to Shunsuke Hashimoto, shunsuke@cheng.es.osaka-u.ac.jp

The slurries-containing tetra-*n*-butyl ammonium bromide (TBAB) solution and its semiclathrate hydrate have attracted a lot of interest as latent heat transport media. These hydrate slurries contain some microparticles of crystal, and the size and shape of these hydrate particles could affect the mobility of slurries. Hence, it is essential to investigate the efficient hydrate-slurry preparation methods and the effect of hydrate particles on the fluid property of slurries for the application to latent heat transport media. In the present study, the effect of agitation on particle size distribution and aggregation of particles was studied to prepare easily flowing TBAB hydrate slurries that were suitable for fluid transport. First of all, the effects of impeller rotational speed and impeller type on the particle size and frequency of aggregation were investigated. The results suggested that the particle size distribution and the frequency of particle aggregation are strongly affected by the intensity of shear rate and its uniformity, which was controllable with impeller type and its rotation speed.

1. Introduction

Recently, a large-scale district (regional) cooling system has attracted attention of many researchers because it works on saving energy and global sustainability due to its high performance of utilization of exhausted heat from large plants or factories [1]. In such system, the pumping energy loss due to the transportation of heat media is not small. To solve this problem, a high-density heat transportation system involving slurries with phase change materials (hereafter, PCM) having latent heat has been developed, for example, ice/water slurries [2]. The utilization of such PCM slurries can reduce flow rate of heat media, since latent heat of some materials is much larger than sensible heat. Fukushima et al. [3] reported the ability of slurries-containing tetra-*n*-butyl ammonium bromide (hereafter, TBAB) semiclathrate hydrate and its solution as latent-heat transport media, which was more favorable than ice/water system because they can be operated at relatively high temperature (*ca.* 285 K) and atmospheric pressure. Unlike ordinary gas hydrates, in these semiclathrate hydrates, the quaternary ammonium cation and anion are incorporated with the hydrogen bonds

of water molecules to construct the hydrate cage [4]. In addition, four butyl groups are one-by-one encaged with a large cage separately in this semiclathrate system. There are various reports about the crystal structure and the role of bromine for the TBAB hydrates [4, 5]. The hydration numbers of these structures are 26 and 38, which are described as Type A (tetragonal) and Type B (orthorhombic), respectively [5, 6]. The concentration of aqueous TBAB solutions results in differences of the crystal structure and thermodynamic stability of TBAB hydrate. TBAB semiclathrate hydrates have become the subject of much attention as an attractive medium for not only refrigerant but also H_2 storage [7–9].

There are a few reports about thermodynamic properties such as phase equilibria and dissociation enthalpy of TBAB hydrate [10] and about rheological property of these hydrate slurries [11] for the application to latent heat transport media. These hydrate slurries contain some microparticles of crystal, and the size and shape of these hydrate particles may affect the mobility of slurries. In addition, with the view of heat conductivity, it is necessary to make hydrate particles smaller and subglobular and to control their agglomerating property so that hydrate particles dissociate rapidly

and uniformly. Therefore, it is essential to investigate the efficient preparation method of hydrate slurries and the effect of hydrate particles on the fluid property of slurries for the application to latent heat transport media. There are some reference papers that investigate the effect of impeller agitation and bottom shape of stirred tank on the particle-size distribution and/or dispersion efficiency in the suspension systems containing polymer particles [12–14]. There, the dispersion efficiency such as the agitating speed for complete floating of solid particles was mainly investigated. In addition, some unique and complicated techniques such as multistage impeller system and unsteady agitation were usually utilized for the dispersion of solid particles. However, there are few findings that discuss the basic relation between the particle size and/or shape and the intensity and configuration of shear field. Furthermore, there is no report about the control of particle property for clathrate hydrates by means of impeller agitation.

Generally, impeller agitation has been adopted as the method for efficient crystallization of hydrate particles. However, there are few reports about the control of particle property for clathrate hydrates by means of impeller agitation. In the present study, we aim at searching for the favorable condition of agitation that minimizes the total power needed for both agitation and pumping of the prepared hydrate slurries and the effect of agitation on particle-size distribution and aggregation of particles to prepare TBAB hydrate slurries that easily flow and are suitable for fluid transport. In this paper, the effects of impeller rotational speed and impeller type on the particle size and frequency of aggregation are investigated. In addition, the key factor to control particle characteristics in TBAB hydrate slurries is briefly discussed.

2. Experimental Section

2.1. Materials. Research grade TBAB (mole fraction purity 0.980) was obtained from Wako Pure Chemical Industries, Ltd. TBAB was used without further purifications. In addition, deionized water was produced using water-manufacturing equipment made by Nihon Millipore K. K.

2.2. Apparatus and Procedures. The experimental apparatus in the present study consisted of the following parts: acrylic cylindrical vessel (diameter, D: 120 mm, height, H: 200 mm, handcrafted), three types of agitating impellers (handcrafted), agitating motors (HEIDON, BLh-300), torque meter (type: YT, Shintou Kagaku, Co., Ltd.), temperature controller (TAITEC, CL-80R), and CCD camera (KEYENCE, VH5910). Figure 1 shows the details of three types of agitating impellers used in the present study: two-bladed paddle (2-BP), Maxblend (Sumitomo Heavy Industries, Ltd., MB), and rotational cylinder (RC). The 2-BP impeller was located at a height of 60 mm. The diameter of shaft was 8 mm. Four baffles (width: 12 mm) were attached in the vessel with 2-BP and MB, while no baffle was attached in the case of RC because uniform flow field was created. In addition, the characteristics of three impellers are summarized in Table 1

Table 1: The characteristics of three impellers used in the present study.

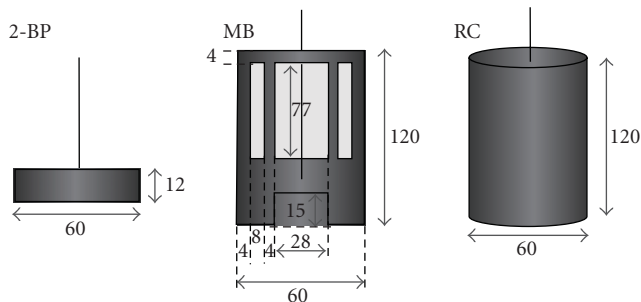|	n_r (rpm)	2-BP	MB	RC
K	—	10	20	—
	100	17	33	10.5
γ_{av} (s^{-1})	200	—	—	21.0
	300	50	100	31.5
Uniformity of shear rate	—	Low	Middle	High

Figure 1: The schematic illustration of three types of impellers used in the present study (the unit of length is mm).

(details for the velocity field of three types of impeller are shown in the former part of Section 3). The average shear rate, γ_{av} can be calculated by use of Metzner and Otto's equation [15] as follows:

$$\gamma_{av} = K \cdot n_r, \tag{1}$$

where K (depending on the type of impeller) and n_r stand for Metzner and Otto's constant and the rotation speed of impeller, respectively. In this case, K was equivalent to 10 for 2-BP and 20 for MB, respectively, which was estimated and correlated systematically by Kamei et al. [16]. In the case of RC (simple shear field), γ_{av} can be generally estimated by the following equation:

$$\gamma_{av} = \frac{(2\pi n_r y)}{(1 - y)}, \tag{2}$$

where y stands for the diameter ratio of cylinder and vessel (in the present study, $y = 0.5$). The γ_{av} values are also listed in Table 1 with K value.

Figure 2 shows the thermodynamic stability of TBAB hydrate (temperature, T-concentration, C diagram) at atmospheric pressure. The TBAB hydrate is stable at the temperatures below the line that is equivalent to the stability boundary of TBAB hydrate. As shown in Figure 2, the stoichiometric concentration of Type A TBAB hydrate is 40.5 wt% where the TBAB hydrate can exist stably at *ca.* 285 K. In the present study, the hydrate fraction in slurries, and H_f was determined by the following equation:

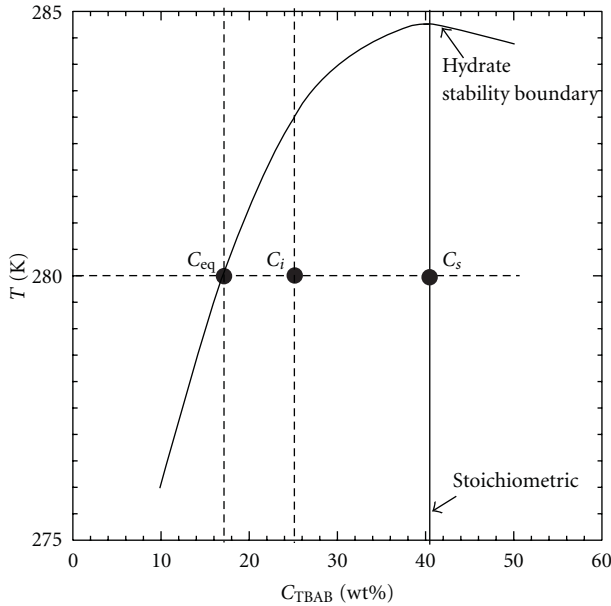$$H_f = \frac{(C_i - C_{eq})}{(C_s - C_{eq})}, \tag{3}$$

FIGURE 2: Temperature composition diagram for the TBAB + water mixed system containing stability boundary of Type A (tetragonal) hydrate [3, 10].

where C_i, C_{eq}, and C_s stand for the initial concentration of TBAB in aqueous solution, steady concentration of TBAB in the liquid phase of slurries, and stoichiometric concentration of Type A TBAB hydrate, respectively. In general, H_f decreases monotonically as temperature rises. In the present study, 20 wt% of TBAB in aqueous solution was adopted as a working fluid.

Firstly, the working fluid (20 wt% solution of TBAB) was poured into the vessel up to 120 mm (liquid height, $h = D$). Then, the fluid was cooled down up to 280.6 K (subcooling degree is *ca.* 0.7 K and then $H_f = ca$. 0.1) and the rotation of impeller was started. After the system reached the cyclostationary state, some seed crystals of Type A TBAB hydrate, which were prepared in advance and annealed at 280.6 K, were injected into the vessel, and then crystallization occurred. Raman spectroscopy preliminarily revealed that only Type A TBAB hydrate formed under the present experimental conditions [8]. In this case, it was confirmed that the particles of TBAB hydrate reached the steady state after an hour. Hence, appropriate amount of hydrate particles was removed up from the mother fluid and observed by use of CCD camera on the petri dish that was chilled with Peltier device. Typical picture of hydrate particles was shown in Figure 3. In the present study, 500 particles in total were used for particle size analyses of each experimental run. The particle diameter was defined as the major axis of rod-like hydrate particle. In addition, the aggregation particle was defined as the particle that consisted of more than two particles. The density of Type A TBAB hydrate particle was measured by means of falling ball method. The density of hydrate particle was comparable with the theoretical value, which could be calculated from the lattice constant of unit cell for tetragonal Type A TBAB hydrate. Additionally, it was slightly larger than that of aqueous

TABLE 2: The summary of experimental results. The average diameter means the overall average value of all TBAB hydrate particles observed in each experimental run.

Impeller	n_r (rpm)	Average diameter (mm)	Aggregation frequency (%)	P (W)
2-BP	100	1.32	14.1	0.02
	300	1.16	1.5	0.21
MB	100	1.13	6.3	0.04
	300	0.77	0.4	1.08
RC	100	0.75	20.1	0.01
	200	0.75	16.6	0.03
	300	0.76	16.2	0.09

solution. In this case, upward flows above a certain level by external force such as impeller rotation are required to float solid particles completely, which is well known as a criterion of impeller rotational speed for the complete floating of solid particles [17]. In the present study, impeller rotational speed in all experiments was more than this threshold value. Hence, it is reasonable to decide that the hydrate particles float completely and well dispersed in the vessel.

The required power for mixing, P, was obtained from rotational torque, T_r, of impeller shaft by the following equation:

$$P = 2\pi n_r T_r. \qquad (4)$$

3. Results and Discussion

Prior to experiments, the flow velocity vector patterns of three types of impeller were obtained from the numerical simulation by the use of commercial CFD software, Rflow (RFLOW, Co., Ltd.). Figure 4 shows the flow velocity vector patterns of (a) 2-BP (with 4 baffles), (b) MB (with 4 baffles), and (c) RC (without baffles). The density and viscosity of fluid were set equal to those of TBAB aqueous solution (1080 kg/m^3 and 0.003 Pa·s, resp.), and general k-ε model was adopted as a turbulent flow model. In calculations, the n_r was set at 100 rpm. As it can be seen in Figure 4, 2-BP generates nonuniform velocity field in both vertical and horizontal directions, where flow velocity is locally high near the impeller and low near the wall. On the other hand, in the case of RC, uniform circulating flow (a large vortex) is vertically generated, and, in particular, uniform rotational flow is circumferentially created. In the case of MB, although there are locally high and/or low flow regions, overall relatively uniform circulating flow is vertically generated. At $n_r = 300$ rpm, the flow is somewhat intensified, while flow pattern remains the same in all impellers.

The Experimental Data. Particle size and distribution, aggregation frequency of particles, and required power for the agitation of slurries obtained in the present study are summarized in Table 2. Hereafter, the detailed discussion about the difference in results for the three impellers is given in each section.
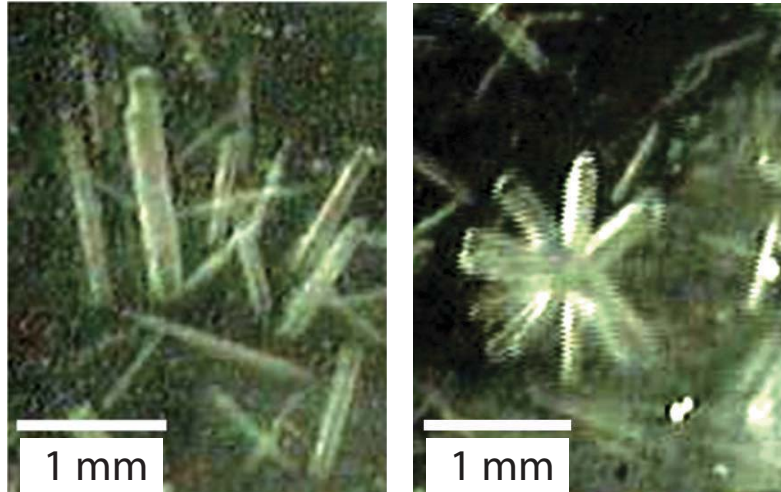
Figure 3: The photos of TBAB hydrate; (a) typical rod-like particles, (b) typical aggregation particles.

3.1. Particle Size and Its Distribution. Figure 5 shows the particle diameter of TBAB hydrates and its distribution for three types of impeller. In the case with 2-BP and RC, the particle diameter and its distribution do not change with the increase in shear rate. On the other hand, they change drastically as shear rate increases in the case with MB. This indicates that the growth of hydrate particle is suppressed considerably under the shear conditions above a certain level. In addition, even though the average shear rate of RC is lowest among three impellers at the equal speed of impeller rotation, the particle diameter and its distribution are relatively small in RC. Hence, the uniformity of shear rate is one of dominant factors for the control of particle diameter and its distribution. In fact, the 2-BP that generates nonuniform flow field exhibits broad size distribution characteristics of hydrate particles. Although the shear rate of MB is inhomogeneous compared with that of RC, the average shear rate of MB at $n_r = 300$ rpm is relatively very high (Table 1). Consequently, it is suggested that the local region of low shear rate can be kept away in the MB due to its large area of blade and particle diameter would become small.

3.2. Aggregation Frequency of Hydrate Particle. The open symbols in Figure 6 stand for the aggregation frequency of hydrate particles. The aggregation frequency becomes smaller in the order of RC, 2-BP, and MB. In addition, it becomes small as the shear rate increases. This indicates that the aggregation of hydrate particles is suppressed by the collision between hydrate particles and impeller blades and/or baffles, and the presence of field of locally high shear rate.

3.3. Required Power for the Agitation of Hydrate Slurries. The closed symbols in Figure 6 represent the required power to agitate hydrate slurries. As mentioned previously, MB can create the flow field that has a distinct advantage for the control of hydrate particles and limit their aggregation. As expected, however, the required power for agitation in MB is

extremely large compared to the other impellers, which is due to the relatively large area of its impeller blade. Incidentally, it is experimentally confirmed that the required power for the agitation of hydrate slurries is almost same as (slightly larger than) that of aqueous solution under the present conditions of hydrate fraction, where the difference between them is at most *ca*. 0.002 W.

3.4. Conceptual Impeller for Efficient Agitation of TBAB Hydrate Slurries. Based on the present experimental results, to prepare the hydrate particles that have small diameter and sharp distribution of diameter, three factors are essential. They are (1) uniformity of shear rate, (2) absence of the local region of low shear rate, and (3) presence of field that has locally high shear rate (or the collision between hydrate particles and impeller blade). Herein, a conceptual impeller that can satisfy above key factors was developed. Figure 7 shows the schematic illustration of this conceptual impeller, velocity vector of its pattern of flow, and its characteristics of generated hydrate particle. As shown in Figure 7(a), this conceptual impeller consists of 2-bladed paddle blade (bottom) and cylinder (top). Figure 7(b) indicates that this conceptual impeller can generate both the region of locally high shear rate (bottom side) and that of uniform shear rate (top side) at the same time. As a result, the uniform and nearly steady circulating flow can be generated. Needless to say, this impeller can prevent the region of low shear rate. In addition, it is expected that the part of impeller blade can prevent the aggregation of hydrate particles. In fact, as shown in Figure 7(c), this conceptual impeller can prepare TBAB hydrate particles that have uniform diameter, and their average diameter is relatively small (0.804 mm). Additionally, the aggregation frequency of TBAB hydrate for this impeller is relatively low (5.6%) and the required power is also low (0.180 W). After all, this conceptual impeller manufactured based on some experimentally obtained dominant factors has good performance for the preparation of TBAB hydrate particles. The findings obtained in the present study are useful for the development of new impeller, which is suitable
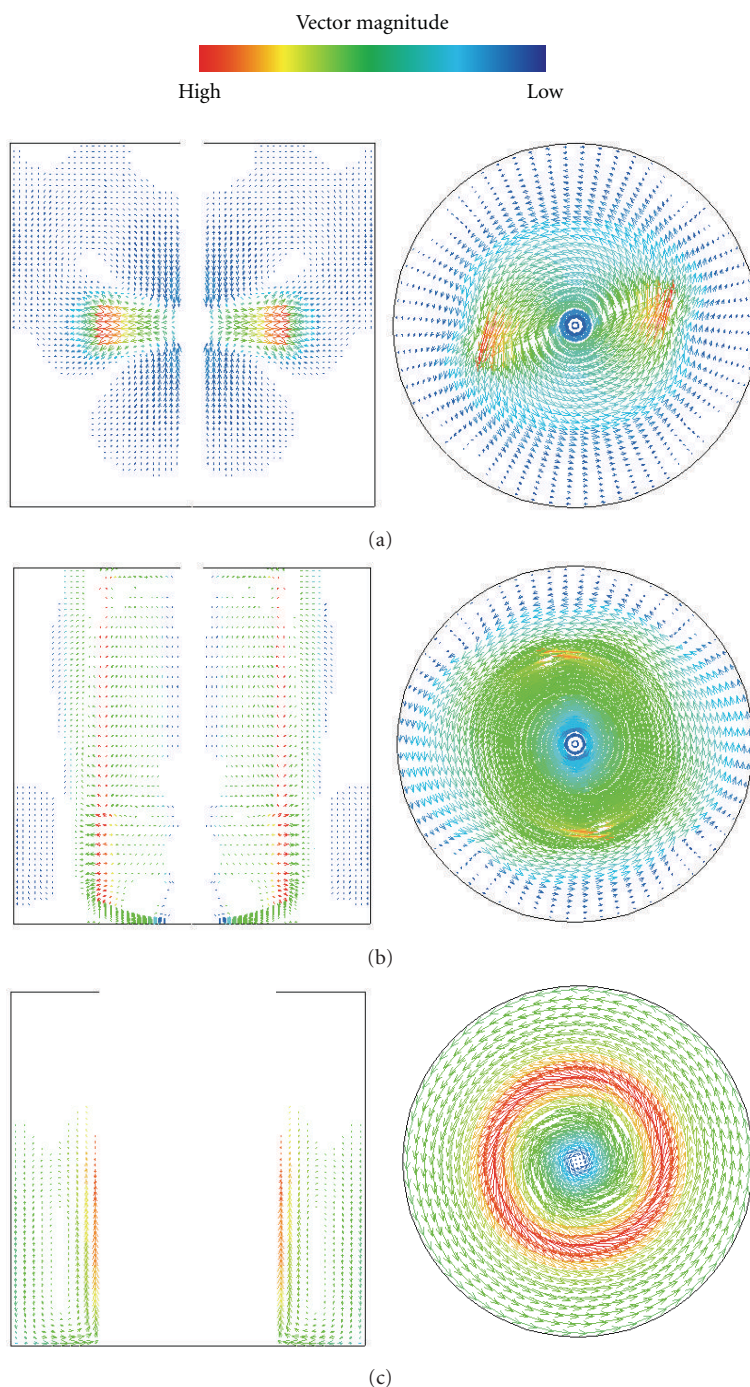
FIGURE 4: The flow velocity-vector patterns of three types of impellers in the vertical and horizontal directions (cross-section containing impeller blade and shaft) ($n_r = 100$ rpm); (a) 2-BP (with 4 baffles), (b) MB (with 4 baffles), (c) RC (without baffles).

for the preparation of TBAB hydrate slurries that easily flow and are suitable for fluid transport.

4. Conclusion

To prepare TBAB hydrate slurries that easily flow and are suitable for fluid transport, the effects of impeller rotational speed and impeller type on the particle size and frequency of aggregation have been investigated. The experimental findings are simply summarized in Table 3. For the

preparation of hydrate particles that have small diameter and sharp distribution of diameter, three factors and their balances are essential as follows: (1) uniformity of shear rate, (2) absence of the region of low shear rate, and (3) presence of field that has locally high shear rate. Based on these factors, a new conceptual impeller has been proposed, which consists of 2-bladed paddle blade (bottom) and cylinder (top). This conceptual impeller has succeeded in the preparation of smaller and uniform TBAB hydrate particles with relatively low agitation power.
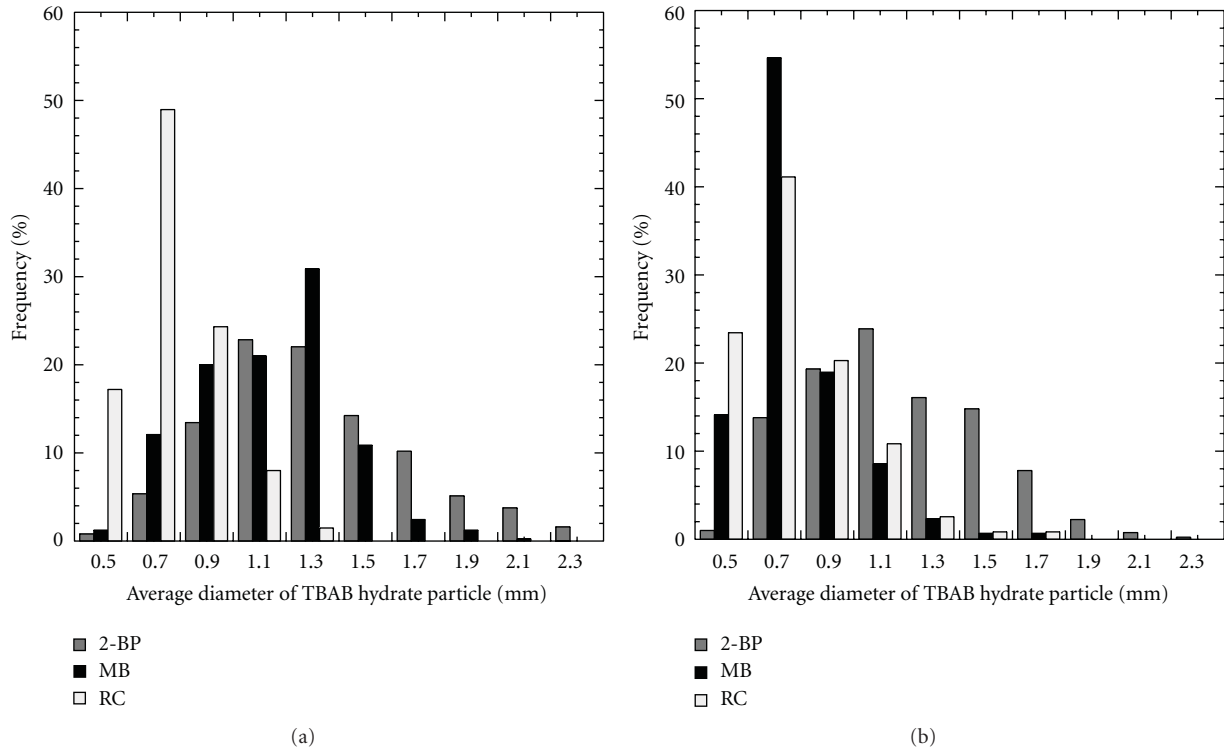
(a)

(b)

FIGURE 5: The particle diameter of TBAB hydrate and its distribution for three types of impeller; (a) $n_r = 100$ rpm, (b) $n_r = 300$ rpm.
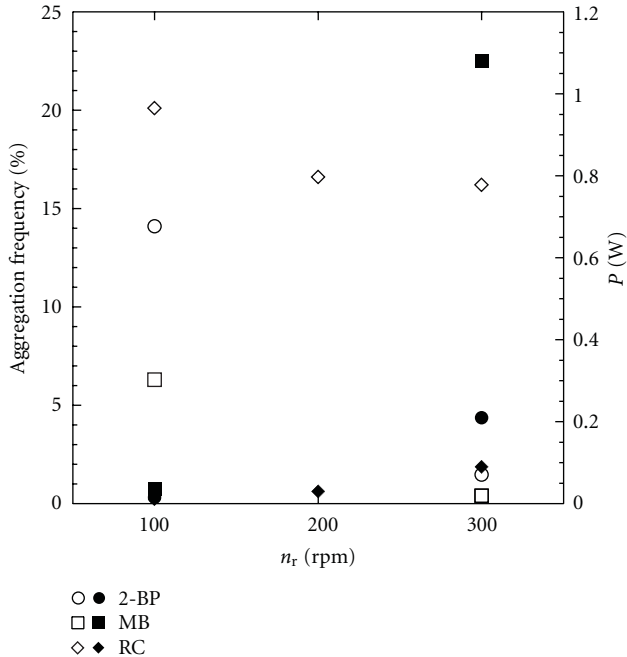

FIGURE 6: The aggregation frequency of hydrate particles (open symbols, left axis) and required power to agitate hydrate slurries (closed symbols, right axis) for three types of impeller.

Notations

C: Concentration, wt%
D: Diameter of vessel, m
H: Height of vessel, m

TABLE 3: The relative results of important factors for the preparation of TBAB hydrate slurries in various impellers. Herein, the boundary between "small" and "large" is defined at the value of 1.0 mm (particle diameter) and 1.0 W (required power). The indexes of "low" and "high" mean the value of <5% and >10%, respectively, and "middle" does the value between them.

Impeller	n_r (rpm)	Particle diameter	Aggregation frequency	Required power
2-BP	100	Large	High	Small
	300	Large	Low	Small
MB	100	Large	Middle	Small
	300	Small	Low	Large
RC	100	Small	High	Small
	300	Small	High	Small
Conceptual	300	Small	Low	Small

h: Height of working fluid, m
H_f: Hydrate fraction in slurries
n_r: Rotation speed of impeller, rpm
P: Required power for agitation, W
T: Temperature, K
T_r: Torque, N·m
y: Diameter ratio of cylinder and vessel
z: Coordinate of z-direction (vertical direction)
γ: Shear rate, s^{-1}.

Acknowledgments

(a)

(c)

(b)
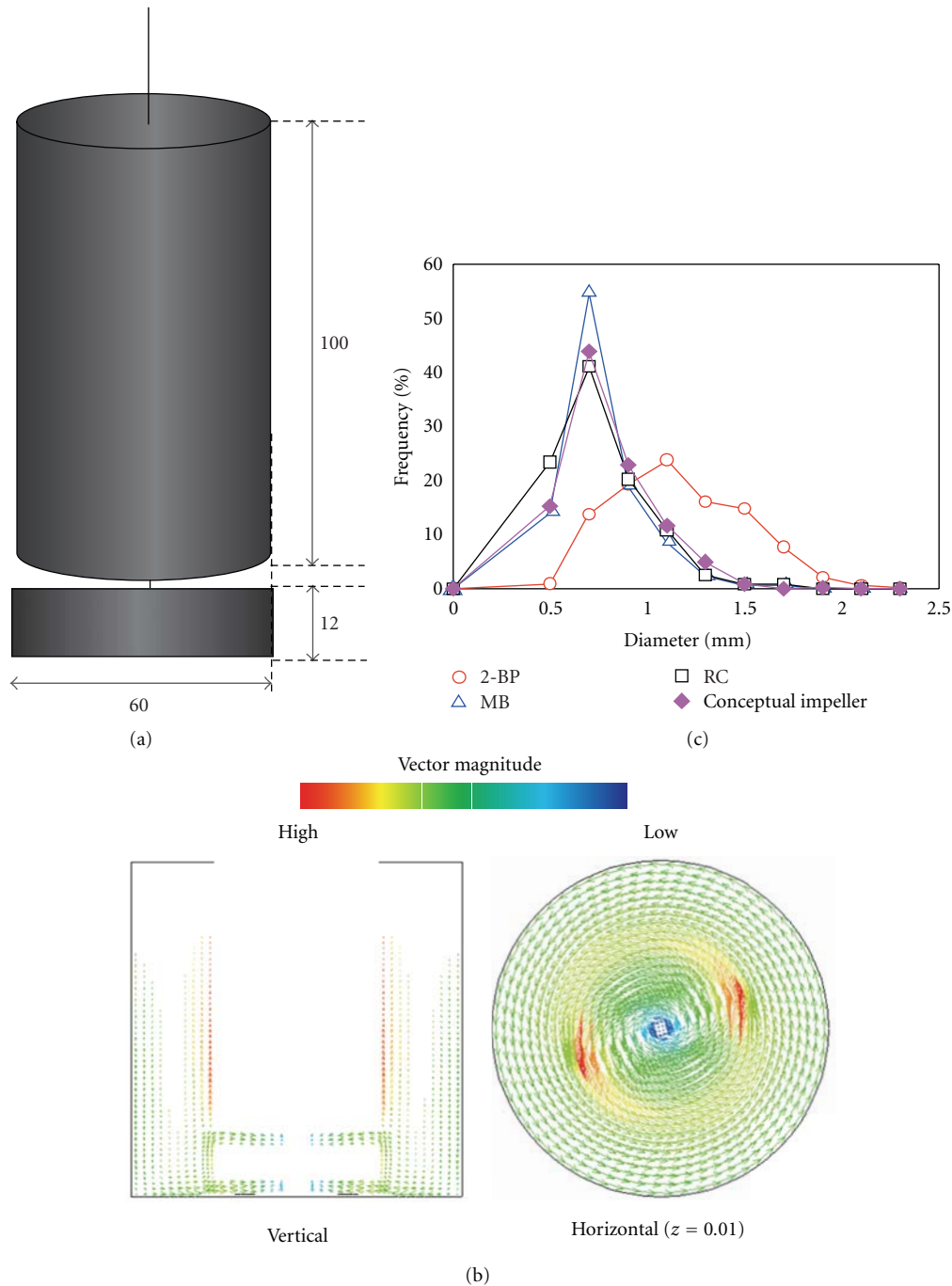
FIGURE 7: The summary of conceptual impeller for efficient preparation of TBAB hydrate slurries; (a) schematic illustration of impeller (the unit of length is mm), (b) flow velocity-vector patterns ($n_r = 300$ rpm), (c) particle diameter and its distribution ($n_r = 300$ rpm).

References

[1] S. Kilkis and B. Kilkis, "An analytical, multi-objective an optimization algorithm for energy efficiency in district cooling systems and green buildings," *ASHRAE Transactions*, vol. 117, pp. a13/1–a13/8, 2011.

[2] S. Fukusako, Y. Kozawa, M. Yamada, and M. Tanino, "Fundamental researches and developments on fine crystallineice slurries," *Transactions of the Japan Society of Refrigerating and Air Conditioning Engineers*, vol. 17, no. 4, pp. 413–437, 2000.

[3] S. Fukushima, S. Takao, H. Ogoshi et al., "Development of High-density Cold Latent Heat with Clathrate Hydrate," *NKK Technical Report*, vol. 166, pp. 65–70, 1999 (Japanese).

[4] L. S. Aladko, Y. A. Dyadin, T. V. Rodionova, and I. S. Terekhova, "Clathrate hydrates of tetrabutylammonium and tetraisoamylammonium halides," *Journal of Structural Chemistry*, vol. 43, no. 6, pp. 990–994, 2002.

[5] W. Shimada, T. Ebinuma, H. Oyama et al., "Separation of gas molecule using tetra-n-butyl ammonium bromide semi-clathrate hydrate crystals," *Japanese Journal of Applied Physics*, vol. 42, no. 2A, pp. L129–L131, 2003.

[6] W. Shimada, M. Shiro, H. Kondo et al., "Tetra-n-butylammonium bromide-water (1/38)," *Acta Crystallographica Section C*, vol. 61, no. 2, pp. o65–o66, 2005.

[7] S. Hashimoto, S. Murayama, T. Sugahara, H. Sato, and K. Ohgaki, "Thermodynamic and Raman spectroscopic studies on H_2+ *tetrahydrofuran+water* and H_2+tetra-n-butyl ammonium *bromide+ water* mixtures containing gas hydrates," *Chemical Engineering Science*, vol. 61, no. 24, pp. 7884–7888, 2006.

[8] S. Hashimoto, T. Sugahara, M. Moritoki, H. Sato, and K. Ohgaki, "Thermodynamic stability of hydrogen + tetra-n-butyl ammonium bromide mixed gas hydrate in nonstoichiometric aqueous solutions," *Chemical Engineering Science*, vol. 63, no. 4, pp. 1092–1097, 2008.

[9] S. Hashimoto, T. Tsuda, K. Ogata, T. Sugahara, Y. Inoue, and K. Ohgaki, "Thermodynamic properties of hydrogen + tetra-n-butyl ammonium bromide semi-clathrate hydrate," *Journal of Thermodynamics*, vol. 2010, Article ID 170819, 5 pages, 2010.

[10] H. Oyama, W. Shimada, T. Ebinuma et al., "Phase diagram, latent heat, and specific heat of TBAB semiclathrate hydrate crystals," *Fluid Phase Equilibria*, vol. 234, no. 1-2, pp. 131–135, 2005.

[11] M. Darbouret, M. Cournil, and J. M. Herri, "Rheological study of TBAB hydrate slurries as secondary two-phase refrigerants," *International Journal of Refrigeration*, vol. 28, no. 5, pp. 663–671, 2005.

[12] S. I. Kondo, M. Motoda, K. Takahashi, and H. Horiguchi, "The influence of the bottom shape of an agitated vessel stirred by dual impellers on the distribution of solid concentration," *Journal of Chemical Engineering of Japan*, vol. 40, no. 8, pp. 617–621, 2007.

[13] K. Shimizua, K. Takahashi, E. Suzukia, and T. Nomura, "Effect of baffle geometries on crystal size distribution of aluminum potassium sulfate in a seeded batch crystallizer," *Journal of Crystal Growth*, vol. 197, no. 4, pp. 921–926, 1999.

[14] A. Barresi and G. Baldi, "Solid dispersion in an agitated vessel," *Chemical Engineering Science*, vol. 42, no. 12, pp. 2949–2956, 1987.

[15] A. B. Metzner and R. E. Otto, "Agitation of non-Newtonian fluids," *AIChE Journal*, vol. 3, no. 1, pp. 3–10, 1957.

[16] N. Kamei, S. Hiraoka, Y. Kato et al., "Development of power correlations for various impellers in an agitated vessel in laminar region based on a numerical analysis of 2-D flow," *Kagaku-kogaku Ronbunshu*, vol. 20, no. 5, pp. 595–603, 1994 (Japanese).

[17] T. N. Zwietering, "Suspending of solid particles in liquid by agitators," *Chemical Engineering Science*, vol. 8, no. 3-4, pp. 244–253, 1958.

Research Article

Design Mixers to Minimize Effects of Erosion and Corrosion Erosion

Julian Fasano,[1] Eric E. Janz,[2] and Kevin Myers[3]

[1] *Mixer Engineering Co., 2673 Stonebridge Drive, Troy, OH 45373, USA*
[2] *Chemineer, Inc., 5870 Poe Avenue, Dayton, OH 45414, USA*
[3] *Department of Chemical & Materials Engineering, University of Dayton, 300 College Park, Dayton, OH 45469-0246, USA*

Correspondence should be addressed to Julian Fasano, j.fasano@mixerengineering.com

A thorough review of the major parameters that affect solid-liquid slurry wear on impellers and techniques for minimizing wear is presented. These major parameters include (i) chemical environment, (ii) hardness of solids, (iii) density of solids, (iv) percent solids, (v) shape of solids, (vi) fluid regime (turbulent, transitional, or laminar), (vii) hardness of the mixer's wetted parts, (viii) hydraulic efficiency of the impeller (kinetic energy dissipation rates near the impeller blades), (ix) impact velocity, and (x) impact frequency. Techniques for minimizing the wear on impellers cover the choice of impeller, size and speed of the impeller, alloy selection, and surface coating or coverings. An example is provided as well as an assessment of the approximate life improvement.

1. Introduction

There are numerous applications of mixers that deal with erosive solids, especially in the minerals processing and power industries. In many of these applications, there is an erosion-corrosion synergistic effect on the wear of a mixer's wetted parts, particularly the impeller. This paper pulls together the authors' research with numerous articles on erosion and erosion corrosion to permit a designer to optimize the cost-based life of eroding mixer parts before replacement is required.

There are a large number of factors that can affect the rate of erosion. Many of these factors have been known and studied to some extent:

(i) chemical environment,

(ii) hardness of solids,

(iii) density of solids,

(iv) difference in liquid and solid density,

(v) percent solids,

(vi) shape of solids,

(vii) fluid regime (turbulent, transitional, or laminar),

(viii) fluid rheology (e.g., pseudoplasticity),

(ix) hardness of the mixer's wetted parts,

(x) young's modulus of the mixer's wetted parts,

(xi) hydraulic efficiency of the impeller (kinetic energy dissipation rates near the impeller blades),

(xii) impact velocity,

(xiii) impact frequency,

(xiv) angle of impact.

Theoretically the rate of volume loss of material is due to the kinetic energy lost when a particle impacts a material [1]. This would suggest a velocity exponent of 2. However, presented below, experimental velocity exponents have ranged from 1.5 to 4.0. The general form of the equation relating erosion rate to velocity is given by

$$E = K \cdot V^n f(\theta), \tag{1}$$

where E = volumetric erosion rate, K = constant (function of all parameters other than V or θ), V = particle velocity or relative velocity for rotating systems (impellers), n = velocity

exponent (can also be a function of other parameters), and θ = impingement angle.

Most investigators have used this general equation form.

Sapate and RamaRao [2] used a power law correlation between volumetric erosion rate and impingement velocity in a nonrotating system. They observed exponents on velocity of 1.91 to 2.52. The velocity exponent showed an increasing trend with increasing hardness of the alloys irrespective of the hardness of the erodent particles and the impingement angle of the alloys investigated.

Stack [3] and others investigated the effect that corrosion plays in an erosion environment. These investigators studied various parameters of the corrosion-erosion environment in a nonrotating system. They observed velocity exponents that ranged from 1.4 to 3.5. They concluded that exponents derived for erosion of alloys under erosion-dominated conditions can be correlated to those derived for the strictly ductile erosion process. These are typically very near the theoretical "2" for the strictly ductile erosion process. However, those for the erosion corrosion dominated regime are higher than for the erosion-dominated regime and were in the 2.5 to 3.5 range. A publication by the Hydraulics Institute [4] suggests that the erosion velocity exponent for pumps in slurry transport is on the order of 2.5–3.0 .

Fort [5] and others studied pitched blade impellers 100 mm in diameter with a blade width of 20 mm in water-solid slurries under turbulent conditions. These impellers were studied at pitch angles of 20°, 35°, and 45°. These studies included a slurry of 18.3% by volume of gypsum having a mean particle diameter of 0.1 mm and a 10% by volume slurry of 0.4 mm mean diameter sand particles. From their studies, they concluded the following.

  (i) Particles of the lower hardness gypsum generated uniform sheet erosion over the entire surface of the impeller, while the particles of sand, having a higher hardness, generated predominately erosion of the leading edges of the impeller blade.

  (ii) The higher the hardness of the blade material, the lower the wear rate of the blade.

  (iii) The wear rate of the leading edge was not a function of pitch angle.

  (iv) Sheet erosion of the blades exhibits a maximum erosion rate between 20° and 45°.

Zheng [6] and others studied the erosion-corrosion synergistic effect in an acidic slurry. The slurry was 10% by weight H_2SO_4 and 15% by weight −60 mesh (<0.251 mm) corundum sand. Their apparatus was a rotating disk with four specimen holders on its edge. They determined the rate of erosion by making electrochemical measurements during rotation. All of their studies were done under turbulent flow conditions. Erosion rate velocity exponents ranged from 1.9 to 4.0. A model was proposed and used which divided the overall erosion rate into an erosion rate via corrosion, an erosion rate via erosion, and an erosion rate due to synergism. The synergism rate was very large and varied between 32 and 99% of the total. The percent contributed by synergism diminished as the alloy became more statically corrosion resistant.

Amelyushkin and Agafonov [7] studied the erosion of cogeneration steam turbine blades caused by water droplets. If kinetic energy is high enough, even water droplets can cause erosion. They found that the toroidal and near root vortices were very intense and caused enhanced wear of the rotor blades. Also they found that they were able to eliminate erosion by making the water droplets small enough. It is expected that these effects are related to grain size. In ductile erosion, plastic deformation may occur first, before metal is removed. If erosion is due to intergranular grain fracture, then if particles are significantly smaller than the metal's grain size, erosion should be minimized. As ductile alloy grain sizes are on the order of $20\,\mu m$, particles smaller than this should have little erosive effect.

Khalid and Sapuan [8] studied wear for a centrifugal pump impeller in a slurry application. Weight and diameter losses were very nearly linear with time over 480 hours of operation. Blade height and depth loss did exhibit some nonlinearity but were modeled as linear. Typical of rotating devices in slurries, more material was lost near the periphery of the impeller than in the center because linear velocities increase with radial distance from the shaft.

López [9] and others studied the effect of corrosion erosion at relatively high velocities on 304 and 420 stainless steel. Velocities ranged from 4.5 to 8.5 m/s. Such velocities are not common in mixing equipment except in high-shear devices. They used a rotating disc device with erosion samples attached to the periphery of the disc. The aqueous liquid for the slurry was composed of 70% by weight H_2SO_4 and 3.5% NaCl. The slurry solids were 30% by weight SiO_2 particles with a mean diameter about 0.25 mm. They found that high-velocity impacts were beneficial. The combined action of erosive and corrosive mechanisms did not lead to a significant increase in mass loss if compared to corrosion tests. They suggested that pores, small cracks, and fresh pits can be covered by the prows and lips that are formed as a consequence of the wedge action of round particles which produces a smoother, uniformly corroded surface. Thus, even though the transport mechanisms which remove corrosion products are greater due to higher velocities, the surface area exposed is smaller.

Corpstein and Fasano [10] studied slurry wear through multilayer paint modeling. The paint layers are on the order of 0.0381 mm thick. The three layers of paint used had an overall thickness of approximately 0.114 mm. This is only about 7% of the blade thickness and did not change the fluid hydraulics over the blade. Erosion was studied using 8.3-inch diameter scaled down axial flow mixing impellers in a sand water slurry. These studies pointed out the strong effects that blade-shedding vortices, could have on erosive wear. Impellers, such as the four-bladed-pitched impeller that generated stronger vortices, suffered the highest degree of localized erosion. The effects of these vortices can completely wear through an impeller blade, leaving holes where the vortices contacted the surface. High-efficiency impeller blades created significantly smaller vortices and as a consequence exhibited much lower localized wear. Vortex
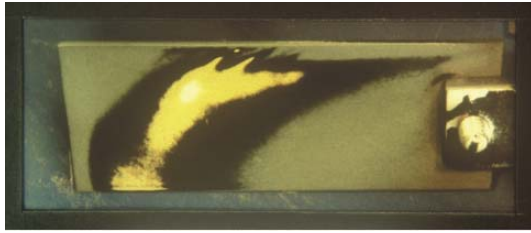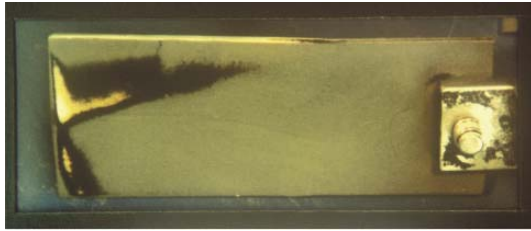
FIGURE 1: Backside of pitched blade impeller.

FIGURE 2: Backside of HE-3 high-efficiency impeller.

FIGURE 3: Wear rate data of Miller and Schmidt.

erosion can be severe and occurs on the backside (low-pressure side) of the impeller blade. Comparisons of the backside wear pattern for a Chemineer HE-3 impeller and a standard generic 45° pitched four-bladed impeller are shown in Figures 1 and 2. The impellers were each 211 mm diameter and operated at 870 rpm in a 10% by weight sand slurry in water. The weight mean particle size of the sand was 360 μm. These backside erosion patterns were made after only 30 minutes of operation, and it is obvious that the erosion on the backside of the 45° four-bladed-pitched impeller was much more severe than the erosion for the Chemineer HE-3 high-efficiency impeller.

Wu [11] and others were also successful in using this technique to study five different style radial flow impellers and a low attack angle (~15°) (6-bladed) pitched impeller. As expected, the hydraulically more efficient six-bladed-pitched impeller experienced the least erosion.

Increased hardness of metals will generally provide an increased life. Miller and Schmidt [12] compared the erosion rates of 16 metals in a recycled slurry test system using 2% by weight silica sand in water. The impeller tip velocity was 15.7 m/s, and the temperature was 16°C. In addition to the erosion rate for each metal, they included the metal's hardness. The best fit for their data was logarithmic. However, probably due to the synergistic corrosion effects, the data was fairly dispersed. A plot of this data is provided in Figure 3. The effect of particle hardness depends on whether erosion is ductile or brittle. For brittle erosion, the effect of particle hardness is much more pronounced than for ductile erosion.

Changes in particle size can change the erosion mechanism. Stachowiak and Batchelor [13] reported that as the particle size was increased from 8.75 μm to 127 μm, the mode of erosion changed from ductile to brittle. The erosion study

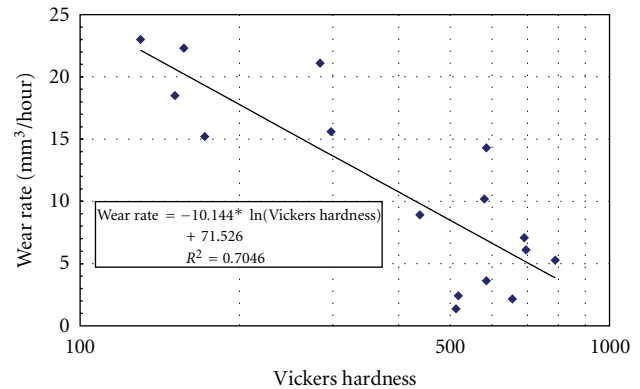was for silicon carbide particles impinging on glass, steel, graphite, and ceramics. The particle velocity was 152 m/s.

2. Design for Erosion Minimization

Because maximum velocities in mixing processes seldom exceed 6 m/s, erosion and corrosion erosion of materials are fatigue processes for most mixing processes. There is generally not enough particle kinetic energy to cause ductile erosion where there is some plastic flow of material. The fatigue process occurs on a micro- or localized scale, and, as with macroscale fatigue, two stages of the erosion process have been observed. There is an incubation period followed by the formation and growth of pits involving the removal of the metal or material. Refer to a materials behavior text such as that by Armstrong and Zerilli [14] for a more in-depth discussion on material behavior.

Due to the vast number of parameters that can affect erosion or erosion-corrosion processes, and the fact that this area of mixer service has not been widely studied, it is very difficult to predict a priori what the rate of erosion will be for any given liquid-solid application. However, there are certain factors within the control of the designer that can be used to optimize the life of the mixer's wetted parts.

Most mixer designers will not have control over the type of slurry, the percent solids, the hardness of the solids, the shape of the solids, the liquid, the pH, and so forth. However designers will generally have control over

(i) the mixer's wetted parts materials, coating, or lining,

(ii) the impeller style,

(iii) the impeller horsepower and speed combination.

2.1. Material Selection. The choice in selecting a material is to either go hard or soft and elastic. All else being equal, when selecting a metal alloy, a higher hardness will lead to a longer life. Thus, when selecting a metal alloy material, select a hard material which will also provide good corrosion resistance.

There are a number of hard surface ceramic coatings such as tungsten carbide or silicon carbide, which could be applied to the high-wear areas such as impeller blades. Ceramics are

the most wear resistant but are low in toughness and impact strength. Ceramic coatings as well must be corrosion resistant to the liquid medium. Ceramics also do not have the ability to absorb much strain. These high strains on flexing blades may allow cracking of the ceramic coating. Ceramic coating applicators should be able to provide the maximum allowable strain for the ceramic coating under consideration. Coatings of the more common ceramic materials tend to be more costly than high-hardness metals, or elastomeric coverings [15].

Glass-lined equipment has a glass hardness of 5 to 6 on the Moh scale. For the great majority of solids, this hardness would be very acceptable. However, there are numerous materials and minerals including, Al_2O_3, SiO_2, WC, SiC, and ZiO_2 that have higher harnesses and would tend to wear away the glass lining. Glass linings have very many of the same limitations as ceramic coatings. They tend to be brittle and cannot tolerate much strain.

Elastomeric coverings on the order of $3/8''$ thick for industrial scale impellers have a long history of providing longer life in slurry applications. Instead of having to absorb most of the particle's impact energy, an elastomer releases most of the energy back to the particle after impact. Elastomeric lining manufacturers and applicators will generally recommend an elastomeric hardness of 40–60 Durometer A for optimum life. As with metals or hard surface coatings, the lining must also be compatible with the fluid medium. An elastomer's hardness is directly related to its corrosion resistance. However, as an elastomer's hardness increases above a 40 A Durometer, its erosion resistance decreases. A Durometer selection of 40–60 A is somewhat of a compromise between erosion and corrosion resistance. Elastomers should not be used when large particles are present. The term "large particles" is relative to the impinging velocity and mass of the particle, as well as the thickness of the elastomeric covering. If the impinging particle can bottom out against the metallic substrate, elastomeric coverings should not be used. Even if most of the slurry might be suitable, a small percentage of tramp particles can do significant damage to the elastomeric covering. Since impact energy is a function of the impingement angle, the leading edges of impeller blades are almost always double wrapped. The most popular elastomeric coverings are natural rubber, neoprene, butyl, chlorobutyl, and hypalon. Improperly applied linings on high-efficiency impellers that significantly change the profile of the blade can cause increased erosion problems. Typically linings are double layered on the leading, trailing, and outside edges of impeller blades. These linings must be adequately feathered such that the transition from the double layer to the single layer is smooth to avoid generation of additional vortices.

Both thermoplastic and thermoset polymers do not have the ability to restore back to the particle most of the kinetic energy and are generally not as good in mixing slurry service. Hercules 1900 UHMWPE, touted as being a very abrasion-resistant polymer, was tested by the authors against polymeric protective coatings elastomers 2001-B (natural rubber Durometer A 30–40) and 1054-B (chlorobutyl rubber Durometer A 35–45). The testing procedure was identical to that specified in the Hercules 1900 UHMWPE bulletin. A

Material	Rate of weight loss, g/hr
Hercules 1900 UHMWPE	0.0975
Polymeric protective coatings 2001-B (natural rubber)	0.0104
Polymeric protective coatings 1054-B (chlorobutyl)	0.0124

50% sand-water slurry was used with a sand weight mean particle size of 53 μm. The specimen tip speed was 2.22 m/s. Weight loss was determined at various time intervals over an 8-hour period. The weight loss versus time was found to be linear with R^2 values for all three falling between 0.93 and 0.94. The rates of erosion were shown in Table 1.

As can be observed, the rate of weight loss for the thermoplastic polymer is 7 to 10 times greater than that for the elastomers tested.

Dickey and Fasano have provided a general reference on materials selection considerations [16].

2.2. Impeller Selection. There are many different impeller styles available to the designer. Selecting the correct impeller can often make a difference in impeller life of two or three times. Erosion of impeller blades can depend heavily on the flow regime, with flow regime being determined by the impeller Reynolds number

$$N_{Re} = \frac{\rho N D^2}{\mu},\qquad(2)$$

where ρ = density, N = impeller rotational speed, D = impeller diameter, μ = viscosity, and N_{Re} = Reynolds number, dimensionless.

Impellers in turbulent flow create shedding vortices that attach themselves to the back of impeller blades. There are a number of techniques that can be used to visualize these vortices. In Figures 4 and 5, telltales attached to the blade are used to visualize these vortices [17]. They are shown for both a relatively inefficient 45° pitched four-blade impeller and the Chemineer HE-3 high-efficiency impeller.

In these figures, the impellers are rotating clockwise when viewed from above. Thus, the blades are moving into the page, and the view is of the backside of the blades. These vortices cause very localized wear emanating from the backside or low-pressure side of impeller blades. These impeller vortices begin to diminish at Reynolds numbers below 10,000, become very weak below a Reynolds number of 500, and have completely disappeared below a Reynolds number of 10. As most slurry particles are heavier than the fluid, the centrifugal effect caused by the vortex will cause particles caught in the vortex to migrate to the OD of the vortex. Thus, the concentration of solids at the periphery of the vortex is much higher, and the rate of solid particle to surface impacts is much greater, increasing locally the rate of erosion. Of course, particles must be small enough to be captured in
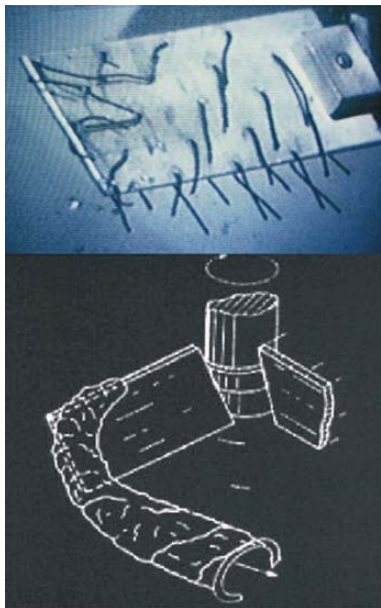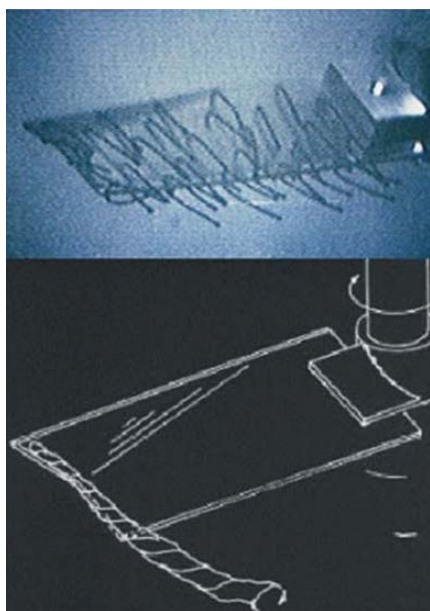
FIGURE 4: Pitched blade impeller vortex.

FIGURE 5: HE-3 impeller vortex.

FIGURE 6: Chemineer Maxflo W impeller.

FIGURE 7: Telltales on D-6 impeller blade.

these vortices before this effect would be observed. On an industrial scale, however, the greatest majority of slurry applications would have particles sufficiently small to be captured by these vortices.

There are a number of relatively efficient wide blade impellers used in solids suspension service. Fasano and Reeder [18] compared the erosion rate between a Chemineer Maxflo W impeller, Figure 6, and a standard 45° four-bladed-pitched impeller (refer to Figure 4).
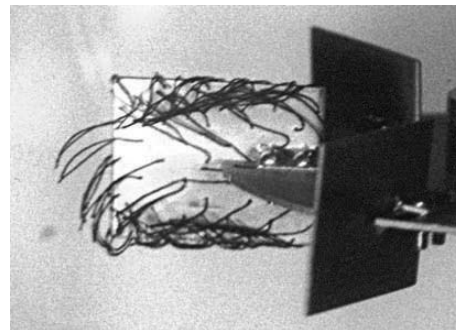
For the same level of solid suspension, these impellers utilize the same impeller diameter at the same speed. Therefore, velocities at the impeller are the same. The rate of erosion however for the pitched-blade impeller was, on a percentage basis, 59% greater than the erosion rate of the Maxflo W impeller.

Radial flow impellers are not very efficient in suspending solids. However, radial flow impellers are efficient in dispersing gasses. In applications where solids are present and a gas must be dispersed, they are often used. As with axial flow impellers, impeller efficiency changes with design. The Rushton or D-6 impeller, introduced in the late 1940s, creates a pair of vortices behind each blade in turbulent flow. These vortices, as we have observed with the pitched-blade impeller, can cause severe erosion from the backside of the blade. Figure 7 photo of the intertwined telltales on the backside of the blade demonstrates the size and nature of these vortices.

There exist today highly efficient radial flow impellers. The Chemineer CD-6 impeller was introduced into the marketplace in 1988, and the even more efficient Chemineer BT-6 was introduced in 1998. Both of these impellers exhibit very little tendency for vortex formation on the backside of the blade. This is demonstrated in telltale photos, in Figures 8 and 9. In each of these photos, the blades are rotating into the plane of the paper.

Under turbulent flow conditions, it is usually very beneficial, both from an erosion standpoint as well as a process efficiency standpoint, to select a high-efficiency style impeller. In transitional flow, there are still benefits to be achieved by the use of a high-efficiency impeller, but not as profound as in turbulent flow. In laminar flow, there is

TABLE 2: Possible process design selections for example.

Impeller diameter, m	Impeller dia./tank dia.	Impeller speed, rpm	Impeller power, kW	Impeller torque, kNm	Impeller tip speed, m/min	Relative wear life*	Approx. relative cap. cost
0.889	0.243	159	3.49	0.210	444	1.00	1.00
1.016	0.278	123	2.94	0.228	392	1.54	1.06
1.143	0.313	102	3.15	0.294	366	1.96	1.25
1.220	0.347	92	3.59	0.372	367	1.95	1.45
1.397	0.382	84	4.05	0.460	369	1.92	1.67
1.524	0.417	75	4.61	0.587	359	2.10	1.95
1.651	0.451	70	5.23	0.713	363	2.02	2.22
1.778	0.486	67	6.32	0.972	374	1.82	2.71
1.905	0.521	65	9.16	1.345	389	1.59	3.35

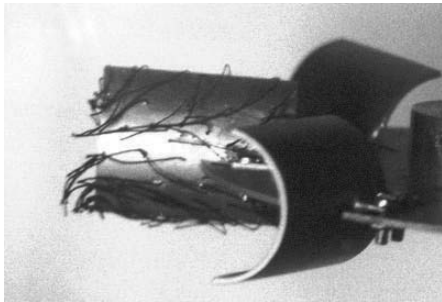*Relative wear based on assumed velocity exponent of 3.5.

FIGURE 8: Telltales on CD-6 impeller blade.

FIGURE 9: Telltales on BT-6 impeller blade.

no advantage in using a high-efficiency impeller either for erosion or solids suspension efficiency.

2.3. Horsepower and Speed Selection. As discussed earlier, erosion is very dependent on velocity, and typically in erosion-corrosion environments, the velocity exponent for the volumetric rate or weight rate of erosion is typically observed to be 2.5 to 4.0. In designing an agitator for the suspension of solids, the designer has a choice of selecting a number of power and speed combinations. Because solid suspension impeller efficiencies change with impeller style, impeller to tank diameter, and off-bottom clearance to tank diameter [19], a number of possible horsepower and speed choices can meet process objectives. The selection of a specific agitator design in the end should come down to economics. There are capital costs and operating costs. Capital costs are largely associated with the general size of the machine. The torque can generally best characterize the capital cost. Operating costs include the energy costs to operate the machine plus any maintenance costs. Maintenance costs include the costs of oil changes, new bearings, new gears, and new seal components, and in the case of erosion applications, the replacement of in-tank wear components, typically impeller blades. A close examination of the various horsepower and speed options should be examined closely in order to make an economic selection.

2.3.1. Example. For the sake of demonstration, let us assume that we need to design an agitator for suspending a 10% solution of sand in water. The sand will be assumed to have a weight mean particle size of $360\,\mu$m. The tank is 3.66 m diameter with a 2 : 1 elliptical dished bottom, and the water-sand slurry will have a liquid volume such that the depth of liquid in the tank is 3.66 m. The sand will be assumed to have a specific gravity of 2.4 and the water a specific gravity of 1.0. The viscosity of water will be assumed to be 1 mPa-s. The process solution requires that the solids be suspended to the "just suspended" condition such that no particles settle on the bottom of the tank for more than 2 seconds. All designs are to utilize a single HE-3 impeller one-third the tank diameter off-bottom. The horsepower, speed, and impeller diameter combinations that satisfy the process objective can be determined using solids suspension design procedures such as the article presented by Corpstein and others [19]. The following designs shown in Table 2 below all satisfy the off-bottom solids suspension process requirement.

Even though using small impellers operating at high speeds reduces capital costs and power, the high tip speeds of these designs lead to short wear lives. Using an intermediate size impeller that minimizes tip speed at the cost of higher capital and power costs maximizes the wear life. As can be observed, the torque and consequently the capital cost

TABLE 3: Comparison of equal suspension to equal tip speed.

Condition	Impeller dia., cm	Impeller speed, rpm	Impeller tip speed, m/min
Full scale design, 144 in. dia. tank	139.7	84	369
Scale-down design based on equal suspension	17.46	456	250
Scale-down design based on equal tip speed	17.46	672	369

increase dramatically with impeller to tank diameter ratios greater than 0.45 due to changes in the flow pattern generated by the impeller.

2.4. Scale-Down Studies. Since there is often an erosion-corrosion synergistic effect that cannot be predicted a priori with today's current data, any material selection should be studied on a smaller scale, before making a final choice. Since it is important to model the same hydraulic behavior over the blade, the authors recommend that the ratio of mean particle diameter to impeller diameter not exceed 0.008. For example, a mean particle diameter of 1 mm would suggest a small-scale impeller no less than 125 mm (4.9 in) diameter. It is also important to ensure that fluid regimes have not changed. If the impeller operation is turbulent on the large scale, it should also be turbulent on the small scale.

An optimum agitator horsepower and speed selection can be made as described above for the full scale. However, in order to determine the rate of erosion, scale-down studies should be made. A geometric scale-down for an equal level of solid suspension will result in a tip speed that will always be lower on the smaller scale, except when scaling down geometrically for very slow settling solids (<0.1 m/min). Wear rate, as previously demonstrated, is a strong function of velocity. Therefore, all scale-down tests should be made at equal tip speed. As an example, if we examine the 1.397 m impeller solution for the above described problem and scale this down to a 0.4572 m diameter tank, we would have the comparison provided in Table 3.

3. Conclusions and Summary

The rate of erosion is dependent on the following major static environmental factors: chemical environment, hardness of the solid particles, density of the solid particles, percent solids, the shape of the solids, the size of the solids including whether or not tramp solids are present, and type of impeller. The dynamic factors affecting erosion rate are fluid regime, impact velocity, impact frequency, and angle of impact. As there are no good means currently of predicting erosion rate, small-scale studies should be conducted emulating as much of the total environment as possible. These small-scale studies should be conducted using equal tip speed to mimic the full-scale rate of erosion.

Erosion in most mixing processes is a fatigue process normally accelerated by a liquid corrosive environment. The fatigue process occurs on a micro- or localized scale, and, as with macroscale fatigue, two stages of the erosion process have been observed. There is an incubation period followed

by the formation and growth of pits involving the removal of the metal or material. One of two routes is generally utilized in dealing with an erosion application. The high-velocity areas such as the blades are either made from hard materials or coated with hard ceramic materials such as tungsten carbide or silicon carbide. Alternatively, the blades are covered with some type of elastomeric covering.

Impeller selection is important especially in turbulent flow conditions. High-efficiency impellers will generally erode at a slower rate because the backside of the blades has minimized shedding vortices. In laminar flow, from an erosion standpoint, most impellers behave similarly due to a lack of vortices. Thus, the selection of the impeller should be based primarily on what is required to accomplish the desired process result.

A number of horsepower and speed selections that satisfy the process requirement should be examined to conduct an economic analysis. The lowest possible speed may not be the most economical. It is best to first design the most cost optimum agitator for the full scale. Then in order to estimate the corrosion rate, scale down on the basis of equal tip speed.

References

[1] R. Chattopadhyay, *Surface Wear, Analysis, Treatment and Prevention*, ASM International, Metals Park, Ohio, USA, 2001.

[2] S. G. Sapate and A. V. RamaRao, "Effect of erodent particle hardness on velocity exponent in erosion of steels and cast irons," *Materials and Manufacturing Processes*, vol. 18, no. 5, pp. 783–802, 2003.

[3] M. M. Stack, F. H. Stott, and G. C. Wood, "The significance of velocity exponents in identifying erosion-corrosion mechanisms," *Journal de Physique IV, Colloque C9, Supplement au Journal de Physique III*, vol. 3, 1993.

[4] *A New Slurry Pump Standard, Pumps and Systems*, The Hydraulic Institute, 2006.

[5] I. Fort, J. Medek, and F. Ambros, "Erosion wear of axial flow impellers in a solid-liquid suspension," *Acta Polytechnica*, vol. 41, no. 1, pp. 23–28, 2001.

[6] Y. Zheng, Z. Yao, X. Wei, and W. Ke, "The synergistic effect between erosion and corrosion in acidic slurry medium," *Wear*, vol. 186-187, no. 2, pp. 555–561, 1995.

[7] V. N. Amelyushkin and B. N. Agafonov, "Special features of erosion wear of rotor blades of cogeneration steam turbines," *Power Technology and Engineering*, vol. 36, no. 6, pp. 359–362, 2002.

[8] Y. A. Khalid and S. M. Sapuan, "Wear analysis of centrifugal slurry pump impellers," *Industrial Lubrication and Tribology*, vol. 59, no. 1, pp. 18–28, 2007.

[9] D. López, J. P. Congote, J. R. Cano, A. Toro, and A. P. Tschiptschin, "Effect of particle velocity and impact angle on

the corrosion-erosion of AISI 304 and AISI 420 stainless steels," *Wear*, vol. 259, no. 1-6, pp. 118–124, 2005.

[10] R. C. Corpstein and J. B. Fasano, "Erosion of rubber covered impeller blades in an abrasive service," *The Indian Chemical Engineer*, vol. 36, no. 1, 1990.

[11] J. Wu, B. Ngyuen, L. Graham, Y. Zhu, T. Kilpatrick, and J. Davis, "Minimizing impeller slurry wear through multilayer paint modelling," *Canadian Journal of Chemical Engineering*, vol. 83, no. 5, pp. 835–842, 2005.

[12] J. E. Miller and F. Schmidt, *Slurry Erosion: Uses, Applications and Test Methods*, ASTM, 1987.

[13] G. W. Stachowiak and A. W. Batchelor, *Engineering Tribology*, Butterworth-Heinemann, 3rd edition, 2005.

[14] R. W. Armstrong and F. J. Zerilli, "Dislocation mechanics based viscoplasticity description of FCC, BCC and HCP metal deformation and fracturing behaviors," in *Proceedings of ASME International Mechanical Congress and Exposition*, pp. 417–428, November 1995.

[15] K. C. Wilson, G. R. Addie, A. Sellgren, and R. Clift, *Slurry Transport Using Centrifugal Pumps*, Springer, 2nd edition, 2005.

[16] D. S. Dickey and J. B. Fasano, *Handbook of Industrial Mixing*, chapter 21, section 9, John Wiley and Sons, New Jersey, NJ, USA, 2004, Edited By Paul, Atiemo-Obeng and Kresta.

[17] J. B. Fasano, "Flow visualization techniques on rotating impellers," in *Proceedings of the Engineering Foundation Mixing Conference XII*, Pitosi, MO, USA, 1989.

[18] J. B. Fasano and M. F. Reeder, "An improved maxflo impeller," in *Proceedings of the North American Mixing Forum, Mixing Conference XVII*, Banff, Canada, August 1999, Paper 2.4.

[19] K. J. Myers, R. R. Corpstein, A. Bakker, and J. B. Fasano, "Solid suspension agitator design with pitched blade and high efficiency impellers," in *Proceedings of the AIChE Annual Meeting*, St. Louis, MO, USA, November 1993.